

Development of Solid State Luminescent Smart Materials for Multi-stimuli Probes

THESIS

Submitted in partial fulfilment
of the requirements for the degree of

DOCTOR OF PHILOSOPHY

by

Mr. Vishal Kachwal

ID. NO. 2014PHXF0015P

Under the supervision of

Prof. Inamur Rahaman Laskar



**BIRLA INSTITUTE OF TECHNOLOGY AND SCIENCE
PILANI (RAJASTHAN)**

July 2020



**Birla Institute of Technology and Science
Pilani – 333 031 Rajasthan, INDIA**

Phone: +91-1596-515675

Mob: + 91-9602213001

Email: ir_laskar@pilani.bits-pilani.ac.in
inamur00@gmail.com

Dr. Inamur Rahaman Laskar
Associate Professor
Department of Chemistry

CERTIFICATE

This is to certify that the thesis entitled “Development of Solid State Luminescent Smart Materials for Multi-stimuli Probes” submitted by Mr. Vishal Kachwal, ID No. 2014PHXF0015P for the award of Ph.D. Degree of the Institute embodies the original work done by him under my supervision.

Signature in full of the Supervisor

Name: Prof. Inamur Rahaman Laskar
Designation: Associate Professor

Date:

Dedicated

*To Maa and Papa who offered me
endless support.*

*To the God (Shyamji) for being with
me all the time*

To Sister who give me all strength.

*To my guru and friends who are
always there to support me*

*To those who believe in hard
work and never-give-up on their*

DREAMS...

Acknowledgements

PhD is a completely new world, one who does offer a significant new contribution to knowledge in their subject. My thesis represents not only my work in the laboratory or on the keyboard, but it is also a milestone achieved in half a decade of work in BITS Pilani and specifically in the laboratory (lab 3105). My experience in the BITS Pilani, Pilani campus has been nothing short of amazing. I remember I reported latterly on my first day to the administration on July 29th, 2014. Since then I have felt at home at BITS Pilani, Pilani campus. I have been given a unique opportunities and taken advantages of them. I have learned that some build the tools and those who utilized them. My passion is to combine all the tools used in cutting edge research, which helps humanity. My thesis is the result of the work of dozens of people, whom I wish to thank. However, the thesis is also the result of many experiences I have encountered at BITS Pilani from the dozens of remarkable individuals. I wish to express my deepest gratitude to all those remarkable individuals. They directly or indirectly helped me in the most memorable journey of my life.

First and foremost, I wish from in-depth heart to thank my supervisor, [Professor Inamur Rahaman Laskar](#), who allowed me to join his group in the BITS Pilani. He has been supportive and directed me since the days I began my work in the laboratory. I always remember he used to say something like that "there is nothing like problem every problem has its solution just think over the time again repeatedly the solution will be at your desk and also you are always the first one in and the last one out working on that problem!". These words encourage me to work more and more. Prof. Laskar supported me not only by providing a ground in his group for almost five and a half years but also academically and emotionally through the rough situation to finish the entire journey. Thanks to him, I had the opportunity to learn many new things. His inspiring hard work and constant motivation have helped me to understand better and remain optimistic during my study. Moreover, during the most difficult situation when writing this thesis, my supervisor has given me the virtuous support, and the freedom I needed to move forward. His forensic scrutiny of my technical writing has been invaluable.

I am immensely thankful to the Vice-Chancellor, Directors, Deputy Directors and Deans of Birla Institute of Technology and Science (BITS) Pilani for providing me with the opportunity to pursue my doctoral studies by providing necessary facilities and financial support.

Acknowledgements

My wholehearted gratitude to Prof. Sanjay Kumar Verma, (earlier Dean, Academic Research Division (ARD)), and Prof. Jitendra Panwar (present Associate Dean, Academic-Graduate Studies and Research (AGSRD)) BITS Pilani, Pilani Campus and Prof Shilpi Garg for managing all the documental works for the CSIR fellowship and Prof. Ram Kinkar Roy and Prof. Ajay Kumar, and Prof. Saumi Ray (earlier DRC Convener), and Prof Inamur Rahaman Laskar (present DRC Convener), Departmental Research Committee (DRC), Department of Chemistry, BITS Pilani, Pilani Campus for their official support and encouragement. I owe my sincere thanks to Dr Hemanth Jadav, earlier, nucleus members of ARD, other members of DRC, Department of Chemistry, BITS Pilani, Pilani Campus for their cooperation and constant support. I, overwhelmingly acknowledge the office staff of AGSRD, whose secretarial assistance helped me in submitting the various evaluation documents in time.

I am profoundly grateful for the mutual support and affection extended by all the respected teachers: Prof. S. C. Sivasubramanian, Prof. Subit K. Saha, Prof Ram Kinkar, Prof Anil Kumar (Ex-Head of Department), Prof Dalip Kumar, Prof. Saumi Ray (present head of Department), Prof. Bharti Khungar, Prof Raveej Sakuja, Prof. Surojit Pande, Prof Indresh Kumar, Prof. Madhushree Sarkar, Prof. Ajay K. Sah, Dr Prashant. Manohar, Dr Bibhas R. Sarkar, Dr Kiran Bajaj, Dr Mirinmoyee and staff members of Department of Chemistry, BITS Pilani, Pilani Campus for their constant guidance and substantial support at different stages during my research period. I am grateful to the members of my Doctoral Advisory Committee, Prof. Shamik Chakraborty and Prof. Paritosh Shukla, for their excellent cooperation in refining my research proposal and thesis. I am also highly thankful to Prof. Anil Kumar for providing opportunities to work in central NMR facility. My extended heartfelt thanks to the office and lab staff Mrs Pusplata to allow me to access the labs equipment and providing some required general chemicals, Mr Suresh, Mr Ashok and Mr Soni for their office work support and My sincere thanks to the Librarian Mr Giridhar Kunkur, BITS Pilani and other library staff for their help in utilizing the library facilities.

I am thankful to my research collaborators, Prof. Angshuman Roy Choudhury, IISER Mohali for Single X-Ray facility and valuable suggestions. I would like to say thanks to Prof Rajdeep Choudhury (BITS Pilani), Prof. Syamantak Mujumdar (BITS Pilani), Prof. Sudeshna M Chowdhury (BITS Pilani) for biological studies, Prof Shibasish Chowdhury (BITS Pilani) for docking studies, Prof Venkatesh K P (BITS Pilani) for dynamic viscosity measurements,

Acknowledgements

Prof. Nigam Rath (Department of Chemistry and Biochemistry and the Centre for Nano Science, University of Missouri-St. Louis) for Single X-ray facility.

Also, I am thankful to Prof. Pere Alemany (University at de Barcelona, Spain), Dr Ram Kinkar Roy (BITS Pilani, Pilani Campus) for validating some of the experimental data through computational calculations. I extend my thanks to Ms Abhilasha Srivastava and Ms Leena fageria for the biological works and fruitful discussion on biology. Extremely thankful to the Dr Amrit, Ms Jagrity and Dr Parva for the computational discussion and work.

I am indebted to my seniors [Dr Parvej alam](#); he thought me a lot how to handle the life situation and how to solve the problems in research. I have learned most of the things related to research during his tenure as a PhD student, [Dr Salem Pasha](#) who reminds me to work until it has done and [Dr Dinesh Kumar Sengottuvelu](#); he is such a nice person, his presence and experience made me learn the new concepts in the research and how to see the problems. I am very much thankful to my lab mates [Mr Pramod Raichure](#), [Mr Ram Prasad Bhatt](#) and [Ms Jagrity](#) for full fruit discussion over all the concepts and helping me in my thesis. It was amazing to stay in Lab no. 3105, my old quarter near Pooja garden and new quarter 21/2f/4 during the journey. My sincere thanks to all my supportive seniors Dr Rituparna, Dr Noorulha, Dr Ashok, Dr Suman, Dr Pragathi, Dr Ganesh, Dr Arun, Dr Archana, Dr Omprakash, Dr Khima, Dr Anoop, Dr Sachin, Dr Meenakshi, Dr Saroj, Dr Sunita, Dr Nisar, Dr Venkat Reddy, Dr Pallavi, Dr Abdul, Dr Faiyaz, Dr Santhosh Kumari, Dr Santhosh, Dr Hitesh, Dr Shusheela, Dr Mukund and Dr Satish for their friendly guidance and motivation.

I would like to pay my special regards to my batch mates Mrs Sonam Sharma, Mrs Vaishali, Ms Bijoya Das, Ms Moyana Das, Mr Abid and Mr Vimal for their support in course work and cheering up all the time during my journey. I thank all the departmental colleagues, friends and my Juniors belonging to the BITS Pilani, Mr Yadav, Mrs Chavi, Ms Mamta Sharma, Ms Neha, Mrs Mamta, Ms Krishma, Mr Mahesha, Mr Dhritabrata, Mr Amol, Mr Bintu, Mr. Santosh, Ms. Ashwariya, Ms. Prachi, Ms Gurpreet Kaur, Mr Sumit, Ms Monika, Ms. Soumona, Ms Divya, Ms Prakriti, Mr Rohitash, Mr Narshima, Mr Prakash, and Mr Dhanjay for their generous assistance in each moment. I am also thankful to all my friends and all other persons whose names are not accommodated here.

Acknowledgements

I must be highly thankful to my unfailing friends Dr Devesh S Agarwal, Dr Nitesh Nadwana, Dr Maish Mehara, Dr Shiv Dhiman for their strong support in a critical situation and making this journey fruitful without them the journey would be hard.

A special acknowledgement goes to my close friends Ms Jyothi Yadav and Mr Vikki Narayan Shinde. Both were a true friend ever since when they have joined in the Department. Ms Jyothi Yadav is an amazing person in too many ways helps me in spiritual connection, her thoughts to grow and help humanity makes the positive environment and for always being there by my side and for their most awaiting tea sessions. Both of them help me in my hard time, hold in difficult times, unflagging love, and immense care all over my PhD.

The existence of me, as a person, as a scholar, was impossible without my great parents. The vision, ethical principles, and teaching about life, which I had inherited from my father (Venugopal Kachwal) is a constant source of inspiration and always accompanies me like a shadow. Words cannot define the love and sacrifice of my mother (Kavita Kachwal). She has unconditionally given me the support and confidence in everything that I strive for. In my successful stints, Papa and maa celebrated louder than me, and I feel confident that they are always there for me. My parent's vision, ethical principles, moral support, endless patience and eternal inspiration, to face any situation in life have guided to the successful completion of this work. I would also like to acknowledge my litter sister (Vaishnavi Kachwal), she makes me forget my stress and My Uncle (Neelesh Kachwal) for the supportive nature towards me.

I am heart full of thanks to the God for providing me with the inner strength, path and mental strength that always pushed me to spend the night in the lab, to stick with the chair, to cry alone and laugh publicly. Whenever I failed to do, my belief in the immense hard work provoked me to hustle in silence and try hard. It was a memorable saga of a journey and thanks, everyone who has been a part of this. May God shower his choicest blessings and prosperity on all those who assisted me in any way during the completion of my PhD.

I duly acknowledge valuable financial support in the form of a research fellowship, infrastructure and financial support during my research work from DST-India, CSIR-New Delhi. BITS Pilani, Rajasthan, UGC.

Thanks to all

Date

Place: Pilani, India

Vishal Kachwal

Table of Contents

<i>Contents</i>		<i>Page No.</i>
<i>Certificate</i>		i
<i>Dedication</i>		ii
<i>Acknowledgements</i>		iii
<i>Table of Contents</i>		vii
<i>Abstract</i>		xiii
<i>List of Abbreviations and symbols</i>		xvi
<i>List of Tables</i>		xx
<i>List of Schemes</i>		xxi
<i>List of Figures</i>		xxii
Chapter-1	Introduction and Research Gap	1-40
1.1	Solid Luminescent Materials	1
1.2	Organic Based Conventional fluorophores for sensing and their disadvantages	1
1.3	Aggregation Caused Quenching (ACQ)	2
1.4	Aggregation Induced Emission	4
1.4.1	JAF (J- Aggregate Formation)	6
1.4.2	ESIPT (Excited State Intramolecular Proton Transfer)	8
1.5	Fluorescent based Variable analyte Responsive Probes	9
1.5.1	pH Sensing Probes	10
1.5.2	Solvatochromic luminescence probes	15
1.5.3	Albumin Sensing	16
1.5.4	Viscosity Responsive Probes	19
1.5.5	Explosive Sensing Probes	22
1.5.5.1	What is Explosive?	22
1.5.5.2	Importance of explosive detection	24
1.5.5.3	Techniques for the detection of explosives	24

Table of Contents

1.6.	Research Gap	29
1.7	Reference	31
Chapter - 2	Materials, Methods and Instrumentation	41-54
2.1	Materials	41
2.1.1	Used Reagents	41
2.2	Methods	42
2.2.1	Synthesis	42
2.2.2	Sample preparation to investigate the 'Aggregation-induced Emission (AIE)' property	42
2.2.3	Fabrication of thin-film on a thin glass substrate for photoluminescence (PL) measurement	42
2.2.4	Fluorescence quantum yield calculations	43
2.2.5	Luminescence quenching titration study in 90% water fraction and in Solution state	44
2.2.6	Experimental procedure for detection limit calculations	44
2.2.7	Calculation of Forster distance, energy transfer rate, the efficiency of energy transfer, the distance between the donor and acceptor	44
2.2.8	Solvatochromism	45
2.3	Instrumentation	45
2.3.1	UV-Visible spectrophotometer	45
2.3.2	Steady-state spectrofluorometer	46
2.3.3	Computational study	47
2.3.4	Docking studies	48
2.3.5	Other instruments	48
2.3.6	Cell culture	51
2.3.7	In vitro cytotoxicity assay	51
2.3.8	Microscopic imaging and cellular uptake studies	51
2.3.9	Co-localization Study	52

Table of Contents

2.3.10	Statistical analysis	52
2.3.11	Dynamic Measurements	52
2.4	Reference	53
Chapter - 3	Hydrogen-Bond Sensitive Multi-Stimuli Probes	55-109
3.1	Aggregation-induced emission active and hydrogen bond sensitive Schiff base with distinct response to various stimuli.	55
3.1.1	Introduction	55
3.1.2	Result and Discussion	58
3.1.2.1	Synthesis and characterization	58
3.1.3	Absorption Properties	59
3.1.4	Emission Properties	62
a	Observation of ESIPT	62
b	Aggregation-induced emission (AIE)	67
c	pH Probe	68
3.1.5	In Vitro Imaging	72
3.1.6	Aluminium (III) Detection	72
3.1.5	Conclusion	77
3.2	AIE active Heteroleptic Bis Cyclometalated Iridium (III) Complex: Role of hydrogen bonding in multi stimuli response	78
3.2.1	Introduction	78
3.2.2	Result and Discussion	80
i	Synthesis	80
i-a	Proof for the presence of Intramolecular Hydrogen bonding	84
ii	Photophysical property	85
a	Absorption and Emission of Complex	85
b	Dual Solvent effect	87
c	Aggregation-induced emission (AIE)	94

Table of Contents

d	pH Probe	96
e	Bovine Serum Albumin (BSA) Detection	98
3.2.3	Docking Studies	101
3.2.4	Conclusion	104
3.3	Reference	104
Chapter - 4	<i>Viscosity Sensitive probe</i>	110-136
4.1	Introduction	110
4.2	Results and Discussion	112
4.2.1	Synthesis	112
a	Synthesis of 1,2,3,3-Tetramethyl-3- indol-1-ium (Iodide) (TI)	112
b	Synthesis of 1,3,3-Trimethyl-2-(4-(pyridine-2-yl) styryl) -3H-indol-1-ium (I-) (TPSI I).	112
c	Synthesis of 1,3,3-trimethyl-2-(4-(pyridine-2-yl)styryl) -3H-indol-1-ium (PF6-) (TPSI PF6)	116
4.2.2	Cyrstal Structure	117
4.2.3	Photophysical property studies	118
4.2.3.1	Viscosity sensing	119
4.2.3.2	Photoinduced Isomerization in Solution State	121
4.2.3.3	Solid State Photoinduced Isomerization	122
4.2.3.4	Mechanism for Photoisomerization	124
4.3	Measurement of intracellular viscosity in cancerous and normal Cells under different conditions	131
4.4	Conclusion	134
4.5	Reference	134
Chapter – 5	<i>Explosive sensing</i>	137-222
5.1	Aggregation-induced enhanced emission (AIEE) active Pyrene derivatives for efficient detection of nitroaromatics	137
5.1.1	Section-I A Multifunctional Pyrene-Pyridine based Ratiometric Explosive Senisng Probe	137

Table of Contents

5.1.1.1	Introduction	137
5.1.1.2	Result and Discussion	138
i	Synthesis and Characterization	139
ii	Photophysical properties	141
ii-a	Absorption and emission property study	141
ii-b	Effect of Protonation (H ⁺) on PyPr	142
ii-c	Excimer Formation	145
ii-d	Aggregation-induced emission enhancement (AIEE)	146
ii-e	Detection of nitroaromatics based explosives	149
ii-f	Metal Ion Al(III) Sensing	152
Section II	Strategically modification of Pyrene-derivatives to improve Sensitivity in explosive sensing to make efficient ultrasensitive probe for explosives	157
5.1.2	Introduction	157
5.1.2.1	Result and Discussion	157
i	Synthesis and Characterization	157
ii	Photophysical properties	162
ii-a	Absorption and Emission spectra	162
ii-b	AIEE property study	164
ii-c	Excimer formation	170
ii-d	Explosive sensing	171
5.1.3	Conclusion	178
5.2	AIEE active conjugated mesoporous Oligomers (CMOs) for low cost detection of nitro-aromatic based explosives	180
5.2.1	Introduction	180
5.2.2	Experimental section	182
i	Synthesis of CMO1 and CMO2	182
ii	Characterization	185
5.2.3	Result and Discussion	194
i	Synthetic strategy and Characterization of Pores	194

Table of Contents

ii	Photophysical studies	198
ii-a	Absorption and Emission Properties	198
ii-b	Aggregation-induced enhanced emission (AIEE)	200
ii-c	Explosive sensing	204
5.2.4	Conclusion	216
5.3	Reference	216
Chapter – 6	Future Scope of the Work	223-226

Appendices

[A-1] List of Publications

[A-2] List of Oral/Poster Presented in Conferences and Workshops

[A-3] Brief Biography of the Candidate

[A-4] Brief Biography of the Supervisor

Abstract

Nature itself is a very beautiful complex system which manages everything single-handed smartly. Nature has many interesting facts and materials which are still to be discovered. In nature, we could find the natural molecular machine which we are trying to mimic in day to day life for the ease of living. The solution by which nature tackle itself to the complex problems etc., if we go on the count, there are plenty of unknown smart materials and facts which scientist either try to reconstruct in the laboratory or to mimic the system. The present thesis entitled “**Development of Solid State Luminescent Smart Materials for Multi-stimuli Probes**” exactly depends on these following three aspects –

- 1) To understand the various facts of nature and mechanism to mimic in the laboratory.
- 2) To discover the factors which are responsible for being smart luminescent materials and
- 3) To utilize these materials for sensing such parameters which are very important in day to day life.

The thesis divided into six chapters. In the **first chapter**, one can find the brief overview about the concepts discussed in the thesis such as hydrogen bonding, fundamentals of fluorescence, a mechanism such as Photoinduced Electron Transfer (PET), Excited State Intramolecular Proton Transfer (ESIPT), Resonance Energy Transfer (RET) etc. and also scope of the work.

In the **chapter Secound**, the detailed of all the materials, instrument utilized and the methods used during the thesis are described.

The **third chapter** describe the role of hydrogen bonding in multi stimuli sensing. The chapter is divided into two parts. Part A describe the unexplored potential of an ESIPT and AIE active benzothiazole type of Schiff -base (BTIP). The BTIP probe was capable of pH sensing and was also tested for internalization in cancerous cells for intracellular imaging. Part B describe on the vital role of hydrogen bonding to explain some unusual photophysical behaviors of an ‘Aggregation-induced emission’ (AIE) active Iridium(III) complex. The predominance of hydrogen bonding leads to the complex’s multifunctional character, viz., sensing ability of base and protein (BSA), pH probing, and solvatochromism. A robust green emission was obtained with the addition of BSA into a solution of Ir(III) complex. The sensitivity of the complex to BSA was measured to be 9.3 pM.

The **fourth chapter** describe about the designed and synthesis of a simple novel ultrasensitive viscosity triggered emission probe TPSI I which showed very weak photoluminescence in a low-viscous environment. In contrast, in the high viscous medium,

Abstract

the emission intensity of the TPSI I probe was significantly enhanced. The very weak photoluminescence of the probe even in the solid-state was due to the continuous motion of the rotating units, which dissipated the excitation energy through non-radiative decay. The ultra-sensitivity of the TPSI I probe to detect diminutive changes in viscosity was verified through Forester Hoffmann equation ($\alpha = 1.02$) and other experimental supports. Finally, the viscosity dependent enhanced photo-luminescence intensity of TPSI I was analyzed using in vitro studies. This work offers a potential and efficient probe for diagnosing of cancerous cell in different state along with distinguishing cells that are exposed to pathological conditions. This work thus offers a potential and efficient probe for detection of altered intra-cellular viscosity or any fluctuations in the viscosity of normal, HUVECs and tumor cells was monitored which can be utilized for pre-diagnosis of diseases.

The **fifth chapter** divided in two groups Part A and Part B. Part A again sub divided into two sections. First section of part A describe simple ratiometric push-pull and ‘aggregation-induced emission enhancement (AIEE)’ active pyrene based compound, 2-(pyren-1-yl)pyridine (PyPr). The synthesized compound was established as a highly selective and sensitive multi-functional sensor that exhibits a ratiometric fluorescent response, detecting nitro explosive (picric acid), $[H^+ \text{ ion}]$ and Al^{3+} [observed sensitivity: 56 nM (12.82 ppb) for picric acid; 2.4 nM (0.27 ppb) for trifluoroacetic acid; 2.3 nM (0.86 ppb) for Al^{3+}]. The probes show emission tuning ability on varying their concentration in solution. Section- II of part A is about the tuning of solid and solution phase emission with simple push-pull ‘Aggregation Induced Enhanced Emission’ (AIEE) pyrene compounds for deeper understanding on the mechanism for selectivity and sensitivity towards the nitro explosives with lowering the detection limit upto ppt (parts per trillion) level. In Part B gives the reports on straightforward strategy for the design and synthesis of highly luminescent conjugated mesoporous oligomers (CMOs) with ‘Aggregation- induced enhanced emission’ (AIEE) feature through Wittig polymerization of the molecular rotor. The quick dissipation of the excited photons was successfully controlled by the restriction of rotation of the phenyl units through the formation of the mesoporous network scaffold in solid/thin film, which provides the high quantum yields for the interlocked CMOs system. Both the CMOs are sensitive and selective to the various nitroaromatics based explosives, whereas CMO1 is more sensitive ($K_{sv} = 2.6 \times 10^6 \text{ M}^{-1}$) towards the picric acid. The increased quenching constant for CMO1 is due to its increased quantum yield and high-energy transfer efficiency. The mechanism for sensing has been studied in detail. The larger pore size and pore density in the mesoporous network of CMO1 are found to be responsible for the greater extent of energy transfer from CMO1 to

Abstract

picric acid. Furthermore, CMO1 has been employed for low-cost filter paper-based detection of trace nitroaromatic containing explosive materials. The final sixth chapter describe the future avenues and direction of the modified probes.

Keywords:-Aggregation-induced emission, Ultrasensitive explosive probes, Albumin sensing, conjugated mesoporous oligomers, photoinduced electron transfer (PET) and resonance energy transfer (RET), pH probes, hydrogen bond effect, caner cell, bioimaging.

List of abbreviations and symbols

Abbreviation/Symbol	Description
α	Alpha
Å	Angstrom
AU	Arbitrary Unit
a	Ongsager cavity radius
ACN	Acetonitrile
n-BuLi	n-Butyl lithium
β	Beta
Bu	Butyl
BE	Binding Energy
BET	Brunauer-Emmett-Teller
Calcd.	Calculated
^{13}C	Carbon-13
Conc	Concentration
CV	Cyclic voltammetry
$^{\circ}\text{C}$	Degree centigrade
c	velocity of light
δ	Delta
CDCl_3	Deuterated chloroform
d	Doublet
dd	Doublet of doublet
DCM	Dichloromethane
DMF	N,N-Dimethylformamide
DMSO-d_6	Deuterated dimethylsulfoxide
DFT	Density Functional Theory
EI	Electron ionization
ESI	Electron spray ionization
EDS	Energy Dispersive Spectroscopy
EtOAc	Ethyl acetate

List of abbreviations and symbols

eV	Electron Volt
Equiv	Equivalent
e.g.	exempli gratia
ϵ	dielectric constant
ϵ	molar extinction coefficient
ξ	spin-orbit coupling constant
Δf	solvatochromic shift
f_w	Water fractions
FTIR	Fourier Transform Infrared Spectroscopy
FESEM	Field Emission Scanning Electron Microscopy
G	Gram
h	Hours
HRMS	High resolution mass spectra
IR	Infrared
Ir	Iridium
IC ₅₀	half maximal inhibitory concentration
ILCT	Intraligand charge transfer
Hz	Hertz
J	Coupling constant
Kcal	Kilocalories
K _{sv}	Stern-Volmer quenching constant
LLCT	Ligand -to- ligand charge transfer
LMCT	Ligand -to- metal charge transfer
λ	Wavelength
k _T	Rate of energy transfer
lm	lumens
MS	Mass spectrometry
M.p.	Melting point
m	Multiplet
mg	Milligram

List of abbreviations and symbols

MHz	Mega hertz
MLCT	Metal -to- Ligand charge transfer
min	Minutes
mL	Milliliter
μM	Micro molar
M	Molar
mmol	Millimole
MW	Microwave
$\bar{\nu}$	Wave number
μ	dipole moment
N_2	Nitrogen gas
NMR	Nuclear magnetic resonance
nm	Nano molar
NIR	Near-infrared Radiation
PEG	Polyethylene glycol
Pt	platinum
PXRD	Powder X-ray Diffraction
^{31}P	Phosphorous-31
ϕ	Quantum efficiency
ppm	Parts per million
ppb	parts per billion
PL	Photoluminescence
ppt	parts per trillion
%	Percentage
rt	Room temperature
R_0	Förstor distance
s	Singlet
π	Pi
h	Planck's constant
σ	standard deviation

List of abbreviations and symbols

t	Triplet
TFA	Trifluoroacetic acid
τ	Tau
θ	Diffraction angle
THF	Tetrahydrofuran
TLC	Thin layer chromatography
TMS	Tetramethylsilane
OTf	Trifluoromethanesulfonate
δ	Parts per million
μL	Microliter
μM	Micromolar
v	Volume
W	Watt

List of Tables

No.	Title	Page No.
3.1.1	Second-order perturbation energies E^2 {donor (i) \Rightarrow acceptor (j)} *	61
3.1.2	Calculated major orbital excitation contributions (%), energy difference (in eV), obtained from electronic transitions analysis with TDDFT (B3LYP) method, basis set 6-31+G(d,p) for organic molecule	62
3.1.3	Table shows the lifetime decay of BTIP in different solvents	65
3.1.4	Comparison of the sensitivity of detection of Al^{3+} (Literature reports vs present work)	75
3.2.1	It shows the emission (λ_{max} , nm), Absorption (λ_{max} , nm), and Quantum yield, radiative and nonradioactive decay rate for complex 1 in different solvents.	92
3.2.2	Binding pockets of top 10 conformations of the complex 1	102
5.1.1	Calculated major orbital excitation contributions (%), energy difference (in eV), obtained from electronic transitions analysis with TDDFT (B3LYP) method for PyPr	141
5.1.2	Calculated significant orbital excitation contributions (%), energy difference (in eV), obtained from electronic transitions analysis with TDDFT (B3LYP) method for PyPh, PyPrCN, PyPm & PyTr	163
5.1.3	Details of the absolute quantum yield of probes with increasing water fraction in THF.	168
5.1.4	It shows quenching efficiency, detection limit, overlaps integral and distance between donor and acceptor.	177
5.2.1	It shows the difference in the intensity of CMO1 in aggregated and non aggregated form	205
5.2.2	It shows the calculated value of overlap integral ($J(\lambda)$), Forster distance (R_0) distance between the donor and acceptor (r).	211

List of Schemes

No.	Caption	Page No.
3.1.1	Synthesis of BTIP	59
3.2.2	Schematic representation of Enol and Keto form of BTIP	62
4.1	Synthesis of Synthesis of 1,2,3,3-Tetramethyl-3H-indol-1-ium (Iodide) (TI), 3,3-Trimethyl-2-(4-(pyridine-2-yl) styryl)-3H-indol-1-ium (I) (TPSI I) & 1,3,3-trimethyl-2-(4-(pyridine-2-yl)styryl)-3H-indol-1-ium (PF ₆ ⁻) (TPSI PF ₆)	112
5.1.1	Synthesis of Pypr [2-(pyrene-1-yl)pyridine]	139
5.1.2	Synthesis of pyrene derivatives and thin film emission image under exciting by UV lamp (λ_{exc} , 365 nm)	158
5.1.3	Schematic representation of the conclusion drawn from the experiments	178
5.2.1	Synthesis of TPE ylide monomer 5.2.4 (NBS = N-Bromosuccinimide	182
5.2.2	Synthesis of Tetrakis(4-bromophenyl)ethylene (5.2.5) and 1, 1, 2,2-tetrakis(4-formyl-(1,1'-biphenyl)) ethane monomer (5.2.6)	183
5.2.3	Synthesis of Tris(4-formyl phenyl)amine (5.2.7)	184
5.2.4	Synthesis of CMO1	184
5.2.5	Synthesis of CMO2	185
5.2.6	Schematic illustration of photoinduced electron transfer (PET) mechanism	209
6.1	Chemical structure of modified Schiff base	223
6.2	Chemical structure of modified Ir(III) bis-cyclometallated Complex	224
6.3	Chemical structure of modified Viscosity sensitive probes	225
6.4	Chemical structure of modified pyrene probes for sensitive nitro explosive detection.	226

List of Figures

No.	Caption	Page No.
1.1	Structure of the fluorescence sensors	1
1.2	Structure of the Multi analyte probe	2
1.3	Few ACQ luminophores	3
1.4	Planar luminophore molecules such as perylene tends to aggregate as discs pile up, due to strong π - π stacking interactions between the aromatic rings, which commonly turns “off” light emission	3
1.5	Few Structure of organic Aggregation Induced Emissive molecules	4
1.6	(a) HPS molecule is non-emissive in solution but becomes highly emissive upon aggregation, due to the restriction of intramolecular rotation (RIR) of the phenyl rotors against the silole stator in the aggregated state b) 10,10',11,11'-tetrahydro-5,5'-bidibenzo[a, d][7]annulenyliene (THBA) behaves similarly as HPS, high emission in aggregated state is due to the restriction of intramolecular vibration.	6
1.7	Structure of cyanine dyes forming J-aggregates	7
1.8	Examples were illustrating the AIE and J-aggregates formation (JAF)	7
1.9	J-aggregates type of arrangements	8
1.10	(a) Representation of different level of ESIPT process (b) Structure of enol (E) and Keto (K) form of the simple (E)-2-(benzo[d]thiazol-2-yl)-5-((2-hydroxybenzylidene) amino) phenol	8
1.11	Earlier probe for pH sensing	11
1.12	Structure of pH probe based on fluorescein	11
1.13	Mechanism of a cyanine dye in pH sensing	12
1.14	Structure of Schiff base type of dye	13
1.15	AIE anthracene dye for pH probing	13
1.16	Structure of the AIE and pH-responsive molecular probe	14
1.17	Dual site fluorescence lysosome targeted pH sensing probe.	15
1.18	Structure of AIE probe based on TPE unit for protein sensing (40-43)	17
1.19	Structure of AIE propeller shape probe for protein Sensing	18
1.20	Structure of tetra aniline	18
1.21	Structure of porphyrin-based rotor for mapping intracellular viscosity	20
1.22	Structure of cyanine and BODIPY type of viscosity probes	21

List of Figures

No.	Caption	Page
1.23	TPE based AIE viscosity sensor for organelle targeting probes	21
1.24	Structure of organelle targeting viscosity probe	22
1.25	Flow chart representing the classification of the explosive materials.	23
1.26	Structure of the explosive sensing probe (58-61)	27
1.27	Chemical structures of compound (64-66)	27
1.28	Chemical structure of 67-71	28
1.29	Chemical structure of fluorophores based on quinoline and benzimidazole (72, 73)	29
2.1	Schematic representation of UV-Visible Spectrometer	46
2.2	Block diagram of a steady-state spectrofluorometer	46
2.3	Experimental setup for measuring the dynamic response of cells	53
3.1.1	It shows the structure of a probe molecule which detects F^- , CH_3COO^- , and $H_2PO_4^-$ ratiometrically through the ESIPT process	56
3.1.2	It shows the structure of the ESIPT active probe molecule for pH and Zn^{2+} detection	56
3.1.3	It shows the structure of the ESIPT active benzothiazole based probe for pH sensing	57
3.1.4	(a) 1H NMR and (a) ^{13}C NMR of BTIP	59
3.1.5	a) Absorbance spectra of the BTIP (10^{-4} M) $\lambda_{max} = 275$ & 370 nm b) Emission spectrum of an BTIP in methanol (10^{-4} M)	60
3.1.6	Structure of probe (a) BTIP, b) HOMO c) LUMO (d) Labelled optimized structure of BTIP form	62
3.1.7	(a) Emission spectra of compound in different solvent (10^{-4} M)	63
3.1.8	(a) Emission spectra of the BTIP with gradual variation of excitation (a) BTIP in methanol (10^{-4} M) (b) BTIP in benzene (10^{-4} M).	64
3.1.9	Lifetime decay of BTIP in the following solvents methanol, cyclohexane, benzene at (a) monitored at 450 nm (b) monitored at 550 nm (c) Lifetime decay calculations using Data Station (Das6) software	65
3.1.10	Packing diagram shows two short contacts $C-H \cdots O$ and $CH \cdots \pi$ in the range of 2.28-2.83 Å and hydrogen bonding between $N \cdots H-O$ (1.733 Å).	66

List of Figures

No.	Caption	Page No.
3.1.11	Comparison of the angle between the crystal structure and calculation from DFT based modelling a) ORTEP structure of compound showing different angle; b) optimized structure from DFT	66
3.1.12	(a) PL spectra of BTIP in different fraction (0-90%) methanol-water fraction (b) plot of PL intensity vs water fraction; (c) fluorescence image of BTIP in different water fractions ($\lambda_{\max}^{\text{ex}}$, 365 nm).	67
3.1.13	Emission spectra of BTIP (10^{-4} M methanol) with increasing concentration of PEG (600)	68
3.1.14	Absorption spectra of compound (methanol, 10^{-4} M solution) in different pH buffer solutions (a) pH1-5 (b) pH6-14. (c) Emission plot of BTIP (1×10^{-4} M, MeOH) in the presence of acid (trifluoroacetic acid, TFA) and base (try ethylamine, TEA), (c, d) $^1\text{HNMR}$ of BTIP in the presence of TFA trifluoroacetic acid.	69
3.1.15	(a) Emission spectra of BTIP (10^{-4} M in methanol) in different pH buffer solutions, (b) image of BTIP in different buffer solutions taken under UV-Lamp $\lambda_{\max} = 365$ nm ;	70
3.1.16	Optimized structure to show a comparison between the angles $\angle\text{C2C3C12}$ and $\angle\text{C14N11C12}$ in (a) BTIP in acidic medium and (b) BTIP in neutral medium. (c, d) proposed mechanism for fluorimetric switching of BTIP in reponse to acid and base	70
3.1.17	Stacked NMR spectra with a comparison between the BTIP in neutral medium and after exposing it to base and acid	71
3.1.18	(a) In vitro cytotoxicity analysis; (b) Fluorescence microscope image of Huh7 cells incubated with BTIP for 24 h.	72
3.1.19	a) PL spectra of the BTIP with $c = 10^{-4}$ M in methanol upon the addition of 1 equivalent of different metal ions (b) image of L ($c = 10^{-4}$ M) with 1 equivalent of different metal ions, respectively; from left to right (under 356 nm UV lamp); (c) 3D column diagrams of the relative PL intensity of BTIP with different metal ions at I_{473} . Pink bars represent the addition of various metal ions to complex L, and blue bars represent the subsequent addition of	73

List of Figures

No.	Caption	Page No.
	Al ³⁺ (1 equivalent) to the solutions mentioned above [1 + different metal ions+Al ³⁺ (d) The absorption spectra of BTIP (1x10 ⁻⁴ M) with a gradual increase in the Al ³⁺ (1x10 ⁻⁴ M) concentration;	
3.1.20	(a) Emission spectra of BTIP(in methanol, 1x10 ⁻⁴ M) titrated with different concentration of Aluminum nitrate; (b) Linear fitting of BTIP with the Al ³⁺ .	74
3.1.21	(a) FTIR spectra of BTIP in absence and presence of aluminum ion (Al ³⁺) (b) Proposed structure (c) ¹ H NMR spectrum of BTIP + Al ³⁺ (d) ¹³ C NMR spectrum of BTIP+ Al ³⁺	76
3.1.22	Mass spectra of complex (BTIP+ Al ³⁺)	77
3.2.1	¹ H NMR spectrum of complex 1 (b) ¹³ C NMR spectrum of complex 1 (c) HRMS spectrum of complex 1	83
3.2.2	(a, b, c) ¹ H, ¹³ C and HRMS spectra of complex 2	84
3.2.3	Optimized geometry of Complex 1 (b) Figure showing the chemical shift of -OH proton of 1 in d6-DMSO & CDCl ₃ and calculation of Hydrogen Bond Acidity (A).	85
3.2.4	(a) Absorbance spectra of Complex 1 in methanol and DCM (1*10 ⁻⁵ M), Frontier molecular orbital diagram of 1 b)HOMO and c) LUMO, calculated by using B3LYP/6-31G+ (d,p)* and LANL2DZ as implemented on Gaussian 09	86
3.2.5	(a) Emission spectra of the compound 1 and 2 in THF (tetrahydrofuran) (1*10 ⁻⁵ M) solutions, (b) Normalized PL spectra of 1 in different solvents (1*10 ⁻⁶ M). ((MET = methanol, BUT = butanol, TBUT = tertiary butanol, TOU = toluene, THF = tetrahydrofuran, BEN = benzene, ETHACE = ethylacetate, DIOX = dioxane, CHCl ₃ = chloroform, CH ₂ Cl ₂ = dichloromethane, ACN = acetonitrile, DMSO = dimethylsulfoxide)) (c) Lippert Mataga plot of 1 between stokes shift vs. f(ε,η) (orientational polarizability)	86
3.2.6	Absorption Spectra of complex in different solvents (1*10 ⁻⁶ M) (MET = methanol, BUT = butanol, TBUT = tertiary butanol, TOU = toluene, THF = tetrahydrofuran, BEN = benzene, ETHACE = ethylacetate, DIOX = dioxane, CHCl ₃ = chloroform, CH ₂ Cl ₂ = dichloromethane, ACN = acetonitrile, DMSO = dimethylsulfoxide).	87

List of Figures

No.	Caption	Page No.
3.2.7	PL spectra of the 1 in the presence of (a) nonhydrogen bonding (NHB) or weak hydrogen bonding acceptors solvents (WHB) (TOU= Toulene, THF = tetrahydrofuran, BEN = benzene, ETHYACE = ethylacetate, DIOX = dioxane) (b) chlorinated solvent (c) Hydrogen bonding acceptors (HBA) solvents (DMSO = dimethyl sulfoxide, ACE = acetone, Acetamide , P=O = hexamethyl phosphoramidate, NMP = N-methyl pyrrolidine) (d) Hydrogen bond donating (HBD) solvents (Met = methanol, ET = ethanol, PRP = propanol, BUT = butanol, TBUT = tertiary butanol, CYCHXOH = cyclohexanol). (e) Image of 1 in different solvent taken under UV-Lamp (365 nm).	88
3.2.8	(a) Emission spectra of 1 in different alcoholic solvent (Met = methanol, ET = ethanol, PRP = propanol, BUT = butanol, TBUT = tertiary butanol, CYCHXOH = cyclohexanol) (a) Lippert Mataga plot of 1 in alcohols between stokes shift vs $f(\epsilon, \eta)$ (orientation polarizability).	89
3.2.9	(a) FTIR spectra of 1 in different solvent (b) Emission spectra of 1 in THF (1×10^{-5} M) by gradually increasing the methanol concentration	90
3.2.10	(a) ^1H NMR peaks of OH functional group of 1 in alcoholic solvents. (b) ^1H NMR of 1 in CDCl_3 mixed with alcoholic solvents	91
3.2.11	Emission spectra of 2 in different solvents (1×10^{-5} M), b) Emission colour of 2 indifferent solvents excited under UV-lamp (λ_{ex} , 365 nm) c) Comparison of 1 and 2 in solvents (methanol and ethanol)	93
3.2.12	The DFT optimized structure of the MeOH-complex in gas (left panel) and solvent phase (right panel) along with their corresponding ELF maps (below). In the solvent phase, we have considered the implicit continuum solvent model for the Methanol. (b) Frontier orbital diagram energy level from DFT of 1 in DCM and Methanol (c) Density difference plots showing the Metal to Ligand Charge Transfer (MLCT) transition in DCM and Methanol. (Blue cloud indicates more electronic charge whereas green cloud indicates less charge.)	94

List of Figures

No.	Caption	Page No.
3.2.13	Emission Spectra of 1 in methanol with gradually increasing the water concentration (from 0% to 90% V/V in 5ml vial) (b) Plot of PL intensity (I) of 1 versus the compositions of the aqueous mixtures, concentration: 1×10^{-5} M .(c) Image of 1 in different methanol/ water mixture under UV-lamp (λ_{ex} , 365 nm); (d) Emission spectra of 1 in methanol/PEG mixtures.	95
3.2.14	DFT optimized structures for the different structural forms of the complex (First two forms (a,b) are hydrogen-bonded in gas phase & solvent phase respectively, and the last one is non-hydrogen-bonded in the gas phase (c))	96
3.2.15	Electron localization function (ELF) and FMO contour maps for the H-bonded ((a) left panel) and without H-bonded ((b) right panel) forms of the complex.	97
3.2.16	(a) Emission spectra of 1 by adding one equivalent amount of base (pKb values are NaOH = 0.2, KOH = 0.5, K_2CO_3 = 3.66, Na_2CO_3 = 4.67, Cs_2CO_3 = 3.05, LiOH = -0.36 values) b) PL emission image of 1 with gradually increasing in the range, (pH1 to pH13) c) Photo-luminescence spectra of 1 in different pH buffer solution (pH1 to pH13) (d) Stacked 1H NMR of 1 a) 1+ trimethylamine (TEA)	98
3.2.17	a) Image of 1 ($c = 10^{-5}$ M) with 1 equivalent of different metals and proteins, respectively, from left to right (1- Na_2SO_4 , 2- $MgSO_4$, 3- $ZnSO_4$, 4- $Al_2(SO_4)_3$, 5- Urea, 6-BSA, 7- Histidine, 8- Creatinine, 9- Cystine, 10- Tyrosine, 11-Lysine, 12-Tryptophan) (under exciting at 365nm with a UV lamp). (b) Emission spectra of 1 ($c = 10^{-5}$ M) with 1 equivalent of different metal salts [Na_2SO_4 , K_2SO_4 , $CaSO_4$, $MgSO_4$, $(NH_4)_2SO_4$, Na_3PO_4 , $ZnSO_4$, $Al_2(SO_4)_3$], creatinine and BSA. (BSA results in green emission and remaining species produces weak yellow emission).	99
3.2.18	(a) UV-Visible spectra of 1 by gradually increasing the BSA concentration (b) Emission intensity of 1 (1×10^{-5} M) with a gradual increase of BSA (10 mg per 10 ml) and (b) linear fitting of 1 with BSA	99
3.2.19	(a) Emission spectra of 1 in the presence of BSA Protein and 90% methanol/water fraction. (b) Image of 1 in the presence of BSA, Protein and 90% methanol/water fraction under UV-Lamp 365 nm	100

List of Figures

No.	Caption	Page No.
3.2.20	(a) Emission spectra of 1 in presence of BSA, BSA+ SDS and (90% aggregate solution (AGG)) (b) PL emission image of 1 in 1(90% f_w), 2 (1+SDS+BSA), 3(1+BSA), 4(1+ SDS), 5(1+ Methanol)	100
3.2.21	(a) Figure shows the B chain of the protein with the best binding pocket for the ligand which is located at the surface of the protein (b) A zoomed view of the best binding pocket is shown along with ligand (c) In the binding pocket, alpha helices are a binding partner of the ligand (d) Hydrogen bonding interactions of the ligand with the residues of the proteins is shown. The hydrogen bond is formed between Thr 466 side chain of B chain of protein and the ligand. In each case, the ligand is shown by ball and stick model (e) Binding of the complex within the hydrophobic pocket of pepsin, (f) Showing the absence of hydrogen bond with the hydroxyl group of 1 and also hydrogen bond formation with the carbonyl of 1 in pepsin.	103
4.1.1	(a) ^1H NMR spectrum of TI (b) ^{13}C NMR spectrum of TI	113
4.1.2	(a) ^1H NMR spectrum of TPSI I in CDCl_3 (b) It shows the zoomed aromatic region of ^1H NMR of TPSI I in CDCl_3	115
4.1.3	(a) ^{13}C NMR spectrum of TPSII (b) HRMS spectra of (a) TPSII (b) Counter ion (I ⁻)	116
4.1.4	(a) ^1H NMR spectrum of TPSI PF_6 in DMSO (b) HRMS spectra of TPSI PF_6 counter ion.	117
4.1.5	ORTEP diagram of a) TPSI I ; b) TPSI PF_6 . It shows the dihedral angle between the plane passing through the cyanine ring and phenyl pyridine ring (c, d) TPSI I and (e) TPSI PF_6 (Green color plane = Plane passing through cyanine ring and red color plane = Plane passing through the phenyl pyridine.).	118
4.1.6	(a) Absorption spectra of TPSI I and TPSI PF_6 in methanol (1×10^{-5} M) (b) Emission spectra of TPSI I and TPSI PF_6 in solid-state	119

List of Figures

No.	Caption	Page No.
4.1.7	(a) Emission Spectra of TPSI I (0.4 mM) in the presence of the solvent with increasing viscosity (1 = DCM, 2 = Methanol, 3 = Ethanol, 4 = DMSO, 5 = Butanol, 6 = Ethylene glycol, 7= Cyclohexanol, 8 = PEG 200, 9 = PEG 300, 10 = PEG 400, 11= PEG 600) (b) Image of TPSI I was recorded under UV-Lamp ($\lambda_{\max}=365$ nm)	119
4.1.8	Emission spectra of (a) TPSI I and (b) TPSI PF ₆ in methanol (C = 1×10^{-5} M) with gradually increasing the viscosity by adding PEG 400	120
4.1.9	Linear fitting between $\log(I)$ (I =PL Intensity of TPSI I, TPSI PF ₆ ; c = 10^{-5} M, in methanol) and $\log(\eta)$ (η = viscosity of solvent), TPSI I = 1.42, $R^2 = 98.4$, TPSI PF ₆ = 0.38, $R^2 = 98$	120
4.1.10	UV-Visible absorption spectra of TPSI I in methanol (1×10^{-5} M) a) recorded the spectra by irradiation with UV-Visible lamp ($\lambda_{\text{exc}} = 365$ nm); (b) absorption spectra were recorded by switching off UV-the lamp (c) UV-Visible absorption spectra of TPSI PF ₆ in methanol (1×10^{-5} M) upon irradiation with UV lamp ($\lambda_{\text{ex}} = 365$ nm) at different time intervals (d) Emission spectra of TPSI I (in methanol, c= 1×10^{-5} M) at different excitation wavelengths ($\lambda_{\text{ext}} = 330 - 520$ nm) (x-axis is the wavelength for the recorded emission, right-hand side y-axis is different excitation wavelength at which the emissions are recorded and left side z-axis is the photoluminescence intensity)	121
4.1.11	(a) Emission spectra of TPSI I (1×10^{-5} M) with gradually increasing the methanol in PEG400 solution; the PL intensity is gradually decreasing with increasing concentration of methanol into PEG	123
4.1.12	(a) UV-VIS spectral changes of TPSI I in solid-state (powder form) upon irradiation at 250 nm as a function of time (b) recoverable without irradiation in the dark for several minutes UV-Vis spectra of TPSI I after expt. (a); (c) on irradiation at 365 nm as a function of time of TPSI I (d) recorded spectra by switching off UV-the lamp after expt. (Approximately two minutes were taken to operate two consecutive reading)	123

List of Figures

No.	Caption	Page No.
4.1.13	(a) UV–Vis spectral changes of TPSI PF ₆ in the solid state (powder form) upon irradiation at 250 nm as a function of time (b) UV-Vis spectra of TPSI PF ₆ on irradiation at 365 nm as a function of time.	124
4.1.14	(a) ¹ H NMR of TPSI I in presence of 1 equivalent of PEG 400; (b) ¹ H NMR of TPSI I without PEG-400 (c) Unit cell of TPSI I consisting of four molecules and four iodides passing through one plane (d) It shows the cage type arrangement of four molecules with a space represented by yellow color (e) It shows the measured distance between the Iodide and molecules in the packing unit cell of TPSI	126
4.1.15	(a) Unit Cell of TPSI I shows the distance between the two centroids (C1-C2) is 3.99 Å (b) Rest of the short contacts between the molecules, apart from short-contacts containing iodide (N2---H2' - 2.680 Å, C23---H21'- 2.734 Å, C18---C9-3.361 Å and H10E---H10B-2.282 Å)	127
4.1.16	(a) It shows the measured distance between PF ₆ ⁻ and the molecules in the unit cell of TPSI PF ₆ (b) It shows the distance of I ⁻ (I1) (iodide) with H15 and H11B in TPSI I (c) distance of PF ₆ with H15, H13 and H10B in TPSI PF ₆ .	127
4.1.17	It shows the mean angle between the plane passing through the molecules (a) TPSI I (1) and TPSI (2) (83.54 degrees) (b) TPSI PF ₆ (1) and TPSI PF ₆ (1) (0 degree), Crystal structure shows the distance between the neighbouring molecules (centroid-centroid) in (c) TPSI I is ~6Å (d) TPSI PF ₆ ~8Å;	129
4.1.18	(a) Packing diagram of TPSI I showing a shape of the square box containing space (b) Packing diagram of TPSI PF ₆ showing a stepwise wave structure.	129
4.1.19	It shows two different dihedral angle between the plane passing through pyridine ring (orange colour) and a plane passing through the phenyl ring of phenyl pyridine (blue colour) in a unit cell (TPSI I (1) first molecule (27.21 degrees) and TPSI I (2) second molecule (25.02 degrees))	130

List of Figures

No.	Caption	Page No.
4.1.20	The Overlapping area of the absorption spectra with emission spectra of (c) TPSI I and (d) TPSI PF6 absorption and emission in the solid-state. (Overlapped integral $J(\lambda)$ for TPSI I = 3.46×10^{16} and TPSI PF6 = 1.912×10^{13})	131
4.1.21	(a) Intracellular viscosity measurement by PSD analysis in HUVECs. A position sensing device-based analysis was performed to estimate alteration in intracellular viscosity of HUVECs after exposure to 30 mM glucose for 24 h. (b, c) Untreated cells served as control. Intracellular viscosity analysis of HUVECs treated with glucose. HUVECs were exposed to 30 mM of glucose and probe molecules (TPSI I, 10 μ M). Control cells were treated with probe only	132
4.1.22	(a) Cytotoxicity analysis after exposure to different concentrations of TPSI I in Huh7 cells. (b) Intracellular viscosity measurement by PSD analysis in tumor cells. A position sensing device-based analysis was performed to estimate alteration in intra-cellular viscosity of Huh7 cells after exposure to 0.5% MC for 24 h. Untreated cells served as control	132
4.1.23	(a) Intracellular viscosity analysis by fluorescence microscopy using TPSI I. Huh7 cells were treated with 0.5% MC and TPSI I (10 μ M). Only TPSI I treated cells served as control. DAPI was used to stain the nucleus. Scale bar: 200 μ m (b) Intracellular viscosity measurement by flow cytometry using TPSI I. Huh7 cells were treated with 0.5% MC and TPSI I (10 μ M). Only TPSI I treated cells served as control. Subsequently, a shift in green fluorescence was monitored through flow cytometry. The overlay images depict the shift.	134
5.1.1	(a) ^1H spectrum of PyPr (b) ^{13}C spectrum of PyPr (c) Mass spectrum of PyPr	140
5.1.2	(a) Emission spectra of the PyPr (b) Absorption spectra of pyrene, PyPr and Py (Pyrene)	141
5.1.3	a) UV-Visible spectra of PyPr and PyPr + H^+ [Methanol ($c = 10^{-5}$ M)]; b) Emission spectra of PyPr and PyPr + H^+ in DCM ($c = 10^{-3}$ M)	142

List of Figures

No.	Caption	Page No.
5.1.4	Frontier Molecular Orbital images of (a) PyPr and (b) PyPr +H ⁺ , calculated by using B3LYP/6-31 g ++(d, p) as implemented on Gaussian 09	142
5.1.5	(a) The normalized emission spectra of PyPr on thin films (c = 10 ⁻³ M) showing reversibility in the presence of acid-base (λ_{\max} = 433 nm for PyPr and 473 nm for PyPr + H ⁺); (b) Thin-film emission color image of PyPr under exposure to acid and base.	143
5.1.6	(a) Absorption spectra of PyPr (1x10 ⁻³ M) with different TFA concentration [1x10 ⁻³ M in methanol (0.01eq)] (the isosbestic point at 284 & 360) nm; (b) Emission intensity of PyPr (1x10 ⁻³ M) with a gradual increase of acid concentration (isosbestic point wavelength = 456 nm; increasing concentration of TFA is marked in the spectrum) (d) Proposed structure of PyPr after protonation with TFA (A protonated form of PyPr = PyPr +H ⁺) and (c) linear fitting of PyPr with acid	144
5.1.7	(a, c) Emission spectra of PyPr and PyPr +H ⁺ with a gradual increase in concentration, respectively; (b, d) image of PyPr and PyPr +H ⁺ , respectively with gradually increasing concentration under excitation at 365 nm.	145
5.1.8	(a) Emission spectra of PyPr (0.1mM) with gradual increase in the water fraction in methanol (b) Plot of intensity (I) values of PyPr (c) Images of the emission of PyPr in methanol-water mixtures with different water volume fractions (f_w) taken under UV illumination (365 nm) (d) Emission spectra of PyPr (0.1mM) with a gradual increase in PEG concentration	146
5.1.9	(a) shows CH--- π interaction of 2.758 Å (b) a strong π - π interaction between the centroids of the two pyrene rings with short contact, 3.57–3.78 Å.	147
5.1.10	(a) Emission spectra of PyPr + H ⁺ (0.1mM) with gradual increase in the water fraction in methanol (b) Plot of intensity (I) values of PyPr + H ⁺ (c) Images of the emission of PyPr+ H ⁺ in methanol-water mixtures with different water volume fractions (f_w) taken under UV illumination (365 nm)	148

List of Figures

No.	Caption	Page No.
5.1.11	(a,b) LUMO level of PyPr and PyPr + H ⁺ (c) Time-resolved fluorescence spectra of PyPr (0% water; black, 30% water; red, 90% water; green). (d) (i) Powder X-ray diffraction patterns of PyPr recorded for various states collected from (i) original form of PyPr, (ii) solid powder collected from 10:90 % MeOH: water mixture (iii) obtained from single-crystal data of PyPr.	149
5.1.12	(a) Absorbance spectra of PyPr with $c = 1 \times 10^{-5}$ M upon the addition of 1 equivalent of different nitro-based explosive/non-explosive compounds (toluene, benzoic acid); (b) Emission spectra of different explosive/non-explosive compounds with PyPr; (c) It shows the image of PyPr with 1 equivalent of explosive/ non-explosive compounds, respectively (from left to right): (i) PyPr (blank); (ii) NT (4-nitrotoluene); (iii) DNB (1,3-dinitro benzene); (iv) DNT (3,5-dinitro toluene); (v) 2,4-DNP (2,4-dinitro phenol); (vi) PA (picric acid); (vii) P (phenol); (viii) BA (benzoic acid) (under $\lambda = 365$ nm excitation).	150
5.1.13	(a) The absorption spectra of PyPr in methanol (1×10^{-3} M) with a gradual increase in the PA (Picric acid) (1×10^{-3} M) concentration (solution of PA was prepared in methanol); (b) Emission spectra of PyPr (1×10^{-3} M) titrated with different concentration of PA; (inset a new peak at (522 nm) gradually increases with overall quenching of fluorescence) (c) linear fitting of PyPr with PA. (d) NMR spectra of (A) PyPr, (B) PA, and (C) PyPr + PA. The downfield ¹ H signals in (C) indicate the presence of the strong interaction of PyPr with PA (PA = picric acid).	151
5.1.14	(a) Frontier molecular orbital images of HOMO and LUMO energy levels of PyPr (ligand) and Picric acid showing intermolecular charge transfer; LUMO of picric acid is less than LUMO of PyPr (b) Absorption spectra of PA and emission spectra of L1 in DCM; the spectral overlap between the emission of PyPr and the absorption of PA is shown in the inset.	152

List of Figures

No.	Caption	Page No.
5.1.15	(a) Bar diagrams of the relative emission intensity of PyPr with different metal ions at I_{405}/I_{530} . Pink bars represent the addition of various metal ions to PyPr and blue bars represent the subsequent addition of Al^{3+} (1 equivalent) to the above-mentioned solutions (PyPr + different metal ions + Al^{3+}); (b) photoluminescence spectra of PyPr with $c = 10^{-3}$ M in methanol upon the addition of 1 equivalent of different metal ions; (c) Image of PyPr ($c = 10^{-3}$ M) in presence of 1 equivalent of different metal ions under excitation with a UV lamp ($\lambda_{max} = 365$ nm).	153
5.1.16	(a) The emission spectra of PyPr upon addition different trivalent metal ion. (b) image of PyPr ($c = 10^{-3}$ M) with 1 equivalent of different trivalent metal ions, respectively; from left to right (under 365 nm UV lamp) (c) PL Intensity comparison between PyPr in the presence of $Al(III)$ and $Fe(III)$ (d) The absorption spectra of PyPr (1×10^{-3} M) with gradual increase in the Al^{3+} (1×10^{-3} M) concentration; (e) Emission spectra of PyPr (1×10^{-3} M) titrated with different concentration of Aluminium nitrate; (f) Linear fitting of PyPr with the Al^{3+}	154
5.1.17	HRMS of PyPr with Al^{3+} (a) $[Al(PyPr)+H]^+$ (b) $[Al(PyPr)_2+2H]^+$, (c) $[Al(PyPr)_3+3H]$	156
5.1.18	(a) PL emission spectra of PyPr in presence of EDTA and Al^{3+} (b) Photograph of PyPr in presence of EDTA and Al^{3+} . (365nm)	156
5.1.19	(a) 1H NMR spectra of PyPh, PyPrCN, PyPm & (b-e) ^{13}C NMR spectra of PyPh, PyPrCN, PyPm & PyTr	160
5.1.20	HRMS mass spectra of (a) PyPh (b) PyPrCN (c) PyPm (d) PyTr	162
5.1.21	(a) Absorption spectra of PyPh, PyPrCN, PyPm & PyTr respectively in solution state (1×10^{-4} M) (b) Emission spectra of PyPh, PyPrCN, PyPm & PyTr respectively in solution (c) Emission spectra of PyPh, PyPrCN, PyPm & PyTr respectively in solution solid state.	163
5.1.22	Frontier molecular orbital image of HOMO and LUMO energy levels of ligands calculated by using B3LYP/6-31++g(d,p) as implemented on Gaussian09.	165

List of Figures

No.	Caption	Page No.
5.1.23	(a) Emission spectra of PyPh (1×10^{-4} M) in different fractions of water in THF (b) Plot of intensity (I) values of PyPh versus the compositions of the aqueous mixtures (c) Images of the emission of PyPh in THF–water mixtures with different water volume fractions (f_w) taken under UV illumination ($\lambda_{exc} = 365\text{nm}$); (d) Emission spectra of PyPh with increasing concentration of PEG. (e) Image of L with increasing viscosity taken under UV illumination ($\lambda_{exc} = 365\text{nm}$)	165
5.1.24	(a) Emission spectra of PyPrCN (1×10^{-4} M) in different Water/THF (0-90%) (b) Plot of intensity (I) values of PyPh versus the compositions of the aqueous mixtures (c) Images of the emission of PyPrCN in THF–water mixtures with different increase water fractions (f_w) taken under UV illumination ($\lambda_{exc} = 365\text{nm}$); (d) Emission spectra of PyPrCN with increasing concentration of PEG	166
5.1.25	(a, e) Emission spectra of PyPm & PyTr (1×10^{-4} M) in different Water/THF (0-90%), respectively (b, g) Plot of intensity (I) values of PyPm & PyTr versus the compositions of the aqueous mixtures, respectively (c, f) Images of the emission of PyPm & PyTr in THF–water mixtures with different increase water fractions (f_w) taken under UV illumination ($\lambda_{exc} = 365\text{nm}$); (d) Emission spectra of PyPm with increasing concentration of PEG. (e) Emission spectra of PyTr (1×10^{-4} M) in different Water/THF (0-90%).	168
5.1.26	(a) The packing diagram of PyPrCN showing short intermolecular contacts, (b) CN1---H22 (2.728 Å), CN1---H17 (2.671 Å), CN1-H5 (2.722 Å), C19---H13 (2.735 Å), N2---H3 (2.708 Å) and π - π interaction (4.65 Å) (c) Showing Zig- Zag packing structure of L2 and (d) Slippage angle is $R^1 = 20.4^\circ$ (J-aggregate $R^1 < 32^\circ$).	168
5.1.27	PyPm Crystal packing (a) shows a strong π - π interaction between the centroids of the two pyrene rings with short contact in the range of 3.872-3.873 Å, (b), (e) Packing diagram shows the interaction of N1---H13 2.624 Å, C16---H6.886 Å, Indicating the dihedral angle (between the two plane passing through pyrene and through pyridine substituted ring) of (c) PyPrCN and (d) PrPm	169

List of Figures

No.	Caption	Page No.
5.1.28	Emission spectra of all the probe with varying the concentration from 10^{-1} M to 10^{-5} M solution in DCM (a) PyPh (b) PyPrCN (c) PyPm (d) PyTr.	170
5.1.29	Image of the probe in THF (1×10^{-4} M) with 1 equivalent of explosive under UV lamp (365nm) respectively (a) PyPh (b) PyPrCN (c) PyPm (d) PyTr. PA=picric acid, NT=nitrotoluene, DNT = dinitrotoluene, DNP = dinitrophenol, NB = nitrobenzene, DNB = dinitrobenzene, DNBz = dinitrobenzoic acid, ANP = aminonitrophenol, Nbz = nitro benzaldehyde.	171
5.1.30	Absorption spectra of probes in presence of explosive materials (1 eq) (a. b) PyPr (1×10^{-5} M) (c, d) PyPm (1×10^{-5} M) (e, f) PyTr (1×10^{-6} M)	172
5.1.31	The absorption spectra of the probe ((a) PyPh, (b) PyPrCN, (c) PyPm (d) PyTr in thf (1×10^{-4} M) with a gradual increase in the PA (Picric acid) (1×10^{-4} M) concentration (solution of PA was prepared in water). Emission spectra of (e) PyPh (1×10^{-4} M), (f) PyPrCN (1×10^{-4} M), (g) PyPm (1×10^{-4} M), (h) PyTr (1×10^{-5}) titrated with different equivalents of PA. Linear fitting of (i) PyPh (j) PyPrCN (k) PyPm (l) PyTr with PA	173
5.1.32	Emission spectra of (a) PyPh 70% f_w (1×10^{-5} M), (b) PyPrCN (1×10^{-5} M) 90% f_w (c) PyPm (1×10^{-5} M) 60% f_w , titrated with different equivalents of PA. Linear fitting of highers quantum yiled water fraction (a) PyPh ($f_w = 70\%$) (1×10^{-5} M) with PA (b) PyPrCN (1×10^{-5} M) ($f_w = 90\%$) with PA (c) PyPm (1×10^{-5} M) ($f_w = 60\%$) with PA	174
5.1.33	Stacked NMR spectra of a) PyPrCN with PA, b) PyPm with PA, c) PyTr with PA d) Spectral overlap is shown in the plot between absorption of PA and emission of PyPh, PyPrCN, PyPm and PyTr.	176
5.1.34	Image of filter paper making circular spot by PyTr and exposing through different explosive under UV lamp.	178
5.2.1	FT-IR spectrum of (a) compound 1, 1, 2, 2-tetrakis(4-formyl-(1,1'-biphenyl))ethane (5.2.6), (b) compound 1,2-Bis1,2-diphenylethene (5.2.4) and (c) CMO1 oligomer	185
5.2.2	(a) ^1H and (b) ^{13}C NMR spectrum of phenyl(p-tolyl)methanone (5.2.1)	186
5.2.3	(a) ^1H and (b) ^{13}C NMR spectrum of 2-Bis(4 methyl phenyl)-1,2-diphenylethene	187

List of Figures

No.	Caption	Page No.
5.2.4	(a) ^1H and (b) ^{13}C NMR spectrum of 1,2-bis(4-(bromomethyl)phenyl)-1,2-diphenylethane (5.2.3)	188
5.2.5	(a) ^1H and (b) ^{13}C NMR spectrum of 1,2-Bis1,2-diphenylethane (5.2.4)	189
5.2.6	(a) ^1H and (b) ^{13}C NMR spectrum of Tetrakis(4-bromophenyl)ethylene (5.2.5)	190
5.2.7	(a) ^1H NMR spectrum of 1, 1, 2, 2-tetrakis(4-formyl-(1,1'-biphenyl))ethane (5.2.6) (b) ^1H NMR spectrum of Tris(4-formyl phenyl)amine (5.2.7)	191
5.2.8	(a) ^1H NMRs pectrum of CMO1 (b) ^1H NMR spectrum of CMO	192
5.2.9	(a) Mass spectrum of compound phenyl(p-tolyl)methanone (5.2.1) (b). Mass spectrum of compound 1,2-bis(4-(bromomethyl)phenyl)-1,2-diphenylethane (5.2.2) (c). Mass spectrum of compound 1,2-Bis1,2-diphenylethane (5.2.4) (d). Mass spectrum of compound Tetrakis(4-bromophenyl)ethylene (5.2.5) (e) Mass spectrum of compound 1, 1, 2, 2-tetrakis(4-formyl-(1,1'-biphenyl))ethane (5.2.6) (f). Mass spectrum of compound Tris(4-formyl phenyl)amine (5.2.7)	194
5.2.10	(a) Nitrogen adsorption-desorption isotherms and the inset show the pore size distribution curves of (a) CMO1 and (b) CMO2, (c) FESEM of CMO1 (left) and CMO2 (right) in powdered form showing the different size of the porous network.	197
5.2.11	The absorption and emission spectra of CMP1 and CMP2 in solution (THF (tetrahydrofuran)) 1mg in 10ml (black = CMP1 and red = CMP2), left side of the graph is absorbance, and the right side is PL intensity	198
5.2.12	Geometry optimization through density functional theory in 9.0 Gaussian software using 6-311G (d,p) as a basis set. (a) Optimized structures of CMO1 & CMO2, (b) HOMO & LUMO energy level diagram of a single repeating unit of CMO1, (c) HOMO & LUMO energy level diagram of a single repeating unit of CMO2	199
5.2.13	Cyclic voltammogram of (a) CMP1 (b) CMP2 (a Pt wire counter electrode and a Pt disc working electrode; an Ag/AgCl pseudo reference electrode; dry acetonitrile containing both polymer and 0.10 M LiClO ₄)	199

List of Figures

No.	Caption	Page No.
	(100mg); ferrocene was used as internal reference). Scan rates: 50 mV/s; E_{ox} onset was (a) 0.5 eV so experimental HOMO is 4.9 eV. (b) 0.7 eV so experimental HOMO is 5.1 eV	
5.2.14	Emission spectra of (a) CMO1; (b) CMO2 in different solvent (TOU = toluene, DIOX = dioxane, THF= tetrahydrofuran, DCM= methylene dichloride, $CHCl_3$ = chloroform, excited at 367 nm, 0.4 mg of both the oligomers were dissolved in 5 ml of each solvents).	200
5.2.15	Photographs of (a) CMO1 (d) CMO2 in THF/water mixtures with different fractions of water taken under UV illumination (365 nm). PL spectra of (b) CMO1, (e) CMO2 in THF/water mixed solvents with varying portions of water (f_w) with excitation at 367 nm. The changes of the PL intensity of (c)CMO1, (f) CMO2 with variation of water fraction in THF (f_w) with excitation at 367 nm	201
5.2.16	PL intensity spectra of (a) CMO1 (c) CMO2 in THF/PEG mixtures vs wavelength (b) CMO1-Plot of PL intensity values versus the fraction of PEG in the mixture. Solution concentration: 1 mg in 10ml ; excitation wavelength: 365 nm.(d) CMO2- Plot of PL intensity values versus the fraction of PEG in the mixture of PEG-water. Solution concentration: 1 mg in 10ml ; excitation wavelength: 365 nm	202
5.2.17	(a) PL spectra of CMO1 in DCM/hexane mixed solvents with varying fractions of hexane (f_h) with excitation at 367 nm, and (b) the changes of the PL intensity of CMO1 in DCM with different hexane fraction (f_h) (excited at 367 nm). (c) Photographs of CMO1 in DCM/Hexane mixtures with different fractions of hexane taken under UV illumination [From the stock solution (1mg of CMO1 in 10ml solvent), 0.5 ml of solution was made into five different vials varying the different concentration of Hexane]	203
5.2.18	Emission plot of 90% aggregate solution (THF- H_2O) with respect to time (a) CMO1 and (b) CMO2. The stacked plot between the emission intensity and average zeta size concerning time (c) CMO1 and (d) CMO2	204

List of Figures

No.	Caption	Page No.
5.1.19	Comparative experiments between the photoluminescence spectra of CMO1 (a) 90% (THF-Water, aggregated solution) (b) 0% (non-aggregated state) with addition of PA. (1mg/10ml stock solution of CMO1 and concentration of PA is 1mM).	205
5.2.20	Emission spectra of (a) CMO1 (f_w , 90% in the mixed solvent) (b) CMO2 (f_w , 90% in the mixed solvent) in presence of different nitro aromatics and non nitro aromatics. Tol = Toluene, 2.Bor = boric acid, 3.ANP = 2-Amino-4nitrophenol, 4. 2Cl NB = 2,4 dinitro chlorobenzene, 5. NT= 4-Nitrotoluene, 6.NB = 4-Nitrobenzene, 7. DNBz = 3,5 Dinitrobenzoic acid, 8= DNT= 2,6 dinitrotoluene, 9 = DNP = 2,4 dinitrophenol, 10. PA= Picric acid, 11.Bl = Blank	206
5.2.21	(a) 3d bar diagram is representing the emission intensity of CMO1 [1mg/ml at $f_w = 90%$ (in water/THF)] in the presence of different nitro-based explosives and non-explosive compounds. (Right side red color cones indicate the quenched intensity of CMO in the presence of PA + different nitroaromatic rings / or non-explosive compounds, left colorful side cones to indicate the intensity of CMO1 + different nitroaromatics / or non-explosive compounds. b) Photoluminescence image of CMO1 in the presence of different explosives (1eq) and non-explosive (1eq) taken under UV-visible lamp (1.Tol = Toluene, 2.Bor = boric acid, 3.ANP = 2-Amino-4nitrophenol, 4. 2Cl NB = 2,4 dinitro chlorobenzene, 5. NT= 4-Nitrotoluene, 6.NB = 4-Nitrobenzene, 7. DNBz = 3,5 Dinitrobenzoic acid, 8= DNT= 2,6 dinitrotoluene, 9 = DNP = 2,4 dinitrophenol, 10. PA= Picric acid, 11.Bl = Blank. c) Emission spectra of CMO1 in THF-Water (v/v =1:9) titrated with different amount of PA. (d) Linear fitting for CMO1 with PA	207
5.2.22	(a) 3d bar diagram is representing the emission intensity of CMO2 [1mg/ml at $f_w = 90%$ (in water/THF)] in the presence of different nitro-based explosives and non-explosive compounds. (Right side red color cones indicate the quenched intensity of CMO2 in the presence of PA + different nitroaromatic rings / or non-explosive compounds, left colorful	208

List of Figures

No.	Caption	Page No.
	side cones to indicate the intensity of CMO2 + different nitroaromatics / or non-explosive compounds. (b) Photoluminescence image of CMO2 in the presence of different explosives (1eq) and non-explosive (1eq) taken under UV-visible lamp (1.Tol = Toluene, 2.Bor = boric acid, 3.ANP = 2-Amino-4nitrophenol, 4. 2Cl NB = 2,4 dinitro chlorobenzene, 5. NT= 4-Nitrotoluene, 6.NB = 4-Nitrobenzene, 7. DNBz = 3,5 Dinitrobenzoic acid, 8= DNT= 2,6 dinitrotoluene, 9 = DNP = 2,4 dinitrophenol, 10. PA= Picric acid, 11.Bl = Blank. (c) Emission spectra of CMO2 in THF-Water (v/v =1:9) titrated with different amount of PA. (d) Linear fitting for CMO2with PA	
5.2.23	It shows the spectral overlap between the absorption of PA and emission & excitation of (a) CMO1 (b) CMO2 indicating the possibility of either inner filter effect or resonance energy transfer mechanism from CMO1, CMO2 to PA, respectively. (PA in water = 1×10^{-5} M, CMO1 CMO2 = 90 % aggregates solution in thf/water fraction (c) Excited State lifetime of CMO1 with gradually increasing the picric acid (PA) amount (PA1 = 200 μ l [1×10^{-5} M], PA2 = 500 μ l [1×10^{-5} M] and PA3 = 1 ml [1×10^{-5} M]) (d) Stern-Volmer plot between the excited state lifetime of CMO1 and with increasing volume of PA. (IRF = instrument response function)	210
5.2.24	(a) FESEM images of CMO1 thin film before exposing to the PA vapours. (b) FESEM images of CMO1 after exposure to the PA vapours	212
5.2.25	(a) FT-IR spectra of the CMO1 before and after exposure to PA.	212
5.2.26	FESEM image of CMO2	213
5.2.27	(a) Emission spectra of CMO1 [1mg/ml at $f_w = 90\%$ (in water/THF)] titrated with increasing concentration of TNT (10^{-6} M). (b) Linear fitting plot of I_0/I [I_0 = Photoluminescence (PL) intensity without any probe; I = PL intensity at variable concentration of TNT] for CMO1 with TNT.	214
5.2.28	Overlapped area of the absorption spectra of PA and TNT with the emission spectrum of CMO1 indicating the energy transfer from CMO1 to PA, respectively. (PA and TNT in water (1×10^{-5} M) and CMO1 90% aggregates solution in thf/water fractions)	214

List of Figures

-
- 5.2.29 a) Top Shows the photographs of CMO1 impregnated test strips with varying concentrations of PA upon illumination at 365 nm; from left to right: blank (B), 1×10^{-4} M, 1×10^{-5} M, 1×10^{-6} M, 1×10^{-7} M, 1×10^{-8} M, 1×10^{-9} M, 1×10^{-10} M, 1×10^{-11} M. below:- Shows the image was taken upon illumination at 365 nm (1) gloves without a trace of picric acid, (2) impregnated test strips without any contact of PA. (3) Gloves showing the powder of picric acid on thumbs (marked with a red circle), (4) Image of the CMO1 impregnated test strips while applying the PA traces, (5) Image of CMO1 impregnated test strips rubbed with PA. (b) Photograph of CMO1 impregnated test strips at ten different places exposing to the powder of various explosives [(1) blank CMO1, (2) Picric acid, (3) 4-Nitrobenzene, (4) 3,5-Dinitrobenzoic acid, (5) 2-Amino-4nitrophenol, (6) 2,6 trinitrotoluene, (7) 2,4 dinitrophenol, (8) 4-Nitrotoluene, (9) benzoic acid, (10) boric acid].

Chapter-1

Introduction and Research Gap

- * *This chapter contains the insights of the thesis and summarizes the different aspects of sensing in terms of properties, application and mode of sensing*
- * *This chapter emphasizes the different types of sensors, types of materials used for sensing, types of analytes for sensing and highlights their significances in day to day life*
- * *The motivation towards the thesis has been presented in this chapter*

1.1 Solid Luminescent Materials

Photoluminescent materials can emit the light without the thermal energy, in response to the exposure to light. The luminescent materials absorb light at a specific wavelength and emit light at a different wavelength. The luminescent materials which emit the light in the solid-state are called as solid luminescent materials.[1] The solid luminescent materials are divided into two groups - inorganic luminescent materials and organic luminescent materials. The inorganic luminescent materials are made up of inorganic semiconductors (CdS, ZnS etc.).[2] The organic luminescent materials also divided into two types purely organic materials and materials which consist of metal complexes. The present thesis deals with the solid organic luminescent materials. The solid organic luminescent materials are applied in various field like sensors and biosensors, electroluminescent materials, lasers, and other optoelectronic devices because of the merits such as no solubility issue, ease of tuning, relatively low cost, and ease of manufacturing.[3]

1.2 Organic based conventional fluorophores for sensing and their disadvantages

Recently there are lots of reports on using the fluorescent probes for sensing the different analytes such as anions, cations, pH as well as organic solvents. In the fluorescence-based technique, sensing relies on the change in the luminescence of the reagents with the sensing materials.[4] Mostly in the literature for pH sensing, fluorescein [5] and 8-hydroxypyrene-1,3,6-trisulfonic acid, Trisodium salt (HPTS) were used [6] (Fig. 1.1).

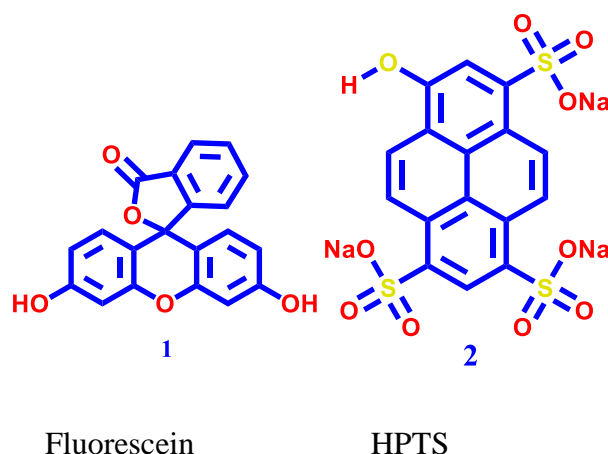


Figure 1.1 Structure of fluorescence sensors.

The reagent HPTS depends on the dissociation of the phenolic hydroxyl group of deprotonated trisulfonated ion. These dyes absorbed the light at a wavelength around the blue region and emitted just above 500 nm.

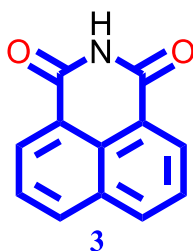


Figure 1.2 Structure of the Multi analyte probe.

Recently among all the organic fluorophore developed for the fluorescent-based techniques, naphthalimides based frameworks are utilized to a significant extent in designing and synthesis of **(3)** (Fig. 1.2) luminescent probes. [7, 8] Luminescent transition metal complex has a more significant Stokes shift and longer lifetime than the conventional organic dyes, [94]. The use of the transition metal complex gives the flexibility to have a wide range of excitation/emission and enables us to use the lifetime based technique.[9] In 2002 Nivens *et al.* developed the multi-layer approach for sensing pH, CO₂ and ammonia. He synthesized the organic sol-gel membranes, in which single layer for pH measurement and dual-layer format for the sensing CO₂ and ammonia.[9]

In most of the applications, luminophores are used in aggregated form or thin-film, such for example, the application in ‘organic light-emitting diode’ (OLED), ‘organic field-effect transistors’ (OFETs) etc.[95] For biological applications, the luminescent molecule is used in the physiological condition or the aqueous medium. The scientist has succeeded in attaching the polar group to make miscible in the water, but because of the intrinsic hydrophobic nature of the conjugated organic molecules, it shows aggregations, and emission is quenched.[95] The emission is also quenched when the luminophores are applied to monitor the environment in the aqueous solution. In many conventional luminophores, with the increasing concentration the emission is quenched; this phenomenon is called ‘Aggregation-Caused Quenching (ACQ).[96] Until Ben-Zhong Tang discovered the opposite phenomenon called ‘aggregation-induced emission’ (AIE), ACQ was dominant for many years and restricting the application of fluorophores in the concentrated solution state or solid-state. [10]

1.3. Aggregation Caused Quenching (ACQ)

Mostly the organic-based conventional luminophore like fluorescein, pyrene, naphthalene, perylene, etc. (Fig. 1.3) is extensively studied in various fields such as light-emitting devices,

chemical sensing, and especially for bio-imaging as these materials are strongly emissive in the dilute solution.[96] However, their emission is reduced or quenched in the concentrated or aggregated state because the conventional fluorophores usually possess planar aromatic cores which favour the occurrence of π - π stacking interactions when becoming closer or gets aggregated [11] (Fig. 1.4). Birks discussed this phenomenon in his classic photo physics book, that is the ACQ effect is “common to most aromatic hydrocarbons and their derivatives”.[12] The main structural reason for such detrimental ACQ effect is because conventional luminophores are typically comprised of planar aromatic rings (e.g., perylene). As, known that organic electronic luminescence is mainly due to the electronic conjugation, therefore the popular strategy to design new luminescent materials is to increase π conjugation by increasing aromatic rings. This results in the bigger disc-like plates which are highly luminescent in the solution state, but their ACQ effects [13, 14] become severe because the chances for such large luminophores to form excimers or exciplexes are also increased.[15] This phenomenon limits the use of the fluorophore and enforces the scientist to use the dilute solution with compromised low sensitivity for sensory applications. [16]

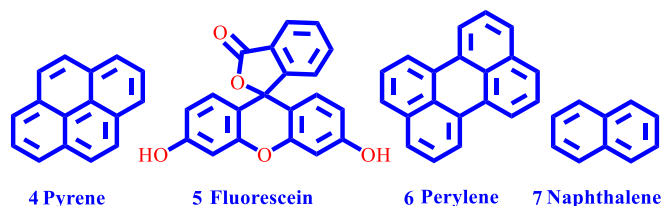


Figure 1.3 Few ACQ luminophores

The ACQ effect made researchers work in turn off mode for sensing, which is insensitive and not suitable for a practical purpose. [17].

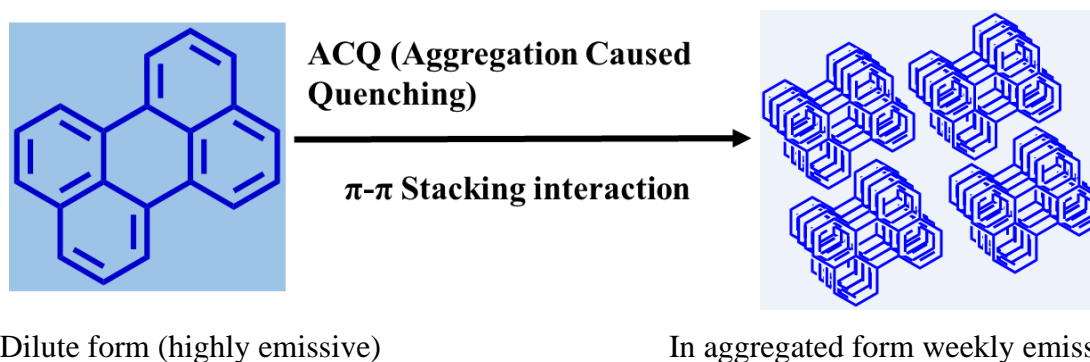


Figure 1.4 Planar luminophore molecules such as perylene tend to aggregate as discs pile up, due to the strong π - π stacking interactions between the aromatic rings, which commonly turns “off” light emission.

1.4 Aggregation- induced emission (AIE)

ACQ is a detrimental effect. Many researchers attempted to modify the ACQ molecules through physical, chemical, and engineering approaches to avoid this effect for successful applications.[18] As an example, to obstruct forming the aggregates, the luminophore cores are covalently attached to the bulky cycles, long alkyl chains, spiral kinks, and or dendric wedges. However, these methods not only solved the issue but created some new issues as solubility and or luminescence decrease in the dilute form[19]. The formation of aggregates is a natural process for molecules which are nearby to each other. Therefore, it was difficult to hamper the formation of aggregation completely. In flagrant contradiction, AIE is a constructive effect. The AIE phenomenon urges to use the aggregated form progressively instead of passively working against it. In 2001 the AIE effect was discovered by Tang and coworkers. The very first molecule in which Tang et al. discovered the AIE property is hexaphenylsilole (HPS). Fascinating result was encouraged to synthesize a series of silole molecules that were found to be non-luminescent in the solution state but emissive in the aggregated state (as nanoparticle suspensions in poor solvents or as thin films in the solid-state). The very constructive effect of AIE made to cure the destructive effect of ACQ. Because of such a development and motivational result, many researchers were fascinated by the application prospects. The last decade was devoted to the generations of new AIE active molecules. As a result, tetraphenylethenes, 8,8a-dihydrocyclopenta[a]-indenes, and fulvenes are used as core and potential molecules for AIE property.[20, 21] (Fig. 1.5)

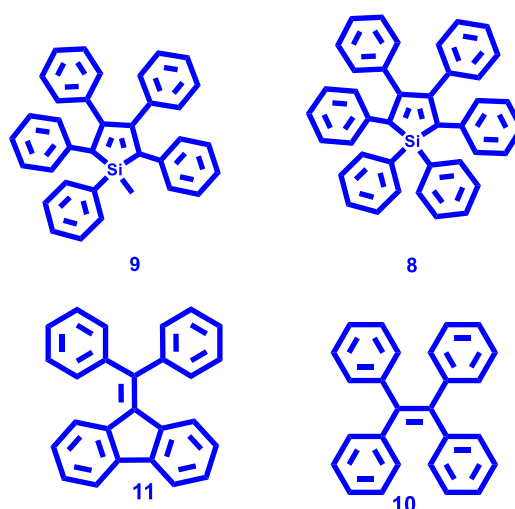


Figure 1.5 Few Structure of organic Aggregation Induced Emissive molecules.

What is the origin of the AIE phenomenon?

In order to design new AIE molecules, it is crucial to understand the mechanism behind the emission in the aggregated state. The most widely accepted cause for AIE is a restriction of intramolecular motion (RIM). RIM includes both the restriction of intramolecular rotation and the restriction of intramolecular vibration of the molecules (Fig. 1.6). If we take an example of the first AIE molecule (HPS) in which all the six phenyl peripheries rotate fastly in the dilute solution. In a dilute solution due to the rotation of the ring, the excitation energy dissipates, which increases the non-radiative decay. However, in the aggregated state, the phenyl rings rotation is restricted due to the physical constraint. The restriction of rotation of rings blocks the non-radiative pathway and thus enables the excitons to decay radiatively.[102] A series of experiments (like increasing Viscosity (Viscochromism), decreasing the solution temperature (thermochromism), and increasing pressure (piezochromism) were performed to modulate the rotation of the phenyl ring to prove that the restriction of the ring caused the increase in the emission of the molecule. In all the controlled experiments, the HPS emits efficiently in a highly viscous medium, at lowered temperature, and at high pressure indicates that the restriction of phenyl rings causes a high increment in the emission. Some of the AIE molecules could not be explained through the RIR mechanism like THBA (10,10',11,11'-tetrahydro-5,5'-bidibenzo[a, d][7]annulenyldiene).[22-26]

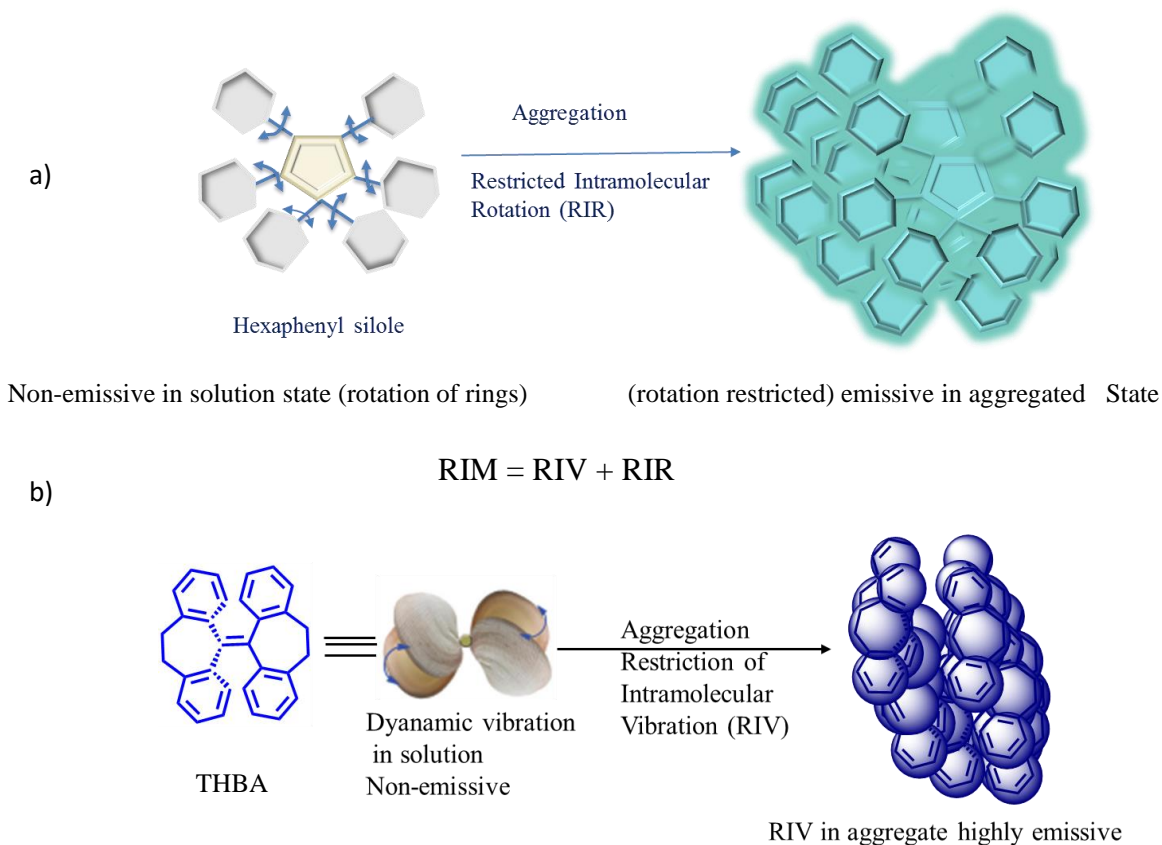


Figure 1.6 (a) HPS molecule is non-emissive in solution and highly emissive upon aggregation, due to the restriction of intramolecular rotation (RIR) of the phenyl rotors against the silole stator in the aggregated state b) 10,10',11,11'-tetrahydro-5,5'-bidibenzo[a, d][7]annulenyliene (THBA) behaves similarly as HPS, highly emissive in the aggregated state due to the restriction of intramolecular vibration.

The THBA consist of two flexible part, in each of which a bendable flexure connects two phenyl rings. This flexure allows the molecules to dynamically vibrate or move in the solution state, which deactivates the radiative pathway. In an aggregated state, due to the physical constraint, the dynamic vibration is restricted, which blocks the non-radiative pathway and emits in the radiatively. These two processes together are called a restriction of motion, which is still considered as the most studied mechanism for the AIE system with bulky rotors. Theoretical and simulation calculations on the lower frequency intramolecular motion of the molecules also support the intramolecular restriction motion. [27]

Apart from the process RIM, there are few other reported processes like JAF (J – Aggregate Formation) [28], ESIPT (Excited State Intramolecular Proton Transfer) [29], TICT (Twisted state Intramolecular Charge Transfer) [30] which can intensify the luminescence to various extents. These processes are interrelated to the AIE mechanism. Researchers attempted to combine the RIM with the above those processes for improving intensity or for applying in ratiometric luminescence probes.

1.4.1 JAF (J- Aggregate Formation).

Form the literature review [31] the broad definition of J-aggregates are as follows – it is a type of probe with an absorption band that has the bathochromic shift of higher absorption coefficient when it aggregates under the influence of solvent or concentration as a result of the supramolecular organization where J stands for the inventor (Jelley). Some researcher has shown that JAF leads to the red-shifted and enhanced luminescence.[32] The above mention process could relate to the ‘aggregation enhanced emission’ (AEE) effect. Here one needs to understand that not every J-aggregate dye is AIE or even AEE.[33] Around 78 years ago, Scheibe et al. and Jelley observed an unusual behaviour of pseudo cyanine chloride (IUPAC name- 1,1'-diethyl-2,2'-cyanine chloride, PIC chloride) in aqueous solution compared to the other solvents like in ethanol. In general, not every AIE leads to J-aggregates or J-aggregates leads to AIE; for example, many cyanine dye form J-aggregates but they are not AIE [34] (Fig. 1.7).

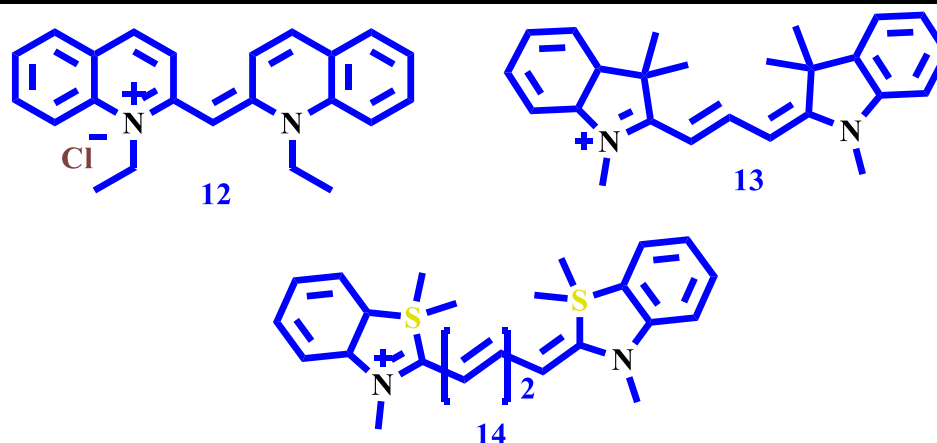


Figure 1.7 Structure of Cyanine dyes forming J-aggregates

Some of them are AIE, but they do not form J-aggregates. However, some molecules do form J-aggregates and exhibit AIE behaviour (Fig. 1.14) [35]. These all examples indicate that JAF is not a fundamental cause for the AIE behaviour. Here if the shifting of emission is observed to a shorter wavelength in the aggregated state (hypochromic shift) concerning its monomer or solution state, the process is called H aggregates, which decreases the luminescence in most cases.

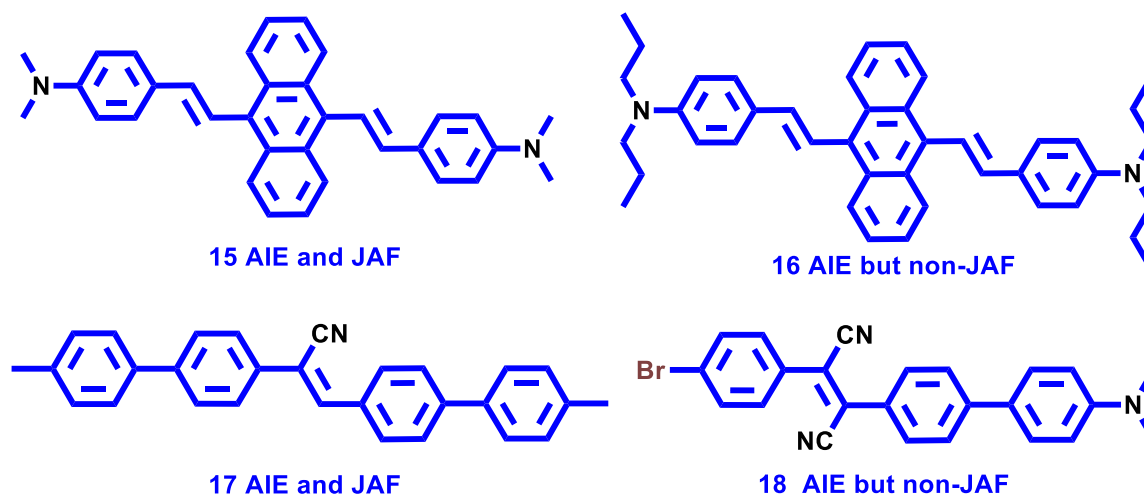


Figure 1.8 Examples were illustrating the AIE and J-aggregates formation (JAF).

An extensive study on J and H aggregates reveals that these aggregates exist in a one-dimensional assembly that could be (a) brickwork (b) ladder (c) staircase type of arrangement [35, 36]. (Fig. 1.9)

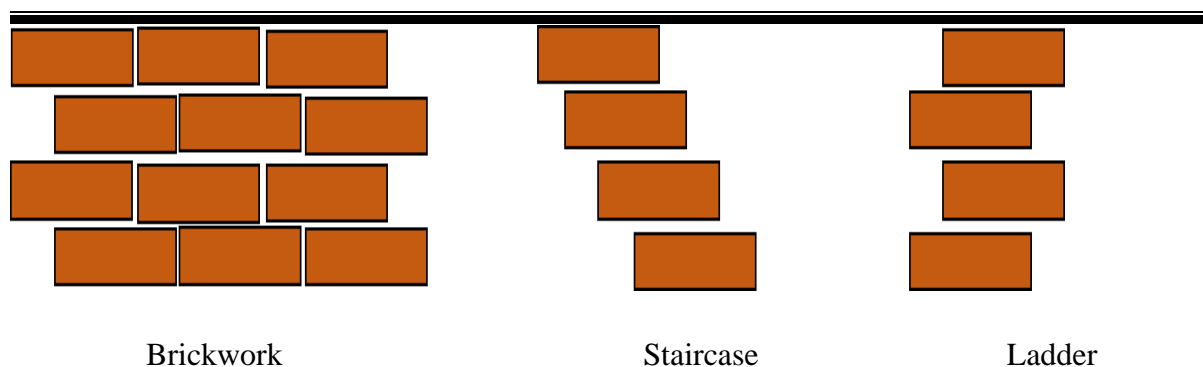


Figure 1.9 J-aggregates type of arrangements.

1.4.2 ESIPT (Excited State Intramolecular Proton Transfer)

ESIPT is a speedy photochemical process (nearly 10^{12} S^{-1}) in which photoinduced proton is transferred via intramolecular hydrogen bonding to produce a tautomer with different electronic structures from the original, exciting form. It is the enol (E) to keto (K) photoisomerization process (Fig. 1.16 a). Waller first reported the ESIPT phenomenon for salicylic acid in 1950. Generally, the ESIPT molecules are usually well-known for their significant stoke shift ($6500\text{-}12500 \text{ cm}^{-1}$). Similar to JAF, the ESIPT process has been considered as the AIE mechanism for some particular ESIPT dyes.[29] If we consider a simple example, as shown in Fig. 1.16(b), the dye is AIE- active ESIPT luminogen. The dynamic intramolecular motion, flexible and twisted structure of the dye dissipates the exciton energy, resulting in the weak fluorescence in the solution.

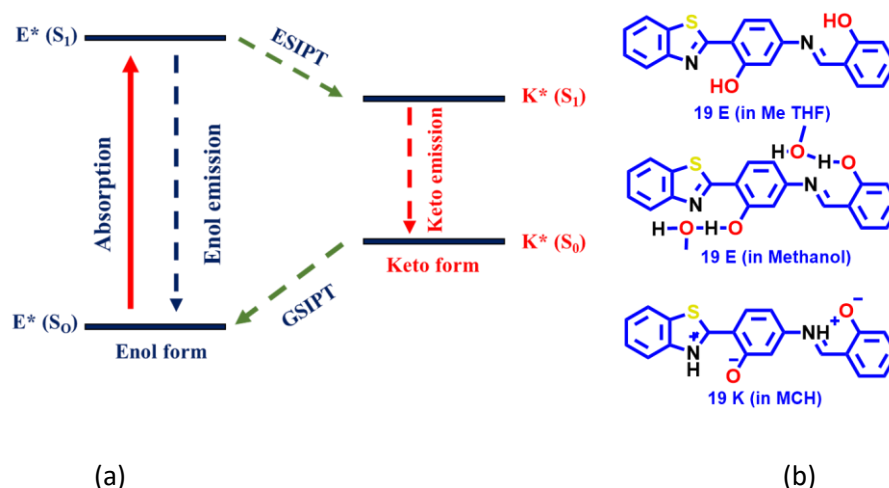


Figure 1.10 (a) Representation of different level of ESIPT process (b) Structure of enol (E) and Keto (K) form the simple (E)-2-(benzo[d]thiazol-2-yl)-5-((2-hydroxybenzylidene) amino) phenol

As the concentration increases or formation of aggregate increases, the molecules of dye come closer and forms intermolecular hydrogen bonding that blocks the molecular motion, leading to the non-radiative decay. When there is a decrease in the temperature of the solvent up to the freezing point, the luminescent intensity is increased. At the freezing temperature, the solvent becomes viscous; still, the ESIPT process is active but obstructs the intramolecular motion within the molecules. The restriction of motion blocks the radiation less decay. So, the blockage leads to an increase in intensity. Therefore, RIM process plays the primary role in the increment of the luminescence intensity. [29, 37-40]

1.5 Fluorescent based Variable analyte Responsive Probes.

Smart materials are high-performance materials that change some of their properties according to the surrounded environment. Such materials could respond differently or the same (for different factors same emission) to the number of factors like humidity, pH, temperature, chemical compounds. These types of materials are cost-effective, less time-consuming, and used in biomedical engineering in sensors and actuators. For example, a material sensitive to pH could be used for measuring pH quantitatively in Cells.[41, 42]

Many variable species in nature could be sensed by appropriately designing the chemically synthesized materials according to the chemical and physical properties of the analytes. Fluorescence technique involving chemical sensor are essential tools in many fields of science and technology because of the visualization of some parameters and species which are intrinsically non-fluorescent, for example, oxygen, pH, temperature, solvents, explosives, metal ions, acid-base (H^+ and OH^-), and or viscosity to name just a few.[43-45]. My thesis revolves around a few of the environmental parameter and species (pH, solvatochromic & specific solvent effect, proteins, Al^{3+} ions, viscosity and explosives) which are sensed by the chemically synthesized materials. These are among the few essential parameters or species relevant to biology as well as the environment. For example, the healthy cell has an alkaline medium, a slight change in its pH causes abnormalities and diseases. The body regulates the pH and temperature through the HOMEOSTASIS. A slight change in the environment of the cells affects the health condition.[46] Increased viscosity increases the resistance to blood flow and thereby increases the work of the heart and impairs organ perfusion as the cell dies or generates the reactive oxygen species, the viscosity of the cell increases.[47] Increased Al^{3+} ion level in body causes the Alzheimer disease. The intracellular sensing of these physical parameters / or ions could help in understanding the fluctuation caused in the cell.

Therefore the probes are very much helpful for early diagnosis of many diseases.[48, 49] Explosive materials are harmful to humanity and mother nature.[143] Explosive materials are very much energetic and pollute the surrounding caused hazardous health problem. Frequently occurring bomb blast is a threat to society. Therefore a sensitive and selective detection of these parameters is necessary.[50])

1.5.1 pH Sensing Probes

pH stands of the 'Potential of Hydrogen'.[51] By determining the pH of the soil, one could determine the condition of the land to decide the type of fertilizer to be used and the type of crops sown.[52] Many biological processes are fixed at a particular pH, knowing the pH one could adjust the medium of the processes.[53] Knowing the pH of the seawater, one can improve the life of the submarines and ships.[54] The Human body has a natural pH of 7.4. The 7.4 pH is needed to run the body efficiently, and the human body always seeks to adjust the pH to 7.4. Variation in pH also has a significant effect, such as knowledge of the pH in both the extracellular and intracellular medium helps us to understand the physiological and pathological processes, including the cell growth and apoptosis, calcium regulation, receptor-based signal transduction, ion transport, etc and living cells critically depend on the pH homeostasis.[55, 56] Most of the proteins and cell organelles have distinct pH ranges. Any abnormality observed in pH values in organelles, etc., is associated with the malfunction of the cell, inappropriate growth in the cell, and also indications of diseases like cancer and Alzheimer's, etc. Several biological processes depend upon the protonation (proton concentration), and deviation from the normal range could lead to severe health problems such as cancer and certain neurological disorders. Thus it is crucial to monitor the pH changes inside the living cells and to study the pathways for diagnosing such diseases.[57, 58] pH is also a critical factor for medicinal, food and drinking water, etc. Qualitative measurement of pH could be achieved by the fluorescence probe that switches on or off at their respective pH.[59] Roger Tsien and co-workers synthesized first pH probe 2',7''-Bis-(2-carboxyethyl)-5-(and-6-)carboxyfluorescein 4 (BCECF) [60](Fig. 1.11)

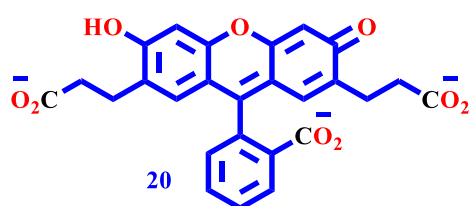


Figure 1.11 Earlier probe for pH sensing

The absorbance of BCECF gets red-shifted from pH 3.6 to 9.7. The disadvantage of this dye is the rate of leakage from the cell increases with increasing the temperature (25-37 °C). To overcome this problem, the researcher tried to modify the BCECF by conjugating the dextran but loses its cell permeability. Meanwhile, many fluorescein derivatives have been developed as a pH probe like BCPCF 2'',7''-bis-(2-carboxypropyl)-5-(and-6-)-carboxyfluorescein, carboxyfluorescein with sulphonic acid, anthrofluorescein and or halogenated fluorescein, etc.[61] Benzo[c]xanthenes dyes include seminaphthofluorones(SNAFRs), seminaphthofluoresceins (SNAFLs), and seminaphthorhodafuors (SNARFs) (Fig. 1.12). These dyes include one benzene ring and one naphthalene ring in the core structure. All these Benzo[c]xanthenes dyes are longer wavelength pH_i indicators (pH_i = 1-9). Here, unlike the fluorescein dye, the emission spectra also show significant pH-dependent shifts. The protonated form of these dye emits in the yellow regions and in the basic condition this dye emits in the red region.-*[62]

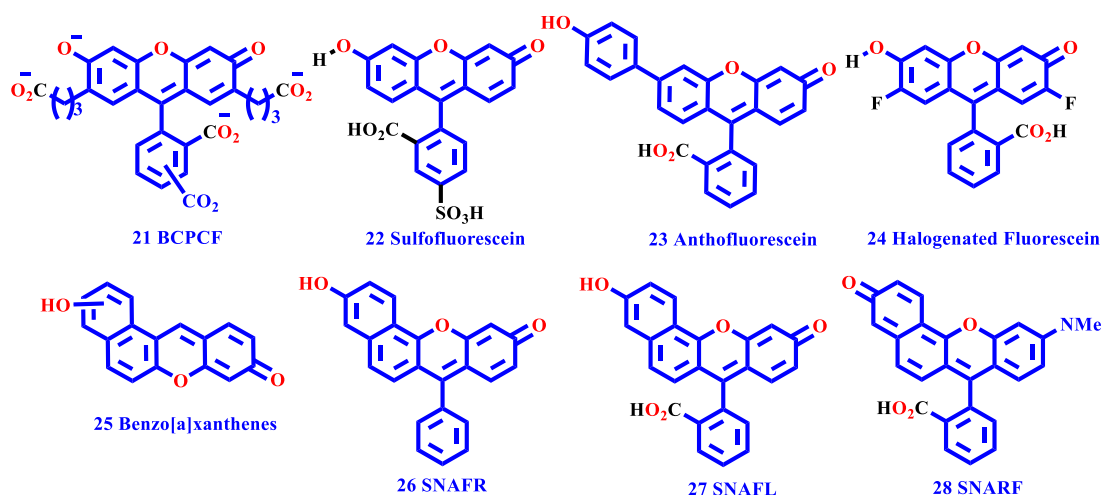


Figure 1.12 Structure of pH probe based on fluorescein

The researchers also tried a cyanine type of dyes as the pH probes because these dyes tend to absorb and emit in the infrared region (IR). The IR region is more advantageous because of minimal cell damage, no autofluorescence, and tissue penetration will be more. Cyanine dye could be divided into two kinds, one with alkylated and another is non-alkylated (in this case photoinduced electron transfer (PET) effect is observed). Non-alkylated cyanine dyes are non-fluorescent where nitrogen is not protonated, but these species are highly fluorescent in their protonated forms. The second type of cyanine dye consists of the fluorophore and nitrogen-containing modulator. By incorporating the PET process, the tuning of emission is achieved. For visualization of small pH changes inside the cells, Briggs et al. introduced the

sulfonic acid functional group. The sulfonic acid group makes the probe soluble in the aqueous medium to prevent the aggregation.[63] The neutral pH fluorescent probe has a tricyanin (Cy) fluorophore coupled with a 4''-(aminomethylphenyl)-2,2'':6'',2'''-terpyridine (Tpy) receptor. At pH 10, the brightness of the neutral probe was observed to be low ($\phi = 0.008$), presumably due to quenching via PET. Protonation of the N atoms circumvents these PET processes (Fig. 1.13), and the dye fluoresces brightly ($\phi = 0.13$) at 750 nm in the aqueous buffer of ca. 7.1. Compound 50 imported into HepG2 cells (it is cell-permeable) is more fluorescent at pH 7.0 than at 7.8 *ex vivo*; this property has been used to follow minor pH changes in the 6.7-7.9 range. Moreover, this probe was shown to have low cytotoxicity and excellent photostability. Many acid cyanine dyes were synthesized for good solubility in the aqueous solution. [60, 64]

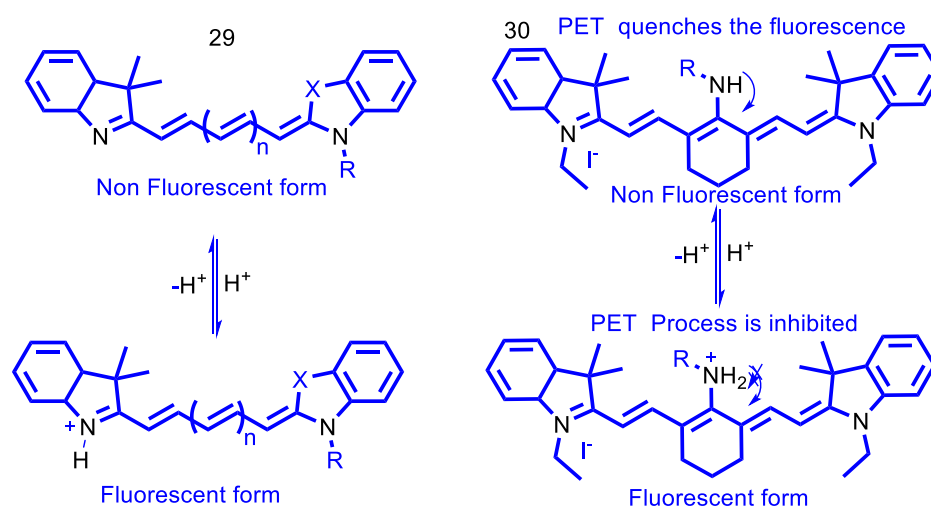


Figure 1.13 Mechanism of a cyanine dye in pH sensing

In Feb 2007, Sibel Derinkuyu et al. utilized two different Schiff bases (Fig. 1.14), namely chlorophenyl imino propenyl aniline (CPIPA) and nitrophenyl imino propenyl aniline (NPIPA) for pH sensing in the alkaline region. These types of dye have long term photostability, high relative signal change, and dynamic working range.[65, 66] Many fluorescent dyes were investigated for pH sensing often in the aqueous solution due to the formation of aggregates; there is a drastic decrease in the emission intensity. This phenomenon called aggregation caused quenching (ACQ), which became a thorny problem in the development of an efficient PL sensing system. Until the discovery of AIE by BZ Tang and Co-workers. AIE materials provide an efficient path to overcome the problem created by ACQ. [66]

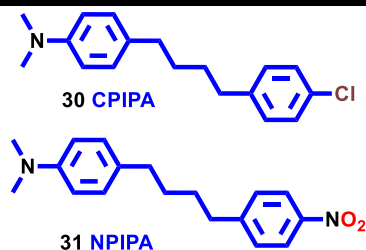


Figure 1.14 Structure of Schiff base type of dye

In 2010, Hongguang Lu et al. synthesized three functionalized AIE 9,10-distyrylanthracene (DSA) derivative namely, 9,10-bis(4-hydroxystyryl)anthracene (32), 9,10-bis{4-[2-(diethylamino) ethoxy]styryl} anthracene (33), and 9,10-bis{4-[2-(N,N,N-triethyl ammonium) ethoxy]styryl}anthracene dibromide (Fig. 1.15). 33 is almost non-luminescent and with meagre quantum yield (Q_f) = 0.25 %. The aggregates in higher AN/water fraction larger than 65% is highly emissive, and when the water fraction increased up to 90%, the fluorescence intensity is increased 55 folds higher than 65 %. [67]

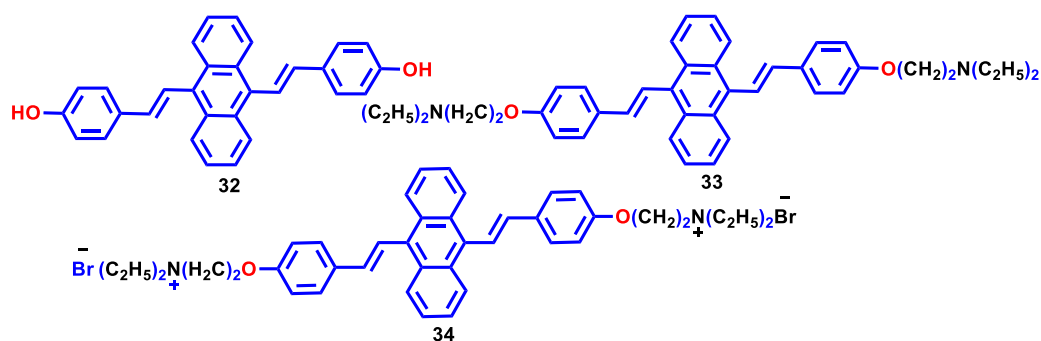


Figure 1.15 AIE anthracene dye for pH probing

The compound 33 is almost non-emissive in acidic solution with a pH lower than 4. The emission intensity increases as the solution pH increases from (4 to 12). This phenomenon occurs because the structure 33 is changed from the separate species to the aggregated cluster in response to the variation in pH. The development of pH sensor for extremely high pH like $\text{pH} > 10$ is necessary, because of alkaline errors and exciton may dissipate energy due to the energy transfer. In 2013, Knut Rurack and Co-workers synthesized BODIPY dye bearing an acidic phenol moiety. The BODIPY dye was embedded into the polyurethane matrix, immobilized on 3D-epoxy-functionalized polymer support. At higher pH due to the complete deprotonation of a phenolic moiety quenches the fluorescence intensity. Due to deprotonation, the phenolate ion becomes electron-rich and highly electron-rich meso substituents commonly quench the fluorescence of the BODIPY core through an efficient

electron transfer process.[68] BZ Tang and Co-workers synthesized a hybrid system that consists of both AIE characters and properties of cyanines. The Red emissive hemicyanine dye contains tetraphenylethene (TPE) moiety for AIE character and N-alkylated indolium group for pH response. The AIE active dye response to the pH in full range, showing (switch + knob) effect at different pH different emission colour and intensities (Switch + knob) effect. Bright red emission at pH <5, moderated red emission at pH -5-7, weak to no emission at pH 7-10, no emission to strong emission at pH 10-14. Further, the AIE-Cy (35) dye was applied in the intracellular pH imaging because of excellent biocompatibility and cell-permeability.[69, 70] In 2015, Jin Huang et al., designed and synthesized ratiometric fluorescent nanoprobe consisted of a gold nanoparticle, short single-stranded oligonucleotide and a dual fluorophore (rhodamine green (donor) and rhodamine red (acceptor) labelled intercalated motif (i-motif) sequence.

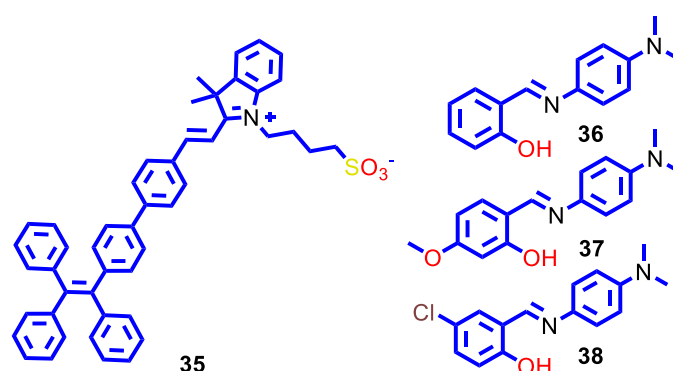


Figure 1.16 Structure of the AIE and pH-responsive molecular probe.

At neutral pH, the dual fluorophore is separated, resulting in a very low FRET between i-motif and rhodamine. At acidic pH, i-motif stands fold in the quadruplex structure and leave the gold nanoparticle, bringing the dual fluorophore close, which increases the FRET process.[71] Baoli Dong and co-workers synthesized site-specific lysosome targeted intramolecular charge transfer-photoinduced electron transfer-fluorescent resonance energy transfer fluorescent probe for monitoring pH changes in the living cells[72] (Fig. 1.17) In 2017, Han Yan et al. synthesized two new AIE pH probes by combining pyrimidine and a phthalimide (2-(4,6-dimethylpyrimidin-2-yl)isoindoline-1,3-dione (PB) and 2-(4,6-bis(4-(dimethylamino) styryl) pyrimidine-2-yl)isoindoline-1,3-dione (NPB)) based on the molecular design Donor-II-acceptor system. The PB and NPB can be easily protonated at the nitrogen side[73]. In 2018, Ema Horak et al. synthesized an AIE benzimidazole

functionalized Schiff base. The benzimidazole probe provides a reversible fluorimetric determination of the pH. The Ema utilized the imino nitrogen of the Schiff base as a protonation site in the acidic medium.[74] Jianbo Wang synthesized three NIR probes based on bond energy transfer and π -conjugation between the TPE moiety and hemicyanine moieties for the sensitive detection of pH changes in the live cells. [75]

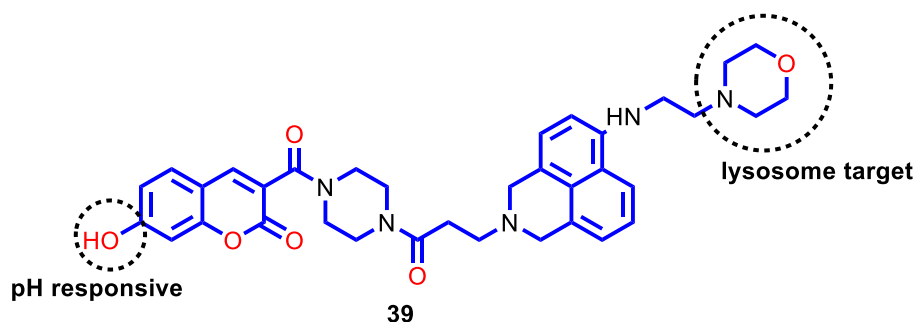


Figure 1.17 Dual site fluorescence lysosome targeted pH sensing probe.

1.5.2 Solvatochromic luminescence probes

Some of the compounds are known to show different responses to light absorption, depending upon the polarity of the medium. These types of compounds are known as solvatochromic probes. The study of polarity around the surrounding medium is important for solute-solvent interactions. Many factors as for examples (solute-solvent interaction, hydrogen bonding, vanderwall interaction, solubility, acid-base equilibria and keto-enol equilibria etc), play the role to study surrounding medium in which the probe is dissolved. The solubility affects the spectroscopic responses due to the environment-induced aggregation.[76] The specific solvent effect, such as hydrogen bonding not only affects the emission property of the probe but also leads to a significant stoke shift. By knowing the mechanism for the small changes in photophysical properties in the micro-level could help to understand the nature of the living cells.[77] The fluorescence technique is promising for sensing and imaging applications. [78] An organic fluorophore is highly useful materials for sensing, but due to autofluorescence from the background which interferes with the selectivity of the targeted species. To overcome the problem, the materials with high quantum yield in solid state and high stoke shifts are necessary.[79] A series of tetraphenyl ethylene containing BODIPY compounds and these compounds show AIE behaviour with solvatochromism. Their emissions are tunable from visible to near-IR with large Stokes shifts up to 142 nm.[79-82]. Many AIE active materials have been synthesized, which exhibited large stokes shifts.[83-85]

1.5.3 Albumin Sensing probes

Chronic Kidney Diseases (CKD) is a worldwide public health problem, with the adverse effect of kidney failure, cardiovascular diseases (CVD), and premature death. According to the organization named Kidney Disease: Improving Global Outcomes (KDIGO) defined CKD as kidney damage glomerular filtration rate (GFR) <60 mL/min/1.73 m² for three months or more, irrespective of the cause.[86] The presence of albuminuria is the principal marker of the kidney damage in many kidney diseases defined as albumin-to-creatinine ratio >30 mg/g of urine sample in two of three spot urine specimens”[87]. In February 2002, the Kidney Disease Outcomes Quality Initiative (K/DOQI) of the National Kidney Foundation (NKF) given the guidelines for defining chronic diseases at different stages and the laboratory measurement for the clinical assessment of the kidney disease.[88] Many methods have been developed based on antigen-antibody interactions for albumin detection due to their excellent performance in terms of sensitivity and selectivity. These methods include radioimmunoassays[89], enzyme-linked immunosorbent assays (ELISA), immunonephelometry[90], solid-phase fluorescent immunoassays[91], liposomal immunoassays[92], magnetic immunoassays[93], and immunoturbidimetry[94]. All these conventional instruments are quite a bit expensive, time-consuming, and also consumes large amounts of expensive antibody reagents.[95] Among all the above techniques, the fluorescent-based technique is used widely because of its higher sensitivity, cost-effective, less experimental time.[96] In 1998 Ma et al. first utilized the fluorescence-based technique for the detection of albumin. In this work, the fluorescence of 2,5-di(ortho aminophenyl)-1,3,4-oxadiazole was enhanced by increasing the concentration of albumin.[97] Several fluorescence reagents for albumin detections and quantifications based on emission enhancement have been developed, such as fluorescamine, o-phthalaldehyde, cyanine dyes, and SYPRO Ruby.[98] For many years, protein sensing could be possible in solution state only when and researchers tried to be away from the aggregation as the luminescent of the probes gets quench.[99] Tong et al. and Co-workers were managed to overcome the problem by introducing the AIE molecule's dimethoxylated TPE derivative, which was further derivatized to give dihydroxylation TPE and then disulfonated TPE (Figure 1.18). All the three TPE derivatives are AIE active. The disulfonated TPE is water-soluble and works as an excellent for protein sensing. Here, the BSA contains hydrophobic binding sites. (the BSA has three pockets of hydrophobic site). The dye interacts with the hydrophobic region of BSA and enters the hydrophobic cavity of the BSA folding structure. The binding of BSA induced

redshifted in $\lambda_{\text{emi}} = 74$ nm. In the hydrophobic cavity the movement of phenyl rotors in the dye gets restricted, and emission is enhanced.[100] In 2010, Lu et al synthesized the anthracene derivatives based (32, 33, and 34) pH sensors and also as BSA sensing.[67] The probe molecule 34 interacts with the BSA, which enhances the fluorescence spectra. In a buffered solution, the cationic amphiphilic dye binds to the biomacromolecules via supramolecular interaction such as hydrophobic interaction and electrostatic interaction. The detection limit reached up to 500ng/ml.[67] In 2013, to improve the sensitivity more, Peng et al designed and synthesized the ratiometric fluorescence probe, 2,2',4,4'-tetrahydroxybenzophenone azine with AIE characteristic (Fig. 1.18). At 7.4 pH, the probes 43 get deprotonated and emit blue fluorescence. The probe after binding to the hydrophobic pocket or the albumin (BSA) the intramolecular rotation is inhibited, which enhances the fluorescence.[101]

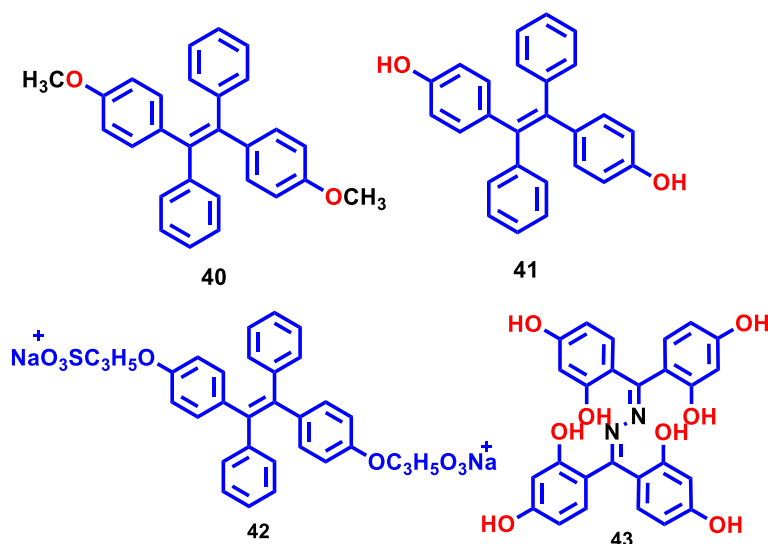


Figure 1.18 Structure of AIE probe based on TPE unit for protein Sensing (40-43).

In 2013, Long et al. synthesized an AIE active distyrylanthracene derivative for turn-on detection of BSA and quantification.[102] In 2015, Li et al. designed a turn-on fluorescent probe with AIE characteristic for quantification albumin. The probe molecule 44 (sodium 4,4'4''-(3,4-diphenyl-1H-pyrrole-1,2,5-trityl) tribenzoate)) were in propeller shape (Fig. 1.19). The detection limit was $2\mu\text{g/ml}$. The mechanism for turn on sense is the interaction with the hydrophobic core and hydrogen bonding between a probe molecule and albumin.[103]. In 2017, Malathi et al. and Co-workers synthesized AIE active benzimidazole attached quinolone derivative

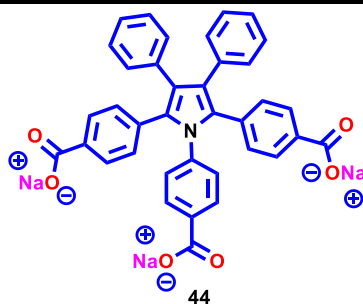


Figure 1.19 Structure of AIE propeller probe for protein Sensing.

. The probe 44 is multi responsive; it responds to pH, Fe (III) and BSA protein. A docking study revealed that the probe is attracted to the hydrophobic core of the BSA.[104] In the same year, Li et al. synthesized a red emissive BODIPY-Triphenylamine AIE active probe. The detection limit was 1.44×10^{-7} M, 1.52×10^{-7} M, 5.37×10^{-8} M. These BODIPY was utilized in cell imaging.[105]

In 2018, Samanta et al. combine the AIE process with the TICT process. They used the D- π -A system (alkylated Cyanine dye as an acceptor and N, N diethylene as a donor). The probe itself gets self-aggregated. The specific binding probe with HAS led to disassembly of self-assembled nano aggregates. The detection limit is nearly 6.5 nM.[106] In 2019, Barbeo et al. designed and synthesized two squaraine-based AIE active probe molecules. After interacting with the BSA in the hydrophobic core, the molecules form the supramolecular adducts with enhanced fluorescence.[107] In 2019, Samanta et al. rationalize the design of AIE active urea derivative for HSA and BSA sensing with a detection limit of $5 \mu\text{g/ml}$.[106] In 2019, Chakraborty et al. utilized the excimeric emission of the pyrene molecules for the detection of the BSA.[108] Very recently Liu et al. synthesized first nitro capped tetraaniline 45 (Fig. 1.20) derivatives with AIE behaviour. The tetraaniline probe molecule is red emissive and ultrasensitive towards the BSA ($8.62 \mu\text{g/ml}^{-1}$).[109]

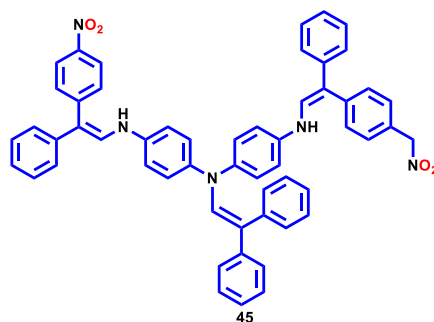


Figure 1.20 Structure of tetra aniline

1.5.4 Viscosity Responsive Probes

There is a famous quote as the great physicist Albert Einstein once stated: “Nothing has happened unless something has moved.” Life to exist, the “rate” at which the molecules can move is all-important and is determined by the viscosity of the medium. Viscosity is a measure of fluid resistance to the flow, which describes the internal friction of the moving fluid. A fluid with large viscosity resists the motion and fluid with low viscosity flows smoothly. In simple words, the term viscosity in material science and engineering is defined as the force or stress involved in the deformation of a material. Formally, viscosity is the ratio of the shearing stress to the velocity gradient. Temperature, pressure, and concentration are the main factors on which the viscosity of the fluid depends.[110, 111] viscosity has a more significant influence in the fluorescence intensity. In a low viscous solvent, the intramolecular motion is predominant in the excitation pathway, whereas in a high viscous solvent, the intramolecular motion is hindered and the fluorescence intensity is enhanced.[112]

Viscosity is an important parameter affecting the transport of molecules and proteins. In the biological point of view, cellular level viscosity change has been linked to the diseases and malfunction of the cell. It also plays a more significant role in drug delivery and cancer therapy.[113, 114] Indeed, the intracellular environment has a particular parameter for the efficient running of life. Changes in the viscosity of these media could create a massive problem in many biological processes like all the diffusion mediated processes, including mass transportation, signal transduction, biomolecule interactions, diffusion of metabolites, and electron transport all of these are closely associated with a variety of diseases. Various studies revealed that the anomalous mitochondrial viscosity is related to neurodegenerative diseases, diabetes, and cell malignancy, while the change in the lysosomal viscosity suggests the diseases of lysosomal storages, inflammation, and even cancer.[208] For determining the macro-level viscosity, there are various well-developed methods; they required macroscopic sample quantities and used mechanical, fluid dynamic approach, falling ball viscometer, and or rotational viscometer for viscosity determination.[115] However, for microscale determination of viscosity remains a challenge to date. Mapping of single-cell viscosity is one of the most challenging tasks. Many methods are applied to measure the changes in the viscosity of the cell among them optical techniques often regarded as non-destructive and minimal damage techniques. The advantage is that these techniques could be used in live

cells and tissues.[116-119] Viscosity measurements were carried out based on the change in the PL intensity first. Theoretically, a strict mathematical relationship between viscosity (η), and quantum yield (ϕ) was developed - the equation is known as the Forster–Hoffmann equation $\log \phi = C + x \log \eta$ in which C is the temperature-dependent constant, x is dye dependent constant the value of which indicates viscosity sensitivity of fluorescence viscosity probe. [120, 121]

The fluorescent technique is mainly used for measurement, mapping, and imaging purposes because of the high contrast and easy visualization in the cellular environment.[122] In response to all the above problems, Luby-Phelps et al. in 1993 designed and synthesized two homologs indocyanine dyes attached to macromolecular Ficoll 70 to measure the intracellular viscosity.[121] However, cell permeability and photostability are the primary concern for this molecule. In 2009, Kuimova et al. used the rotor, constructed on a dimer of porphyrin dimer (44, Fig. 1.21) to map the intracellular viscosity of single cell during the photoinduced cell death. They describe that there is a dynamic increase in the viscosity, which indeed alters the diffusion- dependent kinetics of the cell.[123]

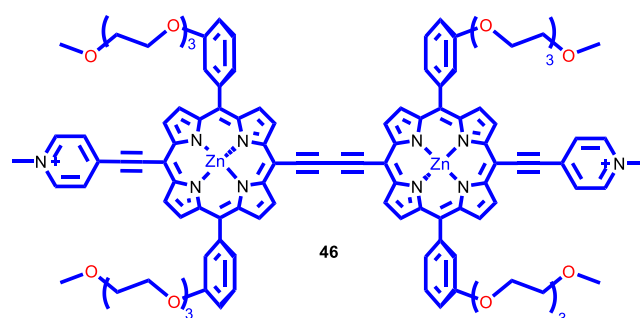


Figure 1.21 Structure of porphyrin-based rotor for mapping intracellular viscosity.

In 2011, Peng et al. designed the ratiometric fluorescence cyanine-based rotor probe to increase the cellular permeability and to decrease the photobleaching effect (Fig. 1.22). To gain more accuracy and reliability, they used the fluorescence ratiometry and fluorescence imaging technique. Here the rotation of the CHO group in the excitation pathway helps the deactivation process, but in a high viscous solvent the rotation is restricted, and emission is enhanced.[124] In 2013, Yang et al. introduced the Forster resonance energy transfer mechanism in the probe molecule consists coumarin where BODIPY acts as a fluorescent receptor, phenyl ring as a rigid spacer and a triphenylphosphonium as a mitochondrial targeting unit (47-50). The C-C bond between the spacer and BODIPY rotates freely in the

low viscous solvent to produce fluorescence quenching whereas the rotation is restricted in the high viscous solvent. The ratiometric fluorescence helped them to study the change in viscosity in the mitochondrial matrix caused by drug monensin and nystatin. [47]

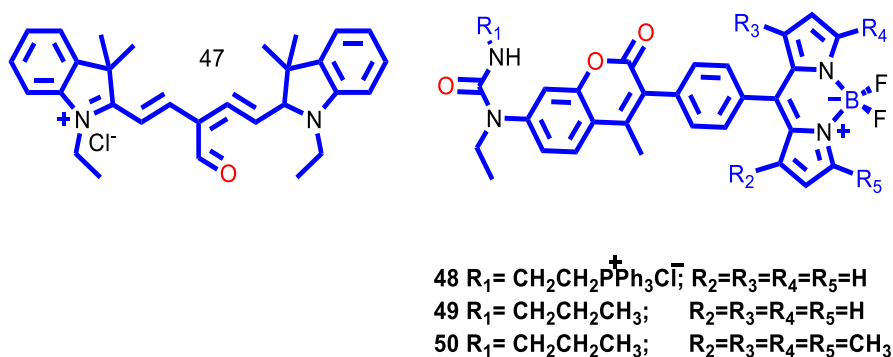


Figure 1.22 Structure of Cyanine and BODIPY type of viscosity probes.

In 2015, D. Telore et al., using a Knoevenagel condensation reaction, synthesized a series of push-pull types of carbazole based viscosity sensing compounds with the AIE characteristic probe.[125] These compounds are insensitive to the polarity of the solvent. Meanwhile, many new fluorophores based on carbazole, cyano-stilbene, triphenylamine, styryl and naphthalimide were synthesized and applied as a probe for viscosity sensor.[126] In 2017, Song et al. synthesized a viscosity probe named VIS-A (51) and VIS-B (52). Accordingly, he designed a probe to fix it in the mitochondria by attaching an anchor (CHO) moiety with the mitochondria-targeted group. Here, -CHO reacted with the proteins in the mitochondria, henceforth it was unable to move outside from the mitochondria. The property helps to quantify the viscosity of mitochondria in the healthy and diseased state. Autofluorescence from the background is the main problem inside the cell so, to remove it, researchers synthesized red-emitting viscosity sensitive dye.[127]

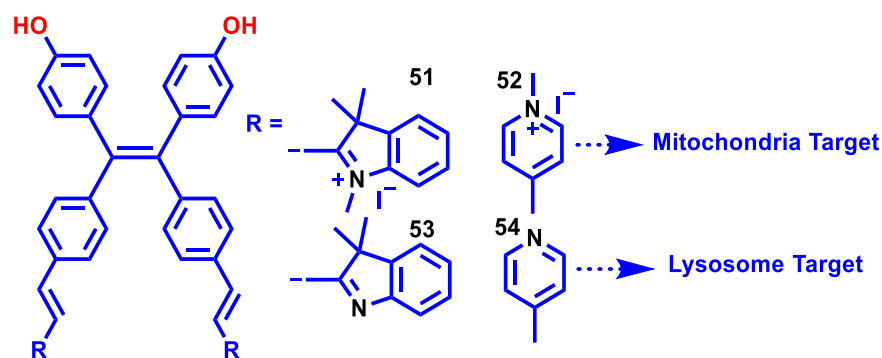


Figure 1.23 TPE based AIE viscosity sensor for organelle targeting probes

Recently, researchers focused on the design and synthesis of viscosity probe with a longer wavelength, long lifetime, and organelle-specific.[128] Wang et al. targeted the lysosomal Viscosity through BODIPY derivative containing morpholine as a lysosome targeting moiety (56). Once the BODIPY derivate (56) diffuses into the lysosome morpholine nitrogen gets protonated. The dye became more hydrophilic and remained in the lysosomes. Due to the protonation, morpholine unit can no longer serve as the electron donor for the PET process. Thus, fluorescence is enhanced in the lysosome. However, the fluorescence highly depends on the pH. At pH 4, the compound shows stronger emission intensity than at pH 7. Owing to it, the dye was used in fluorescence lifetime imaging for quantifying the viscosity in the lysosome.[129] Zou et al. synthesized Pyridium based carbazole derivative (57) for visualizing the dynamic viscosity of mitochondria in mitophagy phage. Here due to the restriction of pyridine ring attached to the carbazole, the fluorescence is enhanced.[130] Very recently, Hao and Co-workers synthesized a series of Ir(III) biscyclometalated phosphine based complex for mitochondrial viscosity two-photon lifetime imaging. These are anti-cancer phosphorescent complexes. The emission intensities and lifetime of the complex are viscosity dependent. Therefore, this kind of study helps to design new small molecules that could induce and monitor therapeutic effects by measuring microenvironment at the subcellular level.[131, 132]

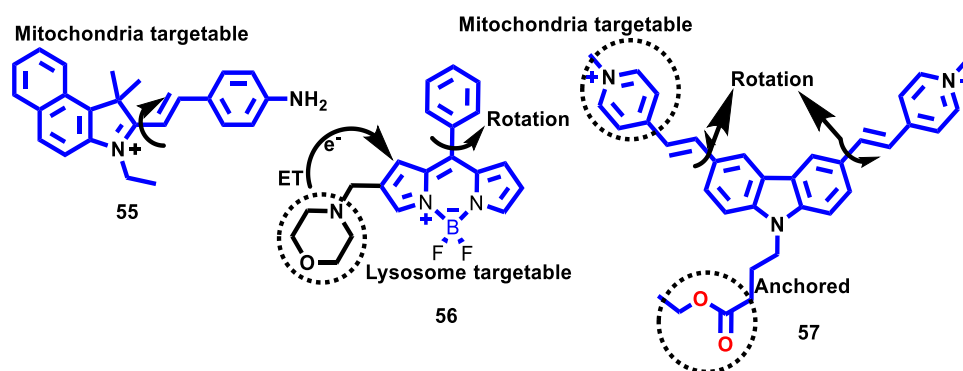


Figure 1.24 Structure of organelle targeting viscosity probe

1.5.5 Explosive Sensing Probes

1.5.5.1 What is Explosive?

Explosive is a substance or a (mechanical or handmade) device that can produce the volume of rapidly expanding gas in an extremely brief period.[133] There are three kinds of explosives.

1. Mechanical explosive is one that wholly depends on physical contact or reaction.
2. Chemical explosive is one with continuous rapid reaction producing more and more heat.
3. Nuclear explosive is sustained with nuclear reaction can be made to take place very rapidly, releasing a large amount of energy.

Recently chemical explosive is used more for terror attack because these explosive are easy to transport and hide. Chemical explosives are two kinds (1) detonating or high explosives, and (2) deflagrating or low explosives, e.g., propellant and pyrotechnics. Detonating or high explosive are again subdivided into two kinds a) primary explosives requires a source of fire, spark or sufficient amount of heat which equals the magnitude of explosives, for example, such explosive includes the lead azide and lead styphnate. b) secondary explosive which includes the nitroaromatic or nitramines which are much more applied in military sites. Secondary explosive is loosely categorized into melt-pour explosives which are based on nitroaromatics, eg, trinitrotoluene (TNT), dinitrotoluene (DNT) and plastic bonded explosives (PBX) which are based on a binder. Crystalline explosive such as hexahydro-1,3,5 trinitroazine (RDX). Again the nitro explosive can be classified as electron-deficient aromatic like trinitrotoluene (TNT), picric acid (PA), 2,4-dinitrotoluene (DNT), 1,3-dinitrobenzene (m-DNB), 2,4,6-trinitrotoluene (TNT) etc., and electron-deficient aliphatic like 2,3-dimethyl-dinitrobutane (DMNB), trinitroglycerin (TNG), 1,3,5-trinitroperhydro-1,3,5-triazine (RDX), octahydro-1,3,5,7-tetranitro-1,3,5,7-tetrazocine (HMX) etc. (Fig 1.25), RDX, HMX, TNT, TNP, TNG, PA explosives are more hazardous and dangerous. According to the recent interview by the Institute for Economics and Peace (IEP) from 1970 to 2019, about an average of 15% of deaths are caused by explosives.[134-138]

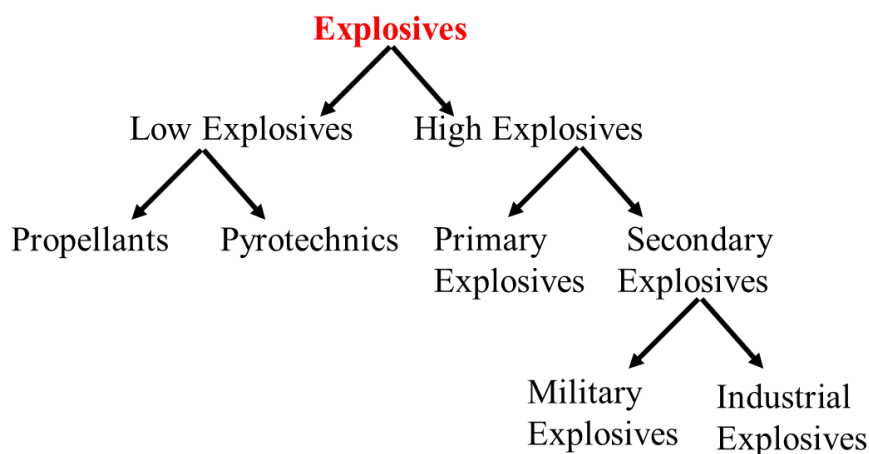


Figure 1.25 Flow chart representing the classification of the Explosive materials.

1.5.5.2 Importance of Explosive detection

The measurement of the explosive on contamination sites provides a rapid warning at manufacturing, storage, and demilitarization of the weapons. Not only warning but the identification and quantification of explosives have also become the emerging topic of interest for all the researches due to their prominent role in the security threat and increasing terrorism. Terrorism, the word itself, replicate the meaning of terror. There are many different definitions of terrorism. It is a charged term. It is used with the connotation of something that is “morally wrong.” In simple words, “the deliberate killing of humans without any cause at random to spread the fear among the world population and force the hand of its political leaders.”

The detection of the explosive is a critical task in the field of forensic science, anti-terrorist activities, and global de-mining projects. Asbury et al. have rightly pointed out the importance of analysis of explosives in two dimensions. One is the threat of illegal use of these compounds for security, creating the fear and chaos among the peoples and thus encouraging terrorist activities.[139] While the increase in terrorist activities, the demand for reliable and rapid detection of luggage also increases. For counter, the active terrorism scanning of explosives in objects of various sizes, ranging from small ring to large containers, became an important aspect. Furthermore, the other is a significant concern about the health risk when these explosives are released in the environment. Nitro compounds can rapidly penetrate the skin causes various problems such as liver damage, renal problem, and anaemia, etc. When these compounds persist in the biosphere, they severely affect the healthy life of humans, fishes, and microorganisms. Therefore the detection of the explosive as well as tracking and locating the place where the explosive materials are buried or kept is a highly essential task, which could help in reducing the continued fatalities from the land mines among the civilians [140-143]

1.5.5.3 Probes for Explosive detection (Techniques for the detection of explosives).

Explosive materials are composed of different materials with low pressure (e.g., TNT, TNP, RDX, HMX, Tertyl, and PETEN). The detection of these compounds is a very complicated task. Moreover, terrorist packs them in the plastic material. According to the literature, the vapor pressure is reduced to 1000 times when they are packed in plastics.[231] So far, various detection techniques have been developed to detect the explosives, including gas chromatography[144], Sniffing dogs[145], Raman spectroscopy[146], cyclic

voltammetry[147], X-ray scanning[148], and ion mobility spectrometry[149]. However, most of the instruments used are expensive, bulky devices and unsuitable for incorporating into a portable system for in-field, remote, or non-contact detection and lack of sensitivity. Spectrophotometric based methods are divided into several types. One of them is ionization mass-spectrometry (IMS) which is highly sensitive for detection and identification, like a swipe of clothing, skin, or objects, will pick up particulates containing explosives residue which may then be analyzed for the molecular mass. The identification of explosives involves a comparative analysis with a library of standards. The disadvantages with IMS are the need for careful instrumental calibrations and the limited portability of most IMS instruments, suggesting that this method may be less than ideal for broader use. Methods using infrared or visible light are advantageous because they provide sensitivity, cost-effective instrumentation, portability, and maintain the ability to detect a wide range of explosive chemical classes. Absorption based detection is the simplest of the other spectrophotometric methods. [150-152] Several kinds of colour-changing chemical sensors have been developed for the rapid onsite detection of explosives. A specific colour reaction is made between the well-known compound cymantrene and related explosive compounds (ERC) for the detection.[153] The technique provides fast and simple detection of explosive fingerprint residues on various surfaces. The detection limit of the proposed technique is about 0.2 ng of DNT.[154] Oh et al., have used spectrophotometric assay for the detection of TNT in culture media, which is basically of the colourimetric based method. It is not so sensitive as expected for the detection of explosive compounds.[155]

Sohn et al. explored the photoluminescence property of polysiloxane derivative through quenching its luminescence by explosive analytes like picric acid, TNT, DNT in the air (4ppb) or seawater (1.5ppt) or underwater land mines. However, these methods are less responsive at the time of intense background colour or background fluorescence. A well-accepted method is a fluorescence-based detection. The principle of fluorescence-based detection mostly relies on the quenching of emission when the target molecule comes in contact with the probe. The broad applicability of this technique in the detection and quantification of explosives arises because of simplicity. The fluorescent sensitive material [like 4-N, N-dimethylamino-4 methylacryloylaminochalcone (DMC), pentiptycene polymer, Nile Red dye, liquid-crystalline (LC) polyfluorenes, etc.] is spread over the suspected area to get the image of an object which indicates the presence of explosive compound or material. Due to the electron-rich behaviour of semiconducting polymers, often, these are used to

detect explosives. Nitroaromatic explosives being electron deficient bind to the electron-rich semiconducting polymers and quench their fluorescence by an electron transfer mechanism. The detection was also carried out on a microfabricated chip and concentrations of 1 ppm of TNB, TNT, DNB, 2,4-DNT could be detected using this method. However, for the case of two nitramines, HMX and RDX could not be detected because of their low vapour pressure. Ladbeck et al. developed a technique for the detection of peroxides based explosives, i.e., HMTD and triacetone triperoxide (TATP), and the limit of detection was 2×10^{-6} mol. Mostly the fluorescence quenching approach has been explored for the analysis of nitrate explosives for the detection of RDX, HMX, TNT, nitromethane, and ammonium nitrate.[156-158] In 2015 M. K. C. et al. synthesized 1,8-naphthyridine (58, 59) based fluorescent sensors for the detection of the picric acid in aqueous medium and the mechanism is found to proceed through both photoinduced electron transfer and resonance.[159] Vishnoi et al. synthesized a fluorescent-based sensor 1,3,5-tris(4-(N, N-dimethylamino)phenyl)benzene (60, 61) which selectively senses the picric acid with a detection limit of 1.5 ppm. Here the proton is transferred from the picric acid to the probe making picrate ion more an electron-deficient. The quenching of fluorescence arises because of the transfer of energy.[160] In 2016, Tian et al. designed and synthesized an ionic liquid-based (62) chemosensor, which forms the charge transfer complex with picric acid through the protonation process. The protonation favours the electrostatic interaction between probe and picric acid. The picric acid is also detected on test paper by this probe. The detection limit is 8.1×10^{-7} M.[161] In the same year, Mahendran et al. utilized the AIE active TPE derivative based on pyrone(63) for explosive sensing. Because of the AIE nature of the molecule, the probe is highly sensitive to picric acid, and the detection limit is 22 nM.[162] In 2017, Sodkhomkhum et al. utilized the pyrene monomeric and excimer emission for PA sensing. The synthesized imidazolylmethylpyrene (64) can sense PA in both ways as fluorescence and colourimetric sensing. Just by changing the solvents, the probe senses the PA in two different ways (i.e., in acetonitrile with the addition of PA the emission is enhanced and in toluene, with the addition of PA the emission is quenched) with a detection limit of 243 ppb and 576 ppb respectively.[163] Wei Huang et al. reported two hyperbranched conjugated polymers with TPE units as core and 1,4-dodecyl-2,5-diethynylbenzene as well as 1,4-bis(dodecyloxy)-2,5-diethynylbenzene as co-monomers and utilized the polymer in explosive sensing in water. The quenching efficiency depends upon the energy transfer mechanism.

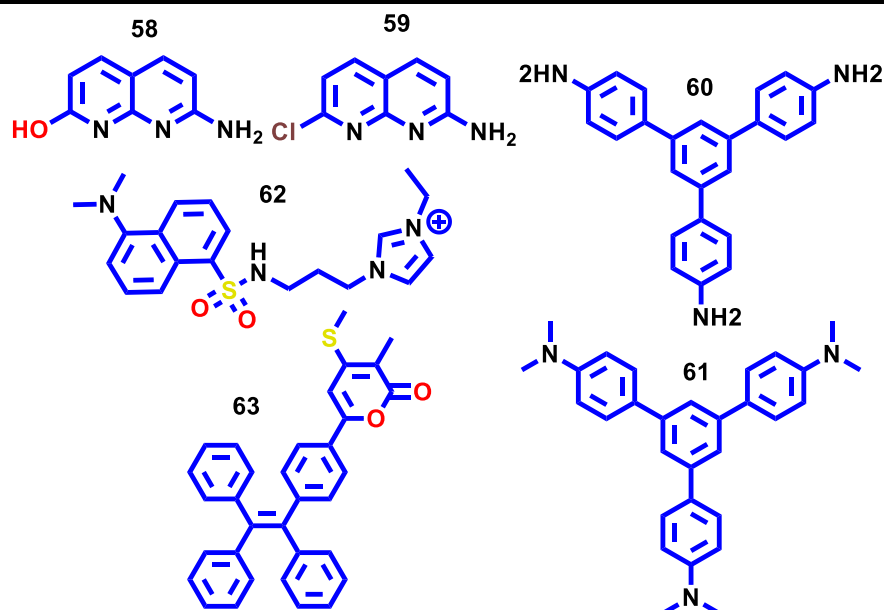


Figure 1.26 Structure of the explosive sensing probe (58-61)

The higher the spectral overlap between the absorbance of the analyte and emission of the fluorescent polymer, the higher is the sensitivity.[164] Li WEN et al., rationally designed and synthesized aggregation-induced emission cationic Ir(III) phosphors. By increasing the alkyl length, they were able to increase the photoluminescence quantum yields 13.6 % to 32.2 %. The longer alkyl group can reduce the strong intermolecular interactions of the emissive core, decreasing the non-radiative channels. The quenching of the complex was attributed to the PET and RET processes. Among them, compound 85 is very sensitive towards picric acid (detection limit = 10 ppb).[165]

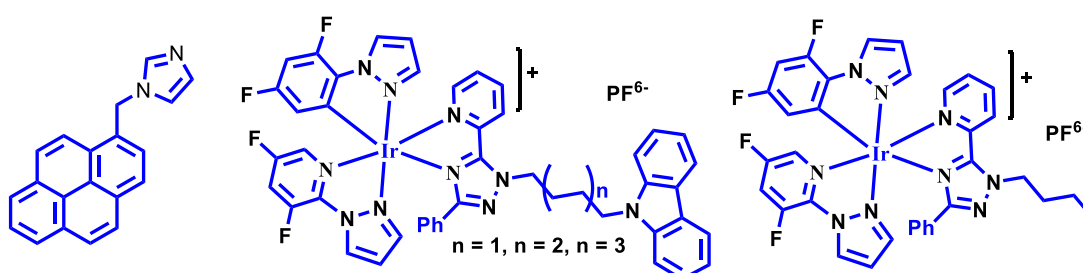


Figure 1.27 Chemical structures of compound (64-66)

In 2018, Giri et al utilized 1,2,3 triazole appended polythiophene for the detection of trace nitroaromatics. Conjugated polymers were synthesized by GRIM (Grignard metathesis reagent) polymerization. Here the electron-withdrawing capacity of 1,2,3 triazole in polymers plays a crucial role in enhancing the detection ability towards the nitroaromatics. The

absorption maxima of polymers were absorbed in 485 nm. The polymer was emissive in the orange spectral region at 573 nm with a significant stoke shift of 7070 cm^{-1} . [166] The polymer makes use of the molecular wire effect for fluorescence quenching. The quenching constant of the K_{sv} was 8.4×10^4 . In the same year, Tao et al. synthesized three AIE active dibenzo[b,d] thiophene skeleton-based compounds. These compounds act as a chemosensor for picric acid in an aqueous medium with a detection limit of 20 ng/cm^2 . [167] Abu Saleh et al. synthesized the pyrene based multifunctional materials. It acts as a sensor for nitric oxide and picric acid. The pyrene Scaffold compound (67) exhibits AIE activity for which the fluorescence quenched in the presence of picric acid. The stern volmer quenching constant was found to be $1.4 \times 10^4\text{ M}^{-1}$. [168] Che et al. synthesized a series of active AIEE Ir(III) complex (68-71). The quenching mechanism was confirmed by mass spectroscopy, ^1H and ^{19}F NMR which reveals that the H-O---H interaction between picric acid and the ancillary ligand is responsible for sensitivity. The detection limits for complexes 68-71 as sensors for TNP are calculated to be 0.23, 0.15, 1.05 and 1.65 mM, respectively. [169] Guo et al. synthesized two AIEE active cycnostilbene derivatives and attached the BF_2 unit for high quantum yield. DFT studies defined the sensing mechanism. The LODs were calculated as $1.26 \times 10^{-6}\text{ M}$ and $1.51 \times 10^0\text{ M}$, respectively. [169] Very recently, Ma et al. synthesized a three-component compound integrated 1,4-dihydropyrrolo[3,2-b]pyrrole (72, 73) with tetraphenylethylene (TPE) and pyridine units. Here the TPE unit shows AIE activity, while pyridine unit for PA sensing. Because of the strong affinity of picric acid towards the pyridine, the detection limit of the compound was 32.5 nM. [170] Dong et al. have significantly worked on conjugated polymer based on polycarbazole and TPE (side chain). The polymer detects the explosive through the excited-state charge transfer between the excited state of the polymer and ground state of the picric acid. [171, 172] The high-efficiency sensing is due to

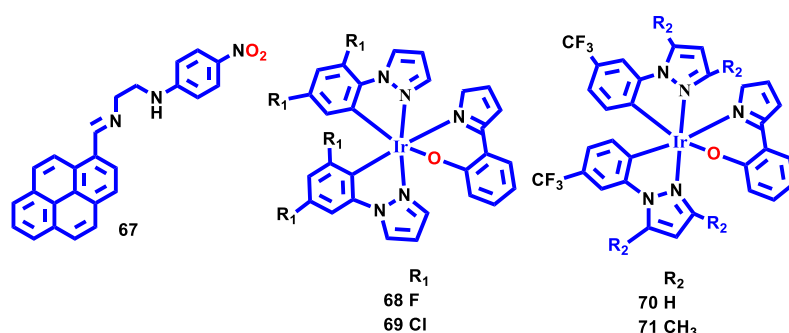


Figure 1.28 Chemical structure of 67-71

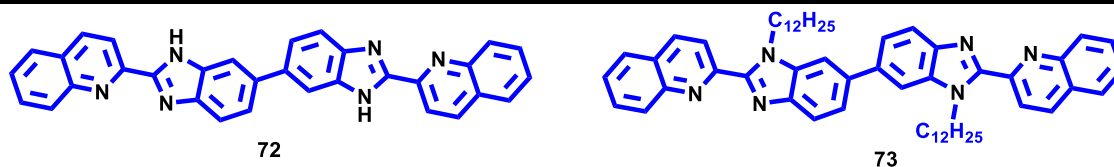


Figure 1.29 Chemical structure fluorophore based on quinoline and benzimidazole (72, 73)

the electron-donor property offered by electron-rich carbazole and the loosely packed structure of 3D polymer nanoaggregates in the aggregated state.

1.6 Research Gap

The present thesis deals with both the development and discovery of the smart, responsive compounds. We have unearthed the potential of an old molecule and also synthesized several new ‘Aggregation-induced Emission’ (AIE) active compounds and used them for sensitive and selective sensing of various important analytes and essential parameters. Smart materials are characterized by their smart, responsive behaviour, which is governed by the chemically active functional groups attached within the molecules. While the majority of the molecules displayed only one or dual specific responsive functions, very limited efforts have been taken to explore the multi-stimuli probes and their applications [173-175] In the field of pH sensing, there is a lack of molecules that are sensitive to the whole range of pH. It is the alkaline nature that keeps our bodies healthy, while diseases are mostly observed to arise in acidic conditions. The alkaline medium produces the alkaline error effect.[176] Most of the developed probe molecules are stick for sensing at a particular pH which makes the probe limited to the ranges of pH. The mechanism for increasing or decreasing the luminescence in the whole range of pH has not been explored.[177] Moreover, the whole imaging of cytoplasm inside the cell utilizing a single pH probe is still rare.[70, 132]

In the field of albumin detection, most of the probes are organic luminophore. Autofluorescence, photobleaching and insensitivity is the main problem for the organic molecules in the biological fluids[178]. In the present situation, no systematic study exists that results in a very sensitive probe molecule to detect albumin (at the level of ng), yet it will be inexpensive.[179, 180] Heavy metal atom can transfer its excited energy to triplet state quickly to act as triplet state emitters. The emission is mainly due to the lowest triplet energy charge-transfer state; therefore, such complex can be used for probing the cation, anions & the biologically essential molecules, proteins more efficiently.[181]. Modification on the cyclometalated ligand provides the opportunity to the tuning of the complex emission

in the entire visible region that facilitate a significant response to the analytes. With combining three or more active functional groups in one molecule to make the compound responsive to different species selectively created a space in modern research. Describing the mechanism for developing efficient new molecules is an important task.

In the field of viscosity sensing, many new AIE probes have been developed and applied for imaging and quantification of the intracellular viscosity.[182] Probe molecules can target the specific organelle for imaging the intracellular viscosity. However, the biocompatibility and sensitivity of these probes remains challenging and required to be improved further for sensitive applications.[124, 129] Researchers used the fluorescence lifetime microscopy for imaging intracellular viscosity with the help of probes sensitive to viscosity. As the cost of the instrument is more, this instrument may not be present in many research centres. So, there is a need to develop a probe with high contrast and high stoke shift. So, the probes could be used in simple fluorescence microscopy for a better image in a simple way.[124, 129] By the intracellular viscosity, one could know the condition of the healthy cells. However, until now, the scientist has focused only on imaging the intracellular viscosity to detect the change in the cell functions and to study the drug effect on the intracellular viscosity of single cells. Moreover, there is a need for ease of synthesis and cost-effectiveness of the probe. The response of the viscosity should be distinguishable from other processes, and the viscosity-based probe molecule should not be affected by the pH and polarity of the cells. Furthermore, the viscosity probe could be utilized to distinguish between the healthy and diseased cells for pre-diagnosis [120].

In the field of explosives, onsite detection of nitro explosives in the solid or gaseous state is a significant challenge to address anti-terrorism. The challenge in the existing research is to obtain the ultra-sensitive probe towards sensing of nitro explosives. There are many probe molecules for sensing nitro explosive in contact mode but a rare case of vapour phase sensing. The existence in contact mode sensitive probe molecules is in few 100 hundreds of ppb (parts per billion) level.[141] Vapour phases sensing of explosives is required for real-time application in military and to reduce mass-destruction from the explosion by detonating explosives in a common people place. It poses a great challenge to design highly sensitive detection of explosives in the non-contact mode because of the inherent lowering of the vapour pressure of nitro based explosives.[139] The use of D-A type and polymer-based AIE materials would be a much better choice for highly sensitive detection of explosive materials.[183, 184] The mechanism underlying to detect explosive materials using

commonly known luminescent materials is mainly operated through photoinduced electron transfer and energy transfer that results from quenching of emission intensity.[166] The HOMO and LUMO energy levels of the probe molecules (AIE active) can be determined by using cyclic voltammetry and UV-VIS spectroscopic techniques. For the case of the AIE probe molecule, it is very convenient to tune the emission wavelength by merely incorporating the different electron-donating / withdrawing substituents in varying positions of the rotor group. Very few probes are used in extremely acidic or basic conditions for detection. To utilize these probe molecules successfully in explosive detection, the AIE luminogen must be stable in variable environmental conditions such as in acidic and basic conditions.[142] Conjugated hyperbranched based polymer or the conjugated polymer networks would be sensitive to detect the vapours of low volatile explosives (RDX/PETN/HMX) from their vapour phase.[141] Nevertheless, the reported conjugated polymers are mostly non-AIE compounds ref. The sensitivity of detection can be further improved through the rational design of choosing appropriate AIE active hyperbranched conjugated polymer with macro-porosity to detect the low volatile explosives.

1.7 Reference

- [1] G. Blasse and B. Grabmaier, in *Luminescent materials*, Springer, 1994, pp. 1-9.
- [2] A. Kitai, *Luminescent materials and applications*, John Wiley & Sons, 2008.
- [3] T. Yu, L. Liu, Z. Xie and Y. Ma, *Science China Chemistry*, 2015, **58**, 907-915.
- [4] M. H. Lee, J. S. Kim and J. L. Sessler, *Chem. Soc. Rev.*, 2015, **44**, 4185-4191.
- [5] H. N. Kim, K. Swamy and J. Yoon, *Tetrahedron Lett.*, 2011, **52**, 2340-2343.
- [6] A. Hakonen and S. Hulth, *Anal. Chim. Acta*, 2008, **606**, 63-71.
- [7] C.-G. Niu, G.-M. Zeng, L.-X. Chen, G.-L. Shen and R.-Q. Yu, *Analyst*, 2004, **129**, 20-24.
- [8] N. I. Georgiev, V. B. Bojinov and P. S. Nikolov, *Dyes Pigm.*, 2011, **88**, 350-357.
- [9] E. Baggaley, J. A. Weinstein and J. G. Williams, *Coord. Chem. Rev.*, 2012, **256**, 1762-1785.
- [10] J. Mei, Y. Hong, J. W. Lam, A. Qin, Y. Tang and B. Z. Tang, *Adv. Mater.*, 2014, **26**, 5429-5479.
- [11] Y. Huang, J. Xing, Q. Gong, L.-C. Chen, G. Liu, C. Yao, Z. Wang, H.-L. Zhang, Z. Chen and Q. Zhang, *Nat. Commun.*, 2019, **10**, 169.
- [12] G. v. Büнау, 1970, **74**, 1294-1295.
- [13] K. D. Chaudhuri, *Zeitschrift für Physik*, 1959, **154**, 34-42.

-
- [14] N. Zhao, J. W. Y. Lam, H. H. Y. Sung, H. M. Su, I. D. Williams, K. S. Wong and B. Z. Tang, 2014, **20**, 133-138.
- [15] S. R. Meech and D. Phillips, *Journal of Photochemistry*, 1983, **23**, 193-217.
- [16] J. Mei, Y. Hong, J. W. Y. Lam, A. Qin, Y. Tang and B. Z. Tang, 2014, **26**, 5429-5479.
- [17] X. Ma, R. Sun, J. Cheng, J. Liu, F. Gou, H. Xiang and X. Zhou, *J. Chem. Edu.*, 2016, **93**, 345-350.
- [18] J. Mei, N. L. C. Leung, R. T. K. Kwok, J. W. Y. Lam and B. Z. Tang, *Chem. Rev.*, 2015, **115**, 11718-11940.
- [19] Z. Li, Y. Q. Dong, J. W. Y. Lam, J. Sun, A. Qin, M. Häußler, Y. P. Dong, H. H. Y. Sung, I. D. Williams, H. S. Kwok and B. Z. Tang, 2009, **19**, 905-917.
- [20] Y. Hong, J. W. Lam and B. Z. Tang, *Chem. Comm.*, 2009, 4332-4353.
- [21] Z. Zhao, B. He and B. Z. Tang, *Chem. Sci.*, 2015, **6**, 5347-5365.
- [22] Z. Li, Y. Q. Dong, J. W. Lam, J. Sun, A. Qin, M. Häußler, Y. P. Dong, H. H. Sung, I. D. Williams and H. S. Kwok, *Adv. Funct. Mater.*, 2009, **19**, 905-917.
- [23] B. Z. Tang and A. Qin, *Aggregation-induced emission: fundamentals*, John Wiley & Sons, 2013.
- [24] Z. Zhao, J. WY Lam and B. Zhong Tang, *Curr. Org. Chem.*, 2010, **14**, 2109-2132.
- [25] N. L. Leung, N. Xie, W. Yuan, Y. Liu, Q. Wu, Q. Peng, Q. Miao, J. W. Lam and B. Z. Tang, *Chem. Eur. J.*, 2014, **20**, 15349-15353.
- [26] M. Gao and B. Z. Tang, *ACS sensors*, 2017, **2**, 1382-1399.
- [27] N. L. Leung, N. Xie, W. Yuan, Y. Liu, Q. Wu, Q. Peng, Q. Miao, J. W. Lam and B. Z. Tang, *Chem. Eur. J.*, 2014, **20**, 15349-15353.
- [28] F. Hu and B. Liu, *Org. Biomol. Chem.*, 2016, **14**, 9931-9944.
- [29] V. S. Padalkar and S. Seki, *Chem. Soc. Rev.*, 2016, **45**, 169-202.
- [30] Y.-C. Chiang, Z.-L. Lai, C.-M. Chen, C.-C. Chang and B. Liu, *J. Mater. Chem. B.*, 2018, **6**, 2869-2876.
- [31] S. L. Yefimova, G. V. Grygorova, V. K. Klochkov, I. A. Borovoy, A. V. Sorokin and Y. V. Malyukin, *J. Phys. Chem. C*, 2018, **122**, 20996-21003.
- [32] F. C. Spano and C. Silva, *Annu. Rev. Phys. Chem.*, 2014, **65**, 477-500.
- [33] S. Choi, J. Bouffard and Y. Kim, *Chem. Sci.*, 2014, **5**, 751-755.
- [34] S. Kirstein and S. Daehne, *Int J Photoenergy*, 2006, **2006**.
- [35] N. J. Hestand and F. C. Spano, *Chem. Rev.*, 2018, **118**, 7069-7163.

-
- [36] F. Würthner, T. E. Kaiser and C. R. Saha-Möller, *Angew. Chem. Int. Ed.*, 2011, **50**, 3376-3410.
- [37] J. Zhao, S. Ji, Y. Chen, H. Guo and P. Yang, *Phys. Chem. Chem. Phys.*, 2012, **14**, 8803-8817.
- [38] J. E. Kwon and S. Y. Park, *Advanced Materials*, 2011, **23**, 3615-3642.
- [39] R. Hu, S. Li, Y. Zeng, J. Chen, S. Wang, Y. Li and G. Yang, *Phys. Chem. Chem. Phys.*, 2011, **13**, 2044-2051.
- [40] G. Yang, S. Li, S. Wang and Y. Li, *Phys. Chem. Chem. Phys.*, 2011, **14**, 789-798.
- [41] D. M. Addington and D. L. Schodek, *Smart materials and new technologies: for the architecture and design professions*, Routledge, 2005.
- [42] B. Konarzewska, 2017.
- [43] W. Turner, S. Spector, N. Gardiner, M. Fladeland, E. Sterling and M. Steininger, *Trends Ecol. Evol.*, 2003, **18**, 306-314.
- [44] M. Schäferling, *Angew. Chem. Int. Ed.*, 2012, **51**, 3532-3554.
- [45] Y. Jeong and J. Yoon, *Inorganica Chim. Acta*, 2012, **381**, 2-14.
- [46] J. A. Kellum, *Critical Care*, 2000, **4**, 6.
- [47] Z. Yang, Y. He, J.-H. Lee, N. Park, M. Suh, W.-S. Chae, J. Cao, X. Peng, H. Jung, C. Kang and J. S. Kim, *J. Am. Chem. Soc.*, 2013, **135**, 9181-9185.
- [48] E. Calzia, Z. Iványi and P. Rademacher, in *Functional hemodynamic monitoring*, Springer, 2005, pp. 19-32.
- [49] M. K. Kuimova, *Phys. Chem. Chem. Phys.*, 2012, **14**, 12671-12686.
- [50] A. Shrivastava and V. B. Gupta, *Chron. Young Sci.*, 2011, **2**, 21.
- [51] M. Peech, *J Methods of Soil Analysis: Part 2 Chemical Microbiological Properties*, 1965, **9**, 914-926.
- [52] R. G. Bates, *Determination of pH: theory and practice*, New York: London: Sydney: John Wiley & Sons, Inc., 1964.
- [53] T. J. Wilding, B. Cheng and A. Roos, *J. Gen. Physiol.*, 1992, **100**, 593-608.
- [54] R. A. Feely, S. R. Alin, J. Newton, C. L. Sabine, M. Warner, A. Devol, C. Krembs and C. Maloy, *Estuar. Coast. Shelf Sci.*, 2010, **88**, 442-449.
- [55] P. Swietach, A. Hulikova, S. Patiar, R. D. Vaughan-Jones and A. L. Harris, *PLoS One*, 2012, **7**, e35949-e35949.
- [56] P. Capuano and G. Capasso, *G Ital Nefrol*, 2003, **20**, 139-150.

-
- [57] D. Lee, K. M. K. Swamy, J. Hong, S. Lee and J. Yoon, *Sens. Actuators B Chem.*, 2018, **266**, 416-421.
- [58] N. Demaurex, *News Physiol. Sci.*, 2002, **17**, 1-5.
- [59] O. Korostynska, K. Arshak, E. Gill and A. Arshak, *Sensors (Basel)*, 2007, **7**, 3027-3042.
- [60] J. Han and K. Burgess, *Chem. Rev.*, 2010, **110**, 2709-2728.
- [61] W. Shi, X. Li and H. Ma, *Methods Appl. Fluores.*, 2014, **2**, 042001.
- [62] J. E. Whitaker, R. P. Haugland and F. G. Prendergast, *Anal. Biochem.*, 1991, **194**, 330-344.
- [63] M. S. Briggs, D. D. Burns, M. E. Cooper and S. J. Gregory, *Chem. Comm.*, 2000, DOI: 10.1039/B007108K, 2323-2324.
- [64] B. Tang, F. Yu, P. Li, L. Tong, X. Duan, T. Xie and X. Wang, *J. Am. Chem. Soc.*, 2009, **131**, 3016-3023.
- [65] S. Derinkuyu, K. Ertekin, O. Oter, S. Denizalti and E. Cetinkaya, *Anal. Chim. Acta*, 2007, **588**, 42-49.
- [66] Z. Yang, W. Qin, J. W. Y. Lam, S. Chen, H. H. Y. Sung, I. D. Williams and B. Z. Tang, *Chem. Sci.*, 2013, **4**, 3725-3730.
- [67] H. Lu, B. Xu, Y. Dong, F. Chen, Y. Li, Z. Li, J. He, H. Li and W. Tian, *Langmuir*, 2010, **26**, 6838-6844.
- [68] M. Hecht, W. Kraus and K. Rurack, *Analyst*, 2013, **138**, 325-332.
- [69] S. Chen, J. Liu, Y. Liu, H. Su, Y. Hong, C. K. W. Jim, R. T. K. Kwok, N. Zhao, W. Qin, J. W. Y. Lam, K. S. Wong and B. Z. Tang, *Chem. Sci.*, 2012, **3**, 1804-1809.
- [70] S. Chen, Y. Hong, Y. Liu, J. Liu, C. W. T. Leung, M. Li, R. T. K. Kwok, E. Zhao, J. W. Y. Lam, Y. Yu and B. Z. Tang, *J. Am. Chem. Soc.*, 2013, **135**, 4926-4929.
- [71] J. Huang, L. Ying, X. Yang, Y. Yang, K. Quan, H. Wang, N. Xie, M. Ou, Q. Zhou and K. Wang, *Anal. Chem.*, 2015, **87**, 8724-8731.
- [72] B. Dong, X. Song, C. Wang, X. Kong, Y. Tang and W. Lin, *Anal. Chem.*, 2016, **88**, 4085-4091.
- [73] H. Yan, X. Meng, B. Li, S. Ge and Y. Lu, *J. Mater. Chem.C.*, 2017, **5**, 10589-10599.
- [74] E. Horak, P. Kassal, M. Hranjec and I. M. Steinberg, *Sens. Actuators B Chem.*, 2018, **258**, 415-423.
- [75] J. Wang, S. Xia, J. Bi, M. Fang, W. Mazi, Y. Zhang, N. Conner, F.-T. Luo, H. P. Lu and H. Liu, *Bioconjugate Chem.*, 2018, **29**, 1406-1418.
- [76] D. Abramavicius and S. Mukamel, *J. Chem. Phys.*, 2011, **134**, 174504.

-
- [77] M. A. Rohman, P. Baruah, S. O. Yesylevskyy and S. Mitra, *Chem. Phys.*, 2019, **517**, 67-79.
- [78] X. Hu, Y. Liu, Y. Duan, J. Han, Z. Li and T. Han, *Spectrochim. Acta, Pt. A: Mol. Biomol. Spectrosc.*, 2017, **184**, 7-12.
- [79] Y.-J. Cho, S.-Y. Kim, M. Cho, W.-S. Han, H.-J. Son, D. W. Cho and S. O. Kang, *Phys. Chem. Chem. Phys.*, 2016, **18**, 9702-9708.
- [80] H.-T. Feng, J.-B. Xiong, Y.-S. Zheng, B. Pan, C. Zhang, L. Wang and Y. Xie, *Chem. Mater.*, 2015, **27**, 7812-7819.
- [81] X. Y. Shen, Y. J. Wang, E. Zhao, W. Z. Yuan, Y. Liu, P. Lu, A. Qin, Y. Ma, J. Z. Sun and B. Z. Tang, *J. Phys. Chem. C*, 2013, **117**, 7334-7347.
- [82] C. F. A. Gomez-Duran, R. Hu, G. Feng, T. Li, F. Bu, M. Arseneault, B. Liu, E. Peña-Cabrera and B. Z. Tang, *ACS Appl. Mater. Interfaces*, 2015, **7**, 15168-15176.
- [83] L. Cai, X. Sun, W. He, R. Hu, B. Liu and J. Shen, *Talanta*, 2020, **206**, 120214.
- [84] Y. Zhan, Z. Yang, J. Tan, Z. Qiu, Y. Mao, J. He, Q. Yang, S. Ji, N. Cai and Y. Huo, *Dyes Pigm.*, 2020, **173**, 107898.
- [85] W. Liu, Y. Wang, J. Yang, X. Li, X. Wang and L. Ma, *Dyes Pigm.*, 2020, **175**, 108149.
- [86] J. D. Kopple, *American Journal of Kidney Diseases*, 2001, **37**, S66-S70.
- [87] A. S. Levey, J. Coresh, E. Balk, A. T. Kausz, A. Levin, M. W. Steffes, R. J. Hogg, R. D. Perrone, J. Lau and G. Eknoyan, *Annals of Internal Medicine*, 2003, **139**, 137-147.
- [88] A. S. Levey, J. Coresh, K. Bolton, B. Culleton, K. S. Harvey, T. A. Ikizler, C. A. Johnson, A. Kausz, P. L. Kimmel, J. Kusek, A. Levin, K. L. Minaker, R. Nelson, H. Rennke, M. Steffes, B. Witten, R. J. Hogg, S. Furth, K. V. Lemley, R. J. Portman, G. Schwartz, J. Lau, E. Balk, R. D. Perrone, T. Karim, L. Rayan, I. Al-Massry, P. Chew, B. C. Astor, D. De Vine, G. Eknoyan, N. Levin, S. Burrows-Hudson, W. Keane, A. Kliger, D. Latos, D. Mapes, E. Oberley, K. Willis, G. Bailie, G. Becker, J. Burrowes, D. Churchill, A. Collins, W. Couser, D. DeZeeuw, A. Garber, T. Golper, F. Gotch, A. Gotto, J. W. Greer, R. Grimm Jr, R. G. Hannah, J. H. Acosta, R. Hogg, L. Hunsicker, M. Klag, S. Klahr, C. Lewis, E. Lowrie, A. Matas, S. McCulloch, M. Michael, J. V. Nally, J. M. Newmann, A. Nissenson, K. Norris, W. Owen Jr, T. G. Patel, G. Payne, R. A. Rivera-Mizzone, D. Smith, R. Star, T. Steinman, F. Valderrabano, J. Walls, J. P. Wauters, N. Wenger and J. Briggs, *American Journal of Kidney Diseases*, 2002, **39**, i-ii+S1-S266.
- [89] J. Woo, M. Floyd, D. C. Cannon and B. Kahan, *Clin. Chem.*, 1978, **24**, 1464-1467.

-
- [90] T.-Y. Lin, C.-H. Hu and T.-C. Chou, *Biosens. Bioelectron.*, 2004, **20**, 75-81.
- [91] B. M. Chavers, J. Simonson and A. F. Michael, *Kidney International*, 1984, **25**, 576-578.
- [92] S. J. Frost, J. Chakraborty and G. B. Firth, *J. Immunol. Methods*, 1996, **194**, 105-111.
- [93] M. Lu, F. Ibraimi, D. Kriz and K. Kriz, *Biosens. Bioelectron.*, 2006, **21**, 2248-2254.
- [94] H. Thakkar, D. J. Newman, P. Holownia, C. L. Davey, C. C. Wang, J. Lloyd, A. R. Craig and C. P. Price, *Clin. Chem.*, 1997, **43**, 109-113.
- [95] J. Rodríguez, J. J. Berzas, G. Castañeda, N. Mora and M. J. Rodríguez, *Anal. Chim. Acta*, 2004, **521**, 53-59.
- [96] J. Xu, M. Wang, Y. Zheng and L. Tang, *Journal*, 2019, **24**.
- [97] G. Verma, M. F. Khan, W. Akhtar, M. M. Alam, M. Akhter and M. Shaquiquzzaman, *Mini Reviews in Medicinal Chemistry*, 2019, **19**, 477-509.
- [98] H. Tong, Y. Hong, Y. Dong, M. Häußler, Z. Li, J. W. Y. Lam, Y. Dong, H. H. Y. Sung, I. D. Williams and B. Z. Tang, *J. Phys. Chem. B*, 2007, **111**, 11817-11823.
- [99] H. Tong, Y. Hong, Y. Dong, M. Häußler, J. W. Y. Lam, Z. Li, Z. Guo, Z. Guo and B. Z. Tang, *Chem. Comm.*, 2006, DOI: 10.1039/B608425G, 3705-3707.
- [100] S.-J. Kim, H.-W. Rhee, H.-J. Park, H.-Y. Kim, H.-S. Kim and J.-I. Hong, *Bioorg. Med. Chem. Lett.*, 2013, **23**, 2093-2097.
- [101] L. Peng, R. Wei, K. Li, Z. Zhou, P. Song and A. Tong, *Analyst*, 2013, **138**, 2068-2072.
- [102] Z. Wang, K. Ma, B. Xu, X. Li and W. Tian, *Science China Chemistry*, 2013, **56**, 1234-1238.
- [103] W. Li, D. Chen, H. Wang, S. Luo, L. Dong, Y. Zhang, J. Shi, B. Tong and Y. Dong, *ACS Appl. Mater. Interfaces*, 2015, **7**, 26094-26100.
- [104] I. Manikandan, C.-H. Chang, C.-L. Chen, V. Sathish, W.-S. Li and M. Malathi, *Spectrochim. Acta, Pt. A: Mol. Biomol. Spectrosc.*, 2017, **182**, 58-66.
- [105] Q. Li, C. Wang and Y. Qian, *J. Photochem. Photobiol. A: Chem.*, 2017, **346**, 311-317.
- [106] S. Samanta, S. Halder and G. Das, *Anal. Chem.*, 2018, **90**, 7561-7568.
- [107] N. Barbero, C. Butnarusu, S. Visentin and C. Barolo, *Chemistry—An Asian Journal* 2019, **14**, 896-903.
- [108] N. Chakraborty, S. Bhuiya, A. Chakraborty, D. Mandal and S. Das, *J. Photochem. Photobiol. A: Chem.*, 2018, **359**, 53-63.
- [109] B. Liu, K. Wang, H. Lu, M. Huang and J. Yang, *New J. Chem.*, 2019, **43**, 11816-11820.
- [110] J. Zhang, B. D. Todd and K. P. Travis, *J. Chem. Phys.*, 2004, **121**, 10778-10786.
- [111] V. Vand, *J. Phy. Chem.*, 1948, **52**, 277-299.

-
- [112] M. A. Haidekker, T. P. Brady, D. Lichlyter and E. A. Theodorakis, *Bioorg. Chem.*, 2005, **33**, 415-425.
- [113] in *digital Encyclopedia of Applied Physics*, DOI: 10.1002/3527600434.eap684, pp. 477-531.
- [114] R. P. Erickson, Z. Jia, S. P. Gross and C. C. Yu, *PLoS Comp. Biol.*, 2011, **7**, e1002032-e1002032.
- [115] A. M. Anderson, Bruno, B.A. and Smith, L.S., in *Mechanical Engineers' Handbook*, 2015, DOI: 10.1002/9781118985960.meh123, pp. 1-28.
- [116] E. O. Puchkov, *Biochemistry (Moscow) Supplement Series A: Membrane and Cell Biology*, 2013, **7**, 270-279.
- [117] A. D. Keith, E. C. Pollard and W. Snipes, *Biophys. J.*, 1977, **17**, 205-212.
- [118] K. Luby-Phelps, in *Int. Rev. Cytol.*, eds. H. Walter, D. E. Brooks and P. A. Srere, Academic Press, 1999, vol. 192, pp. 189-221.
- [119] M. Yanai, J. P. Butler, T. Suzuki, A. Kanda, M. Kurachi, H. Tashiro and H. Sasaki, 1999, **277**, C432-C440.
- [120] V. W. Burns, *Biochem. Biophys. Res. Commun.*, 1969, **37**, 1008-1014.
- [121] K. Luby-Phelps, S. Mujumdar, R. B. Mujumdar, L. A. Ernst, W. Galbraith and A. S. Waggoner, *Biophys. J.*, 1993, **65**, 236-242.
- [122] T. Walter, D. W. Shattuck, R. Baldock, M. E. Bastin, A. E. Carpenter, S. Duce, J. Ellenberg, A. Fraser, N. Hamilton, S. Pieper, M. A. Ragan, J. E. Schneider, P. Tomancak and J.-K. Hériché, *Nat. Methods*, 2010, **7**, S26-S41.
- [123] M. K. Kuimova, S. W. Botchway, A. W. Parker, M. Balaz, H. A. Collins, H. L. Anderson, K. Suhling and P. R. Ogilby, *Nature Chemistry*, 2009, **1**, 69-73.
- [124] X. Peng, Z. Yang, J. Wang, J. Fan, Y. He, F. Song, B. Wang, S. Sun, J. Qu, J. Qi and M. Yan, *J. Am. Chem. Soc.*, 2011, **133**, 6626-6635.
- [125] R. D. Telore, M. A. Satam and N. Sekar, *Dyes Pigm.*, 2015, **122**, 359-367.
- [126] D. Su, C. L. Teoh, L. Wang, X. Liu and Y.-T. Chang, *Chem. Soc. Rev.*, 2017, **46**, 4833-4844.
- [127] X. Song, N. Li, C. Wang and Y. Xiao, *J. Mater. Chem. B.*, 2017, **5**, 360-368.
- [128] S.-C. Lee, J. Heo, H. C. Woo, J.-A. Lee, Y. H. Seo, C.-L. Lee, S. Kim and O.-P. Kwon, *Chem. Eur. J.*, 2018, **24**, 13706-13718.
- [129] L. Wang, Y. Xiao, W. Tian and L. Deng, *J. Am. Chem. Soc.*, 2013, **135**, 2903-2906.

-
- [130] Z. Zou, Q. Yan, S. Ai, P. Qi, H. Yang, Y. Zhang, Z. Qing, L. Zhang, F. Feng and R. Yang, *Anal. Chem.*, 2019, **91**, 8574-8581.
- [131] L. Hao, Z.-W. Li, D.-Y. Zhang, L. He, W. Liu, J. Yang, C.-P. Tan, L.-N. Ji and Z.-W. Mao, *Chem. Sci.*, 2019, **10**, 1285-1293.
- [132] M. Tantama, Y. P. Hung and G. Yellen, *J. Am. Chem. Soc.*, 2011, **133**, 10034-10037.
- [133] R. W. Armstrong and W. L. Elban, *Mater. Sci. Technol.*, 2006, **22**, 381-395.
- [134] A. L. Lehnert and K. J. Kearfott, *Nucl. Technol.*, 2010, **172**, 325-334.
- [135] J. I. Steinfeld and J. Wormhoudt, 1998, **49**, 203-232.
- [136] P. W. Cooper and S. R. Kurowski, *Introduction to the Technology of Explosives*, John Wiley & Sons, 1996.
- [137] J. Oxley, *Explosives detection: potential problems*, SPIE, 1995.
- [138] M. Marshall and J. C. Oxley, in *Aspects of Explosives Detection*, eds. M. Marshall and J. C. Oxley, Elsevier, Amsterdam, 2009, DOI: <https://doi.org/10.1016/B978-0-12-374533-0.00002-7>, pp. 11-26.
- [139] M. J. Lefferts and M. R. Castell, *Analytical Methods*, 2015, **7**, 9005-9017.
- [140] U. Willer and W. Schade, *Anal. Bioanal. Chem.*, 2009, **395**, 275-282.
- [141] Y.-w. Wu, A.-j. Qin and B. Z. Tang, *Chin. J. Polym. Sci.*, 2017, **35**, 141-154.
- [142] X. Sun, Y. Wang and Y. Lei, *Chem. Soc. Rev.*, 2015, **44**, 8019-8061.
- [143] M. Jurcic, W. J. Peveler, C. N. Savory, D. O. Scanlon, A. J. Kenyon and I. P. Parkin, *J. Mater. Chem. A* 2015, **3**, 6351-6359.
- [144] M. E. Walsh, *Talanta*, 2001, **54**, 427-438.
- [145] I. Gazit and J. Terkel, *Appl. Anim. Behav. Sci.*, 2003, **81**, 149-161.
- [146] M. Gaft and L. Nagli, *Opt. Mater.*, 2008, **30**, 1739-1746.
- [147] M. Krausa and K. Schorb, *J. Electroanal. Chem.*, 1999, **461**, 10-13.
- [148] Z. Ying, R. Naidu, K. Guilbert, D. Schafer and C. R. Crawford, 2007.
- [149] R. G. Ewing, D. A. Atkinson, G. A. Eiceman and G. J. Ewing, *Talanta*, 2001, **54**, 515-529.
- [150] M. S. Meaney and V. L. McGuffin, *Anal. Bioanal. Chem.*, 2008, **391**, 2557.
- [151] M. E. Germain and M. J. Knapp, *Chem. Soc. Rev.*, 2009, **38**, 2543-2555.
- [152] J. V. Goodpaster and V. L. McGuffin, *Anal. Chem.*, 2001, **73**, 2004-2011.
- [153] J. S. Caygill, F. Davis and S. P. J. Higson, *Talanta*, 2012, **88**, 14-29.
- [154] L. M. Dorozhkin, V. A. Nefedov, A. G. Sabelnikov and V. G. Sevastjanov, *Sens. Actuators B Chem.*, 2004, **99**, 568-570.

-
- [155] Z. Bielecki, T. Stacewicz, J. Janucki, A. Kawalec, J. Mikołajczyk, N. Pałka, M. Pasternak, T. Pustelny and J. Wojtas, *Metrol. Meas. Syst.*, 2012, 3-28.
- [156] S. Singh, *J. Hazard. Mater.*, 2007, **144**, 15-28.
- [157] S. J. Toal and W. C. Trogler, *J Mater. Chem.*, 2006, **16**, 2871-2883.
- [158] M. J. Kangas, R. M. Burks, J. Atwater, R. M. Lukowicz, P. Williams and A. E. Holmes, *Crit. Rev. Anal. Chem.*, 2017, **47**, 138-153.
- [159] M. K. Chahal and M. Sankar, *Anal. Methods*, 2015, **7**, 10272-10279.
- [160] P. Vishnoi, S. Sen, G. N. Patwari and R. Murugavel, *New J. Chem.*, 2015, **39**, 886-892.
- [161] X. Tian, X. Qi, X. Liu and Q. Zhang, *Sens. Actuators B Chem.*, 2016, **229**, 520-527.
- [162] V. Mahendran, K. Pasumpon, S. Thimmarayaperumal, P. Thilagar and S. Shanmugam, *J. Org. Chem.*, 2016, **81**, 3597-3602.
- [163] R. Sodkhomkhum, M. Masik, S. Watchasit, C. Suksai, J. Boonmak, S. Youngme, N. Wanichacheva and V. Ervithayasuporn, *Sens. Actuators B Chem.*, 2017, **245**, 665-673.
- [164] W. Huang, E. Smarsly, J. Han, M. Bender, K. Seehafer, I. Wacker, R. R. Schröder and U. H. F. Bunz, *ACS Appl. Mater. Interfaces*, 2017, **9**, 3068-3074.
- [165] L.-L. Wen, X.-G. Hou, G.-G. Shan, W.-L. Song, S.-R. Zhang, H.-Z. Sun and Z.-M. Su, *J. Mater. Chem.C.*, 2017, **5**, 10847-10854.
- [166] D. Giri, S. N. Islam and S. K. Patra, *Polymer*, 2018, **134**, 242-253.
- [167] T. Tao, Y. Gan, J. Yu and W. Huang, *Sens. Actuators B Chem.*, 2018, **257**, 303-311.
- [168] A. S. M. Islam, M. Sasmal, D. Maiti, A. Dutta, B. Show and M. Ali, *ACS Omega*, 2018, **3**, 10306-10316.
- [169] W. Che, G. Li, X. Liu, K. Shao, D. Zhu, Z. Su and M. R. Bryce, *Chem. Comm.*, 2018, **54**, 1730-1733.
- [170] Y. Ma, Y. Zhang, X. Liu, Q. Zhang, L. Kong, Y. Tian, G. Li, X. Zhang and J. Yang, *Dyes Pigm.*, 2019, **163**, 1-8.
- [171] W. Dong, Z. Ma, P. Chen and Q. Duan, *Mater. Lett.*, 2019, **236**, 480-482.
- [172] W. Dong, T. Fei, A. Palma-Cando and U. Scherf, *Polym. Chem.*, 2014, **5**, 4048-4053.
- [173] M. Rajeshirke and N. Sekar, *Dyes Pigm.*, 2019, **163**, 675-683.
- [174] D. Wang, Y. Jin, X. Zhu and D. Yan, *Prog. Polym. Sci.*, 2017, **64**, 114-153.
- [175] J. A. McCune, S. Mommer, C. C. Parkins and O. A. Scherman, *Adv. Mater.*, 2020, **32**, 1906890.

- [176] S. Capel-Cuevas, M. P. Cuéllar, I. de Orbe-Payá, M. C. Pegalajar and L. F. Capitán-Vallvey, *Anal. Chim. Acta*, 2010, **681**, 71-81.
- [177] B. Shi, Y. Gao, C. Liu, W. Feng, Z. Li, L. Wei and M. Yu, *Dyes Pigm.*, 2017, **136**, 522-528.
- [178] C. Huang, G. Ran, Y. Zhao, C. Wang and Q. Song, *Dalton Trans.*, 2018, **47**, 2330-2336.
- [179] A. Jahanban-Esfahlan, A. Ostadrahimi, R. Jahanban-Esfahlan, L. Roufegarinejad, M. Tabibiazar and R. Amarowicz, *Int. J. Biol. Macromol.*, 2019, **138**, 602-617.
- [180] N. Barbero, C. Butnarusu, S. Visentin and C. Barolo, *Chem. Asian J.*, 2019, **14**, 896-903.
- [181] Z. q. Chen, Z. q. Bian and C. h. Huang, *Adv. Mater.*, 2010, **22**, 1534-1539.
- [182] X. Peng, Z. Yang, J. Wang, J. Fan, Y. He, F. Song, B. Wang, S. Sun, J. Qu and J. Qi, *J. Am. Chem. Soc.*, 2011, **133**, 6626-6635.
- [183] J.-B. Chen, B. Li, Y. Xiong and J. Sun, *Sens. Actuators B Chem.*, 2018, **255**, 275-282.
- [184] M. M. Islam, Z. Hu, Q. Wang, C. Redshaw and X. Feng, *Mater. Chem. Front.*, 2019, **3**, 762-781.

Chapter-2

Materials and Methods

* *It contains the details of chemical used for the synthesis, calculation methods and instruments used for all the experiments included in thesis.*

2.1 Materials

2.1.1 Used Reagents

Sodium hydride, 4-(pyridine-2-yl) benzaldehyde, Glucose, Methylcellulose, (2,3-bis[2-Methoxy-4-nitro-5-sulfophenyl]-2H-tetrazolium-5-carboxanilide, 2,3,3-trimethyl-3H-indole, 2-phenyl pyridine, salicylaldehyde, potassium hexafluorophosphate, and 3-hydroxypicolinic acid were purchased from Sigma Aldrich Chemical Company.

2-phenyl pyridine, Trifluoroacetic acid, acetic acid, Pyrene-1-boronic acid, Iridium(III) chloride hydrate, trifluoromethane sulphonic acid, trimethylamine, Tetrakis (triphenylphosphine) palladium(0), 2-chloro pyridine, 2-Ethoxy ethanol, and 2-Bromo pyridine were procured from TCI. 2,4,6-trichloro-1,3,5-triazine purchased from Alfa Aesar.

2-Amino benzothiazole, salicylaldehyde, acetic acid, Bromo-pyridine, sodium carbonate, bromopyridine, bromobenzene, 2-chloronicotinonitrile, 2-bromopyrimidine, methyl iodide sodium carbonate, (4-(Trifluoromethyl)phenyl)boronic acid, (4-cyanophenyl)boronic acid, (4-hydroxy phenyl)boronic acid, (4-methoxyphenyl)boronic acid, (2,4-dimethoxy phenyl)boronic acid, para- tolyl)boronic acid, (4-(dimethylamino)phenyl)boronic acid, (4-aminophenyl)boronic acid, 4-(diphenylphosphaneyl)phenyl)boronic acid, and 4-(tertiary-butyl)phenyl)boronic acid were purchased from Spectrochem chemicals company Ltd.

The UV-Vis grade solvents (Dichloromethane, Hexane, Ethanol, Ethyl acetate, Toluene, 1, 4-dioxane, Chloroform, Acetone, and Acetonitrile) were procured from Merck Company. PEG(400), PEG(600), PEG(300) and PEG(200), Dichloromethane, Hexane, Ethyl acetate, Methanol, Isopropanol, Butanol, Heptanol, Hexanol, Toluene, and 1,4-dioxane were also bought from Spectrochem.

Benzoic acid, 3,5 dinitrotoluene, 1,3 dintro benzene, 2,5 dintro phenol, 2,4,6-trinitrophenol, and metal nitrate salts were procured from Merck Company. $[\text{Ir}(\text{F}_2\text{ppy})_2\text{Cl}]_2$ bridge complex was prepared according to a reported procedure [1,3]

NaOH, Triethylamine, Trifluoroacetic acid, and Acetic Buffer solutions (pH 1-pH 14) have been made by using KCl-HCl, KH_2PO_4 -HCl, KH_2PO_4 -NaOH and NaOH acetic acid. For selectivity of anions, different metal salts ($\text{Na}_2\text{S}_2\text{O}_3$, KI, KBr, KF, KCl, NaNO_3 , Na_2SO_4 , $\text{Al}_2(\text{SO}_4)_3$, K_2SO_4 , etc.) were procured from SD fine.

Dimethylthiazol-2-yl)-2, 5-Diphenyltetrazolium Bromide) from SRL, fetal bovine serum (FBS; Invitrogen; Gibco Life Technologies), Human cancer cell line, Huh7 (a kind gift from Dr. Soma Banerjee, affiliation, Huh7 (Human hepatocellular carcinoma) were procured from NCCS Pune, India. 3-(4,5-Dimethylthiazol-2-yl)-2,5-diphenyltetrazolium bromide (MTT) and 2,3-bis[2-Methoxy-4-nitro-5-sulphophenyl]-2H-tetrazolium-5-carboxanilide inner salt (XTT) was purchased from Himedia [2].

2.2 Methods

The probes were designed according to their respective targets.

2.2.1 Synthesis

Synthesis of all the probes and the intermediates were included in their respective chapters.

The probes were structurally characterized by ^1H and ^{13}C NMR spectroscopy, HRMS (High-resolution mass spectrometer) were included in the respective chapters. After structural characterization, all the photophysical property studies were carried

2.2.2 Sample preparation to investigate the 'Aggregation Induced Emission (AIE)' property

A set of solution of AIE compounds was prepared in the range of 10^{-4} to 10^{-6} M. For sample preparations, two solvents were chosen, one in which the AIE compound is soluble and in the other, the AIE compounds are insoluble, but the two solvents must be miscible with each other. Then different samples (0-95%) were prepared by the addition of different volume fraction (f_w) of two solvents in 5 ml vial. For example, concentration (conc). of 0% water: 10^{-6} M of complex in 0.5 ml THF (rest is 4.5 mL THF); conc. of 30% water: 10^{-6} M of complex in 0.5ml (rest is 3.0 ml THF and 1.5 ml of water), conc. of 60% water: 10^{-6} M of complex in 0.5ml (rest is 1.5 ml THF and 3 ml water), conc. of 90% water: 10^{-6} M of complex in 0.5ml (rest is 4.5 ml of water).

2.2.3 Fabrication of thin-film on a thin glass substrate for photoluminescence (PL) measurement

The 10^{-4} M solution of Probes derivative in THF/DCM was prepared. 2-3 drops of the solution were placed on a thin glass substrate ($2 \times 2 \text{cm}^2$), and the solvent was allowed to evaporate slowly.

CMO1 and CMO2 were dissolved in the toluene (1mg/1ml). 0.2ul of solution were deposited on circular thin cover glass by a drop-casting technique and made it to dry for an hour at room temperature followed by the vacuum for three hours in the oven at 80°C. For FESEM, the thin films were exposed to the picric acid for one day to complete the filling of the pores.

2.2.4 Fluorescence quantum yield calculations

The quantum yield was calculated in two ways

1. Relative quantum yield, and 2. Absolute quantum yield

1. Relative quantum yield

The fluorescence relative quantum yield (ϕ) of the compounds was calculated concerning quinine sulfate [4] ($\phi = 0.55$) in 0.1N H₂SO₄ excitation at 350 nm, Rhodamine 101 ($\phi = 1$) in methanol excitation at 450 nm and Rhodamine 6G ($\phi = 0.95$) in water [5] the commonly used fluorescence standard. Fluorescence spectra were recorded for solutions of absorbance less than 0.1 and more than 0.05 at the excitation wavelength. Generally, the most extended wavelength band maximum was chosen for excitation. In the case of a system with an isosbestic point in the absorption spectra, the excitation was carried out at isosbestic wavelength.

The quantum yield of the samples was calculated using Equation 2.1.

$$\phi_{Sample} = \phi_{Standard} \times \frac{F_{Sample}}{F_{Standard}} \times \frac{A_{Standard}}{A_{Sample}} \times \frac{n_{Sample}^2}{n_{Standard}^2}$$

ϕ is fluorescence quantum yield,

F is the area under the curve of corrected fluorescence spectra,

A is the absorbance at the excitation wavelength.

n = refractive index

2. Absolute Quantum yield.

For the solid-state absolute quantum yield of the samples was measured in the Quanta ϕ integrating sphere-based instrument Quanta- ϕ is a quantum yield and CIE measurement accessory for the fluorometers. It consists of large 150 mm (6 inches) sphere for higher accuracy and precision QY values, and also it has a bottom-loading drawer for solid/powder samples which eliminates the contamination.[6]

2.2.5 Luminescence quenching titration study in 90% water fraction and Solution state

Luminescence quenching titration studies in the water a (9:1, v/v) were carried out with gradual increasing picric acid (PA) concentration (2 μ M, 4 μ M, and so on) in a micro quartz cuvette keeping the total volume 1.5 mL. For each addition, at least three fluorescence spectrums were recorded at 298K to obtain concordant value.

2.2.6 Experimental procedure for detection limit calculations

Detection limit = $3\sigma/m$, where σ is the standard deviation of new measurements, m is the slope between the plot of PL intensity versus sample concentration [7-8].

To determine the Signal/Noise ratio, the emission intensity of the synthesized compounds in 90% water fraction and solution without PA was measured by ten times, and the standard deviation of blank measurements was determined.

2.2.7 Calculation of Forster distance, energy transfer rate, the efficiency of energy transfer, the distance between the donor and acceptor [9]

The rate of transfer for a donor and acceptor separated by a distance r is given by Equation 2.2

$$R_0^6 = 8.79 * 10^{-5} (\kappa^2 \eta^4 Q_D J(\lambda)) \text{ (in } \text{\AA}^6)$$

Where Q_D is the quantum yield of the donor in the absence of acceptor, η is the refractive index of the medium, r is the distance between the donor and acceptor, and τ_D is the lifetime of the donor in the absence of acceptor. The refractive index (η) is typically assumed to be 1.4 for biomolecules in aqueous solutions. The term κ^2 is a factor describing the relative orientation in the space of the transition dipoles of the donor and acceptor. κ^2 is usually assumed to be equal to 2/3, which is appropriate for dynamic random averaging of the donor and acceptor. $J(\lambda)$ is the overlap integral value between the emission spectra of donor and absorption spectra of the acceptor. Which is calculated by the Matlab (2019(a)) software.

For a donor-acceptor pair at a fixed distance, the efficiency of energy transfer is given by Equation 2.3

$$E = R_0^6 / (R_0^6 + r^6)$$

The rate of energy transfer $k_T(r)$ is given by equation 2.4

$$K_T(r) = 1/\tau_D (R_0/r)$$

The efficiency of energy transfer for a single donor-acceptor pair at a fixed distance is given by Equation 2.5

$$E = R^6 / R_o + r^6$$

2.2.8 Solvatochromisim

The solvent effect on the emission spectra of the probe is interpreted in terms of the Lippert Mataga Plot. Lippert Mataga describes the Stoke shifts in terms of the dipole moment in the excited state. The Lippert-Mataga equation describes the energy relates to the refractive index (η), and dielectric constant (ϵ) of the solvent is given by Equation 2.6

$$(\nu_{ab} - \nu_{fl}) = \left(\frac{2(\mu_e - \mu_g)^2}{hc a^3} \right) \Delta f + constant$$

$$\text{Where } \Delta f = \frac{(\epsilon - 1)}{(2\epsilon + 1)} - \frac{(n^2 - 1)}{(2n^2 + 1)}$$

ϵ is the dielectric constant of a particular solvent, n is the refractive index of a particular solvent, h is Planck's constant, c is the velocity of light, 'a' is the Onsager cavity radius and μ_G and μ_E is the ground state and excited state dipole moment of the fluorophore, respectively Δf is the solvent polarity parameters. $\Delta\nu = \nu_{abs} - \nu_{em}$ is the solvatochromic shift (in cm^{-1}) between the maxima of absorption and fluorescence emission [$\nu_{abs} = 1/\lambda_{abs(max)}$, $\nu_{em} = 1/\lambda_{em(max)}$].

2.3 Instrumentation

2.3.1 UV-Visible spectrophotometer

Absorption spectroscopy is the most widely used spectroscopic tool that provides useful information about the sample understudied. It refers to a spectroscopic device that measures the absorption of radiation, as a function of frequency or wavelength, due to its interaction with a sample. The environmental effects alter the relative energy of ground and excited states, and this alteration causes spectral shifts. The absorbance (A) of an absorber (concentration C) having a molar extinction coefficient ϵ_λ at wavelength λ is given by Equation 2.7.

$$A = \log\left(\frac{I_0}{I}\right) = \epsilon_\lambda c l$$

Where A is absorbance (optical density), I_0 , and I represent the intensity of the incident and transmitted light, respectively, c is the concentration of the light-absorbing species, and l is the path length of the light-absorbing medium in a decimeter. A matched pair of 10 cm quartz cuvettes (Hellma, 1 cm light path, capacity 3.5 ml, Model: 100-QS) was used for absorption

measurements. UV-Vis absorbance spectra were recorded using a Shimadzu Spectrophotometer (model UV-1800 and 2550). The block diagram of the instrumentation is shown in Figure 2.1

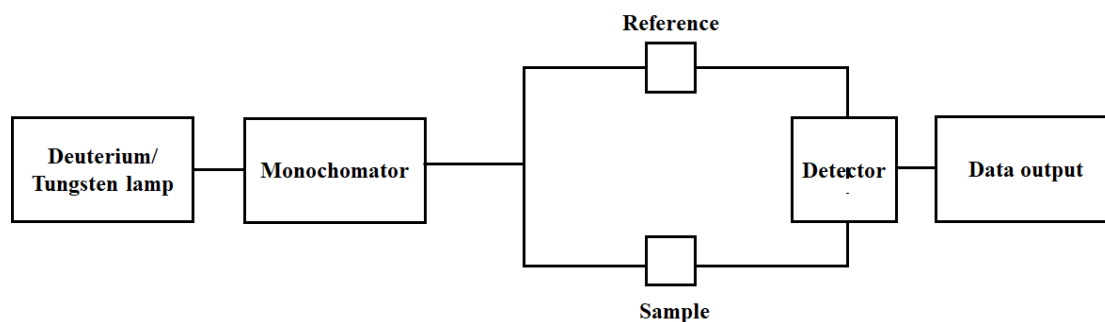


Figure 2.1 Schematic representation of UV-Visible Spectrometer

2.3.2 Steady-state spectrofluorometer

In the thesis, fluorescence measurements were performed using a Horiba Jobin Yvon Fluoromax-4 and Fluorolog scanning spectrofluorometer. The spectrofluorometer irradiates a sample with suitable excitation light and measures the fluorescence emitted from the irradiated sample to perform a qualitative or quantitative analysis. The block diagram of the instrument is shown in Figure 2.2. The brief description of its components is given below:

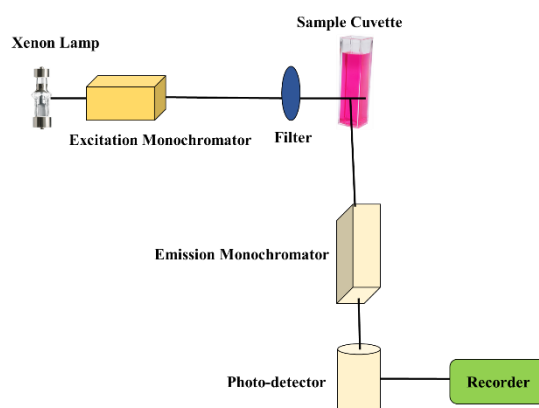


Figure. 2.2 Block diagram of a steady-state spectrofluorometer.

This instrument is equipped with a light source of 1905-OFR 150-W Xenon lamp. The lamp housing is provided with ozone self-decomposition. This instrument contains Czerny Turner monochromators for excitation and emission. The vital part of monochromator is a reflection grating. A grating disperses the incident light utilizing its vertical grooves. The gratings in this instrument contain 1200 grooves mm^{-1} , and are blazed at 330nm (excitation) and 500nm (emission). Blazing is etching the grooves at a particular angle to optimize the grating's reflectivity in a specific spectral region. This instrument uses

a direct drive for each grating, to scan the spectrum at up to 200 nm s⁻¹, with accuracy better than 0.5 nm, and repeatability of 0.3 nm. The scan range of this instrument is 240-850 nm. The cell holder holds a cell filled with the sample.

The emission monochromator selectively receives fluorescence emitted from the sample and the photomultiplier tube (PMT) measures the intensity of the fluorescence. The monochromator has a diffraction grating whose size is the same as that of the excitation monochromator to collect the most significant possible amount of light.

The detector in this system consists of a photomultiplier tube for both photometry and monitor sides. Generally, the Xenon lamps used on spectrofluorimeter are characterized by very high emission intensity and a continuous radiation spectrum. However, their tendency to unsteady light emission will result in more significant signal noise if no countermeasure is incorporated. Besides, the discrepancy in the radiation spectrum of the Xenon lamp and in the spectral sensitivity characteristics of the photomultiplier tube (these criteria are generally called instrument functions) causes misshape in the spectrum. To overcome the above-mentioned factors, the photomultiplier tube monitors a portion of excitation light and feeds the resultant signal back to the photomultiplier tube for fluorescence scanning. This scheme is called the light-source compensation system. The slits widths are adjustable from the computer in units of bandpass or millimetres. This preserves maximum resolution and instant reproducibility. The steady-state fluorescence anisotropy measurements were performed with the same steady-state spectrofluorimeter fitted with a polarizer attachment (105UV polarizers), manufactured by POLACOAT Co., USA. The measurement was obtained by placing one polarizer on each of the excitation and emission sides. The sample was taken in a Quartz cuvette (Hellma, 1 cm light path, capacity 3.5 ml, Model: 101-QS) with four walls transparent to measure the excitation and emission spectra.

Time correlated single photon counting (TCSPC) spectra of the iridium complex and Organic molecules in different solvents were obtained through exciting the sample with a Spectrofluorometer FLS920s Edinburgh (AIRF, JNU, New Delhi) and Spectrofluorometer at BITS Pilani, Pilani campus

2.3.3 Computational study

The Density Functional Theory (DFT) calculations were performed using the Gaussian 09 program suite [10,11]. Beckes three-parameter hybrid exchange functional with

the Lee-Yang-Parr gradient-corrected correlation (B3LYP functional)[12,13], for larger correlation (CAM-B3LYP) and the basis set 6-31G(+), 6-31G(++)(d,p), LANL2Z, level [10] were used in both the DFT and TD-DFT methods. All calculations were performed using the Integral Equation Formalism-Polarizable Continuum Model (IEF-PCM) for the solvents[14].

2.3.4 Docking Studies

The complex used in docking was Heteroleptic Iridium (III) complex. The coordinates were generated with the help of the Gaussian 09 program suite¹ and were first optimized in the DFT (Density Functional Theory) using B3LYP functional, and the basis set LANL2Dz and 6-31g (d,p) used in both the DFT and TD-DFT methods.

The result of DFT calculation was then read as input for Auto Dock 4.2, a semi-empirical free energy force field-based docking software to carry out the docking simulation.[15] The receptor used in this study is Bovine Serum Albumin (PDB ID: 3V03), which is a 583 amino acids long protein. All the heteroatoms were removed from 2V03 to make the receptor-free of any ligand before docking. The program “AutoDock Tools” was used to prepare, run, and analyze the docking simulations. Solvation parameters, polar hydrogen’s, and Kollman united atom charges were added to the receptor for the preparation of protein in docking simulation. Gasteiger charge was assigned, and then non-polar hydrogens were merged in the ligand. One for each atom type, present in the ligand being docked as it stores the potential energy arising from the interaction with the macromolecule. This grid must surround the region of interest (active site) in the macromolecule. In the present study, the binding (active) site on the protein was not known, so the total protein was considered for the binding site prediction. Therefore, the grid was centered on the protein. The grid box size was set at 126, 84, and 102 Å for *x*, *y*, and *z*, respectively, and the grid, center was set to 64, 25 and 32 for *x*, *y* and *z* respectively, which covered the whole protein. Docking software AutoDock 4.2 Program supplied with AutoGrid 4.0 and AutoDock 4.0 was used to produce grid maps. The spacing between grid points was 1.0 angstroms.

2.3.5 Other instruments

The oxidation and reduction potential were measured in cyclic voltammetry (CV) recorded on a potentiostat/galvanostate model 263 A. The platinum, glassy carbon, and Ag/AgCl electrodes were used as a counter, working and reference electrodes, respectively and the scan rate was maintained to 100 mVs⁻¹.

The complexes were dissolved in acetonitrile and THF (10 mL) and 0.1 M lithium perchlorate (LiClO_4) was added to the solution (used as the supporting electrolyte). The whole experiment was conducted under a nitrogen atmosphere.

The dynamic light scattering (DLS) measurements of the aggregates of complexes were carried out in Zeta Sizer, model Nano ZS (ZEN 3600, Malvern Instruments, UK). Samples were filtered before the measurements with a 0.22- μM filter (Durapore, PVDF). The wavelength of the laser light was 6328 Å, and the scattering angle was 173°. At least five sets of measurements were carried out for each sample at ambient conditions. The scattering intensity signal of the sample is passed to a digital signal processing board called a correlator, which compares the scattering intensity at successive time intervals to derive the rate at which the energy is varying. This information is then passed to a computer, and the data were analyzed with the Zetasizer software to obtain size information.

The size and shape of the nanoparticles were measured by scanning electron microscopy (SEM) using a JEOL JSM-6700F FESEM instrument at MNIT Jaipur and field emission scanning microscopy Modal-“APREO S” (FESEM) at BITS PILANI.

The FT-IR spectra were recorded in ABB Boman MB 3000 instrument, FTIR Shimadzu (IR prestige-21), and Perkin Elmer Spectrum 100. The complexes were mixed with dry potassium bromide (KBr) powder and pellets were prepared. The pellets have been used to record FT-IR.

^1H NMR, ^{13}C NMR, and ^{31}P NMR, ^{19}F spectra were recorded in a 400 MHz Bruker spectrometer using CDCl_3 and DMSO as solvent and tetramethylsilane (TMS, $\delta = 0$ ppm for ^1H and ^{13}C NMR), and phosphoric acid (H_3PO_4 , $\delta = 0$ ppm for ^{31}P NMR) as internal standard with a 400 MHz Bruker spectrometer instrument at BITS Pilani, Pilani campus.

High-resolution MS (HRMS) was carried out with a (TOF MS ES^+ 1.38 eV) VG Analytical (70-S) spectrometer and Q-ToF micro mass spectrometer instrument at IISER Mohali and BITS Pilani, Pilani campus.

Time correlated single photon counting (TCSPC) spectra of the iridium complex in THF was obtained through exciting the sample with a picosecond diode laser (IBH Nanoled) using a Spectrofluorometer FLS920-s Edinburgh (AIRF, JNU, New Delhi) and time-resolved fluorescence measurements, Horiba Jobin Yvon Fluorocube-01-NL picosecond time-correlated single-photon counting (TCSPC) experimental setup was used at BITS Pilani. All the fluorescence lifetime decays were collected at the magic angle of 54.7° with a vertical

excitation beam using a TBX photon detection module (TBX-07C). IBH DAS-6 decay analysis software has been used for the analysis of decays. The lamp profile of the TCSPC instrument was measured with the help of a scatterer, Ludox, procured from Aldrich Co., WI

The solid-state quantum yield of the thin film sample was measured using a calibrated integrating sphere in a Gemini Spectrophotometer (model Gemini 180) at BITS Pilani, Pilani Campus.

Luminescence images of cells and photostability of the molecules were performed by drop-casting the sample solution on a glass slide and images were captured using an Olympus IX 81 microscope provided with a digital camera.

Microwave reactions were carried out in a CEM Discover (mode 1908010). All the reactions were performed under a nitrogen atmosphere, and the progress of the reaction was monitored using thin-layer chromatography (TLC) plates (pre-coated with 0.20 mm silica gel).

BET analysis were performed in Multi BET analysis using Quanta Chrome Nova-2200 Instrument (Material and Research Centre, Bangalore).

X-ray Single Crystal structure analysis: Single-crystal X-ray diffraction data for the compounds were recorded on Bruker AXS KAPPA APEX-II CCD and Rigaku Mercury375/M CD (XtaLAB mini) diffractometer respectively by using graphite Monochromated Mo – K radiation at 100.0(1) K by using Oxford crytosystem. The data sets collected Bruker AXS KAPPA APEX-II [16] Kappa were collected using Bruker APEX-II suit, data reduction, and integration were performed by SAINT V7.685A12 (Bruker AXS, 2009) and absorption corrections and scaling were done using SADABS V2008/112 (Bruker AXS).[17] The data sets, which were collected on XtaLAB mini diffractometer, were processed with Rigaku Crystal Clear suite 2.0. The crystal structures were solved by using SHELXS2013 [18]. And were refined using SHELXL2013 available within Olex2. All the hydrogen atoms have been geometrically fixed and improved using the riding model except the hydride anion, coordinating with Ir, which has been located from the difference Fourier map and were refined isotropically. All the diagrams have been generated using Mercury 3.1.1. Geometric calculations have been done using PARSTR and PLATONR. Powder X-ray diffraction (PXRD) was measured by using Rigaku mini flex II desktop X-ray diffractometer. Prof. Nigam's instrument model etc.

2.3.6 Cell culture:

Huh7 (Human hepatocellular carcinoma) and MCF7 (Human breast cancer cells) were procured from NCCS, Pune, India. Briefly, cells were cultured in Dulbecco's modified eagles' medium (DMEM; Invitrogen) supplemented with 10% Fetal bovine serum (FBS; Gibco Life Technologies), 100U/mL-1 penicillin and 100µg/mL⁻¹ streptomycin (Invitrogen) and were maintained at 37° C and 5% CO₂. Cells were grown to 80% confluency before any treatment.

2.3.7 In vitro cytotoxicity assay.

In vitro cytotoxicity assays were performed following procedures de-scribed earlier by Kovooru et al.[19] Briefly, cells were seeded at a density of 8×10^3 in 96 well plates and incubated overnight. The cells were then treated with different doses of either TPSI1 or Methylcellulose (MC) for 24hr. XTT (2,3-bis[2-Methoxy-4-nitro-5-sulfophenyl]-2H-tetrazolium-5-carboxanilide inner salt) was added to the treated cells in each well, and cells were incubated for 3hr. Absorbance was measured at wavelength 480nm with a differential filter of 630nm using a Multiskan Microplate Spectrophotometer (Thermo Scientific). The percentage of viable cells was calculated using the formula: Viability (%) = (mean absorbance value of treated cells)/mean absorbance value of control) *100.

2.3.8 Microscopic imaging and cellular uptake studies

For microscopy, cells were seeded on coverslips in a 6-well plate, and after overnight culture, they were treated with the compound for 2hr. To analyze viscosity-dependent alterations in fluorescence, Huh-7 cells were pre-treated with PEG or Glucose or MC for 10hr before the addition of the compound. In studies performed using primary culture Human Umbilical Vein Endothelial Cells (HUVECs), cells were grown on gelatin-coated cover glasses for overnight, followed by treating the cells with 30mM of glucose for 24hr. Treated HUVECs were then incubated with compound for 4hr. After that, media was removed, cells were rinsed in 0.1M phosphate buffer saline (PBS) and then fixed using methanol at -20°C for 10min. The coverslips with fixed cells were mounted with anti-fade mountant (Thermo Scientific) on a glass slide and visualized under a fluorescence microscope (Zeiss Axio Scope A1). For flow cytometry, cells grown in 6-well plates were exposed to PEG or Glucose or MC for 10hr followed by incubation with the compound for 2hr. The cells were then harvested, collected and suspended in PBS followed by acquisition using flow cytometer (CytoFlex, Beckmann

Coulter). A shift in fluorescence in the green filter was monitored; the data were analyzed using CytExpert software. For fluorimetric analysis, cells were seeded at a density of 1×10^5 in 6 well plates, and after 10hr of treatment, the cells were lysed using Triton-X buffer and centrifuged at 15000 rpm for 15min. The absorbance of the supernatant was recorded using a microplate reader (Fluoroskan Ascent).at 485 nm (excitation) and 530 nm (emission) wavelength (2)

2.3.9 Co-localization Study

For nucleus co-localization studies HeLa cells were seeded into a 4-well chamber slide in 500 μ L supplemented DMEM medium and allowed to adhere overnight. Then cells were incubated with an aqueous solution of the compound (final concentration, 170 μ M) for 4 hrs. Next, cells were washed with PBS buffer solution and fixed with 4% paraformaldehyde for 20 min. Then cells were permeabilized by adding 500 μ L 0.3% Triton X-100 in PBS solution for 20 min. Then, the cell nucleus was stained with an aqueous solution of propidium iodide. Next, fixed cells were mounted with 50% glycerol and imaged under the fluorescence microscope.

2.3.10 Statistical analysis

The obtained data were analyzed using the Prism® software (Version 5.01; GraphPad Software Inc., USA). The effect of various treatments was statistically analyzed using the one-way ANOVA test, and the level of $p < 0.05$ was considered as statistically significant. All data points represent the mean of independent measurements. Uncertainties were expressed as standard deviations in the form of bars.

2.3.11 Dynamic Measurements:

The cultured cells were placed on the actuation unit (piezoelectric patch). Piezo disc is driven by a function generator, a chirp signal up to 1MHz frequency range, and 3V (peak to peak), which was applied to the Piezo disc using an arbitrary function generator (Tektronix, AFG1022). Prepared cell culture was placed over the cross slide, and dynamic input was applied on the slide for the excitation of the cells. A microscope was used for the determination of the location of the cells in the dish. A Position-Sensitive Device (PSD) (Hamamatsu, S1880) was used as an optical position sensor (OPS) with signal processing circuit (Hamamatsu, C4674-01) to measure the exact position of an incident light spot in two-dimensions on a sensor surface. Laser (RLM650TA-020R, Laser century) was focused on the

cells and got refracted to the PSD. A schematic (Fig. 2.3) demonstrating the process is provided (Fig. 2.3). Displacement in the cells was traced by PSD, and the oscilloscope gave the digital output voltage, proportional to the movement. A digital oscilloscope (Tektronix, TBS 1102B) was used to measure the voltage output from PSD in the time domain. We took FFT of the time data to obtain the frequency response of the cells, and a rectangular window was used for the better resolution of the sample rate in the oscilloscope. Response measurements were taken on the cell and the base. We took the transfer function of the cell concerning base to take away all base related modes. The same procedure was repeated for different cell types. The frequency-domain response was processed in MATLAB; to evaluate the quality factor, a measure of damping present in the sample using 3 dB frequencies were used. Let, ξ be the damping ratio, then the time constant of the cell is given by $\tau=1/(\xi\omega_n)$, where ω_n is the natural frequency. The viscosity of the cell was determined using lamb relation given by Equation 2.8 [20]

$$\mu = \frac{\rho^2}{\tau(n-1)(2n+1)}$$

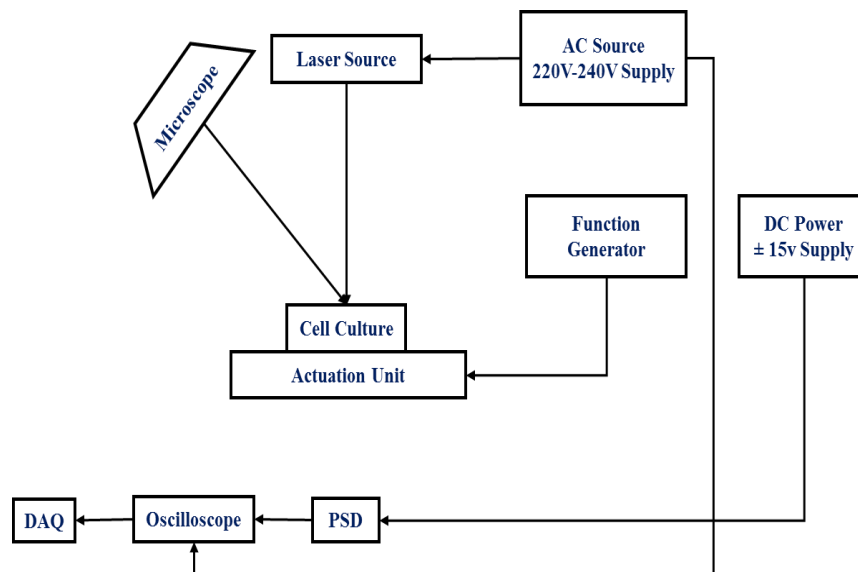


Figure 2.3 Experimental setup for measuring the dynamic response of cells.

2.4. References

[1] C. Xu, Z. -Q. Wang, X.-M. Dong, X.-Q. Hao, X.-M. Zhao, B.-M. Ji, M.-P. Song, *Inorg. Chim. Acta*, 2011, **373**, 306.
 [2] R. Choudhury, Assistant Professor, Department of Biology, BITS Pilani, Pilani campus, Pilani, India.

-
- [3] A.F. Rausch, M.E. Thompson, H. Yersin, *Inorg. Chem.*, 2009, **48**, 1928.
- [4] G.G. Guilbault, Practical fluorescence, Marcel Dekker Inc., New York, 1973.
- [5] D. Magde, G.E. Rojas, and P. Seybold, Solvent Dependence of the Fluorescence Lifetimes of Xanthene Dyes. *Photochem. Photobiol.* 1999, **70**, 737, 1999.
- [6] N. Hasebe, K. Suzuki, H. Horiuchi, H. Suzuki, T. Yoshihara, T. Okutsu and S. Tobita, *Anal. Chem.*, 2015, **87**, 2360-2366.
- [7] M.-H. Yang, P. Thirupathi, K. -H. Lee, *Org. Lett.*, 2011, **13**, 5028.
- [8] L.N. Neupane, J.M. Kim, C.R. Lohani, K.-H. Lee, *J. Mater. Chem.*, 2012, **22**, 4003.
- [9] S. Kaur, V. Bhalla, V. Vij, M. Kumar, *J. Mater. Chem. C*, 2014, **2**, 3936.
- [10] M. J. Frisch, G. W. Trucks, H. B. Schlegel, G. E. Scuseria, M. A. Robb, G. Cheeseman, V. Barone, B. Mennucci and G. A. Petersson, et al., Gaussian 09, 2010, Revision C. 01, Gaussian, Inc., Wallingford, CT, 2010.
- [11] A. D. Becke, *J. Chem. Phys.*, 1993, **98**, 5648.
- [12] S. Marković and J. Tosović, *J. Phys. Chem. A*, 2015, **119**, 9352.
- [13] G. M. Morris, R. Huey, W. Lindstrom, M. F. Sanner, R. K. Belew, D. S. Goodsell and A. J. Olson, *J. Comput. Chem.*, 2009, **30**, 2785-2791.
- [14] Li, H., & Jensen, J. H. *Journal of computational chemistry*, (2004), 25(12), 1449-1462
- [15] K. A. Majorek, P. J. Porebski, A. Dayal, M. D. Zimmerman, K. Jablonska, A. J. Stewart, M. Chruszcz and W. Minor, *Mol Immunol*, 2012, **52**, 174-182. (Dr Shibashish Chowdhury, Biological Department , BITS Pilani, Pilani campus)
- [16] APEX2, SADABS, and SAINT; Bruker AXS Inc. Madison, Wisconsin, USA, 2008
- [17] M.Nardelli. *J. Appl. Crystallogr.* 28, 1995, 569.
- [18] 7Sheldrick, G. M. "SHELXS-2013/1, program for the solution of crystal structures." *Germany: University of Göttingen* (2013).
- [19] Lohitesh, K.; Saini, H.; Srivastava, A.; Mukherjee, S.; Roy, A.; Chowdhury, R. *Oncology reports*, 2018, 39 (6), 2787-2796.
- [20] Collaborative work by Dr Venkatesh K P – Department of Mechanical Engineering, BITS Pilani, Pilani Campus, Rajasthan, India

Chapter-3

Hydrogen bond Sensitive Multi-stimuli Probes

* *This Chapter explore the vital role of hydrogen bonding in multi stimuli sensing*

Hydrogen-Bond Sensitive Multi-Stimuli Probes

3.1 Aggregation-induced emission active and hydrogen bond sensitive Schiff base with a distinct response to various stimuli.

3.1.1 Introduction

Smart or stimuli-responsive materials involve a class of materials that change one or more properties by changing the external stimuli, such as temperature, pressure, pH, solvent, hydrophobic or hydrophilic environment, and electric or magnetic fields.[1-4] The luminescent property of the materials mainly depends upon the molecular arrangement, flexibility of conformational changes, and interaction between the molecules.[5] An easy way to trigger the luminescent property is to disturb the molecular arrangement and flexibility of the molecules, this could be done in many ways, and one of the easiest ways is to introduce the intra or intermolecular hydrogen bonding sites.[6, 7] The presence of intra or intermolecular hydrogen bonding in a molecule may disturb the physical or chemical property of the molecules by the influence of the external stimuli.[8-10] For many years, the definition of the hydrogen bonding is given as follows: “**hydrogen bond** is an electrostatic attraction between polar molecules in which hydrogen is bound to a larger atom, such as oxygen or nitrogen.” [11] Hydrogen bonding is not a wholly ionic or covalent bond. However, it is an attraction between the positive and negative charged atoms.[11, 12] In 2011, core specialized group of ‘H-bonding and other intermolecular interactions’ under IUPAC described the hydrogen bonding as “An attractive interaction between a hydrogen atom from a molecule or a molecule X–H in which the H is attached with a more electronegative group or a group of atoms in the same or a different molecule (inter or intra molecule), in which there is evidence of bond formation.” The typical representation of the hydrogen bonding is X–H---Y–Z, where the dots denote the bond. X–H represents the hydrogen bond donor and the acceptor may be an atom or an anion [13, 14]. Stimuli-responsive fluorescence (FL) materials with their emission behaviour of reversible manner by the external stimuli are of great importance.[14, 15] Among them AIE, multi-stimuli sensitive materials are of particular interest because of their structural tunability, functional controllability, and easy emission tunability.[16, 17] However, owing to the lack of clear guidelines on the design strategy, reports on the multi-stimuli AIE fluorescent probes are rare.[18-21] Supramolecular interaction such as π - π interaction, dipole-dipole interaction, and hydrogen bonding plays an essential role in the structural rearrangement by applying the external stimuli.[22, 23] This chapter described the stimulation caused by the hydrogen bonding within the molecule. This stimulation of probes is applied for the detection of the

various stimuli like pH, base, solvents, Al^{3+} ions, and biomolecules. The strength of the hydrogen bonding depends on the electro-negativity of the donor atom through which the H-atom is connected and depends on the accepting ability of an atom to which is forming a hydrogen bond. Therefore in the present day, the interest is much growing in generating new hydrogen bonding sites in molecular probes/systems.[24] To this end, the Schiff base-based structure is very easy to synthesis and very sensitive to the hydrogen bonding.[25-27] In the literature, it is reported that the intramolecular hydrogen-bonded Schiff base exhibits a phenomenon called as excited-state intramolecular proton transfer (ESIPT).[28, 29]

More than 5000 research article related to the ESIPT fluorophore has been published since the 1950s.[30] Wu et al. developed a probe (1&2) (Fig. 3.1.1) based on the inhibition of the ESIPT process by strong, accepting capabilities. In this article, ratiometric detection is possible due to the difference between donating and accepting ability between the probe and analytes (F^- , CH_3COO^- , and H_2PO_4^-), which inhibits the ESIPT.[31]

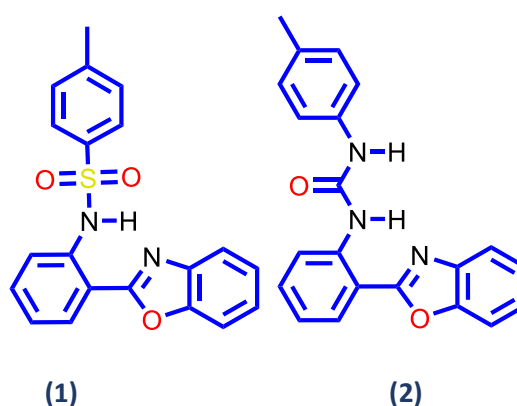


Figure 3.1.1 It shows the structure of a probe molecule which detects F^- , CH_3COO^- , and H_2PO_4^- ratiometrically through the ESIPT process.

In 2016, Yan et al. synthesized an AIE active ESIPT probe with a large stoke-shift as a fluorescent sensor for pH and Zn^{2+} .[32] (Fig. 3.1.2)

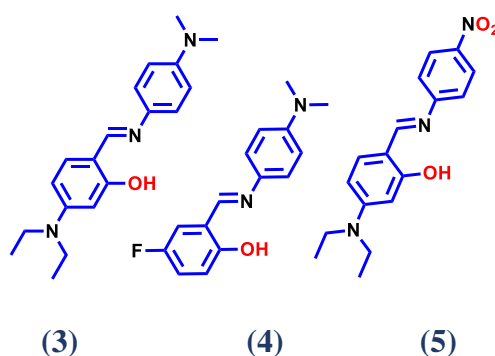


Figure 3.1.2 It shows the structure of the ESIPT active probe molecule for pH and Zn²⁺ detection

The probes diethylamine derivatives (3-5) are stable in the acidic medium due to the negative inductive effect of the substituent group on the salicylaldehyde moieties and phenylamine moieties. The Schiff base compounds are sensitive in the acidic medium, so the compound can be stabilized by reducing the electron density of C=N of the probe.[33] Therefore fluorine in 4 and nitro in 5 have a strong electron-withdrawing character, which stabilizes these compounds in acidic medium and reduce the electron density around C=N. 2-(2-hydroxyphenyl)benzothiazole (HBT) is a classical ESIPT molecule with an intramolecular H-bond between its (-OH) proton donor and proton acceptor (-N=) groups.[33] In 2018, Kai li et al., synthesized benzothiazole based AIEgens with tunable ESIPT probes for physiological pH sensing. (Fig 3.1.3) The article describes the mechanism and change in the emission of the probe in the pH. In the basic medium, the cyan fluorescence emission of the 7 is around 484 nm. In the acidic medium, the cyan fluorescence emission quenches to give yellow emission at 554 nm. This character suggests that the intramolecular H-bond containing AIEgens may be an ideal strategy for the development of fluorescent chemosensors for pH sensing.[34]

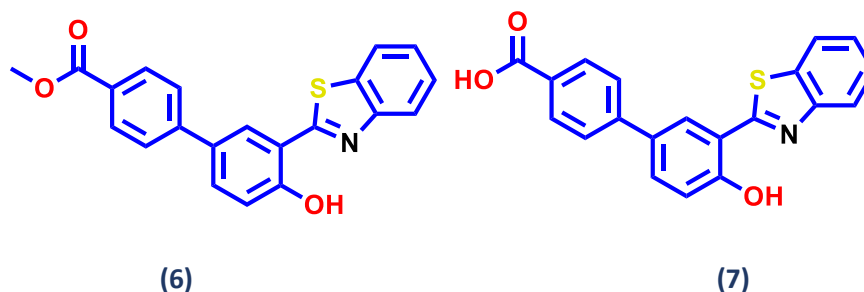


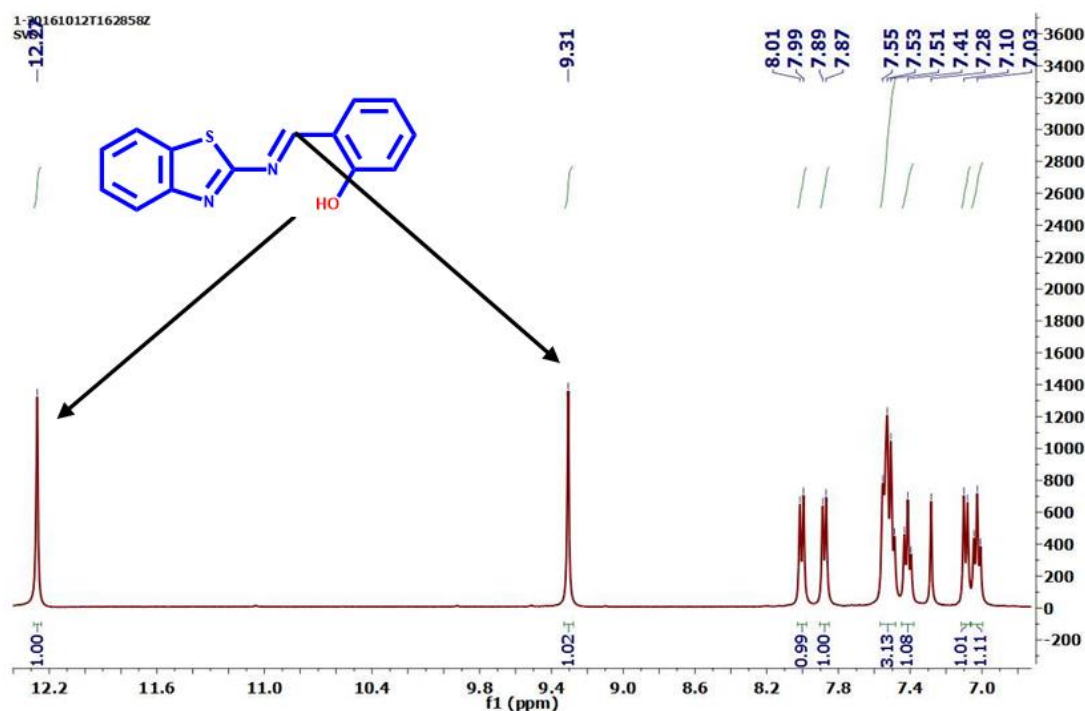
Figure 3.1.3 It shows the structure of the ESIPT active benzothiazole based probes for pH sensing

To date, very few probes are designed based on the strategy that combines the AIE molecules with ESIPT active properties for multi stimuli sensing. Most of the reported, pH probes response at particular pH give specific response either for acidic, basic, and or neutral medium. The whole range of pH sensing is rare.[35] It is the alkaline nature that keeps our body healthy, while diseases are mostly observed to arise in acidic conditions. Therefore it is necessary to sense the whole range of pH accurately. Most of the fluorescent-based probes used for pH imaging are restricted to measuring a particular pH rather than imaging the entire

organelle in the cells. The main reasons for this are the cell permeability[36, 37] and the inability of the probe to sense the entire pH range of the cell.[38, 39] These reports encourage scientists to design a probe for pH. The sensitivity could be increased by incorporating hydrogen bonding with AIE + ESIPT properties in the molecules.[40]

3.1.2 Results and Discussion

3.1.2.1 Synthesis and characterization. The Schiff base ((E)-2-((benzo[d]thiazole-2-ylimino)methyl)phenol (BTIP) was readily synthesized with the help of the known procedure [41] by a condensation reaction of 2-amino benzothiazole and salicylaldehyde in methanol with good yields (90%). ^1H NMR and ^{13}C NMR of BTIP are well matched with the reported data [41] ^1H NMR (400 MHz, CDCl_3) 12.27 (1 H, s), 9.31 (1 H, s), 8.00 (1 H, d, J 8.0), 7.88 (1 H, d, J 7.9), 7.52 (3 H, dd, J 17.2, 8.9), 7.41 (1 H, t, J 7.5), 7.28 (1 H, s), 7.09 (1 H, d, J 8.3), 7.03 (1 H, t, J 7.4) and ^{13}C 1H (400 MHz, CDCl_3) 12.27 (1 H, s), 9.31 (1 H, s), 8.00 (1 H, d, J 8.0), 7.88 (1 H, d, J 7.9), 7.52 (3 H, dd, J 17.2, 8.9), 7.41 (1 H, t, J 7.5), 7.28 (1 H, s), 7.09 (1 H, d, J 8.3), 7.03 (1 H, t, J 7.4).(Fig. 3.1.4)



(a)

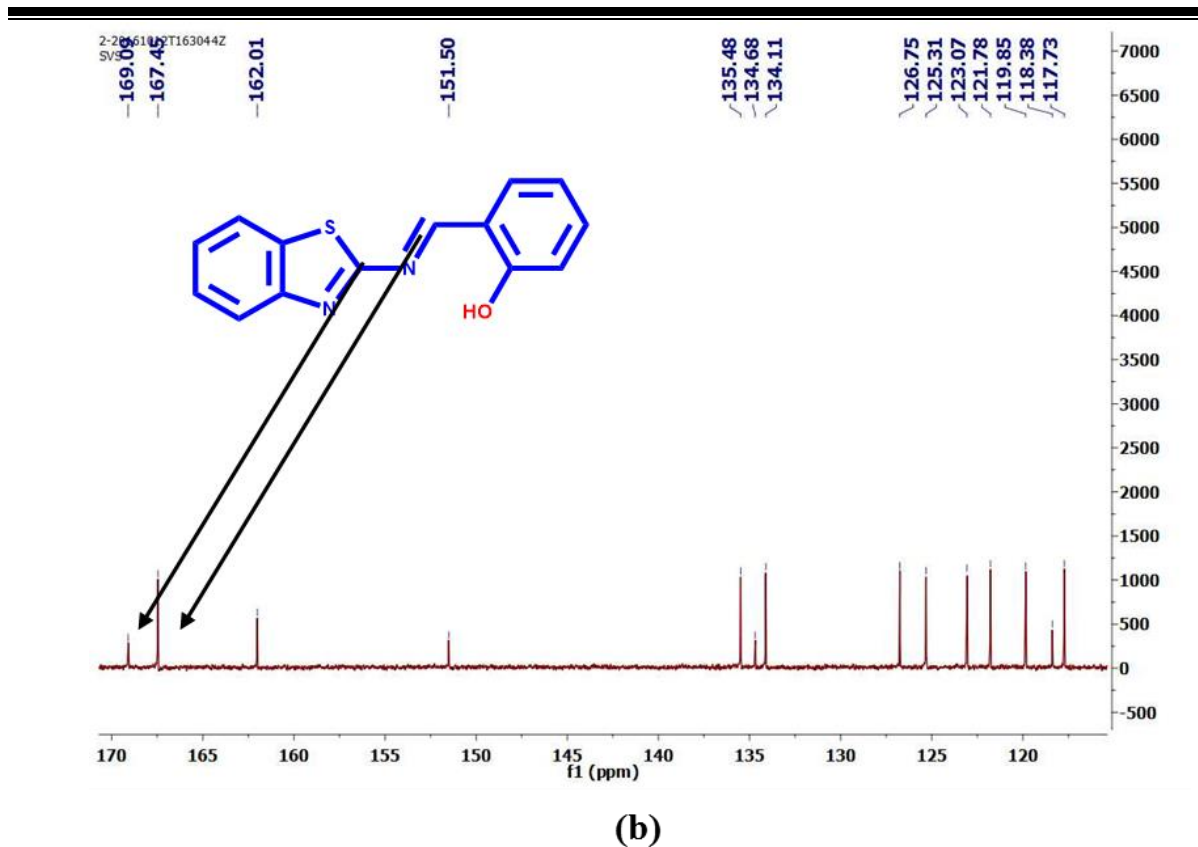
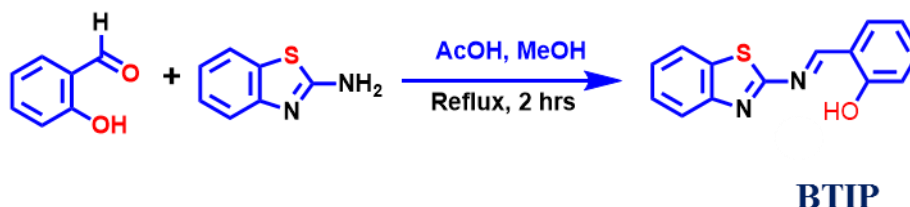


Figure 3.1.4 (a) ^1H NMR and (a) ^{13}C NMR spectrum of BTIP



Scheme 3.1.1 Synthesis of BTIP

3.1.3 Absorption spectra

The absorption spectra of BTIP in DCM and methanol show peaks in the ranges of 255–290 nm and 300–350 nm (Fig. 3.1.5 a). For defining each transition, the theoretical calculation with Natural Bond Order (NBO) analysis was carried out. NBO analysis (inbuilt- in Gaussian 9.0) was carried out by considering all the possible interactions between the filled donor (Lewis) NBOs and empty acceptor (non-Lewis) NBOs and estimating their energy importance using second-order perturbation theory.[42] For each pair of the donor (i) and acceptor (j) NBOs, the stabilization energy $E^{(2)}$ associated with electron delocalization between the donor and acceptor was estimated as:[43]

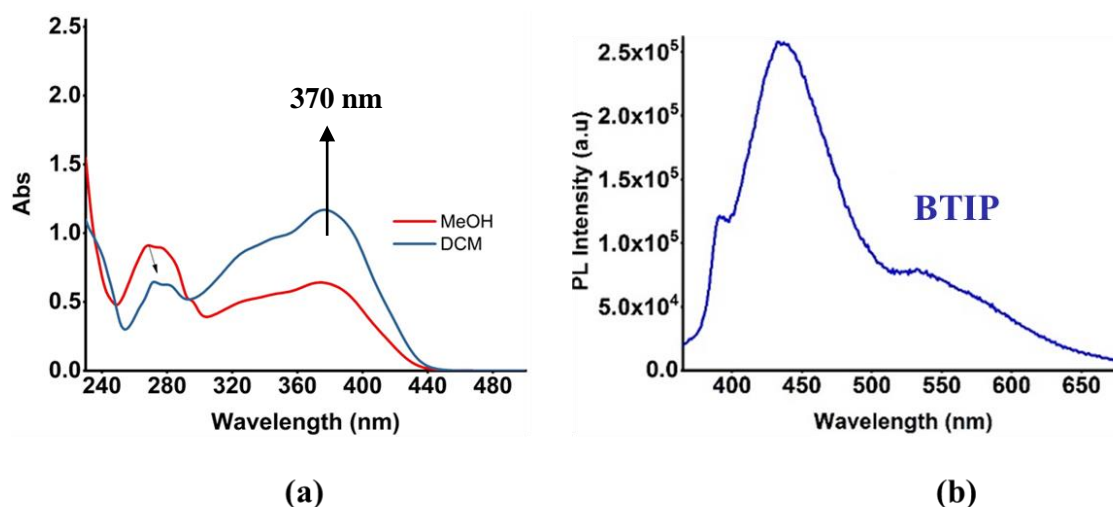


Figure 3.1.5 a) Absorbance spectra of the BTIP (10^{-4} M) $\lambda_{\text{max}} = 275$ & 370 nm a) Emission spectrum of BTIP in methanol (10^{-4} M)

$E^{(2)} = \Delta E_{ij} = q_i(F_{ij})^2/(E_j - E_i)$ where q_i is the donor orbital occupancy, E_j and E_i are diagonal NBO Fock matrix elements, and F_{ij} is the off diagonal NBO Fock matrix element. The larger the $E^{(2)}$ value, the more intensive the interaction between the electron donor and acceptor NBOs. The results of the second-order perturbation theory analysis of the Fock matrix at the B3LYP/6-31+G(d,p) level are given in Table 3.1.1.

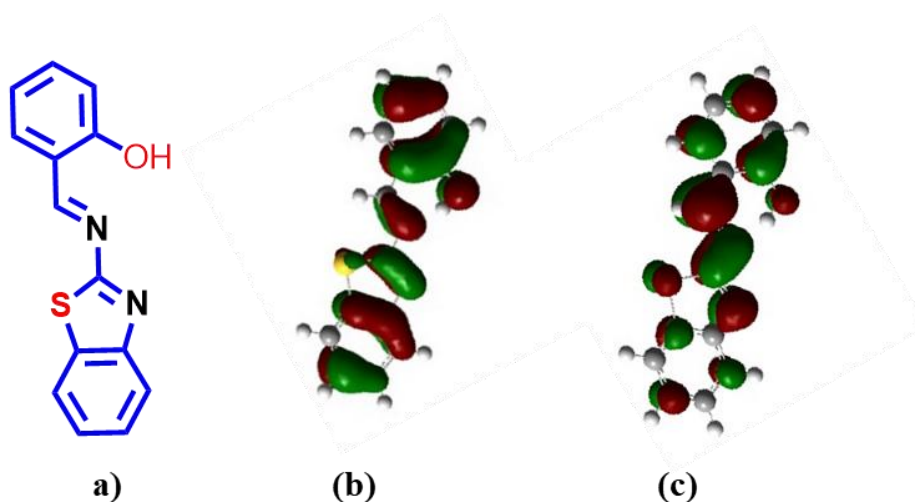
The strong intramolecular interactions of Lewis-type donor NBOs (π , σ , n (lone pair)) with non-Lewis type acceptor NBOs (π^* , σ^* , n^* (lone pair)) are detailed in Table 3.1.1. It is evident from the data in Table 3.1.1 that significant interactions between the donor and the acceptor NBOs are $n_{N11} \rightarrow n^*_{H24}$, $n_2 O_{23} \rightarrow \pi^*_{C1-C2}$ and $\pi_{C3-C4} \rightarrow \pi^*_{N11-C12}$ with $E^{(2)}$ values of $42.12 \text{ kcal mol}^{-1}$, $35.09 \text{ kcal mol}^{-1}$ and $28.71 \text{ kcal mol}^{-1}$, respectively. However, when the occupancies of those acceptor NBOs, namely n^*_{H24} , $\pi^*_{N11-C12}$, and π^*_{C1-C2} , are considered, it was found that $\pi^*_{N11-C12}$ has the lowest occupancy (0.24337). Therefore, it is rational to conclude that the strongest intramolecular charge transfer in BTIP happens due to shifting of π electrons from the phenolic ring to the $-C_{12}=N_{11}$ NBO. The NBO analysis can also explain the intramolecular hydrogen bonding. In March 2009, Liu et al. reported the crystal structure of this organic molecule at room temperature.[44] It is clear from the crystal structure that the BTIP has an intramolecular hydrogen bond between the N of imine and H-O of Salicylaldehyde, with an $N \cdots H-O$ distance of 1.733 \AA . The NBO analysis also shows that there is an electron transfer of $n_1 N_{11} \rightarrow n^*_{H24}$ with an $E^{(2)}$ value close to 42.12 kcal

mol^{-1} , which signifies that the intramolecular hydrogen bonding provides sufficient stabilization to the molecule.

Table (3.1.1) Second-order perturbation energies E^2 {donor (i) \rightarrow acceptor (j)}

Donor NBO (i)	$q^{(i)}(e)$	Acceptor NBO (j)	$q^{(j)}(e)$	$E^{(2)}$ Kcal/mol	$E(j) - E(i)$ (a.u.)	$F(i,j)$ (a.u.)
π C ₁ -C ₂	1.59543	π^* C ₅ -C ₆	0.37022	25.67	0.28	0.076
π C ₃ -C ₄	1.61420	π^* C ₁ -C ₂	0.36746	22.73	0.27	0.071
		π^* N ₁₁ -C ₁₂	0.24337	28.71	0.24	0.078
π C ₅ -C ₆	1.60869	π^* C ₃ -C ₄	0.44187	26.91	0.26	0.076
π N ₁₁ -C ₁₂	1.86988	π^* C ₁₄ -N ₁₈	0.35408	21.54	0.33	0.080
π C ₁₆ -C ₂₀	1.59618	π^* C ₂₁ -C ₂₂	0.37257	20.64	0.28	0.068
π C ₂₁ -C ₂₂	1.63218	π^* C ₁₆ -C ₂₀	0.41489	20.89	0.27	0.068
		π^* C ₁₇ -C ₁₉	0.42175	21.90	0.26	0.068
n 1 N ₁₁	1.83883	σ^* C ₁₄ -S ₁₅	0.11773	15.80	0.51	0.081
		n*H ₂₄	0.45576	42.13	0.53	0.145
n 2 S ₁₅	1.70643	π^* C ₁₄ -N ₁₈	0.35408	24.32	0.25	0.070
		π^* C ₁₇ -C ₁₉	0.42175	20.46	0.27	0.068
n 2 O ₂₃	1.81508	π^* C ₁ -C ₂	0.36746	35.09	0.33	0.101

The absorbance peaks in the ranges of 255–290 nm and 300–350 nm which were attributed, respectively, to the π - π^* transition within the aromatic rings and π - π^* transitions within C=N groups.[45] The peak at 370 nm is due to intramolecular charge transfer (ICT transition) involving the whole molecule. These intramolecular charge transfers peaks ($\lambda_{\text{max}} = 370$ nm) and π - π^* transitions are assigned to the electronic transition between (i) HOMO \rightarrow LUMO and (ii) HOMO-2 \rightarrow LUMO, respectively (Table 3.1.2).



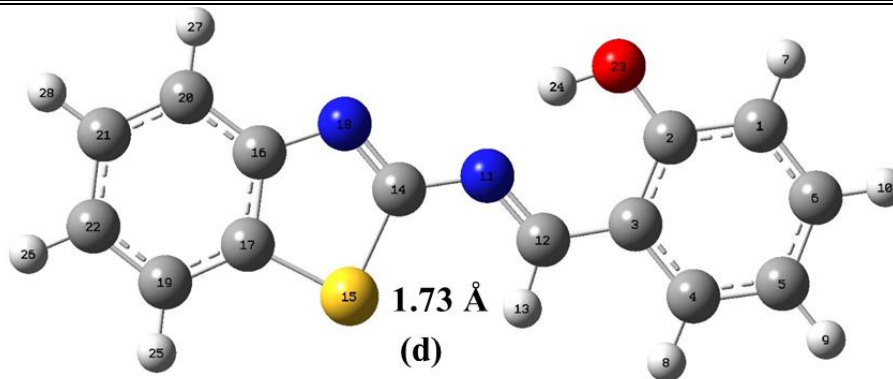


Figure 3.1.6 a) Structure of BTIP, b) HOMO c) LUMO (with isovalue 0.4) (d) Labelled optimized structure of BTIP form

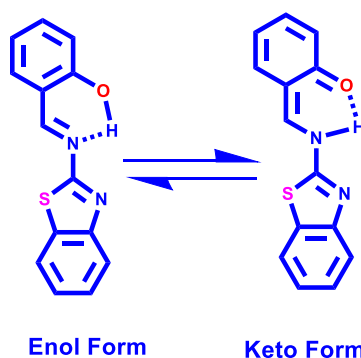
The HOMO is well distributed over the whole BTIP structure (Fig.3.1.6 b), more on heteroatoms and ring conjugations. The LUMO primarily lies on the imine C=N part (Fig. 3.1.6 c).

Table 3.1.2 Calculated major orbital excitation contributions (%), energy difference (in eV), obtained from electronic transitions analysis with TDDFT (B3LYP) method, basis set 6-31+G(d,p) for organic molecule

States	Major orbital contribution (%)	excitation	ΔE , eV	Wavelength, nm	Oscillator strength
S1	HOMO – LUMO (95)		3.1479	393	0.7535
S2	HOMO-1 – LUMO (86)		3.4825	356	0.0038
S3	HOMO-2 – LUMO (83)		3.6056	343	0.3717
S4	HOMO-4 – LUMO (93)		4.1272	300	0.0000

3.1.4 Emission Properties

a) Observation of ESIPT (Excited-state intramolecular proton transfer))



Scheme 3.1.2 Schematic representation of Enol and Keto form of BTIP

The spectral properties of the BTIP in methanol shows two emission bands with λ_{\max} at 450 nm and 540 nm (excited at 350 nm) (in a polar protic solvent, the formation of the intermolecular hydrogen bond is favoured than intramolecular hydrogen bonding) (Fig. 3.1.5 b). In non-polar solvents (cyclohexane, dioxane and DCM), the BTIP shows two emission bands same as polar solvent at wavelength 450 and 540 nm excited at 350 nm. However, in aprotic polar solvents (DMSO, DMF), the longer wavelength emission band shows a bathochromic shifted emission from the original value of 540 nm to 580 nm, which is more intense than the peak intensity at 450 nm (Fig. 3.1.7). Most of the reported ESIPT probe molecules have two emission band which are assigned as keto at longer wavelength and enol at shorter wavelength.[30, 46] So, here it may be assumed as the λ_{\max} at 450 nm from the enolic and the keto form with λ_{\max} at 540 nm [30] To confirm the ESIPT process, the emission spectra of the BTIP at different excitation wavelengths in the λ_{\max} range of 310–440 nm was recorded. It was found that at lower excitation wavelengths, both forms exist. Still, at the lower excitation wavelength, the enolic form is the predominant one, while with decreasing excitation energy, the amount of the keto form increases (Fig. 3.1.8 a).

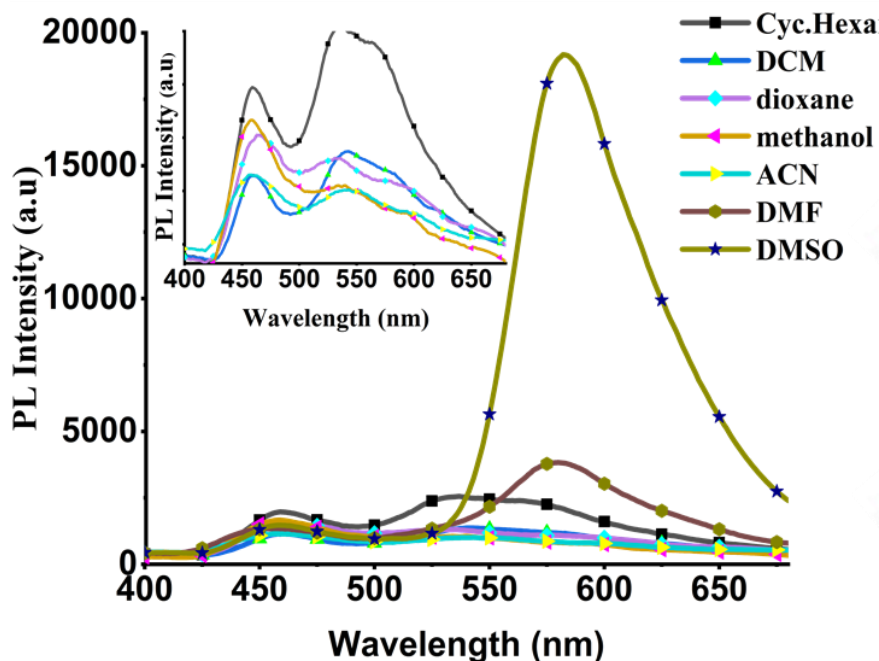


Figure 3.1.7 (a) Emission spectra of the compound in different solvent (10^{-4} M),. (Cyc Hexa – Cyclohexane, DCM = methylene dichloride, THF- tetrahydrofuran, ACN- acetonitrile, DMF = dimethyl formamide, DMSO = dimethylsulfoxide)

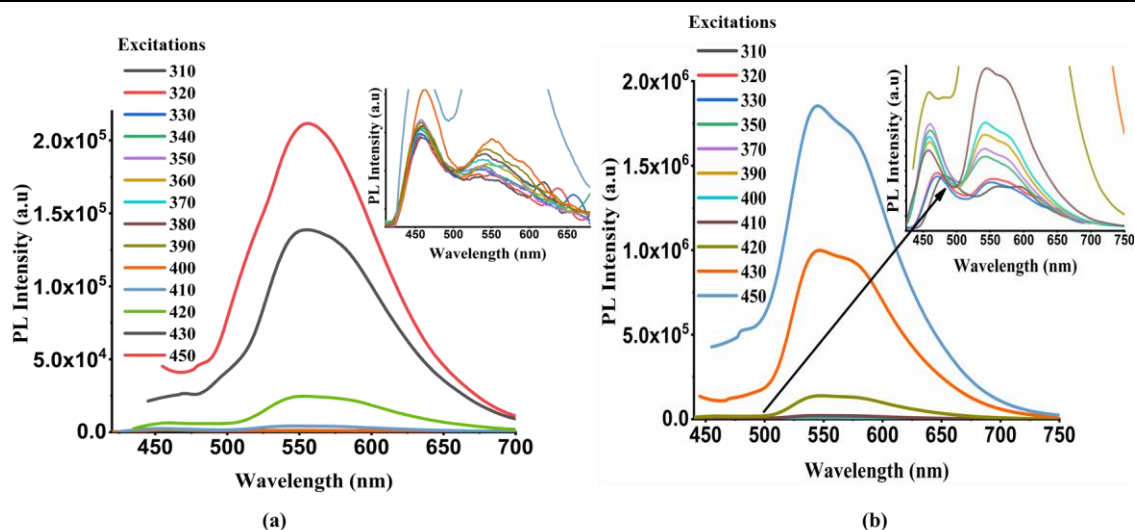
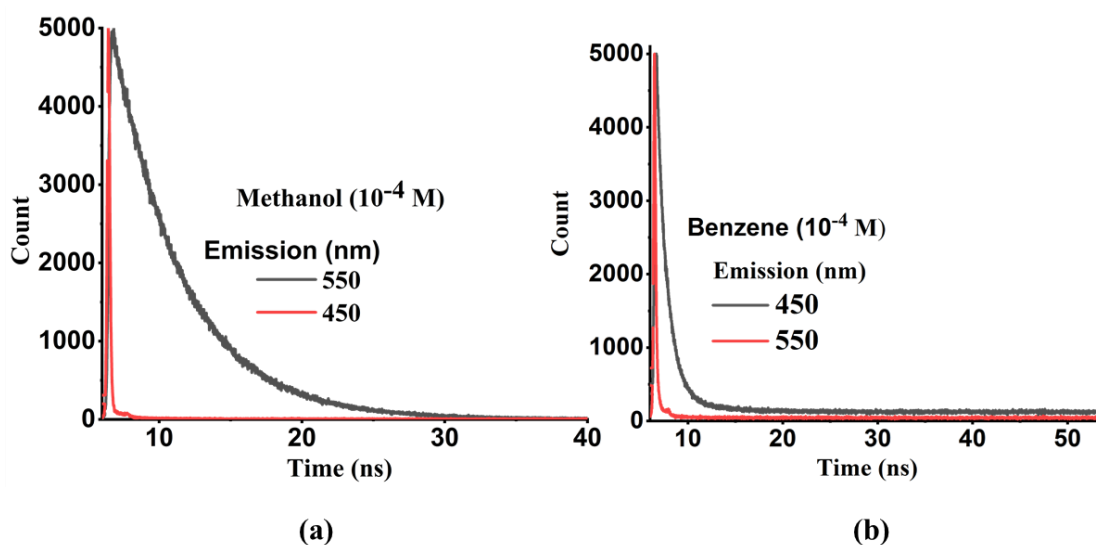


Figure 3.1.8 (a) Emission spectra of the BTIP with gradual variation of excitation (a) BTIP in methanol (10^{-4} M) (b) BTIP in benzene (10^{-4} M).

Also, in benzene, both forms exist at lower excitation wavelengths, but by progressively increasing the excitation wavelength, the amount of the keto form gradually increases (Fig. 3.1.8 b). The life-time decay experiment gave the support, i.e., the observation of bi-exponential decay (monitoring at λ_{\max} 450 and 550 nm) ensures the existence of both forms in benzene and decay was more when monitored with $\lambda_{\max} = 550$ nm (Table 3.1.3) (Fig. 3.1.9 c). By comparing the life-time decay of BTIP in solvents, the excited state lifetime decay of the keto form was higher in methanol (polar solvent) and lower in the benzene (non-polar solvent) (Table 3.1.3) [Fig. 3.1.9 (a, b, c)]. The case was reversed for the case of enol form (Table 3.1.3) (polar solvent favours the keto form, and non-polar solvents favour the enol form[47]).



(c) Life-time decay calculations

For Methanol at 450 (calculated using three exponential)

$$T_1 = 9.526196 \text{ E}^{-10} \text{ sec} \quad B1 = 2.654491\text{E}^{-02}$$

$$T_2 = 4.294975 \text{ E}^{-11} \text{ sec} \quad B2 = 0.2778857$$

$$T_3 = 4.935449 \text{ E}^{-09} \text{ sec} \quad B3 = 6.874496\text{E}^{-03}$$

In methanol at 550 nm (calculated using 4 exponential)

$$T_1 = 3.746238\text{E}^{-10} \text{ sec} \quad B1 = 1.158852$$

$$T_2 = 3.706972\text{E}^{-10} \text{ sec} \quad B2 = 1.173263$$

$$T_3 = 3.610108\text{E}^{-09} \text{ sec} \quad B3 = 4.54028\text{E}^{-04}$$

$$T_4 = 8.839286\text{E}^{-11} \text{ sec} \quad B4 = 0.3490632$$

For Benzene at 450nm (Calculated using 2 exponential)

$$T_1 = 1.014294\text{E}^{-09} \text{ sec} \quad B1 = 6.174804\text{E}^{-02}$$

$$T_2 = 3.046374\text{E}^{-09} \text{ sec} \quad B2 = 0.0050996$$

In benzene at 550nm (Calculated using 2 exponentials)

$$T_1 = 1.066542\text{E}^{-10} \text{ sec} \quad B1 = 0.2011084$$

$$T_2 = 8.949348\text{E}^{-10} \text{ sec} \quad B2 = 5.463318\text{E}^{-03}$$

Figure 3.1.9 Lifetime decay of BTIP in the following solvents: methanol, cyclohexane, benzene at (a) monitored at 450 nm; (b) monitored at 550 nm (c) Life-time decay calculations using Data Station (Das6) software.

Table 3.1.3 It shows the lifetime decay of BTIP in different solvents

Solvent	Average Lifetime		
	λ_{emi}	450 nm	550nm
Methanol		0.20 ns	0.34ns
Benzene		1.16ns	0.12ns

The following changes were obtained on the angles of enol form in between the optimized structure and crystal structure: $\angle C_2C_3C_{12} = 121.33^\circ$ and $\angle C_{12}N_{11}C_{14} = 122.85^\circ$ (obtained from optimization), $\angle C_2C_3C_{12} = 120.67^\circ$ and $\angle C_{12}N_{11}C_{14} = 121.22^\circ$ (obtained from the crystal structure). As observed, there is a little twist in the angle of the enol form (optimized structure), which makes the ring flexible to be in motion (vibrations) in the enol form and

therefore this might be the reason for the less intense emission intensity than keto form (Fig. 3.1.11). (If the salicylaldehyde part is incapable of forming hydrogen bonding, then it is flexible enough to have movement and which opens up the path for non-radiative decay for less fluorescence.)

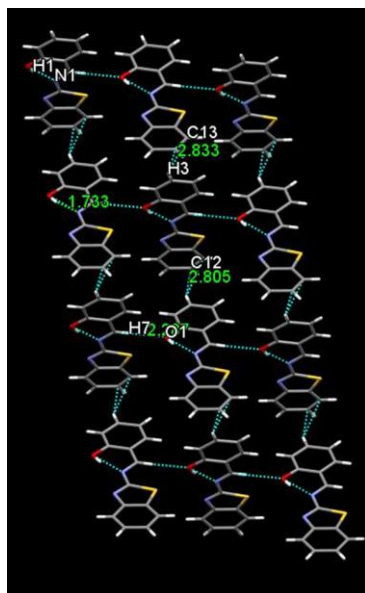


Figure. 3.1.10 Packing diagram shows two short contacts C–H···O and CH··· π in the range of 2.28-2.83 Å and hydrogen bonding between N··· H–O (1.733 Å).

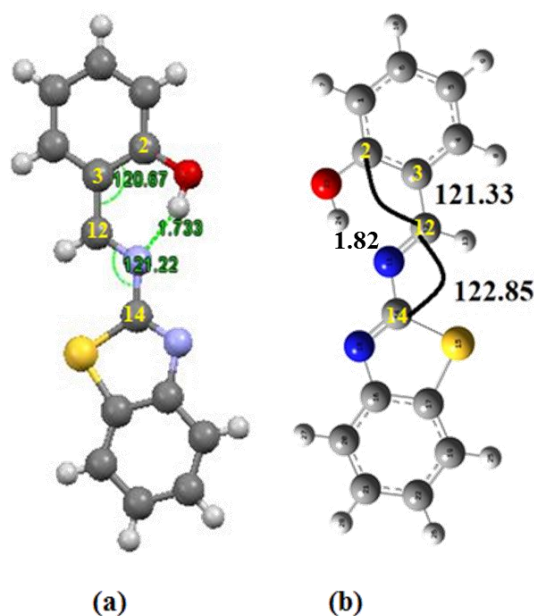


Figure 3.1.11 Comparison of the angle between the crystal structure and calculation from DFT based modelling a) ORTEP Structure of compound showing different angle; b) optimized structure from DFT;

b) Aggregation-induced emission (AIE)

The BTIP has very weak emission in common organic solvents (methanol, acetonitrile, DCM etc.) and it emits yellow light ($\lambda_{\max} = 540$ nm) in its solid form. We have investigated AIE by recording the emission spectra of the BTIP in different fractions (0-90%) of methanol/water fraction. The emission intensity increases with an increase in the percentage of water in methanol. (Fig. 3.1.12). The absolute quantum yield was calculated for a thin-film sample of BTIP and was found to be higher (8.66%) than the quantum yield in solution (0.33%). These results confirm that the BTIP is a typical AIE active material.

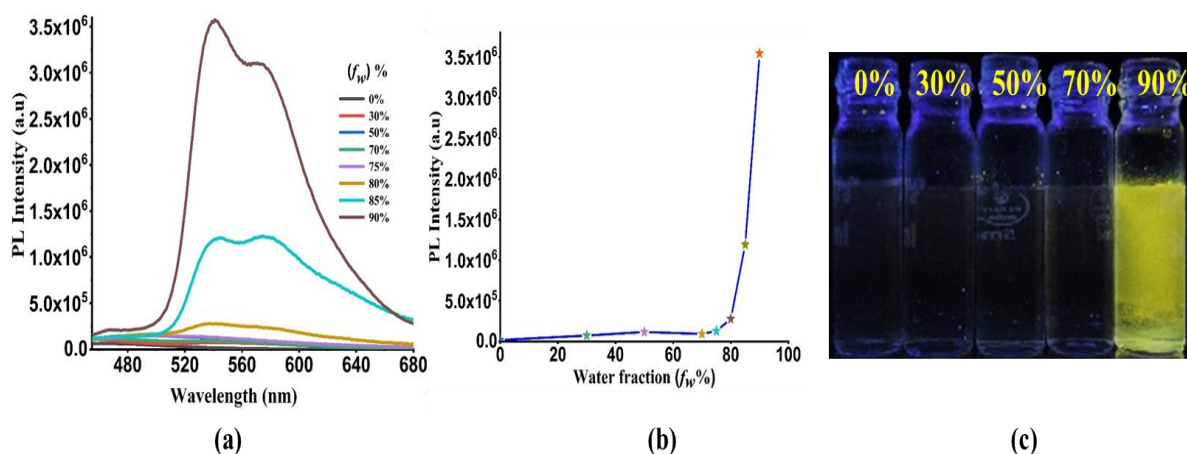


Figure.3.1.12 (a) PL spectra of BTIP in different fraction (0-90%) methanol-water fraction (b) plot of PL intensity vs water fraction; (c) fluorescence image of BTIP in different water fractions (λ^{ex} 365 nm).

From a crystal structure, an intramolecular hydrogen bonding ($\text{N}_{11} \cdots \text{H}_{24} - \text{O}$; 1.733 Å) and two inter-molecular short contacts of $\text{C} - \text{H}_{13} \cdots \text{O}_{23}$ and $\text{CH}_{10} \cdots \pi$ with distances 2.287 and 2.833 Å, respectively were observed. The molecules in the solid-state are aggregated in a J-type packing arrangement (head-tail) in a zig-zag manner[48], (Fig 3.1.10). To prove the AIE mechanism, the emission of BTIP was recorded with gradual increasing concentration of polyethylene glycol (PEG) into the solution of BTIP, leading to the gradual enhancement of the PL intensity that supports the restriction of the rotation (salicylaldehyde part rotation is restricted) (Fig. 3.1.13). Therefore, the presence of inter or intramolecular hydrogen bonding between the molecules (Fig 3.1.13) restricts the motion, leading to the AIE. (Because of the hydrogen bonding only the rotation is restricted, it is also shown in figure 3.1.10. the sentence is interlinked with the above)

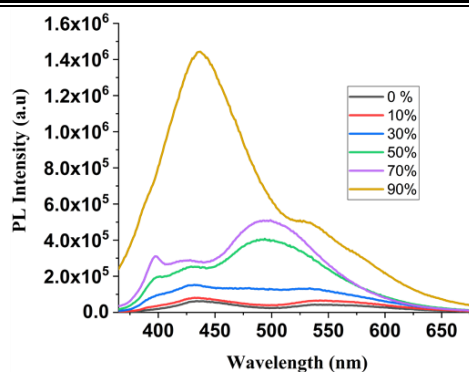
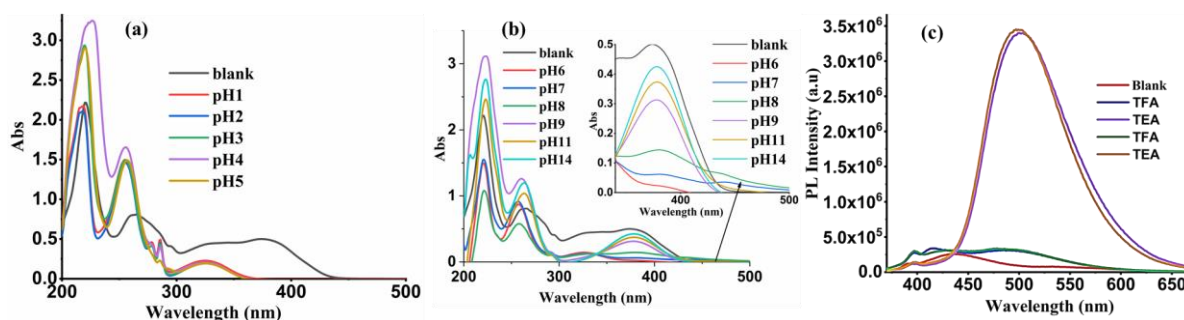


Figure 3.1.13 Emission spectra of BTIP (10^{-4} M methanol) with increasing concentration of PEG (600)

c) pH Probe

From the literature, most of the Schiff-base compounds are sensitive to acid, i.e., $[H^+]$ ion concentration. The present synthesized compound responds to the pH of the medium. In acidic pH (1 to 5), a blue-shifted absorption of the BTIP is observed when compared to the absorption taken in methanol without acid (Figure 3.1.5 a) It appears that in the acidic condition both the imine groups and the ring nitrogen atoms are protonated. This fact is supported by an observation of two new 1H NMR peaks at ~ 9.86 ppm and ~ 10.24 ppm in acidic medium, assigned to imine and ring nitrogen atoms, respectively (Fig. 3.1.14 c). By gradually adding the acid to the BTIP and simultaneously recording the 1H NMR spectra, one could observe that the integral area of the peak around ~ 9.86 ppm is more compared to the peak 10.26 (Fig 3.1.14 c) which was attributed to imine nitrogen and then in the higher acid concentration the integral area of both the peaks show near to one that means both the protons are protonated. Generally, the imine nitrogen is readily available for protonation and deprotonation.[49, 50] To check the stability of the BTIP, we recorded the emission of BTIP in the presence of acid and base several times. The emission intensity is reversible in the presence of a base. (Fig 3.1.14 c). Therefore, it may be concluded that the BTIP is a stable compound in acid and base.



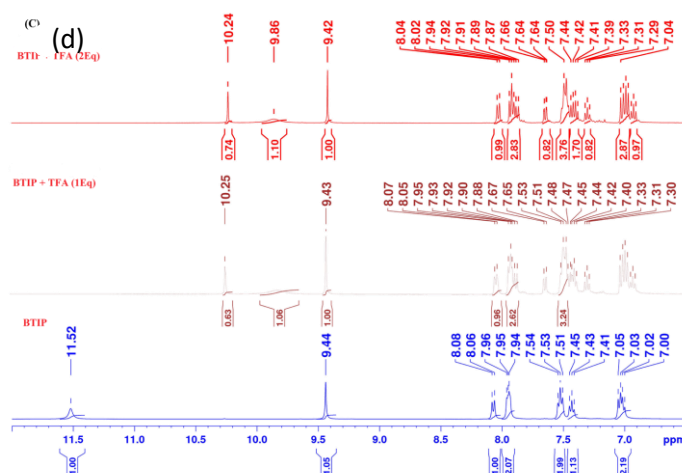
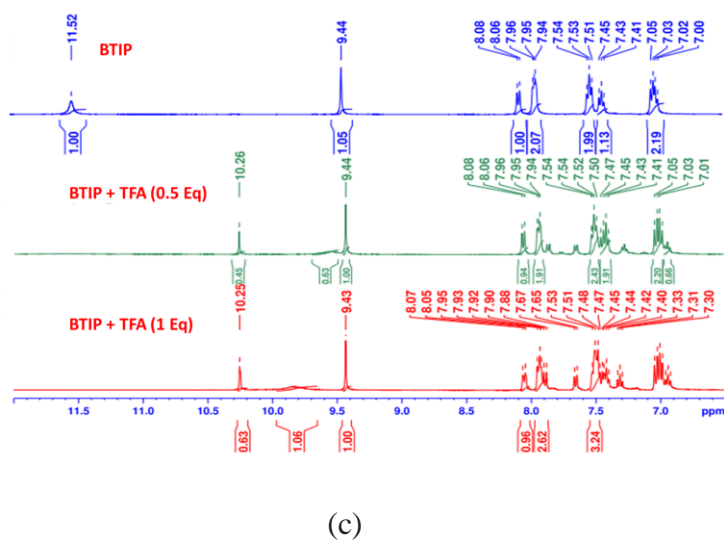


Figure 3.1.14 Absorption spectra of compound ($\text{MeOH } 1 \times 10^{-4} \text{ M}$) in different pH buffer solutions (a) pH1-5, (b) pH 6-14 (c) Emission plot of BTIP ($1 \times 10^{-4} \text{ M}$, MeOH) in the presence of acid (trifluoroacetic acid, TFA) and base (triethylamine, TEA) (c, d) ^1H NMR of BTIP in the presence of TFA trifluoroacetic acid

Hence, the protonated form of the BTIP interrupts the intramolecular hydrogen bonding, and a UV-Vis absorption spectral shift is also observed from 270 to 255 nm (Fig.3.1.14 a). In the emission spectra, the original peak at $\lambda_{\text{max}} = 540 \text{ nm}$ disappears in acidic pH (1–5), while a peak at $\lambda_{\text{max}} = 450 \text{ nm}$ remains intact with an observation of a new peak at $\lambda_{\text{max}} = 484 \text{ nm}$ starts to appear at higher pH (at what pH 6) (Fig. 3.1.15 a). The image of BTIP in different pH range from 1-13 was taken under hand-held UV lamp exciting at 365 nm; one could notice the change in the emission colour from low pH to high pH (Fig. 3.1.15 b). As discussed above, under acidic conditions, the imine nitrogen atoms are protonated, and the

distance between the phenolic group and the imine N (O–H···N) increases. As a result, the existing original hydrogen bonding of the imine N and the hydroxyl H gets disturbed. This fact is supported by DFT calculations, which show that the BTIP is twisted after protonation, i.e., the angle, $\angle C_{12}C_3C_2$ of the optimized geometries in both neutral and acidic medium are found to 121.3° , and 128.2° , respectively, and those of $\angle C_{12}N_{11}C_{14}$ is 122.9° and 124.1° , respectively (Fig. 3.1.16 a, b).

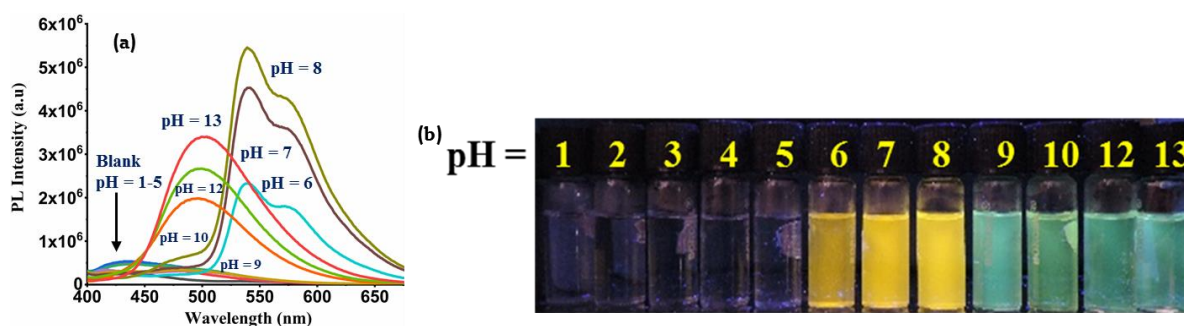


Figure 3.1.15 (a) Emission spectra of BTIP (10^{-4} M in methanol) in different pH buffer solutions, (b) image of BTIP in different buffer solutions taken under UV-lamp ($\lambda_{exc} = 365$ nm) ;

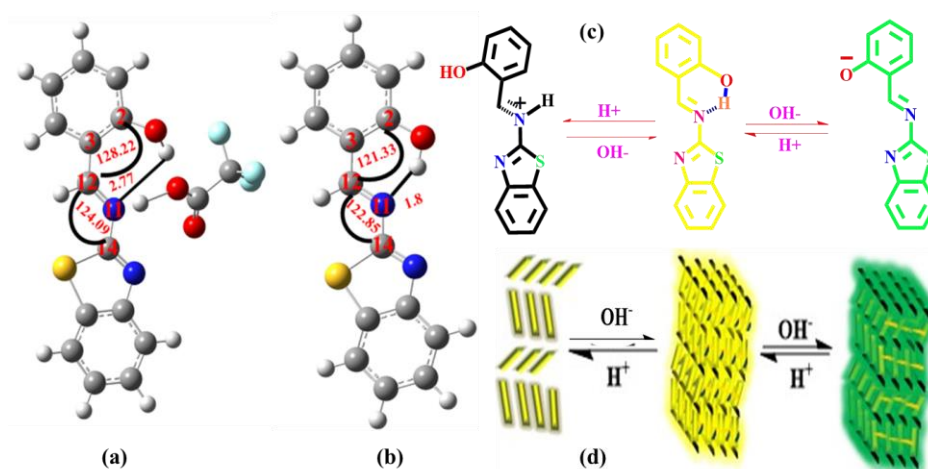


Figure 3.1.16 Optimized structure to show a comparison between the angles $\angle C_2C_3C_{12}$ and $\angle C_{14}N_{11}C_{12}$ in (a) BTIP in acidic medium and (b) BTIP in neutral medium. (c and d) proposed mechanism for fluorimetric switching of BTIP in response to acid and base.

The change in the angle and increased distance in between N_{11} and hydroxy group in the protonated form confirms that the salicylaldehyde part in the molecule is more twisted than the molecule present under neutral conditions (pH ~ 7). As there is a disturbance in the hydrogen bonding, the salicylaldehyde part is flexible enough to have movement which opens the path for non-radiative decay. The above results lead to a non-radiative transition in

an acidic medium leading to non-emission under acidic conditions (pH = 1–5). In physiological pH (i.e., 6–8), the BTIP forms aggregate because of the interplay of interactions (intermolecular hydrogen bonding and short contacts between two neighbouring molecules, Figure 3.1.10). The absorption spectra clearly show the increase of the tail end (Fig. 3.1.14 a), which supports aggregate formation. The size of the BTIP aggregates in neutral pH is similar to the size in the 90% water fraction (454 nm). The sizes of the aggregated particles in both solutions were measured using a Zetasizer (454 nm). With increasing pH from 9 to 13, the extent of proton abstraction increases; high negative charge is generated, leading to the formation of protonated and deprotonated structures (Fig. 3.1.16 c, d). This fact is supported by a red-shifted absorption and emission spectrum (Fig 3.1.15 a). For further support, we recorded the $^1\text{H-NMR}$ spectrum of the BTIP in the presence of a base. As per our prediction, in the $^1\text{H-NMR}$ spectrum of the BTIP, the peak at $\delta = 11.52$ is originally obtained from an OH proton, which disappears in the presence of a base and reappears in the presence of a proton source ($\delta = 11.52$; Fig. 3.1.17). These results show that in basic conditions, hydroxyl protons become deprotonated.

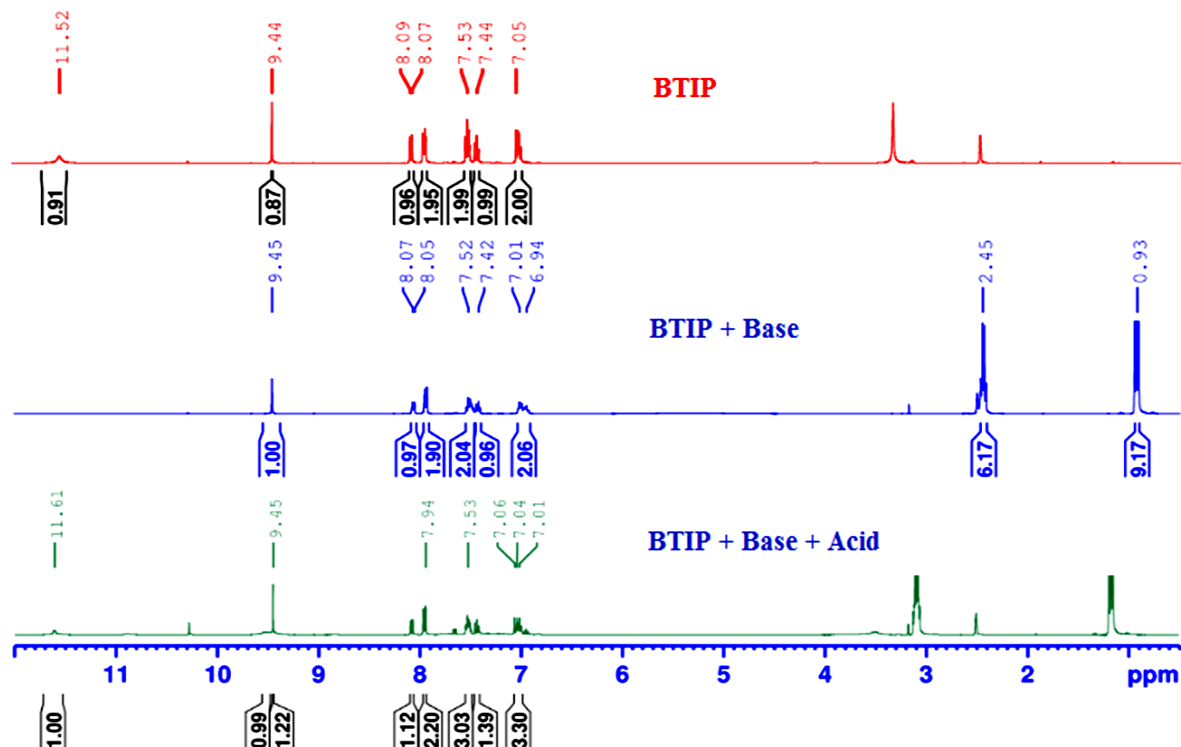


Figure 3.1.17 Stacked NMR spectra with a comparison between the BTIP in neutral medium and after exposing it to base and acid

3.1.5 *In Vitro* Imaging

In a cancer cell, the pH is increased in comparison to the normal cells (around 8 vs 7.2) while the extracellular pH is reduced (around 6.8 vs 7.4).[51]. The quantification and detection of the intracellular pH in a cancer cell is essential for monitoring cancer progression and response of the cell to the various treatments.[52] In this study, we analysed the effect of the BTIP on human cancer cells, hepatocellular carcinoma (Huh7), by MTT assay. The cells were exposed to various concentrations of the compound for 24 hr and then assessed for cytotoxicity by MTT assay. A clear dose-dependent cytotoxicity was observed. The IC 50 value was observed to be 50 μM (Fig. 3.1.18 a). The value at this micromolar concentration indicates that the probe molecule is not highly cytotoxic to the cells and hence ensures that it will be promising in bioimaging applications. To confirm internalization, the Huh7 cells were treated with the compound for 24 h and visualized under a fluorescence microscope. A representative figure of the same demonstrates the presence of green fluorescence inside the cells, indicating efficient internalization of the compound (Fig. 3.1.18 b). Here, the imine group act as an electron acceptor and salicylaldehyde as an electron donor. Schiff-base type molecules have low toxicity and can easily penetrate cells.

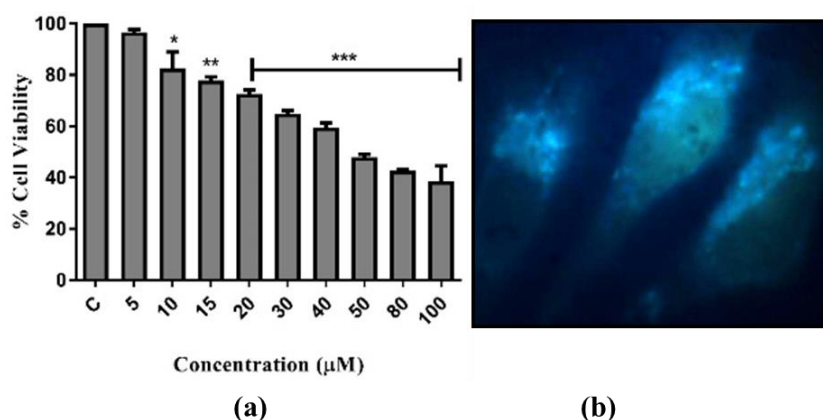


Figure 3.1.18 (a) *In vitro* cytotoxicity analysis; (b) Fluorescence microscope image of Huh7 cells incubated with BTIP for 24 h.

3.1.6 Aluminium (III) Detection

The AIE BTIP was screened with different metal salts containing the metal ions Zn(II), Mg(II), Ca(II), Pb(II), Ni(II), Cd(II), Co(II), Al(III), Hg(II), Na(I) and K(I). The emission was drastically increased in the case of the Al(III) ion, with λ_{max} at 480 nm (Fig. 3.1.19 a). The interference of other metals was studied as shown in the 3D bar diagram, where the small

pink pyramids show the low emission intensity with different metal ions (Fig. 3.1.19 c). When mixed with Al(III), the emission intensity increased (see the blue pyramids in Fig. 3.1.19 c). The other anions do not make any appreciable changes in the emission colour under excitation at 365 nm (Fig. 3.1.19 b). We have attempted to explore the mechanism behind this observation. As we increase the concentration of aluminium ions, the peak intensity is increased at λ_{\max} 375 nm and 277 nm. The appearance of the isosbestic points at 428 nm and 289 nm clearly shows the interaction of the compound with Al^{3+} ions (Fig. 3.1.19 d). The fluorescence titrations show a gradual increase in the emission at $\lambda_{\max} = 480$ nm (Fig. 3.1.20 a). A linear relationship was obtained from 15 μl to 36 μl , which highlights the sensitivity of Al (III) towards the BTIP. (Fig. 3.1.20 b) The detection limit was estimated and found to be 12 pM. Such a low value indicates the very high sensitivity of the probe molecule in comparison to the literature report (Table 3.1.4). The change in the emission spectrum indicates the strong interaction between the BTIP and Al(III), which is supported by the IR infrared Spectroscopy measurement (Fig 3.1.21 a) and ^1H and ^{13}C NMR spectra of the mixture. (Fig 3.1.21 c, d)

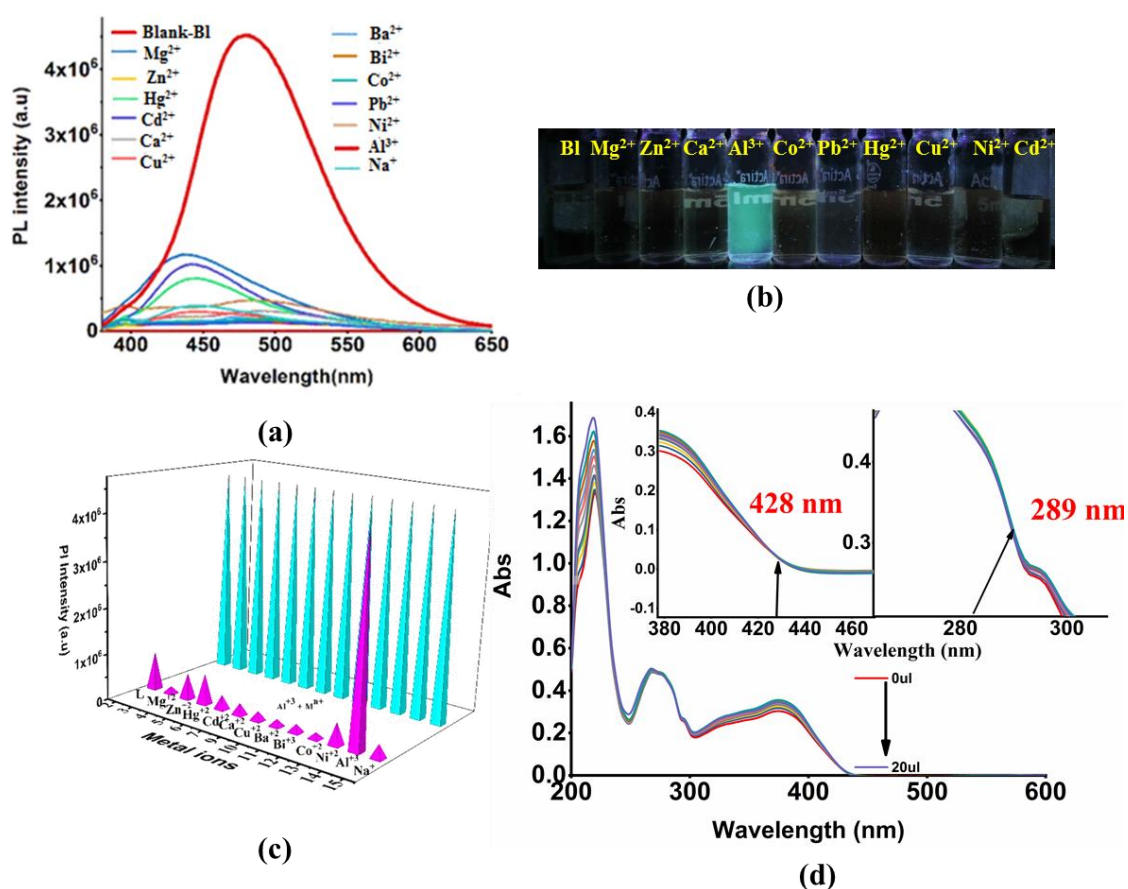


Figure 3.1.19 (a) PL spectra of the BTIP with $c = 10^{-4}$ M in methanol upon the addition of 1 equivalent of different metal ions; (b) image of emission of L ($c = 10^{-4}$ M) with 1 equivalent

of different metal ions, respectively; from left to right (under 356 nm UV lamp); (c) 3D column diagrams of the relative PL intensity of BTIP with different metal ions at I_{473} . Pink bars represent the addition of various metal ions to complex L, and sky blue bars represent the subsequent addition of Al^{3+} (1 equivalent) to the solutions mentioned above [1 + different metal ions + Al^{3+}] (d) The absorption spectra of BTIP (1×10^{-4} M) with a gradual increase in the Al^{3+} (1×10^{-4} M) concentration;

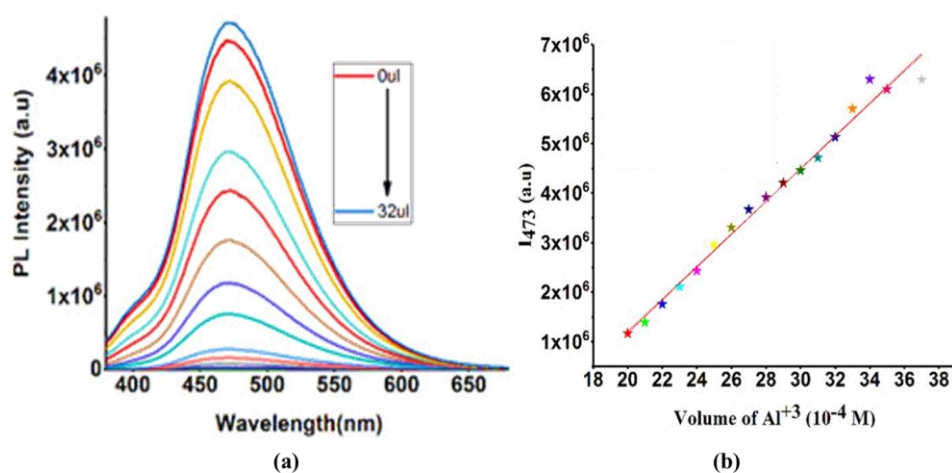


Figure 3.1.20 (a) Emission spectra of BTIP (in methanol, 1×10^{-4} M) titrated with different concentration of Aluminum nitrate; (b) Linear fitting of BTIP with the Al^{3+} .

After isolation and purification of the complex, it was characterized using 1H , ^{13}C and IR spectroscopy. On analysing the 1H NMR of this complex in D_2O , there are only five proton peaks obtained, which are a deshielded singlet proton at 9.23 ppm, single doublet hydrogen at 7.80 ppm, a multiplet of two hydrogens at 7.45 and a triplet of single hydrogen at 7.27 (Fig. 3.1.21 c). It was not possible to predict the structure solely based on 1H NMR spectrum. Therefore, to elucidate the structure of the compound, we examined the FTIR spectra. From the FTIR spectra, the imine bond disappears. The observation of an IR peak at 1663 cm^{-1} indicates the presence of a carbonyl group (1663 cm^{-1}). By comparing the IR spectra of the BTIP with that of the Al (III) complex, the OH peak at 3431 cm^{-1} disappears, and a new peak at 3382 cm^{-1} is generated, further confirming Ar–H (Ar–aromatic) stretching (Fig. 3.1.21 a). The NMR spectra and IR spectra reveal to us that the BTIP forms a complex with the Al(III) complex with Al (III) ions. When we compile the results, the structure is a tris complex of an Al^{3+} ion chelated to bidentate salicylaldehyde which is cleaved from the BTIP. Finally, the HRMS peak at 437 m/z (M–H) (Fig. 3.1.22) suggests the probable structure (Fig. 3.1.21 b) of the complex which might be the reason for the high selectivity and sensitivity of

the probe towards Al (III). (One of the reasons for the selectivity might be hard and soft acid-base theory as, aluminium is hard acid it requires hard donor site such as N and O in its coordination sphere, most of the reported Al(III) probes incorporate with nitrogen and oxygen and in the ESIPT probe, the ESIPT process is inhibited after complexation of Al(III) followed by the chelation enhanced fluorescence effect. The presence of other metal ion does not able to hamper the ESIPT process and form the complex).

Table 3.1.4 Comparison of the sensitivity of detection of Al³⁺ (Literature reports vs present work)

cc	Reference	Detection Limit in solution
1	<i>Dalton Trans</i> , 2015, 44 , 18902-18910	1.03 μM
2	<i>J Fluoresc</i> , 2016, 26 , 43–51	48 nM
3.	<i>Inorg. Chem</i> , 2016, 55 , 9212–9220	0.5 Nm
4	<i>Sens. Actuators, B</i> , 2017, 239 , 1194–1204	0.461 μM
5.	<i>Anal. Chim. Acta</i> , 2017, 958 38-50	50 nM
6.	<i>J. Photochem. Photobiol. Chemistry</i> , 2017, 332 , 273–282	34 nM
7.	<i>Sens. Actuators, B</i> , 2017, 244 , 914–921	3.6 μM
8.	<i>Dyes Pigm.</i> , 2017, 139 , 136-147	9.24 μM
9.	<i>Chem. Commun</i> , 2014, 50 , 11833	~2.08 μM
10.	<i>Talanta</i>,2018,178,796-804	26.7 nM
11	<i>NJC</i> 2018 doi 10.1039/c7nj03964f	2.4 nM
12	<i>J. Photochem. Photobiol</i> , 2018 , 353, 77-85	5.7 nM
13	<i>Sens. Actuators, B</i> , 2018 ,255,366-373	4.369 μM
14	<i>BTIP</i>	12 pM (456 ppt)

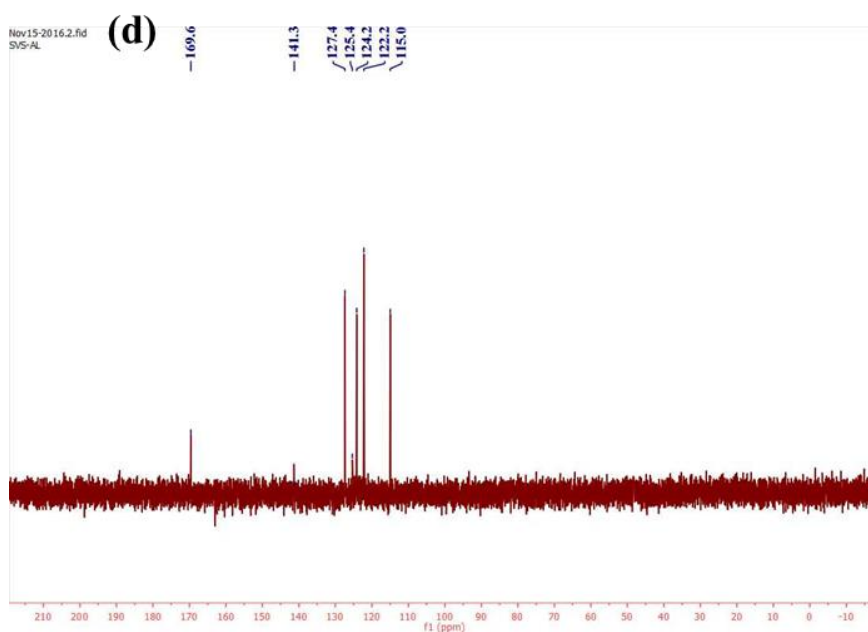
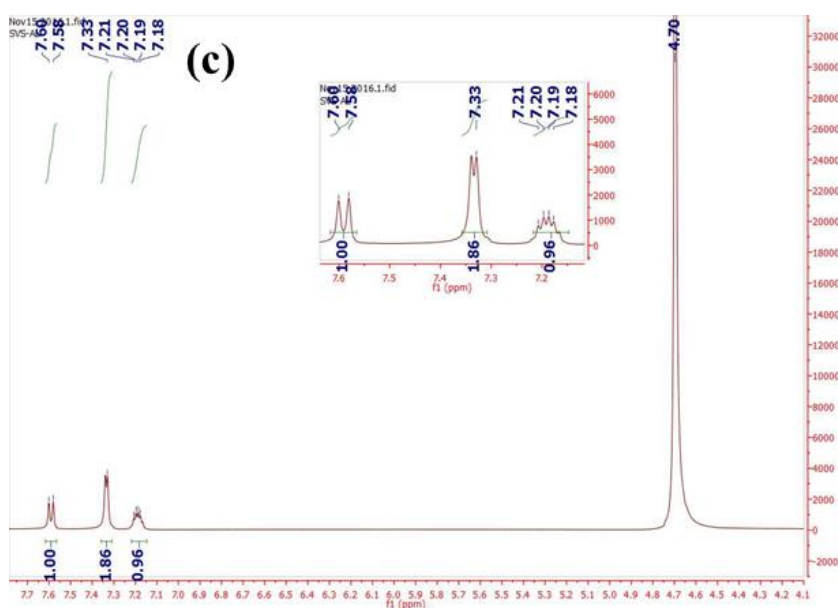
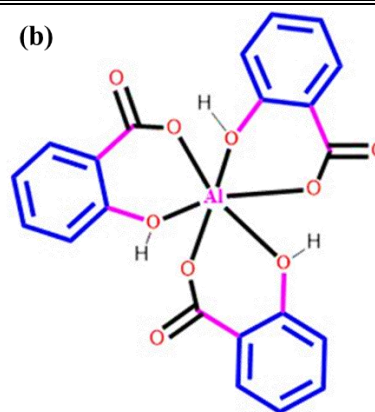
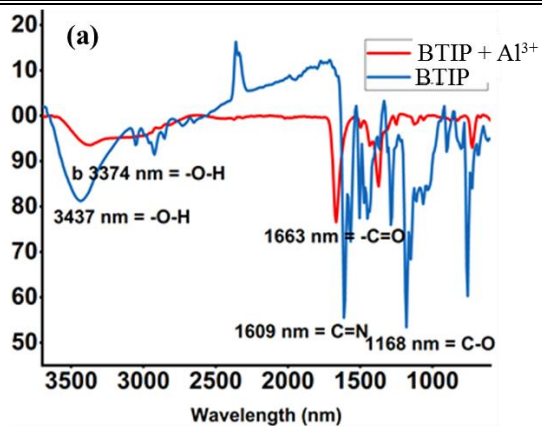


Figure 3.1.21 (a) FTIR spectra of BTIP in absence and presence of aluminium ion (Al^{3+}); (b) Proposed structure; (c) ^1H NMR spectrum of BTIP + Al^{3+} ; (d) ^{13}C NMR spectrum of BTIP + Al^{3+}

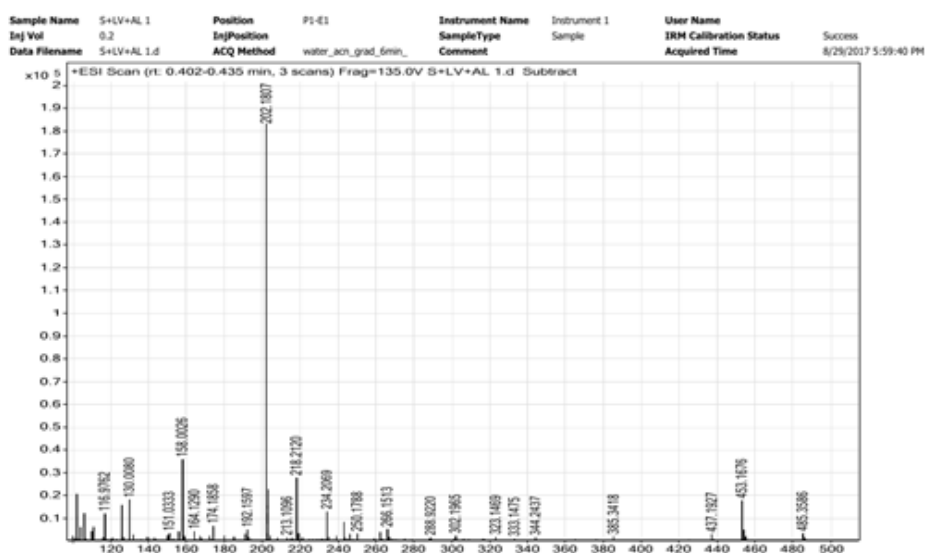


Figure 3.1.22 Mass spectra of complex (BTIP + Al^{3+})

3.1.7 Conclusion

The part of the chapter explored the hidden potential of a simple benzothiazole based organic compound. The ESIPT and AIE behaviour exhibited by BTIP has been rationalized. The variation of slight acidic and basic conditions may lead to an indication of fatal diseases, which make the compound very much useful in practical application for full range pH sensing. BTIP was found to be non-cytotoxic to human cancer cells and its internalization into the cells, promising it for applications into bioimaging. The sensitive detection limit of Al(III) by the simple organic probe molecule is noteworthy (12 pM/ 456ppt).

3.2 - AIE active Heteroleptic Bis Cyclometalated Iridium (III) Complex: Role of hydrogen bonding in multi stimuli response.

3.2.1 Introduction

The conventional organic fluorescence-based chemosensor is considered as an effective molecular tool for the detection of various analytes.[53] Fluorescence signals, however, high interference is caused by the background scattering emission and the autofluorescence of biological samples.[54] Typical organic solid luminescent molecules have either small Stokes shift or often result in significant overlap between the absorption and emission spectral profiles.[55] A feasible method to overcome this problem is to develop such a molecule which has larger Stokes shift with phosphorescence emission.[56, 57] Recently, Ir³⁺ complex has attracted much more attention for the application of the OLED (organic light Emitting Diode), sensing, and bioimaging.[58] Phosphorescent Ir(III) complex shows much better quantum efficiency because of both singlet and triplet excitons.[59] Among them, cyclometalated Ir(III) complex exhibits excellent quantum efficiency, for example, Ir-(Ppy)₃ (fac-tris(2-phenyl pyridine) Iridium(III)).[60-62] In the case of homoleptic complexes (IrL₃), it is difficult to tune the emission because of less substrate scope.[63] In contrast, in heteroleptic complexes (IrL₂L') (L= cyclometalating ligands & L'= monoanionic bidentate ligands) the tuning of the emission is possible, and also the substrate scope is more. The luminescence of these types of Ir(III) complex is mainly dependent on the C^N ligand.[64] The high excited-state lifetime is due to the strong spin-orbital coupling (SOC) in Ir³⁺ complex, which facilitates the efficient intersystem crossing (ISC) of the singlet excited state to triplet excited state. The emission of such type of complex mainly arises from the triplet Metal-to ligand charge transfer (³MLCT) or a mixture of ³MLCT and triplet ligand centred (³LC) transitions.[18, 65] Such types of lowest energy state charge transfer transitions of the complex are susceptible to the surrounding. Therefore, such a complex can be used for probing the cation, anions, pH, biologically essential molecules, and proteins.[66, 67]

In the rigid molecular system in which the difference between the dipole moment of the ground and the excited state is relatively large, the S₁ state attains the intramolecular charge transfer state (ICT) upon photoexcitation. In such cases, the solvent plays a vital role in the relaxation dynamics of the excited state.[68] For such molecules the emission behaviour changes with the different class of solvents like for aprotic solvents the dipole-dipole interactions between the excited state and solvent molecules and for the protic solvent along

with the dipole-dipole interactions the orientational motion of the solvent molecules may also be affected by the specific interaction with the solvent molecules.[69, 70] Many research groups carried out several experiments to define the hydrogen bonding between the molecules.[75] The hydrogen bonding is described as one of the important phenomena of physics, chemistry and biological field.[71] Although many articles are published on the structure and electronic properties of inter and intramolecular hydrogen bonding there is very little information about the structure and properties of the electronically excited state of the Ir(III) biscyclometalated complex. [72-74]

In 2013, Jesus M et al. synthesized a series of blue-green Ir(III) bis and tris cyclometalated complex with 1-benzyl-4-(2,6-di fluorophenyl)-1H-1,2,3-triazole (dfptrBn) as an ancillary ligand.[75] The molecules exhibit solvatochromic behaviour due to strong MLCT character in the excited state.[76] For pH sensing, Aya Konda and co-workers developed Ir(III) complex containing diethylamino, guanidine and iminoimidazolidinyl groups on 2 benzyloquinoline.[77] The emission intensity changes upon protonation of the basic group. Parvej et al., synthesized a multi stimuli AIE active mono cyclometalated Ir(III) rollover complex, which is sensitive to the H^+ ions concentration. The protonated form of the complex is sensitive to the solvents and show the solvatochromic property in solvents containing oxygen—the emission property changes due to the generation of new lower-lying MLCT transition state.[78] Jiang et al. synthesized an iridium complex for sensing glutamine. The strategy was to modulate the charge transfer characteristics by synergistic coordination and intermolecular hydrogen bonding interaction.[79] Zhen Yang et al. developed a multi stimulus water-soluble iridium complex for BSA sensing, Cu^{2+} and cell imaging. In the presence of the BSA, the emission intensity is enhanced due to the formation of the BSA-encapsulated iridium composite materials.[80] In 2018, Huang et al. synthesized a water-soluble phosphorescent iridium complex as a sensor turn-on sensor for human serum albumin. The complex emission intensity is decreased in the presence of acid and resumed its emission when albumin concentration increases due to the hydrophobic and electronic interaction between the albumin and complex.[81] A very simple strategy was utilized by Ohno, et al., and Li et al., for pH sensing using Ir(III) complex. The strategy was to incorporate such an ancillary ligand which could respond on protonation and deprotonation. Both the groups have incorporated the Schiff base ligand with free protonation site so that on change in the pH alter the metal to ligand charge transfer (MLCT) state of the complex.[82, 83]

Considering the above facts for the strategy and design of probes which give distinct responses to multi-stimuli, it is proposed that a probe molecule, which may turn up into an efficient multi-stimuli sensing material should have the following characteristics: 1) the probe should contain both accepting and donating sites for hydrogen bonding; 2) the probe should have the triplet metal to ligand charge transfer (MLCT) transition state for sensitive to the surrounding medium.

From the extensive literature study, we found an ($[\text{Ir}(\text{PPy})_2(\text{Pic-OH})]$) Ir(III) bis cyclometalated complex containing PPy = 2-phenylpyridine as main ligand and Pic-OH = 2-hydroxy picolinic acid as an ancillary ligand reported by S. Yi et al., possesses active hydrogen bonding.[84] The hydrogen bonding might be sensitive to the surrounding medium. Matteo M. *et al.* modified $\text{Ir}(\text{PPy})_2(\text{Pic-OH})$ complex into a series of water-soluble metallo surfactants and described their self-assembling properties.[85] In the literature, there are a very few articles in which the $\text{Ir}(\text{PPy})_2(\text{Pic-OH})$ was modified by chelating hydroxyl group-containing $-\text{BF}_2$ moiety and the chelated complex was tested for bioimaging applications. Also, the lanthanides chelated complex was utilized to study the energy transfer mechanism between Ir(III)/Ln(III) dyads.[86, 87] The single crystal for $\text{Ir}(\text{PPy})_2(\text{Pic-OH})$ was reported by Yi *et al.*[84] From the single crystal, it was ascertained the presence of intramolecular hydrogen bonding in the complex. The presence of intramolecular hydrogen bonding and iridium(III) ion as heavy metal may make the complex sensitive to the surrounding environment. The present section of chapter third describes the vital role of hydrogen bonding to explain unusual photophysical behaviours of an AIE active Ir(III) complex.

3.2.2 Result and Discussion

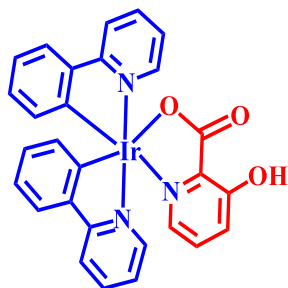
i) Synthesis

$[\text{Ir}(\text{ppy})\text{Cl}]_2$:- The dimeric chloro-bridged Ir(III) complex, namely $[\text{Ir}(\text{ppy})\text{Cl}]_2$ was synthesized by a known method. [88]

(2-carboxy-3-OH-pyridyl)bis((2-pyridyl)phenyl)iridium, Complex 1 :

The chloro-bridged iridium dimer $[\text{Ir}(\text{ppy})_2\text{Cl}]_2$ (1eq), 3-hydroxy-picolinic acid (2.5 eq) and sodium carbonate (4.5 eq) were suspended in 2-ethoxyethanol and overnight heated at 135 °C. To the resulting suspension, distilled water was added in order to further promote the precipitation of the product. A bright yellow microcrystalline solid was obtained and filtered, washed with ether dried. (Yield 80%)

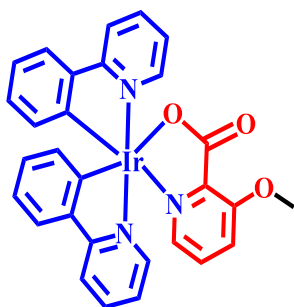
^1H δ_{H} (400 MHz, CDCl_3) 13.84 (1 H, s), 8.74 (1 H, d, J 5.2), 7.91 (1 H, d, J 7.8), 7.87 (1 H, d, J 8.1), 7.76 (1 H, t, J 7.5), 7.62 (1 H, d, J 3.4), 7.54 (1 H, d, J 5.4), 7.40 (1 H, d, J 8.1), 7.27 (1 H, s), 7.23 – 7.16 (1 H, m), 7.03 – 6.97 (1 H, m), 6.98 – 6.92 (1 H, m), 6.92 – 6.87 (1 H, m), 6.85 – 6.75 (1 H, m), 6.39 (1 H, d, J 7.4), 6.22 (1 H, d, J 7.5). ^{13}C



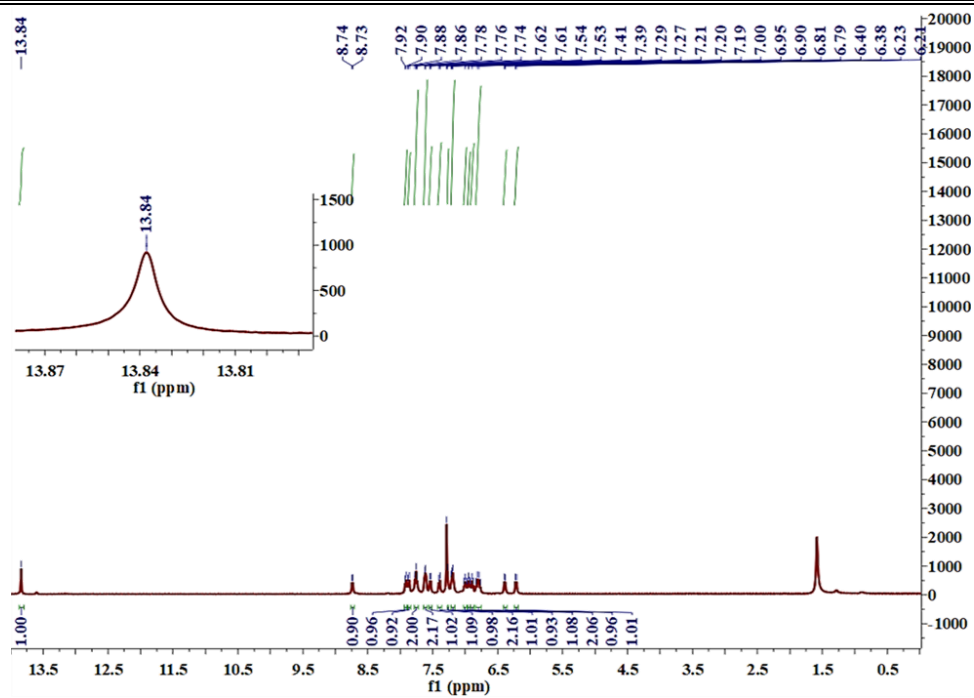
NMR (101 MHz, CDCl_3) δ 177.56, 169.18, 167.54, 160.59, 148.85, 148.59, 148.12, 145.98, 144.19, 143.90, 139.72, 137.34, 137.20, 134.88, 132.55, 132.42, 129.98, 129.69, 129.59, 126.46, 124.30, 124.15, 122.32, 122.16, 121.79, 121.19, 119.06, 118.55. (Fig 3.2.1)

(2-carboxy-3-OCH₃-pyridyl) bis((2-pyridyl)phenyl)iridium Complex 2: Complex 1 (1eq), methyl Iodide (3.5 eq) and K_2CO_3 (5 eq) were suspended in 5 mL of N,N dimethylformamide (DMF) and heated at 90°C for 48 h. Then, the mixture was cooled down, and CH_2Cl_2 was added. The organic layer was washed with distilled H_2O , dried, and the solvents evaporated till solid appears. The desired product was purified from the crude by column chromatography. The desired fractions were collected and dried (Yield 90%).

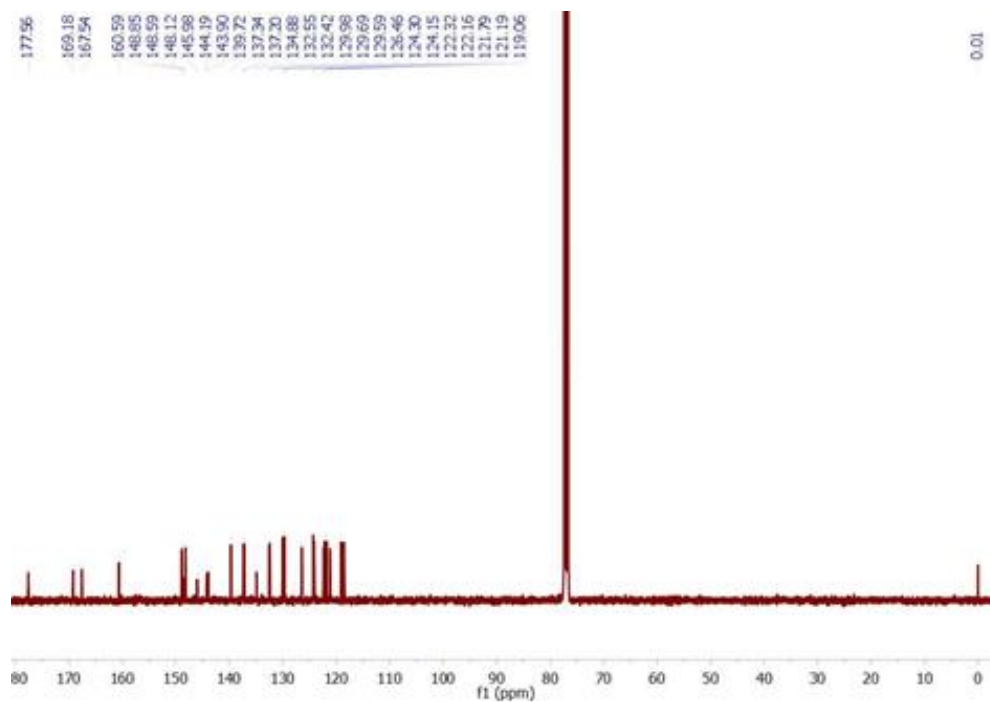
^1H NMR δ_{H} (400 MHz, CDCl_3) 8.83 (1 H, d, J 5.7), 7.87 (2 H, dd, J 20.4, 8.2), 7.73 (2 H, dd, J 10.7, 5.0), 7.64 – 7.59 (2 H, m), 7.59 – 7.53 (2 H, m), 7.44 (2 H, dd, J 7.3, 6.1), 7.25 (1 H, dd, J 8.7, 5.1), 7.16 (1 H, t, J 6.9), 6.98 – 6.91 (2 H, m), 6.86 (1 H, t, J 7.3), 6.81 (1 H, t, J 7.3), 6.74 (1 H, dd, J 8.1, 6.7), 6.41 (1 H, d, J 7.5), 6.17 (1 H, d, J 7.6), 4.02 (3 H, d, J 9.8). ^{13}C ^{13}C NMR (101 MHz, CDCl_3) δ 171.69,



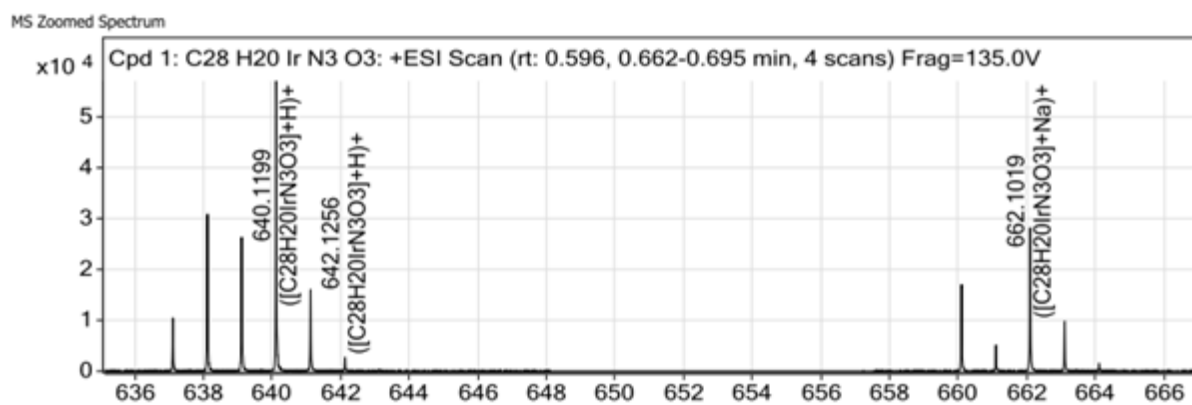
169.13, 167.69, 159.61, 149.12, 149.06, 148.73, 148.07, 144.07, 140.74, 137.06, 136.98, 132.55, 132.41, 129.96, 129.50, 128.64, 124.32, 124.06, 122.18, 121.95, 121.47, 121.06, 120.91, 119.01, 118.37, 77.33, 56.34. (Fig 3.2.2)



(a) ^1H NMR spectrum of complex 1

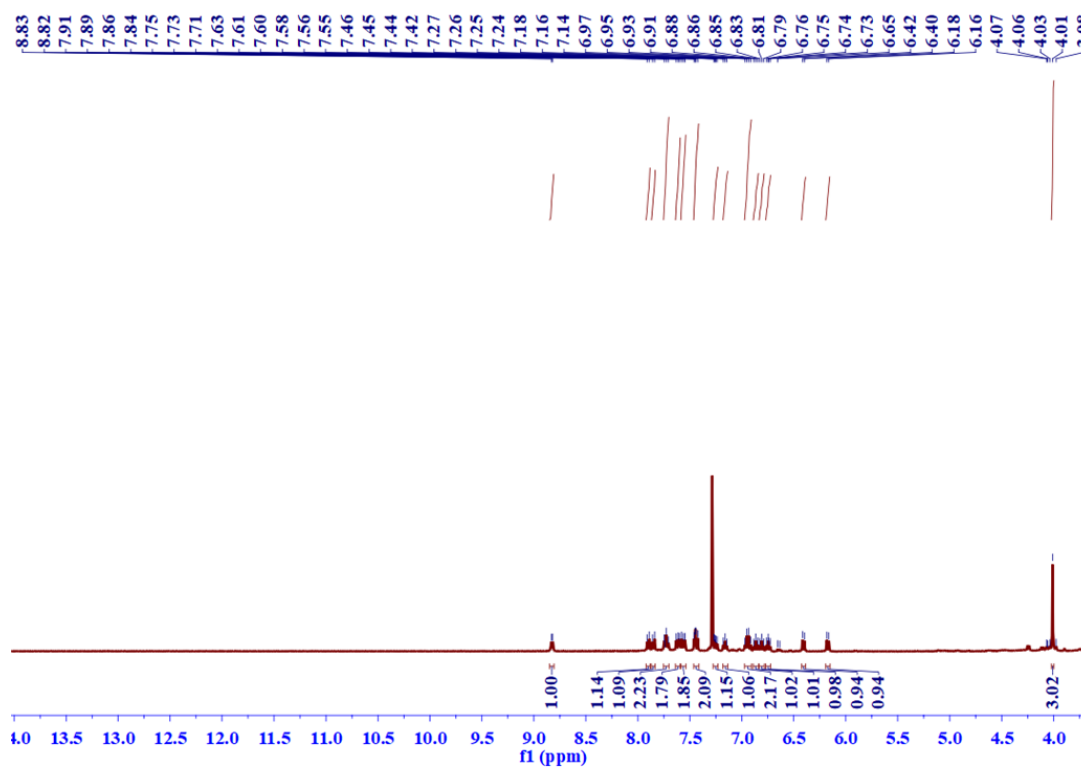


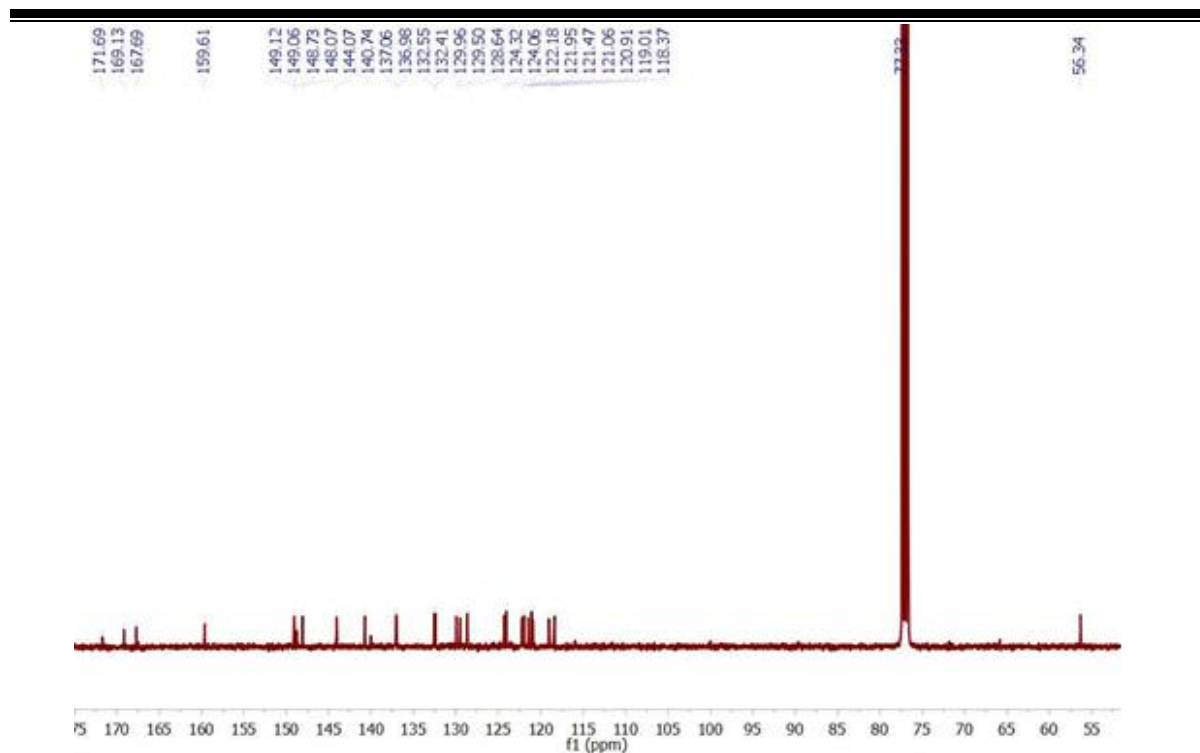
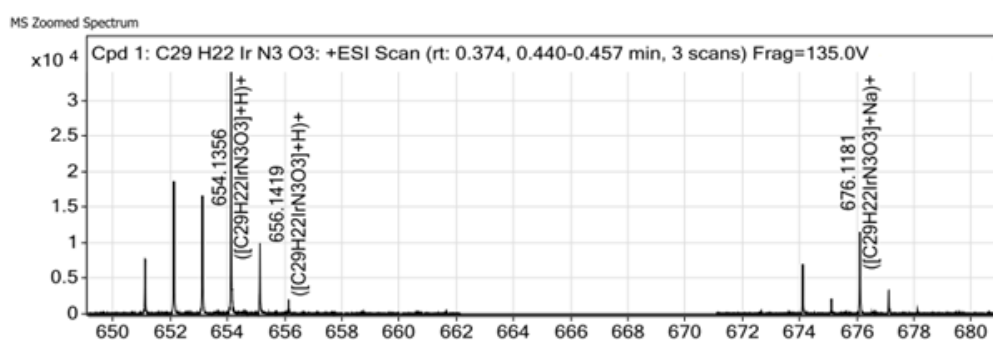
(b) ^{13}C NMR spectrum of complex 1



(c) HRMS spectrum of complex 1

Figure 3.2.1 (a) ¹H NMR spectrum of complex 1 (b) ¹³C NMR spectrum of complex 1 (c) HRMS spectrum of complex 1

(a) ¹H NMR spectrum of complex 2

(b) ^{13}C spectrum of complex 2

(c) HRMS spectrum of complex 2

Figure 3.2.2 (a, b, c) ^1H , ^{13}C and HRMS spectra of complex 2**i-a) Proof for the presence of Intramolecular Hydrogen bonding**

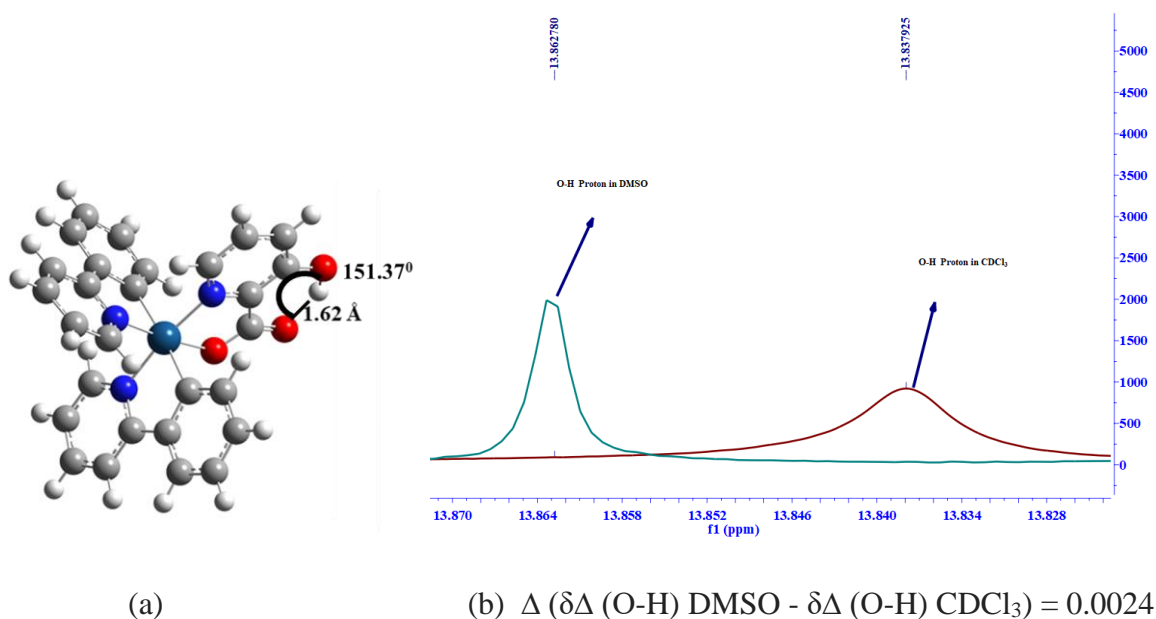
The geometry of the complex was optimized in DFT (Density Functional Theory) using (B3LYP functional), the basis set LANL2Dz and 6-31g (d,p) used in both the DFT and TD-DFT. The optimized structure obtained from the DFT based calculations shows the intramolecular distance, and the angle, (O-H---O=C, $\angle\text{O-H---O}$) is 1.61 Å, $\angle 151.37^\circ$, (Fig. 3.2.3 a) respectively. Supporting the presence of the H-bonding as per the definition of hydrogen bonding and as observed in the crystal structure reported by Seungjun Yi et al. Further to prove the presence of hydrogen bonding in the complex we carried out several

experiments. According to the recent report by Abraham et al., the extent of internal hydrogen bonding could be determined by calculating the value of ‘Solute Hydrogen Bond Acidity’ (A).[89, 90] The ‘A’ value of an N-H or O-H (or S-H) group is the indicator of the hydrogen bond state. If the value of A is equal to zero or less than zero, then the O-H group is taking part in the internal hydrogen bonding. If the value of ‘A’ is above 0.020, then external hydrogen bonding is readily observed. The following equation calculates the value of A

$$\delta\Delta = \delta(\text{DMSO}) - \delta(\text{CDCl}_3) \quad (1)$$

$$A = 0.0065 + 0.133 \delta\Delta \quad (2)$$

Therefore recorded the ^1H NMR of complex 1 in CDCl_3 , DMSO and calculated the chemical shift $\delta\Delta$ ($\delta\Delta(\text{O-H})_{\text{DMSO}} - \delta\Delta(\text{O-H})_{\text{CDCl}_3}$). Substituting the $\delta\Delta$ in the equation, $A = 0.0065 + 0.133(\delta\Delta)$ (where A is hydrogen bond acidity) (Fig. 3.2.3), to find out A. The calculated value of A (0.0098) is in support of strong intramolecular hydrogen bonding.



$$A = 0.0065 + 0.133(\delta\Delta) = 0.0098$$

Figure 3.2.3 (a) Optimized geometry of Complex 1 (b) Figure showing the chemical shift of -OH proton of 1 in d_6 -DMSO & CDCl_3 and calculation of Hydrogen Bond Acidity (A).

ii) Photophysical property

a) Absorption and Emission of Complex

The absorption spectrum of the compound 1 in dichloromethane (DCM) shows the characteristic $^1\pi-\pi^*$ (ligand centre) transition with λ_{max} at ~281 nm and $^1\text{MLCT}$ in the range

of 385-460 nm (Fig 3.2.4 a).[91] Besides, a relatively weaker absorption is observed with λ_{\max} at ~480 nm, which may be attributed to $^3\text{MLCT}$ [92], a forbidden transition. From the DFT studies, it is observed that the significant part of HOMO lies on the phenyl ring of phenyl pyridine (ppy) ligand and Ir(III), with a minor extent observed on the carbonyl group (C=O) (Fig 3.2.4 b) and

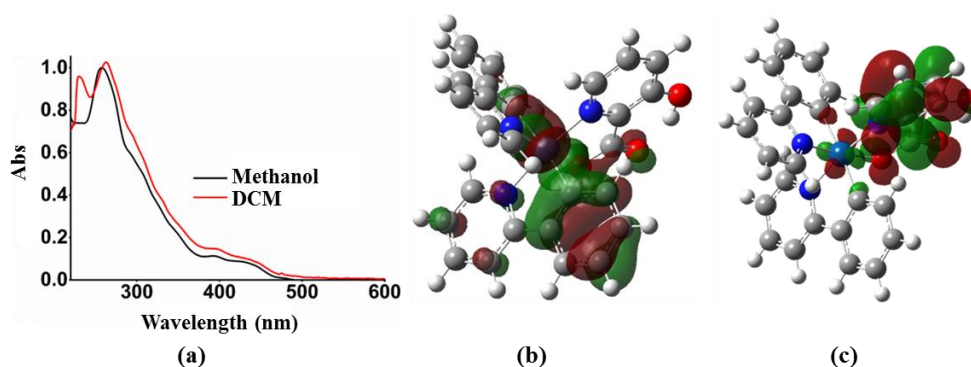


Figure 3.2.4 (a) Absorbance spectra of Complex 1 in methanol and DCM (1×10^{-5} M), Frontier molecular orbital diagram of 1 b)HOMO and c) LUMO, calculated by using B3LYP/6-31G+ (d,p)* and LANL2DZ as implemented on Gaussian 09

the LUMO majorly lies on the picolinate group (ancillary ligand) (Fig. 3.2.4 c). The structured peak in the emission spectra observed from the complexes, 1 & 2, at room temperature in THF (Fig 3.2.5 a). The lifetime of the complexes was recorded and observed in the microsecond regime (0.22 and 0.16 μs , for 1 and 2, respectively). It was observed a bathochromic shift (λ_{\max} 483 nm \rightarrow 570 nm) in the emission spectra with increasing the solvent polarity (Fig 3.2.5 b). All these experiments support the nature of the lowest excited state that has the character of both $^3\text{MLCT}$ (metal to ligand charge transfer) and ^3LC (Ligand centred) states.

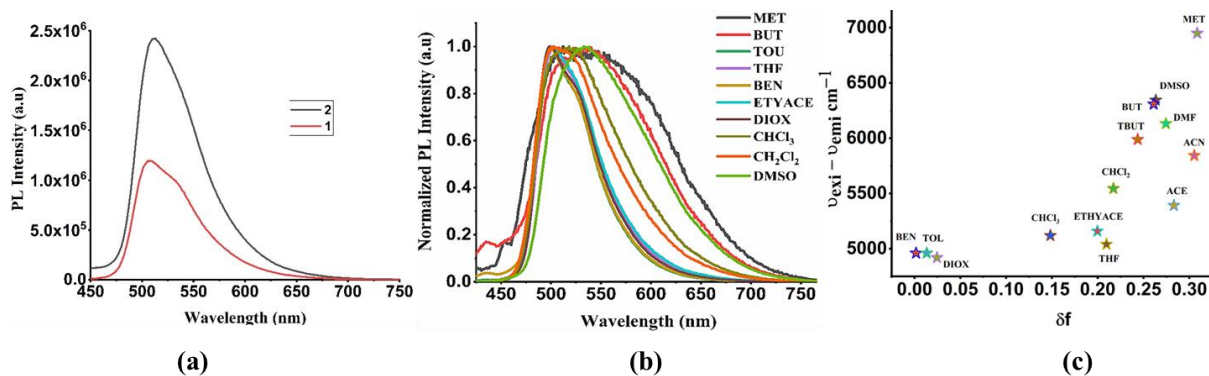


Figure 3.2.5 (a) Emission spectra of the compound 1 and 2 in THF (tetrahydrofuran) (1×10^{-5} M) solutions, (b) Normalized PL spectra of 1 in different solvents (1×10^{-6} M). ((MET =

methanol, BUT = butanol, TBUT = tertiary butanol, TOU = toluene, THF = tetrahydrofuran, BEN = benzene, ETYACE = ethylacetate, DIOX = dioxane, CHCl_3 = chloroform, CH_2Cl_2 = dichloromethane, ACN = acetonitrile, DMSO = dimethylsulfoxide)) (c) Lippert Mataga plot of 1 between stokes shift vs. $f(\epsilon, \eta)$ (orientational polarizability)

b) Dual Solvent effect

The ground state of the complex was not much affected by the solvents, and the evidence for this was obtained from the absorption spectra of various solvents with different polarities (Fig 3.3.6).

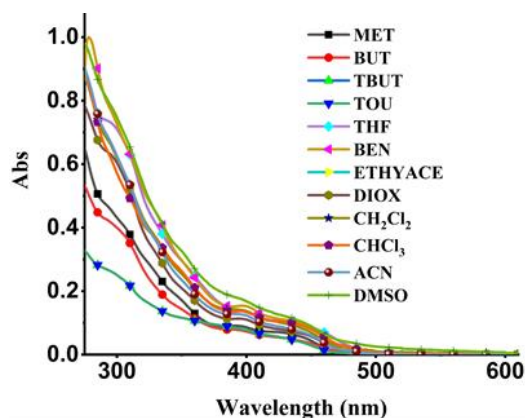


Figure 3.3.6 Absorption Spectra of complex in different solvents (1×10^{-6} M) (MET = methanol, BUT = butanol, TBUT = tertiary butanol, TOU = toluene, THF = tetrahydrofuran, BEN = benzene, ETYACE = ethylacetate, DIOX = dioxane, CHCl_3 = chloroform, CH_2Cl_2 = dichloromethane, ACN = acetonitrile, DMSO = dimethylsulfoxide).

The observed significant change in emission spectra (Fig. 3.2.5 b) in comparison to the absorption spectra with a variation of solvent polarity indicate that the solvent molecules reorient themselves in the presence of a new excited state dipole of the complex. As the emission of the complex was originated from the $^3\text{MLCT}$ [92], the excited state was more affected by the polar protic solvents than the non-polar solvents. Therefore the following was observed: in a non-polar solvent (non-hydrogen bonding or weakly hydrogen bond acceptor) green emission with structured peak (Fig. 3.2.7 a), in chlorinated solvent greenish-yellow with semi-structured spectra (Fig. 3.2.7 b), polar aprotic solvent (hydrogen bond accepting molecule) yellowish-green with semi-broad peak (Fig.3.2.7 c), and quenching with broad emission spectra in polar protic solvent (hydrogen bond donor molecule) (Fig.3.2.7 d). The observed quenching of emission in polar protic solvents may be explained by the formation of intermolecular interaction of alcohols that leads to the non-radiative decay.[93] The

quenching phenomenon was investigated to understand the type of interaction involved in this case. The Lippert-Mataga plot was obtained for 1 (Fig. 3.2.5 (c)) in various solvents with different polarities. The Lippert-Mataga[94] plot will be linear if the emission property of the compound depends upon solvent polarity. The non-linearity of the graph suggests us that along with the polarity, there might be some specific interaction between the probe and solvent.

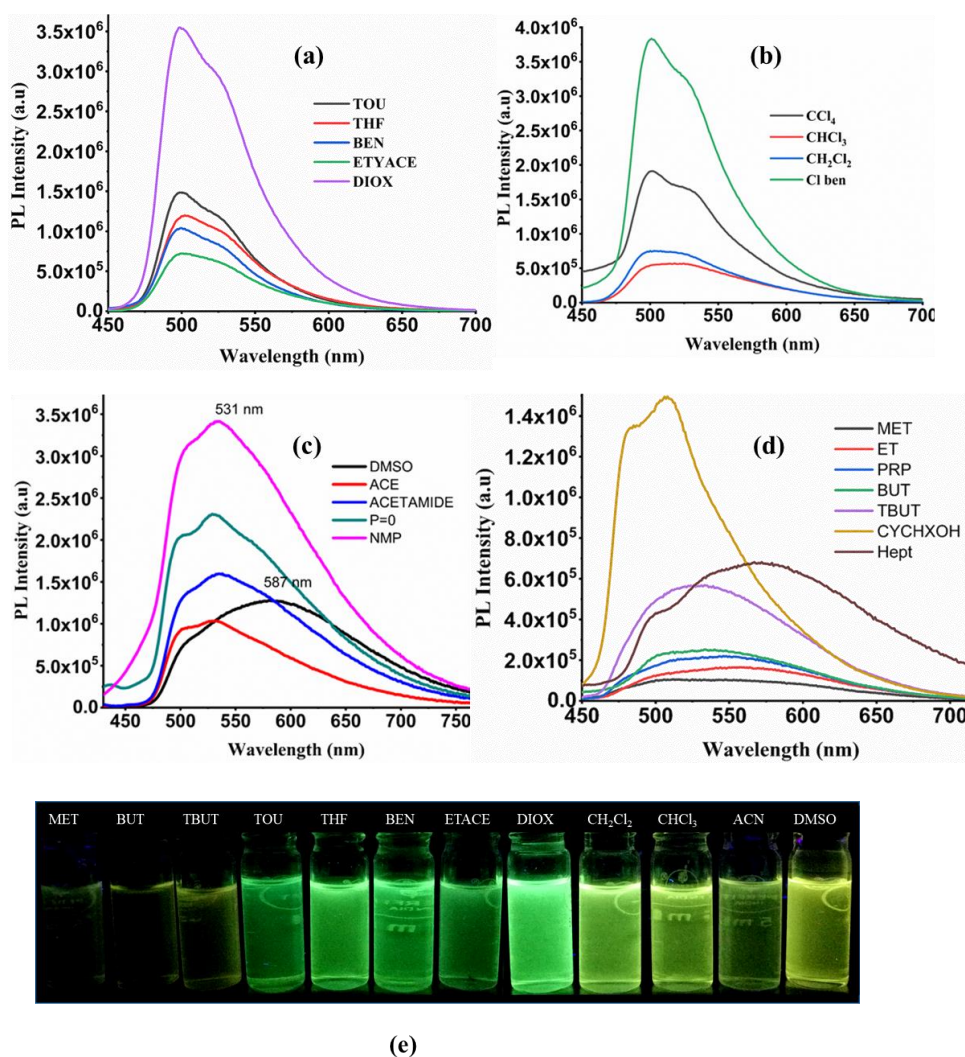


Figure 3.2.7 PL spectra of the 1 in the presence of (a) Nonhydrogen bonding (NHB) or weak hydrogen bonding acceptors solvents (WHB) (TOU= Toulene, THF = tetrahydrofuran, BEN = benzene, ETHYACE = ethylacetate, DIOX = dioxane) (b) Chlorinated solvent (c) Hydrogen bonding acceptors (HBA) solvents (DMSO = dimethyl sulfoxide, ACE = acetone, Acetamide , P=O = hexamethyl phosphoramidate, NMP = N-methyl pyrrolidine) (d) Hydrogen bond donating (HBD) solvents (Met = methanol, ET = ethanol, PRP = propanol,

BUT = butanol, TBUT = tertiary butanol, CYCHXOH = cyclohexanol). (e) Image of 1 in different solvent taken under UV-Lamp (365 nm).

From the Lippert plot, a couple of observation can be drawn

(a) Considering the totality of the solvent, it is observed that there was a deviation of the line from the linearity with increasing polarity of solvents.

(b) However, while looking at the case of alcohols, the linearity of Lippert-Mataga plot is well followed (Fig. 3.2.8 b).

It concludes that in addition to the general interaction operative between the probe and solvents, another specific interaction (hydrogen bonding) for a particular class of solvents should be included. It is clear from the emission spectra and image of complex 1 in different solvent taken under UV-Vis lamp (365 nm) (Fig. 3.2.7 d) that 1 have different behaviour

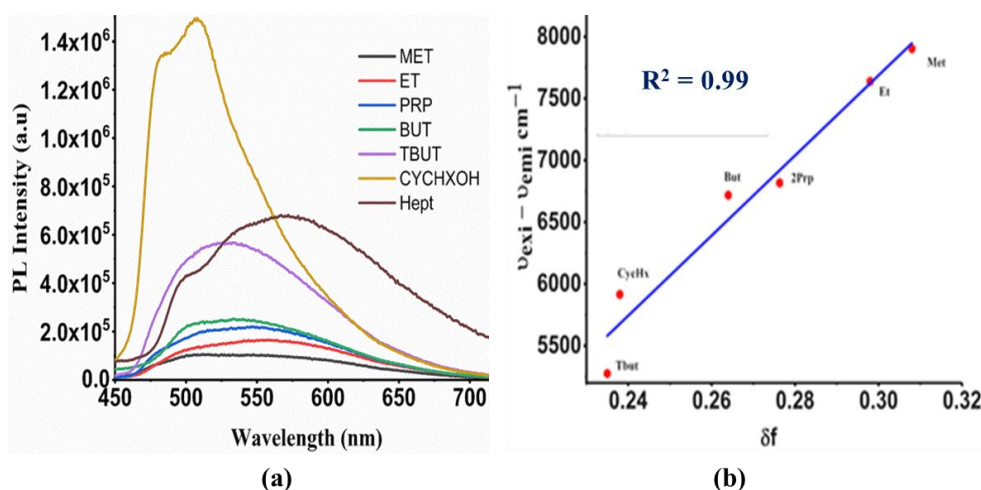


Figure 3.2.8 (a) Emission spectra of 1 in different alcoholic solvent (Met = methanol, ET = ethanol, PRP = propanol, BUT = butanol, TBUT = tertiary butanol, CYCHXOH = cyclohexanol) (a) Lippert Mataga plot of 1 in alcohols between stokes shift vs $f(\epsilon, \eta)$ (orientation polarizability).

in a different class of solvents. In the chlorinated solvents, the deviation of 1 may be due to the moderate dipole-induced dipole interaction (chlorinated solvents are at the borderline of the polar and non-polar solvents, they have higher dipole moment than the non-polar solvents) with the chlorine in chlorinated solvents and the compound that might be the reason for such change.[95] DMSO (Dimethyl sulphoxide), DMF (Dimethylformamide), acetone, DMA (Dimethyl Acetamide), (P=O), *etc.* are polar aprotic solvents that act as hydrogen bond

acceptor in the formation of hydrogen bonding with the complex 1 (Fig. 3.2.5 c). As DMSO has a higher accepting ability of hydrogen bond [96], this results in a significant stoke shift (133 nm) in comparison to other aprotic solvents. As polar protic solvents methanol has the highest tendency to donate the hydrogen bonds to complex 1. Therefore in the presence of methanol complex 1 acts as a hydrogen bond acceptor (C=O, carbonyl group) in hydrogen bonding. The emission intensity of the complex gradually increases with an increase in the chain length of the alcohol series (methanol → ethanol → propanol → butanol, *etc.*). In particular, if the alcohols are sterically hindered (branched chain), the emission intensity is higher in comparison with the regular chain length (butanol and tertiary butanol, propanol and isopropanol) of the analogues (Fig. 3.2.8 a). The emission property of complex 1 depends upon three factors- hydrogen bonding capacity, viscosity and hydrophobic nature of the medium. As the chain length of alcohols increases, the hydrogen bond donating capacity decreases, moreover, as the chain length increases, the hydrophobic nature and viscosity of the solvent increase.[97] Therefore due to the increase in the viscosity and hydrophobic nature of the solvent leads to the restriction of intramolecular motion of the complex; thus, the emission intensity is increased. To gain the shreds of evidence for the above facts, three experiments were carried out 1) recording of FTIR (Infrared Spectra) of complex 1 is performed in various solvents, and it was observed that in methanol there was no observation of carbonyl stretching peak which supposed to be observed at $\sim 1627\text{ cm}^{-1}$ (Fig 3.2.9 a). The disappearance of the peak arises due to the formation of a strong hydrogen bond between the carbonyl group of 1 and the hydroxylic group in methanol.

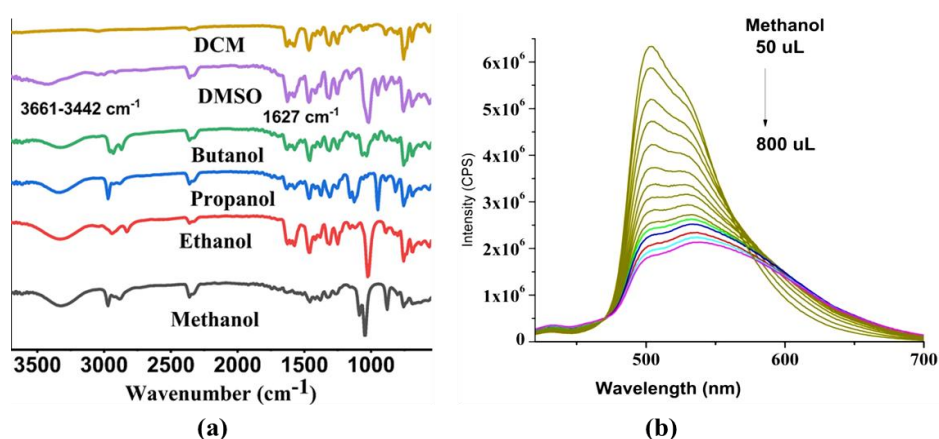
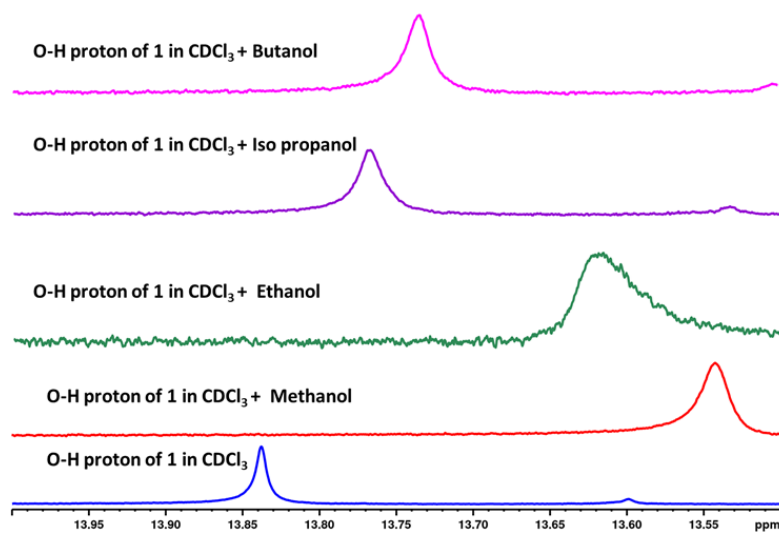
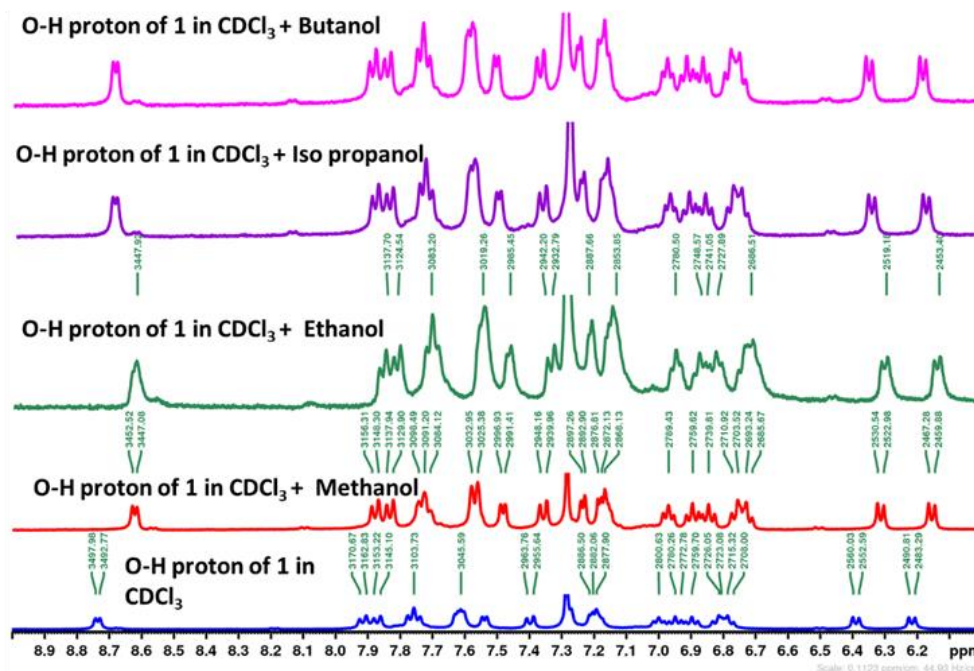


Figure 3.2.9 (a) FTIR spectra of 1 in different solvent (b) Emission spectra of 1 in THF ($1 \times 10^{-5}\text{ M}$) by gradually increasing the methanol concentration

2) recording the ^1H NMR of **1**, the O-H proton peak is observed at 13.83 ppm in CDCl_3 . It is shifted to the more shielded region after adding a drop of methanol to the compound **1** in CDCl_3 , as shown in the figure. Furthermore, we have carried out ^1H NMR of compound **1** in CDCl_3 by adding different alcohols with higher analogues (ethyl/propyl/butyl). In all these cases, the O-H proton peak is shifted to the shielded region. (Fig 3.2.10 a,b)



(a)



(b)

Figure 3.2.10 (a) ^1H NMR peaks of OH functional group of **1** in alcoholic solvents. (b) ^1H NMR of **1** in CDCl_3 mixed with alcoholic solvents

3) Recorded the emission spectra of the complex in THF (1×10^{-5} M) with gradually increasing the concentration of the methanol (50 μ l to 800 μ l). The emission intensity quenches with the bathochromic shift, as the methanol concentration increased (Fig. 3.2.9 b). All these experiments indicate that the ground state formation of strong intermolecular hydrogen bonding of the compound 1 with methanol affects both excited states and also ground state too.

In the literature, the related derivative of the picolinate complex explains that the carboxyl group of picolinate ligand act as a strong acceptor of H-bond. So, a strong hydrogen bond donating molecule being in closer proximity to 1, makes it acts as hydrogen bond acceptor. From the lifetime and quantum yield data of 1 in different solvents, the non-radiative decay was calculated and found that the 1 in methanol shows the highest non-radiative rate constant (Table 3.2.1), which can be explained by the ‘energy gap law.’

In support of the hydrogen bonding effect in emission of 1, compound 2 (analogue of 1) was dissolved in various solvents and recorded the emission spectra. The emission spectrum of 2 is observed to go a similar bathochromic shift upon increasing the solvent polarity. However, there is less quenching effect observed in the presence of alcohols, unlike 1 (Fig 3.2.11 a, b, c). From the above, all experiments, the polarity of the solvent effects (general effects) the emission spectra of both complexes. The complete quenching in the polar protic solvent may be arising due to the hydrogen bonding, which is present in 1 and absent in 2, as in 2 the hydrogen in the hydroxyl group is replaced by the methyl group in the ancillary ligand.

Table 3.2.1 It shows the emission (λ_{\max} , nm), absorption (λ_{\max} , nm), and quantum yield, radiative and nonradioactive decay rate for complex 1 in different solvents.

S..No	Solvents	Emission (λ_{\max}) (nm)	Absorption (λ_{\max}) (nm)	Lifetime (ns)	Quantum yield (absolute) of 1 in solution	(K_{nr})(ns^{-1})	(K_r) (ns^{-1})
1	Methanol	600	400	6.2	0.03	0.15645	4.8×10^{-3}
2	Heptanol	570	400	35.8	0.11	0.02486	3.0×10^{-3}
3	Dioxane	499	400	92	5.40	< 0(-0.04)	0.0586
4	DCM	504	400	70	2.77	<0 (-0.02)	0.0395
5	DMSO	582	400	65.5	3.79	<0(-0.04)	0.057

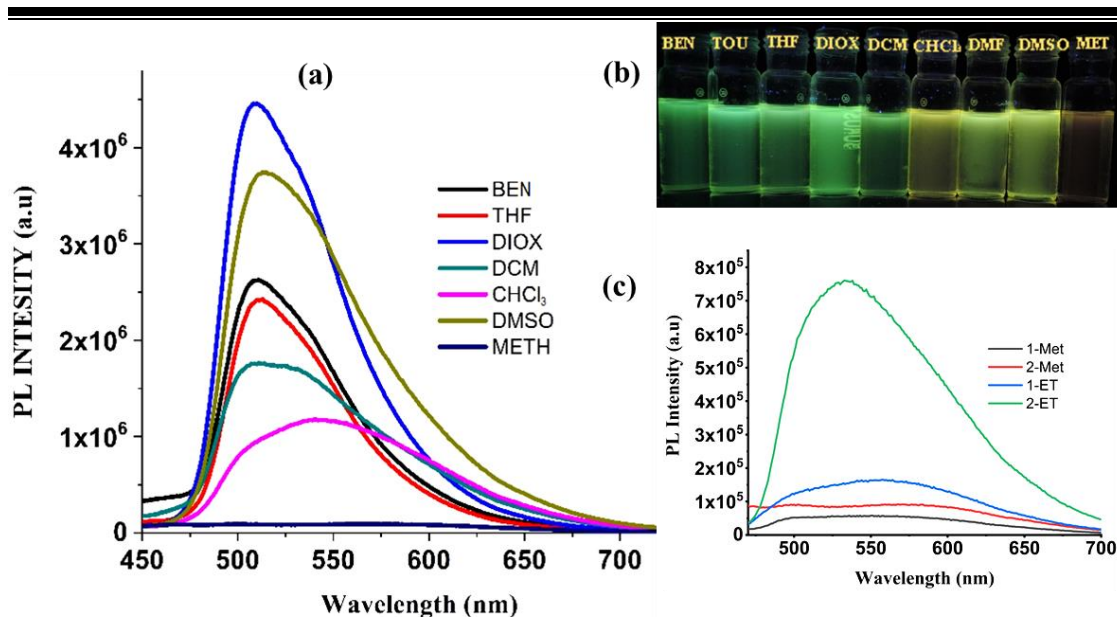


Figure 3.2.11 (a) Emission spectra of 2 in different solvents (1×10^{-5} M), b) Emission colour of 2 in different solvents excited under UV-lamp (λ_{ex} , 365 nm); c) Comparison of 1 and 2 in solvents (methanol and ethanol)

The theoretical support was given on the mechanism by DFT calculation of complex 1 with methanol. On moving from gas to solvent phase (methanol), the strength of intramolecular H-bonding decreases (increase in the distance for C=O---OH interaction, 1.58 \AA to 1.61 \AA) and intermolecular H-bonding increases (decrease in the distance for C=O---HO-Me, 1.89 \AA to 1.81 \AA) (Fig. 3.2.12 (a) top). This modulation in the corresponding electronic structure of the complex in two different phases is also evident from the electron localization function (ELF) maps (Fig. 3.2.12 (a) bottom). From the optimized geometry of 1 in DCM, the HOMO lies on the two phenyl-pyridine ligands and iridium (III). Subsequently, LUMO primarily located on the picolinate ligand, and the difference between the excited state and ground state is 3.61 eV [Fig 3.2.12 (DCM) b]. Whereas in the presence of methanol, the HOMO is majorly concentrated on the Ir (III) with some minor contributions from the phenyl pyridine, and LUMO is on the picolinate part. Because here methanol is acting as a hydrogen bond donor and carbonyl group in the complex as hydrogen bond acceptor. The energy gap between them is 1.51 eV [Fig. 3.2.10 (Methanol) b]. The MLCT charge transfer contribution in methanol is 18%, and in DCM is 33%. The HOMO–LUMO gap and MLCT character are more in DCM than in methanol, which favours the poor emission in methanol. (Fig 3.2.12 c)

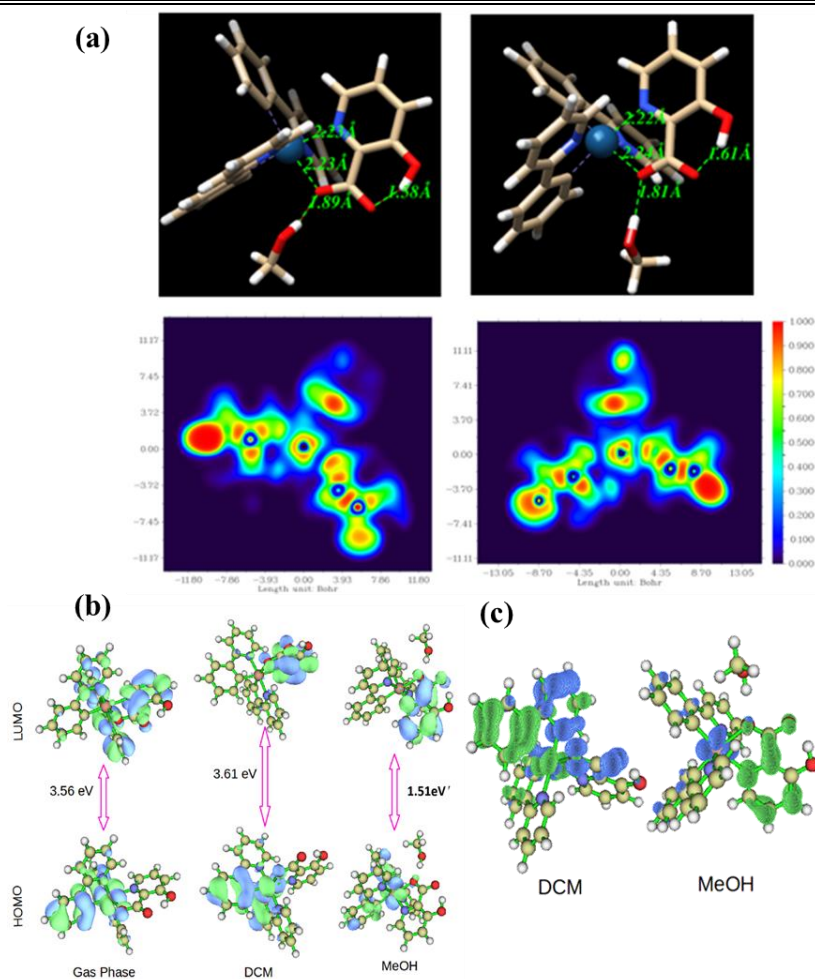


Figure 3.2.12 (a) The DFT optimized structure of the MeOH-complex-1 in gas (left panel) and solvent phase (right panel) along with their corresponding ELF maps (below) (6-31G (d,p) and LANL2DZ). In the solvent phase, we have considered the implicit continuum solvent model for the Methanol. (b) Frontier orbital diagram energy level from DFT of 1 in DCM and Methanol (c) Density difference plots showing the Metal to Ligand Charge Transfer (MLCT) transition in DCM and Methanol. (Blue cloud indicates more electronic charge whereas green cloud indicates less charge.)

c) Aggregation-induced emission (AIE)

A set of solutions with a different methanol-water fraction (0-90% v/v in 5 ml vial) were prepared. The emission spectra of each solution were recorded (Fig. 3.2.13 a). The emission intensity gradually increases with increasing the concentration of water as shown in (Fig. 3.2.13 b) The image of the vial containing different water fraction under UV-lamp is given below (Fig 3.2.13 c). This phenomenon is called as AIE.

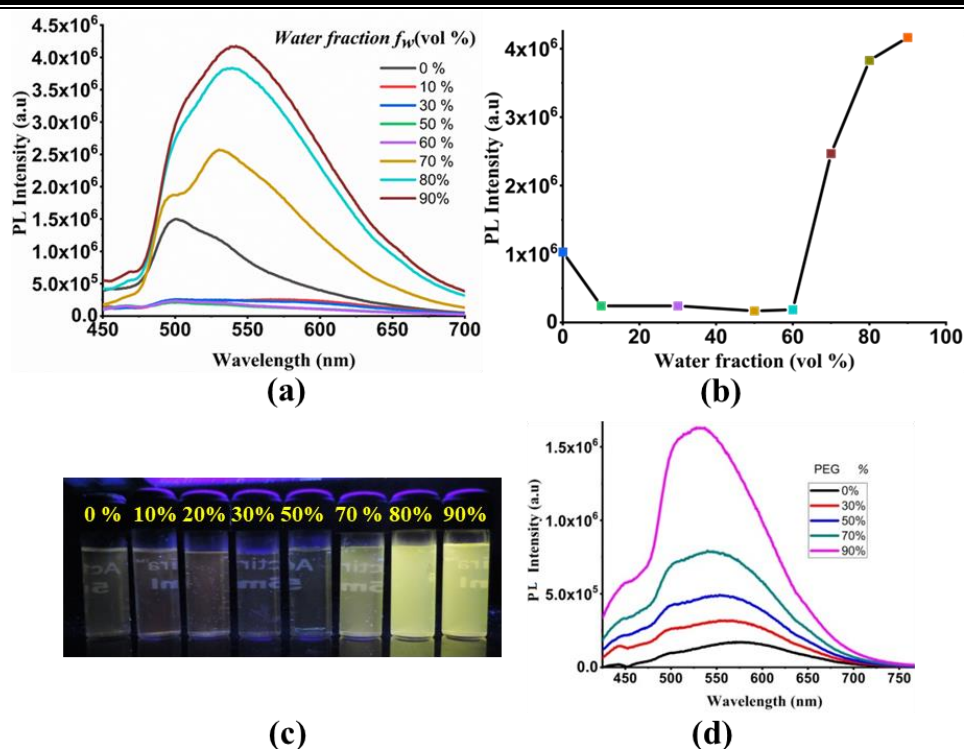


Figure 3.2.13 (a) Emission Spectra of 1 in methanol (1×10^{-5} M) with gradually increasing the water concentration (from 0% to 90% V/V in 5ml vial) (b) Plot of PL intensity (I) of 1 versus the compositions of the aqueous mixtures, concentration: 1×10^{-5} M. (c) Image of 1 in different methanol/ water mixture under UV-lamp (λ_{ex} , 365 nm); (d) Emission spectra of 1 in methanol/PEG mixtures.

To know the which mechanism (Restriction intramolecular motion) cause AIE nature, the emission spectra of 1 was recorded in methanol with a gradual increase in the viscosity of medium through the addition of PEG600; the emission intensity was found to increase (Fig. 3.2.13 d) and from the crystal structure of 1 reported by Yi et al., the intramolecular hydrogen bonding, $[\text{C}=\text{O} \cdots \text{H}-\text{O}, 1.828 \text{ \AA}]$ was confirmed, and also few short contacts are observed in the packing diagram of crystal.

The DFT calculation of 1 was carried out in different structural forms, hydrogen-bonded (gas and solvent phase) and non-hydrogen bonded (gas phase). [Fig 3.2.14 (a, b, c)] The calculation at CAM-B B3LYP/cc-pvTZ level of theory (on the B3LYP/6-31G(d,p)) optimized geometry predicted the conformation without hydrogen-bonded gas-phase structure is 20.67 kcal/mol higher energy than the hydrogen-bonded one. These findings can be analytically correlated to the relative H-bonding strength of the complex, i.e., 20.67 kcal/mol in the solution phase. Indeed, the hydrogen-bonded conformation is energetically

favourable, and we have the theoretically realized the restricted motion of the picolinate due to the substantial H-bonding interactions.

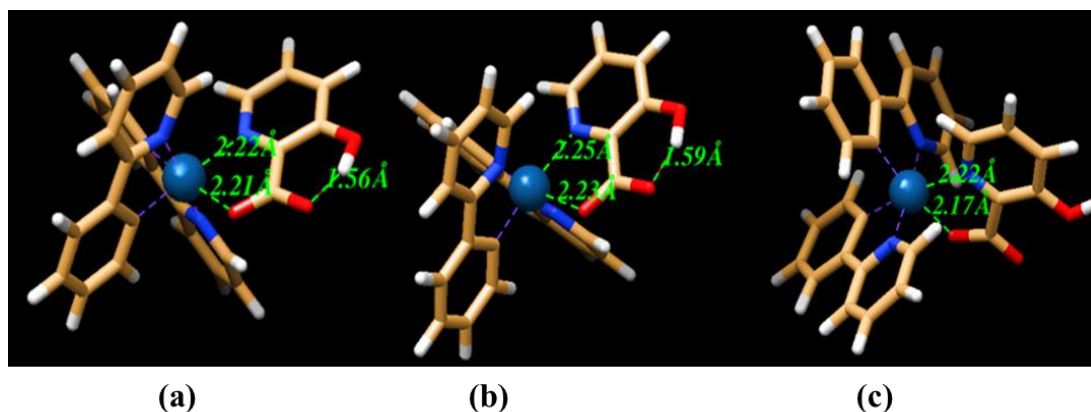


Figure 3.2.14 DFT optimized structures for the different structural forms of the complex [(first two forms (a and b) are hydrogen-bonded in the gas phase and solvent phase, respectively, and the last one is non-hydrogen bonded in the gas phase (c))].

A minimal impact of the H-bonding interaction to the electronic perturbations in the complex is distinguished from a comprehensive ELF (electron localization function) and FMO (frontier molecular orbital) analysis as reported in (Fig. 3.2.15top). It is important to note that certain (but not significant) changes due to the formation of H-bonding can be visualized from the ELF and FMO maps. The characteristic change in the LUMO orbital due to weak and long-range interaction like H-bonding⁶⁴ is evident from the contour maps in (Fig 3.2.15). From the experimental data, theoretical calculation and crystal structure, it was clear that the increase in the emission intensity may be due to the restriction of the intramolecular motion of the picolinate group.

d) pH Probe

The presence of intramolecular hydrogen bonding makes the complex sensitivity to the external stimuli. Therefore, the sensitivity of intramolecular hydrogen bonding was tested with different bases and pH buffer solution (1-13). The emission intensity of 1 is increased in the presence of base with different basicity (Fig. 3.2.16 a). As emission of 1 is sensitive to the basic environment, the fluorescent spectra of 1 were recorded in the whole range of pH. It is observed that the emission property of the complex remains unaffected in acidic pH. In contrast, in the basic pH (8-13), the emission intensity increases gradually (Fig. 3.2.16 b, c). To investigate the mechanism for sensing basicity, compound 1 was mixed with 0.1 equivalent of triethylamine, and the ¹H NMR of this mixture was recorded. From the NMR

spectra, we noticed that the observed OH peak at δ , 13 ppm disappears in the presence of triethylamine (Fig. 3.2.16 d). The result explains that 1 exists in the neutral form in acidic/neutral conditions. However, if the pH is higher than seven, it gets deprotonated.

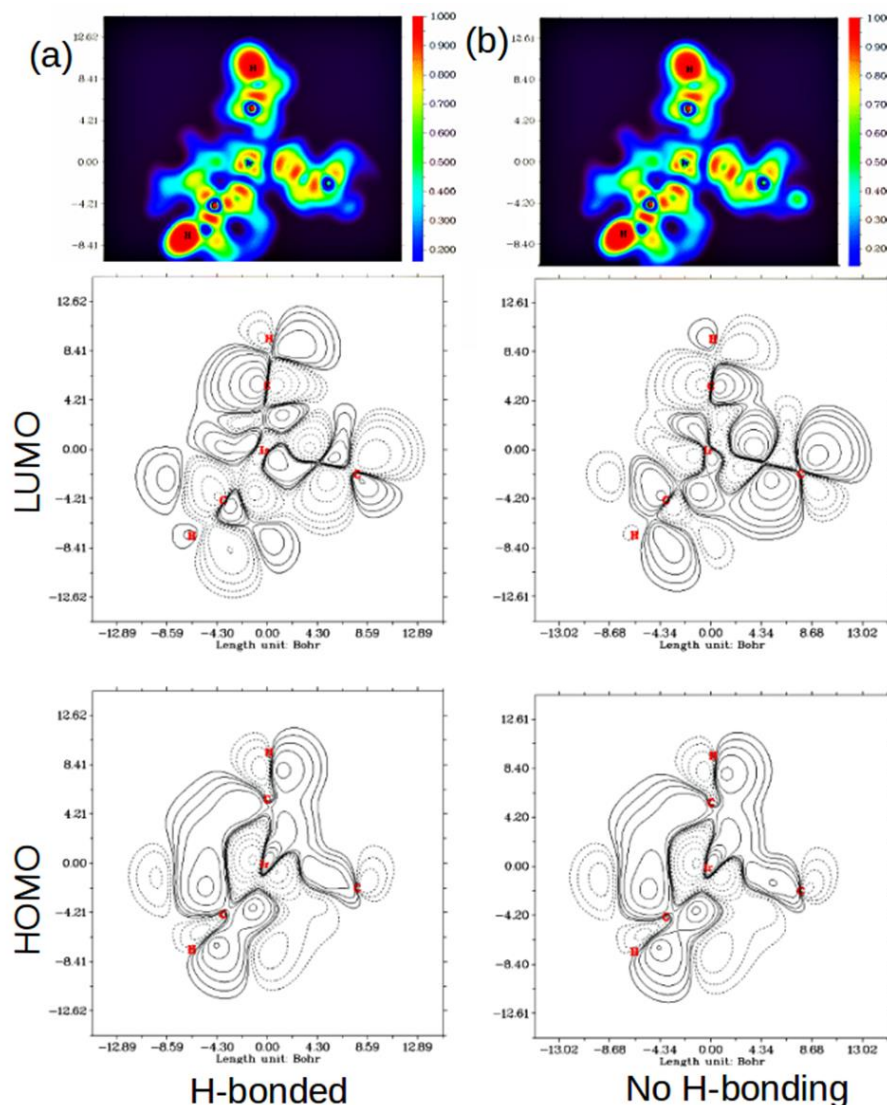


Fig 3.2.15 Electron localization function (ELF) and FMO contour maps for the H-bonded ((a) left panel) and without H-bonded ((b) right panel) forms of the complex.

Therefore, at higher pH (>7), the OH is deprotonated, and the negative charge is generated, which endows 1 with good solubility in the buffer solution. The formation of negative charge and loss of hydrogen bonding might be the reason for the observed hypochromic shift with green emission in basic conditions. Therefore, complex 1 could be utilized as the sensing materials for determining the basicity of the salts.

gradually (Fig. 3.2.18 b). A linear relationship obtained at a concentration range of 0.0044 eq to 0.088 eq (Fig 3.2.18 c). The limit of detection was found to be 9.3 pM. Because of its hydrophobic nature, molecule 1 binds firmly within the hydrophobic pockets of BSA protein, and this might be the reason for enhanced emission.

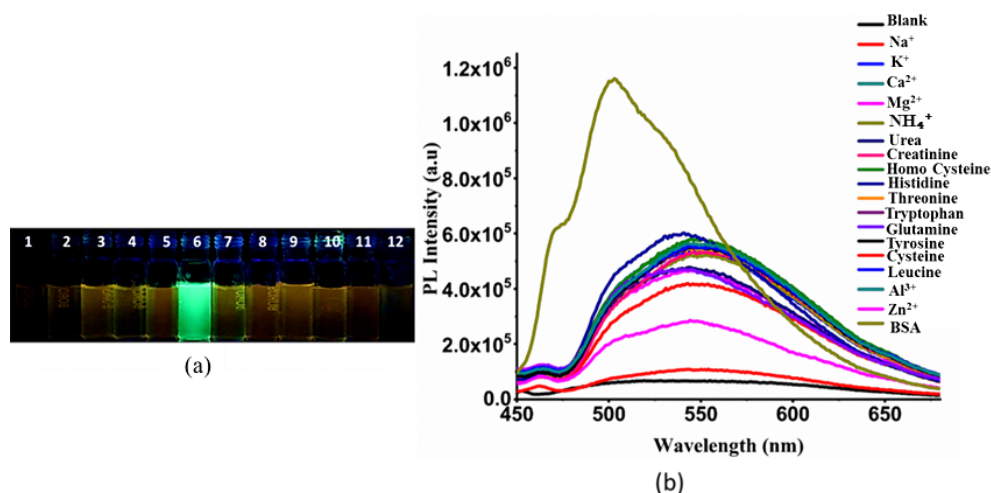


Figure 3.2.17 (a) Image of 1 ($c = 10^{-5}$ M) with 1 equivalent of different metals and proteins, respectively, from left to right (1- Na_2SO_4 , 2- MgSO_4 , 3- ZnSO_4 , 4- $\text{Al}_2(\text{SO}_4)_3$, 5- Urea, 6- BSA, 7- Histidine, 8- Creatinine, 9- Cystine, 10- Tyrosine, 11-Lysine, 12-Tryptophan) (under exciting at 365nm with a UV lamp). (b) Emission spectra of 1 ($c = 10^{-5}$ M) with 1 equivalent of different metal salts [Na_2SO_4 , K_2SO_4 , CaSO_4 , MgSO_4 , $(\text{NH}_4)_2\text{SO}_4$, Na_3PO_4 , ZnSO_4 , $\text{Al}_2(\text{SO}_4)_3$], creatinine and BSA. (BSA results in green emission and remaining species produces weak yellow emission).

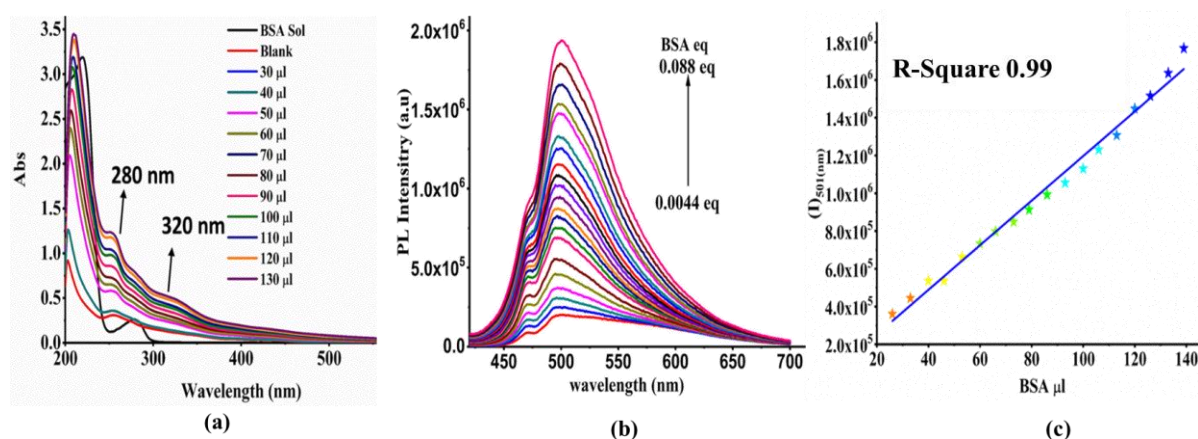


Figure 3.2.18 (a) UV-Visible spectra of 1 by gradually increasing the BSA concentration (b) Emission intensity of 1 (1×10^{-5} M) with a gradual increase of BSA (10 mg per 10 ml) and (c) linear fitting of 1 with BSA.

Therefore, enhanced emission is due to the restriction of the motion of the 1 within the hydrophobic pocket. This phenomenon is also observed when 1 treated with porcine pepsine protein. In this case, the intensity of emission peak at 540 nm gets enhanced [Fig 3.2.19 (a,b)] which may be due to binding of 1 within the hydrophobic pocket of pepsin.

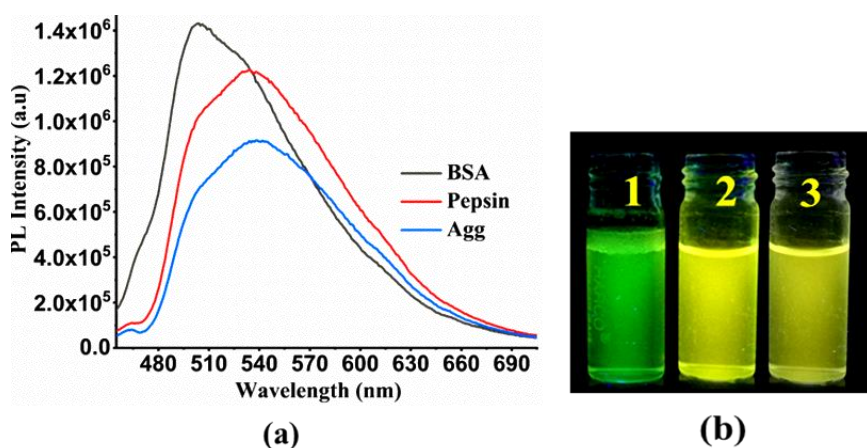


Figure 3.2.19 (a) Emission spectra of 1 in the presence of BSA, Protein and 90% methanol/water fraction. (b) Image of 1 in the presence of BSA, Protein and 90% methanol/water fraction under UV-Lamp 365 nm.

However, unlike BSA, the shift in emission peak is not observed. The change of emission wavelength in BSA may be due to the presence of hydrogen bonding through the hydroxyl group of 1

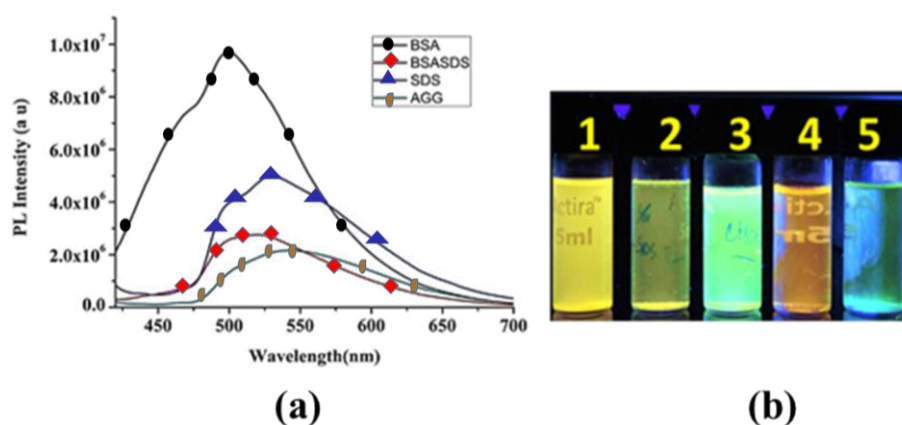


Figure 3.2.20 (a) Emission spectra of 1 in presence of BSA, 1 in presence of BSA+ SDS and (90% aggregate solution (AGG)) (b) PL emission image of 1 in 1(90% f_w), 2(1+SDS+BSA), 3(1+BSA), 4(1+ SDS), 5(1+ Methanol).

Firstly, in order to support the hydrophobic interaction of 1 with BSA, the effect of sodium dodecyl sulfate (SDS) on complex 1 was examined. The emission of 1 was recorded in the

presence of the following analytes: 1) BSA (Bovine Serum Albumin); 2) BSA + SDS; 3) SDS (Sodium Dodecyl sulfate). It was observed that the emission intensity was quenched in the vial 2 (BSA+ SDS+1) (Fig. 3.2.20 a, b). So, from the literature, it is well known that the SDS surfactant unfolds the BSA, 8; therefore, it is proposed that 1 is sensitive to protein (BSA) folding-unfolding. Furthermore, to acquaint with the cavity where 1 may be fitting and to know the interactions, the molecular docking studies of 1 with BSA and 1 with pepsin protein was studied.

3.2.3 Docking Studies

Molecular docking studies of complex 1 with BSA protein identifies possible interaction mode of the ligand with BSA. The binding energies of the top ten binding poses of the complex are between -6.4 kcal/mol to -4.69 kcal/mol (Table 3.2.3). These ten binding modes were within eight different pockets of the host protein. Binding mode one, three and seven are within the same pocket in chain B while each of the other interactions of ligand and host was through the different binding pocket. Binding pockets of poses four, five and nine were located on the chain A. In contrast, the rest of the pockets were located on chain B. The binding site of the ligand with lowest binding free energy (-6.4 kCal/mol) is located on the surface of the protein (Fig. 3.2.21 a). A closer look into the binding site (Fig. 3.2.21 b) and other binding pockets (Table 3.2.3) on chain B released that multiple ligand molecules may bind to a protein molecule which could lead to aggregation-induced fluorescence spectra. In the best binding pose, ligand interacts with protein through Gln416, Ser418, Thr419, Thr466, Val468, Lys499, and Lys533 (Fig. 3.2.21 c). Among these residues, the side chain of Thr466 are hydrogens bonded with the ligand (Fig. 3.2.21 d). Interestingly, both the pockets have patches of negatively charged. The surface may enhance the binding affinity of positively charged iridium-containing ligand molecules; this might be the reason for the intense green emission. Similar studies of complex 1 with pepsin were carried out. The docking of 1 into pepsin protein (PDB ID: 4PEP) predicts that the ligand binds deep into the pocket surrounded by many hydrophobic side chain (Fig. 3.2.21 e). However, the hydroxyl group of the ligand is beyond hydrogen bond limit of any of the host electronegative atoms (Fig. 3.2.22.f) which could explain the observed unchanged peak position during the aggregation-induced emission of Iridium (III) complex. Therefore, the complex can be used as a sensitive probe for BSA sensing.

Table 3.2.2 Binding pockets of top 10 conformations of the complex 1

S. No.	Chain identifier of the binding pocket	Binding Energy (kcal/mole)	Close Residues
1	B	-6.4	Gln416, Ser418, Thr419, Thr466, Val468, Lys499, Lys533
2	B	-6.06	Arg194, Trp213, Arg217, Lys221, Lys294, Val342, Asp450, Cys447
3	B	-6.04	Pro415, Gln416, Ser418, Thr419, Thr466, Val468, Lys499, Lys533
4	A	-6.03	Arg194, Trp213, Arg217, Glu291, Val292, Lys294, Pro338, Val342
5	A	-5.9	Asp111, Pro420, Ile522
6	B	-5.52	Asp111, Lys114, Arg144
7	B	-5.26	Pro415, Gln416, Val468, Lys499, Tyr496, Ala500, Lys533
8	B	-5.16	Tyr155, Asn158, Gly162, Pro281, Leu283, Glu284
9	A	-4.86	Glu17, His18, Pro281, Leu282, Leu283
10	B	-4.69	Glu48, Phe49, Thr52, Glu73, Lys76

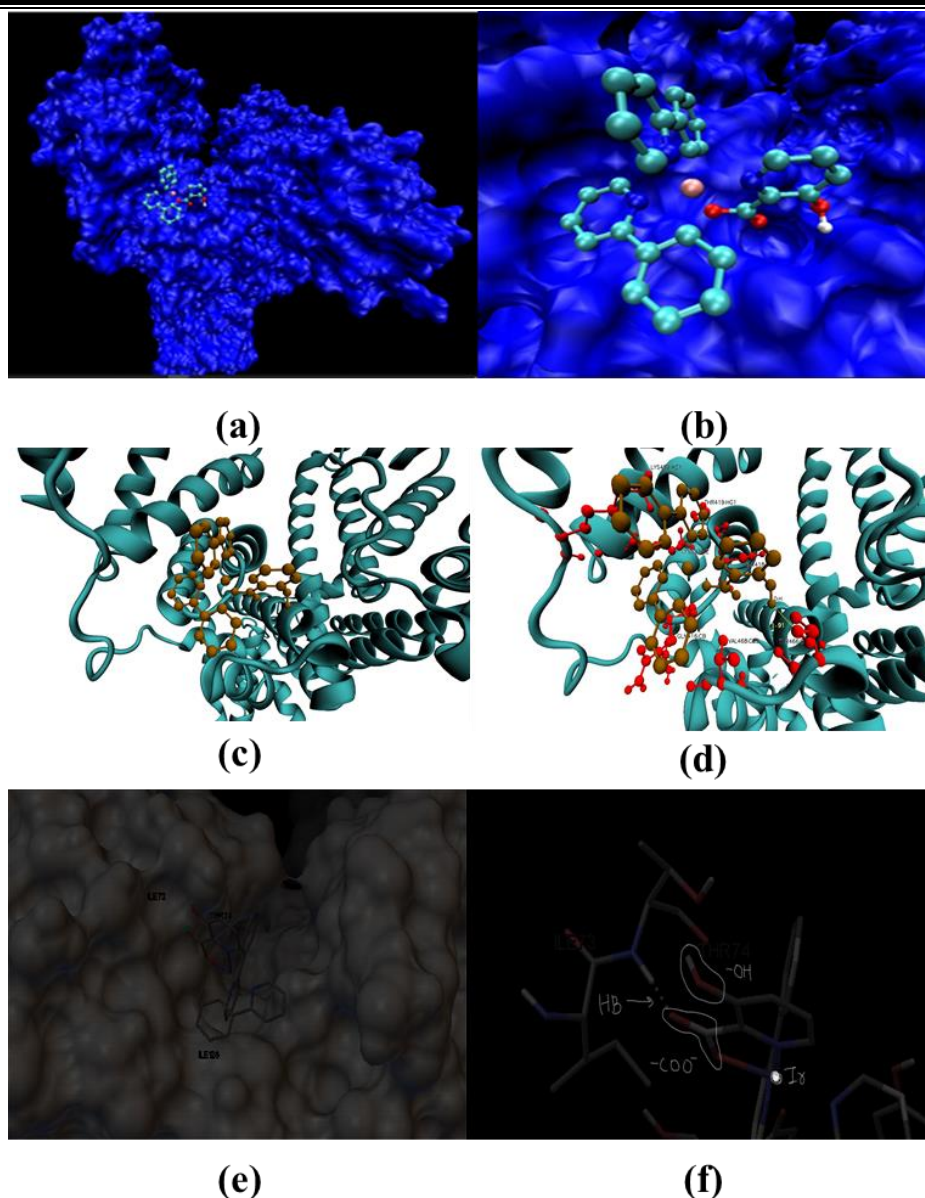


Fig 3.2.21 (a) Figure shows the B chain of the protein with the best binding pocket for the ligand which is located at the surface of the protein (b) A zoomed view of the best binding pocket is shown along with ligand (c) In the binding pocket, alpha helices are a binding partner of the ligand (d) Hydrogen bonding interactions of the ligand with the residues of the proteins is shown. The hydrogen bond is formed between Thr 466 side chain of B chain of protein and the ligand. In each case, the ligand is shown by ball and stick model (e) Binding of the complex within the hydrophobic pocket of pepsin, (f) Showing the absence of hydrogen bond with the hydroxyl group of 1 and also hydrogen bond formation with the carbonyl of 1 in pepsin.

3.2.4 Conclusion

The complete potentiality of an 'AIE' active heteroleptic Ir (III) picolinate complex (1) has been explored. The luminescence property of the complex has been used to detect different hydrogen bond donating solvents (HBD), hydrogen bond accepting solvents (HBA), weakly forming H-bonded solvents (WB) & non-bonded (NB) solvents. It was observed that the complex shows variable sensitivity to the bases depending on the strength of the basicity of bases and hence has been exploited as a pH sensor successfully. Moreover, it was used for the selective and sensitive detection of BSA, and the measured detection limit was 9.3 pM. The value is quite low compared with other reported probes molecules.[98-100] Hence, a single compound, 1 has been used in a multi-application. The mechanism for sensing has been discussed in detail. The study inspires to design the single potential entity which can be used up for multiple purposes.

3.3 Reference

- [1] M. A. C. Stuart, W. T. Huck, J. Genzer, M. Müller, C. Ober, M. Stamm, G. B. Sukhorukov, I. Szleifer, V. V. Tsukruk and M. Urban, *Nat. Mat.*, 2010, **9**, 101-113.
- [2] P. Theato, R. O'Reilly, Sumerlin, R. K. O'Reilly and T. H. Epps III, *Chem. Soc. Rev.*, 2013, **42**, 7055-7056.
- [3] R. Yerushalmi, A. Scherz, M. E. van der Boom and H.-B. Kraatz, *J. Mater. Chem.C.*, 2005, **15**, 4480-4487.
- [4] D. Roy, J. N. Cambre and B. S. Sumerlin, *Prog. Polym. Sci.*, 2010, **35**, 278-301.
- [5] M. Teng, X. Jia, X. Chen, Z. Ma and Y. Wei, *Chem. Comm.*, 2011, **47**, 6078-6080.
- [6] Y. Sagara, S. Yamane, M. Mitani, C. Weder and T. Kato, *Adv. Mater.*, 2016, **28**, 1073-1095.
- [7] Y. Liu, X. Tao, F. Wang, J. Shi, J. Sun, W. Yu, Y. Ren, D. Zou and M. Jiang, *J. Phys. Chem. C*, 2007, **111**, 6544-6549.
- [8] M. Zakerhamidi, A. Ghanadzadeh and M. Moghadam, *Spectrochim. Acta, Pt. A: Mol. Biomol. Spectrosc.*, 2011, **79**, 74-81.
- [9] P. Song and F.-C. Ma, *Int. Rev. Phys. Chem.*, 2013, **32**, 589-609.
- [10] G.-J. Zhao and K.-L. Han, *Acc. Chem. Res.*, 2012, **45**, 404-413.
- [11] R. Kumar, J. Schmidt and J. Skinner, *J. Chem. Phys.*, 2007, **126**, 05B611.
- [12] S. J. Grabowski, *Chem. Rev.*, 2011, **111**, 2597-2625.

- [13] E. Arunan, G. R. Desiraju, R. A. Klein, J. Sadlej, S. Scheiner, I. Alkorta, D. C. Clary, R. H. Crabtree, J. J. Dannenberg and P. Hobza, *Pure Appl Chem*, 2011, **83**, 1637-1641.
- [14] W. Chen, Y. Pan, J. Chen, F. Ye, S. H. Liu and J. Yin, *Chin. Chem. Lett.*, 2018, **29**, 1429-1435.
- [15] S. Mukherjee and P. Thilagar, *Angew. Chem. Int. Ed.*, 2019, **58**, 7922-7932.
- [16] J. Zhang, A. Li, H. Zou, J. Peng, J. Guo, W. Wu, H. Zhang, J. Zhang, X. Gu, W. Xu, S. Xu, S. H. Liu, A. Qin, J. W. Y. Lam and B. Z. Tang, *Mater. Horiz.*, 2020, **7**, 135-142.
- [17] P. Shi, X. Zhang, Y. Liu, Y. Duan, Y. Li, Z. Li and T. Han, *Mater. Lett.*, 2020, **263**, 127214.
- [18] P. Alam, C. Climent, P. Alemany and I. R. Laskar, *J. Photochem. Photobiol. C: Photochem. Rev.*, 2019, **41**, 100317.
- [19] M. Rajeshirke and N. Sekar, *Dyes Pigm.*, 2019, **163**, 675-683.
- [20] M. Ibarra-Rodriguez, B. M. Munoz-Flores and V. M. Jimenez-Perez, *J. Lumines.*, 2018, **198**, 342-349.
- [21] T. Lin, X. Su, K. Wang, M. Li, H. Guo, L. Liu, B. Zou, Y.-M. Zhang, Y. Liu and S. X.-A. Zhang, *Mater. Chem. Front.*, 2019, **3**, 1052-1061.
- [22] P. A. Hunt, C. R. Ashworth and R. P. Matthews, *Chem. Soc. Rev.*, 2015, **44**, 1257-1288.
- [23] Y. Xu, X. Song and C. Hao, *J. Lumines.*, 2019, **215**, 116733.
- [24] K. Girigoswami and N. Akhtar, *Int. J. Nano. Dimens.*, 2019, **10**, 1-17.
- [25] A. R. Chowdhury, P. Ghosh, B. G. Roy, S. K. Mukhopadhyay, N. C. Murmu and P. Banerjee, *Sens. Actuators B Chem.*, 2015, **220**, 347-355.
- [26] B. Naskar, R. Modak, Y. Sikdar, D. K. Maiti, A. Bauzá, A. Frontera, A. Katarkar, K. Chaudhuri and S. Goswami, *Sens. Actuators B Chem.*, 2017, **239**, 1194-1204.
- [27] M. Kumar, A. Kumar, M. S. H. Faizi, S. Kumar, M. K. Singh, S. K. Sahu, S. Kishor and R. P. John, *Sens. Actuators B Chem.*, 2018, **260**, 888-899.
- [28] T. Iijima, A. Momotake, Y. Shinohara, T. Sato, Y. Nishimura and T. Arai, *J. Phys. Chem. A*, 2010, **114**, 1603-1609.
- [29] M. Jadhao, O. R. Meitei, R. Joshi, H. Kumar, C. Das and S. K. Ghosh, *J. Photochem. Photobiol. A: Chem.*, 2016, **326**, 41-49.
- [30] V. S. Padalkar and S. Seki, *Chem. Soc. Rev.*, 2016, **45**, 169-202.
- [31] S. Liu, L. Zhang, P. Zhou, Y. Yang and W. Wu, *Sens. Actuators B Chem.*, 2018, **255**, 401-407.
- [32] L. Yan, T. Qing, R. Li, Z. Wang and Z. Qi, *Rsc. Adv.*, 2016, **6**, 63874-63879.
- [33] X.-F. Yang, H. Qi, L. Wang, Z. Su and G. Wang, *Talanta*, 2009, **80**, 92-97.

- [34] K. Li, Q. Feng, G. Niu, W. Zhang, Y. Li, M. Kang, K. Xu, J. He, H. Hou and B. Z. Tang, *ACS Sensors*, 2018, **3**, 920-928.
- [35] Y. Hong, J. W. Y. Lam and B. Z. Tang, *Chem. Soc. Rev.*, 2011, **40**, 5361-5388.
- [36] B. Rose and W. R. Loewenstein, *Nature*, 1975, **254**, 250-252.
- [37] H. J. Kim, C. H. Heo and H. M. Kim, *J. Am. Chem. Soc.*, 2013, **135**, 17969-17977.
- [38] Q. Rao, M. Yang, G. Liu, H. Zhang, H. Xu, J. Wang, Y. Tian, J. Yu, A. Wang and H. Zhou, *Dyes Pigm.*, 2019, **169**, 60-65.
- [39] V. V. Khramtsov, *Curr. Org. Chem.*, 2005, **9**, 909-923.
- [40] R. T. K. Kwok, C. W. T. Leung, J. W. Y. Lam and B. Z. Tang, *Chem. Soc. Rev.*, 2015, **44**, 4228-4238.
- [41] W.-G. Jia, H. Zhang, T. Zhang, D. Xie, S. Ling and E.-H. Sheng, *Organometallics*, 2016, **35**, 503-512.
- [42] A. D. Kulkarni and D. G. Truhlar, *Journal of Chemical Theory and Computation*, 2011, **7**, 2325-2332.
- [43] F. Weinhold and C. R. Landis, *Valency and bonding: a natural bond orbital donor-acceptor perspective*, Cambridge University Press, 2005.
- [44] A. M. Asiri, S. A. Khan, K. W. Tan and S. W. Ng, *Acta Crystallographica Section E*, 2010, **66**, o1826.
- [45] R. M. Issa, A. M. Khedr and H. Rizk, 2008, **55**, 875-884.
- [46] K.-C. Tang, M.-J. Chang, T.-Y. Lin, H.-A. Pan, T.-C. Fang, K.-Y. Chen, W.-Y. Hung, Y.-H. Hsu and P.-T. Chou, *J. Am. Chem. Soc.*, 2011, **133**, 17738-17745.
- [47] M. A. Rauf, S. Hisaindee and N. Saleh, *Rsc. Adv.*, 2015, **5**, 18097-18110.
- [48] F. Würthner, T. E. Kaiser and C. R. Saha-Möller, 2011, **50**, 3376-3410.
- [49] A.-E. Bejan and M.-D. Damaceanu, *J. Photochem. Photobiol. A: Chem.*, 2019, **378**, 24-37.
- [50] Y. Hu, T. Han, N. Yan, J. Liu, X. Liu, W.-X. Wang, J. W. Y. Lam and B. Z. Tang, *Adv. Funct. Mater.*, 2019, **29**, 1902240.
- [51] K. A. White, B. K. Grillo-Hill and D. L. Barber, *J. Cell Sci.*, 2017, **130**, 663-669.
- [52] H. Hou, Y. Zhao, C. Li, M. Wang, X. Xu and Y. Jin, *Scientific Reports*, 2017, **7**, 1759.
- [53] J. Wu, W. Liu, J. Ge, H. Zhang and P. Wang, *Chem. Soc. Rev.*, 2011, **40**, 3483-3495.
- [54] J. R. Lakowicz, *Topics in fluorescence spectroscopy: volume 4: probe design and chemical sensing*, Springer Science & Business Media, 1994.
- [55] J. Demas and B. DeGraff, in *Top. Fluoresc. Spectrosc.*, Springer, 2002, pp. 71-107.

- [56] J. Zhao, S. Ji, W. Wu, W. Wu, H. Guo, J. Sun, H. Sun, Y. Liu, Q. Li and L. Huang, *Rsc. Adv.*, 2012, **2**, 1712-1728.
- [57] I. Sánchez-Barragán, J. Costa-Fernández, A. Sanz-Medel, M. Valledor and J. Campo, *Trends in Analytical Chemistry*, 2006, **25**, 958-967.
- [58] H. Wu, T. Yang, Q. Zhao, J. Zhou, C. Li and F. Li, *Dalton Trans.*, 2011, **40**, 1969-1976.
- [59] V. Fernández-Moreira, F. L. Thorp-Greenwood and M. P. Coogan, *Chem. Comm.*, 2010, **46**, 186-202.
- [60] Y. You and S. Y. Park, *Dalton Trans.*, 2009, 1267-1282.
- [61] J. M. Fernandez-Hernandez, E. Longhi, R. Cysewski, F. Polo, H.-P. Josel and L. De Cola, *Anal. Chem.*, 2016, **88**, 4174-4178.
- [62] Y. You and W. Nam, *Chem. Soc. Rev.*, 2012, **41**, 7061-7084.
- [63] M. Lepeltier, F. Dumur, B. Graff, P. Xiao, D. Gigmes, J. Lalevée and C. R. Mayer, *Helv. Chim. Acta*, 2014, **97**, 939-956.
- [64] L. Flamigni, A. Barbieri, C. Sabatini, B. Ventura and F. Barigelletti, in *Photochemistry and Photophysics of Coordination Compounds II*, Springer, 2007, pp. 143-203.
- [65] Y.-J. Cho, S.-Y. Kim, M. Cho, K.-R. Wee, H.-J. Son, W.-S. Han, D. W. Cho and S. O. Kang, *Phys. Chem. Chem. Phys.*, 2016, **18**, 15162-15169.
- [66] X. Shang, D. Han, L. Zhao, L. Li and S. Lv, *Photochem. Photobiol. Sci.*, 2019, **18**, 1075-1080.
- [67] Q. Zhao, F. Li and C. Huang, *Chem. Soc. Rev.*, 2010, **39**, 3007-3030.
- [68] W. Liptay, in *Excited states*, Elsevier, 1974, vol. 1, pp. 129-229.
- [69] P. Rietsch, F. Witte, S. Sobottka, G. Germer, A. Becker, A. Güttler, B. Sarkar, B. Paulus, U. Resch-Genger and S. Eigler, *Angew. Chem. Int. Ed.*, 2019, **58**, 8235-8239.
- [70] H. Liu, S. Yan, R. Huang, Z. Gao, G. Wang, L. Ding and Y. Fang, *Chem. Eur. J.*, 2019, **25**, 16732-16739.
- [71] G. A. Jeffrey and W. Saenger, *Hydrogen bonding in biological structures*, Springer Science & Business Media, 2012.
- [72] J. Li, P. I. Djurovich, B. D. Alleyne, M. Yousufuddin, N. N. Ho, J. C. Thomas, J. C. Peters, R. Bau and M. E. Thompson, *Inorg. Chem.*, 2005, **44**, 1713-1727.
- [73] R. Gao, D. G. Ho, B. Hernandez, M. Selke, D. Murphy, P. I. Djurovich and M. E. Thompson, *J. Am. Chem. Soc.*, 2002, **124**, 14828-14829.
- [74] X. Wang, J. Li, M. E. Thompson and J. I. Zink, *J. Phys. Chem. A*, 2007, **111**, 3256-3262.

- [75] J. s. M. Fernández-Hernández, J. I. Beltrán, V. Lemauro, M.-D. Gálvez-López, C.-H. Chien, F. Polo, E. Orselli, R. Fröhlich, J. r. m. Cornil and L. De Cola, *Inorg. Chem.*, 2013, **52**, 1812-1824.
- [76] D. M. Manuta and A. J. Lees, *Inorg. Chem.*, 1986, **25**, 3212-3218.
- [77] A. Kando, Y. Hisamatsu, H. Ohwada, T. Itoh, S. Moromizato, M. Kohno and S. Aoki, *Inorg. Chem.*, 2015, **54**, 5342-5357.
- [78] P. Alam, G. Kaur, S. Chakraborty, A. R. Choudhury and I. R. Laskar, *Dalton Trans.*, 2015, **44**, 6581-6592.
- [79] Q. Jiang, M. Wang, L. Yang, H. Chen and L. Mao, *Anal. Chem.*, 2016, **88**, 10322-10327.
- [80] Q. Liu, B. Yin, T. Yang, Y. Yang, Z. Shen, P. Yao and F. Li, *J. Am. Chem. Soc.*, 2013, **135**, 5029-5037.
- [81] C. Huang, G. Ran, Y. Zhao, C. Wang and Q. Song, *Dalton Trans.*, 2018, **47**, 2330-2336.
- [82] A. Nakagawa, Y. Hisamatsu, S. Moromizato, M. Kohno and S. Aoki, *Inorg. Chem.*, 2014, **53**, 409-422.
- [83] Z. q. Chen, Z. q. Bian and C. h. Huang, *Adv. Mater.*, 2010, **22**, 1534-1539.
- [84] S. Yi, J.-H. Kim, Y.-J. Cho, J. Lee, T.-S. Choi, D. W. Cho, C. Pac, W.-S. Han, H.-J. Son and S. O. Kang, *Inorg. Chem.*, 2016, **55**, 3324-3331.
- [85] M. Mauro, G. De Paoli, M. Otter, D. Donghi, G. D'Alfonso and L. De Cola, *Dalton Trans.*, 2011, **40**, 12106-12116.
- [86] H. Sun, L. Yang, H. Yang, S. Liu, W. Xu, X. Liu, Z. Tu, H. Su, Q. Zhao and W. Huang, *Rsc. Adv.*, 2013, **3**, 8766-8776.
- [87] D. Sykes, A. J. Cankut, N. M. Ali, A. Stephenson, S. J. Spall, S. C. Parker, J. A. Weinstein and M. D. Ward, *Dalton Trans.*, 2014, **43**, 6414-6428.
- [88] P. Alam, G. Kaur, A. Sarmah, R. K. Roy, A. R. Choudhury and I. R. Laskar, *Organometallics*, 2015, **34**, 4480-4490.
- [89] E. Arunan, G. R. Desiraju, R. A. Klein, J. Sadlej, S. Scheiner, I. Alkorta, D. C. Clary, R. H. Crabtree, J. J. Dannenberg and P. Hobza, *Pure Appl. Chem.*, 2011, **83**, 1619-1636.
- [90] M. H. Abraham, R. J. Abraham, W. E. Acree Jr, A. E. Aliev, A. J. Leo and W. L. Whaley, *J. Org. Chem.*, 2014, **79**, 11075-11083.
- [91] H.-T. Kim, J. H. Seo, J. H. Ahn, M.-J. Baek, H.-D. Um, S. Lee, D.-H. Roh, J.-H. Yum, T. J. Shin, K. Seo and T.-H. Kwon, *ACS Energy Letters*, 2016, **1**, 991-999.
- [92] S. Yi, J.-H. Kim, Y.-J. Cho, J. Lee, T.-S. Choi, D. W. Cho, C. Pac, W.-S. Han, H.-J. Son and S. O. J. I. c. Kang, 2016, **55**, 3324-3331.
- [93] Y. You and S. Y. Park, *J. Am. Chem. Soc.*, 2005, **127**, 12438-12439.

- [94] J. R. Lakowicz, *Principles of fluorescence spectroscopy*, Springer Science & Business Media, 2013.
- [95] W. R. Bergmark, A. Davis, C. York, A. Macintosh and G. Jones, *J. Phys. Chem.*, 1990, **94**, 5020-5022.
- [96] M. Rosés, C. Ràfols, J. Ortega and E. Bosch, *Journal of the Chemical Society, Perkin Transactions 2*, 1995, 1607-1615.
- [97] M. Assael and S. Polimatidou, *Int. J. Thermophys.*, 1994, **15**, 95-107.
- [98] I. Manikandan, C.-H. Chang, C.-L. Chen, V. Sathish, W.-S. Li and M. Malathi, *Spectrochim. Acta, Pt. A: Mol. Biomol. Spectrosc.*, 2017, **182**, 58-66.
- [99] L. Wang, L. Yang and D. Cao, *Sens. Actuators, B. Chem.*, 2015, **221**, 155-166.
- [100] A. Jahanban-Esfahlan, A. Ostadrahimi, R. Jahanban-Esfahlan, L. Roufegarinejad, M. Tabibiazar and R. Amarowicz, *Int. J. Biol. Macromol.*, 2019, **138**, 602-617.

Chapter-4

Viscosity-triggered emission (VTE) Active Probes For Differentiating Cancer Cells

- * *Designed and synthesized a simple novel ultrasensitive viscosity triggered emission probe (TSSJ I) which showed very weak photoluminescence in a low-viscous environment.*
- * *In contrast, in the high viscous medium, the emission intensity of the (TSSJ I) probe was significantly enhanced*
- * *This work offers a potential and efficient probe for detection of altered intra-cellular viscosity or any fluctuations in the viscosity of normal, HUVECs and tumor cells was monitored which can be utilized for pre-diagnosis of diseases.*

Viscosity Triggered Emission Probe for Differentiation of Cancer Cells

4.1 INTRODUCTION

In a biological system, the viscosity plays a vital role on the microscopic level up to systematic level.[1] The increase in the viscosity harms the homeostasis, cellular proliferation, and tissue differentiation. Previous reports describe the intracellular viscosity of the single-cell, which strongly linked it to the cytoskeleton pattern within a cell type. [2, 3] The cytoskeleton is a dynamic network of three intermediate filaments, namely actin filaments (composed of F-actin, i.e., a polymerized form of G-actin molecules), microtubules (arranged of two isoforms of tubulin, i.e., α - and β -tubulins) and intermediate filaments.[2] The intracellular viscosity also governs metabolic regulation and cellular metabolism. A small change in the cellular volume leads to more substantial changes in the chemical activity in the cells. According to the growth condition, cells modify the surface area of the internal organelle, which relates to the organelle volume, which plays a vital role in the regulatory metabolism in cells.[4, 5] Therefore, identifying intracellular viscosity of a single cell could be more informative to fundamentally understand how such changes in intracellular viscosity influence changes in cellular behaviour by altering the function/interaction/localization of molecules in various physiological and pathological conditions. For many years, researchers have explored the mechanics and viscoelastic properties of different cells by employing various techniques such as AFM (atomic force microscopic), optical tweezers, magnetic tweezers, micropipette aspiration, magnetic twisting cytometry, microfluidic cytometry, microplate stretchers, microrheology, optical stretchers.[6, 7] Among this AFM is widely used to know the viscoelasticity because of high sensitivity, high resolution, high magnetic property, real-time imaging, concerning the other technique and also this technique is reliable for samples which are liquid state.[8] Using such technique Lee and co-workers studied the behaviour of cancerous cells such as regulation of matrix geometry and rigidity, cell proliferation, cytoskeletal reorganization.[9] Their study mainly focused on the cancerous cell microenvironment sensing the exogenous cues and quantification of cell-substrate interaction. Similarly, very recently, Xie et al. investigated the viscoelastic behaviour of cancer cell and healthy cells using the micropipette aspiration technique combined with the standard linear viscoelastic robust model.[10]

In recent years for microscopic level fluorescent technique is widely utilized because of quick response, high contrast and selectivity.[11] Molecular rotors are termed for a molecule which consists of two parts that can easily rotate relative to each other. In common the part which has the larger motion of inertia is stated as stationary (the stator) and the part with the smaller motion of inertia as the rotor. In the absence of a fixed mounting, the rotator and the stator both turn around the same axle. [12, 13] There is no clear rule for the classification of the molecular rotor. There are different criteria for the classification such as phase angle, rotation angle and molecular compounds.[14-16] These molecular rotors are triggered by the external stimuli such as light, viscosity, pressure, polarity and temperature.[17]

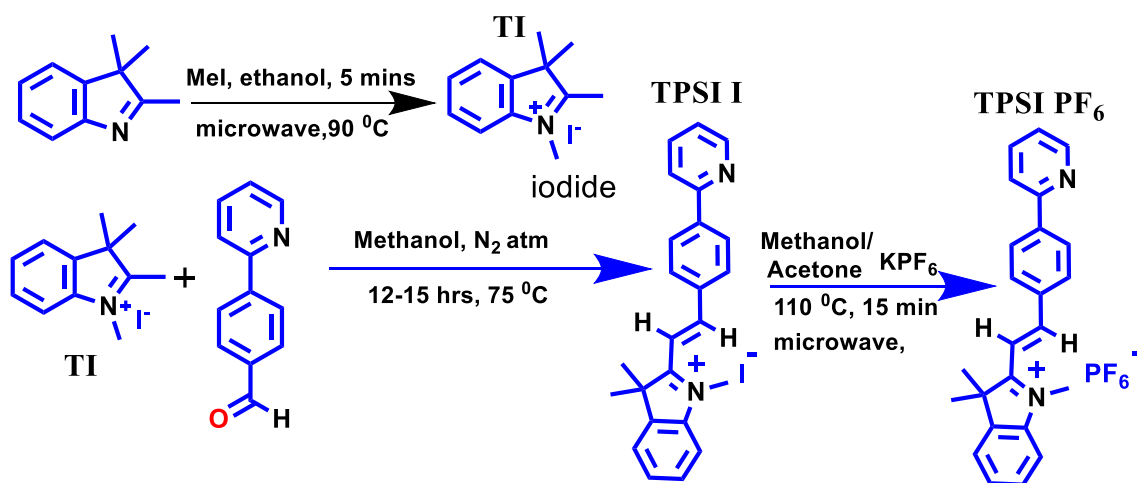
Fluorescent molecular rotors (FMRs) are widely used as viscosity probes in the various medium.[18-20] Fluorescent molecular rotors are the π conjugated molecules. Many Fluorescence Molecular Rotors (FMR) has been designed and synthesized to measure the intrinsic and extrinsic viscosity using the concept of Twisted Intramolecular Charge Transfer (TICT).[21] The emission property of these molecules depends on the rotating ability of the attached rotors. The competition of the off/on state of emission depends on the radiative vs non-radiative decays that can be regulated by the speed of rotation. Hence, the speed of the rotation of FMRs can be restricted with a variation of the viscosity in the surrounding medium.[1, 22] Push-pull, BODIPY, cyanine's, and porphyrin-based FMRs have been used as platforms in applications as viscosity sensors.[23] The high viscosity sensitivity of FMRs is essential for their ability as viscosity probes. Viscosity sensitivity is related to the fluorescence (FL) contrast (I/I_0) of FMRs (I = FL intensities in high viscosity media and I_0 = FL intensities in low-viscosity media).[24] The FL contrast strongly depends on the rotation ability of the molecular rotators. In addition to introducing rotators with high rotation ability, several scientists attempted to improve further by introducing multiple numbers of rotators into a single entity.[25] Among all kind of FMRs cyanine type of probes used as viscosity sensors due to their photophysical behaviours and ease to synthesis. The absorption and FL emission spectra of cyanine derivatives are tunable by controlling the length of the π -conjugated polymethine chain.[26] The Peng et al. reported a Penta methylene cyanine dye incorporating CHO group in the π -conjugated bridge. In the viscous medium, the CHO groups rotation hindered and the PL intensity increases.[27] In 2018 Fe et al., synthesized two-photon ratiometric fluorescent based on the cyanine molecules. The probes consist of two rotating sites to increase the sensitivity.[28] In 2020 sang Jun park synthesized a NIR

probe for mitochondrial sensing.[29] Although in these cases, there can improve the sensibility, the complicated synthetic approach making these techniques are less feasible.

Therefore, to increase the contrast and sensitivity, we have designed and synthesized a probe molecule (TPSI1 and TPSI2) in a simple route. Containing cyanine rotators, the molecule is easy to transform into *cis-trans* isomerism through vinyl bond by photoexcitation. The superior sensitivity of TPSI I towards viscosity has been successfully employed to differentiate the cancerous cells with the healthy cells by fluorescence technique. The combined effect of cyanine rotor and photoisomerization of the molecule leads to the enhanced sensitivity on sensing viscosity. The rotator consisting of phenyl pyridine as a linear shape shaft connected to the cyanine rotor through the double bond facilitates to enter inside the cell.

4.2 Results and Discussion

4.2.1 Synthesis

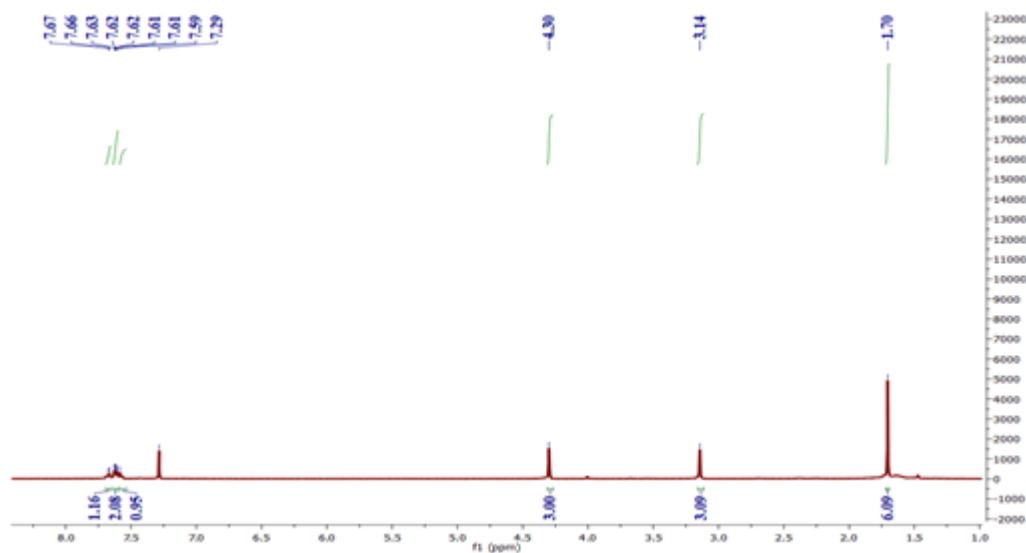


Scheme 4.1 Synthesis of 1,2,3,3-Tetramethyl-3H-indol-1-ium (Iodide) (TI), 3,3-Trimethyl-2-(4-(pyridine-2-yl) styryl)-3H-indol-1-ium (I) (TPSI I) & 1,3,3-trimethyl-2-(4-(pyridine-2-yl)styryl)-3H-indol-1-ium (PF₆⁻) (TPSI PF₆)

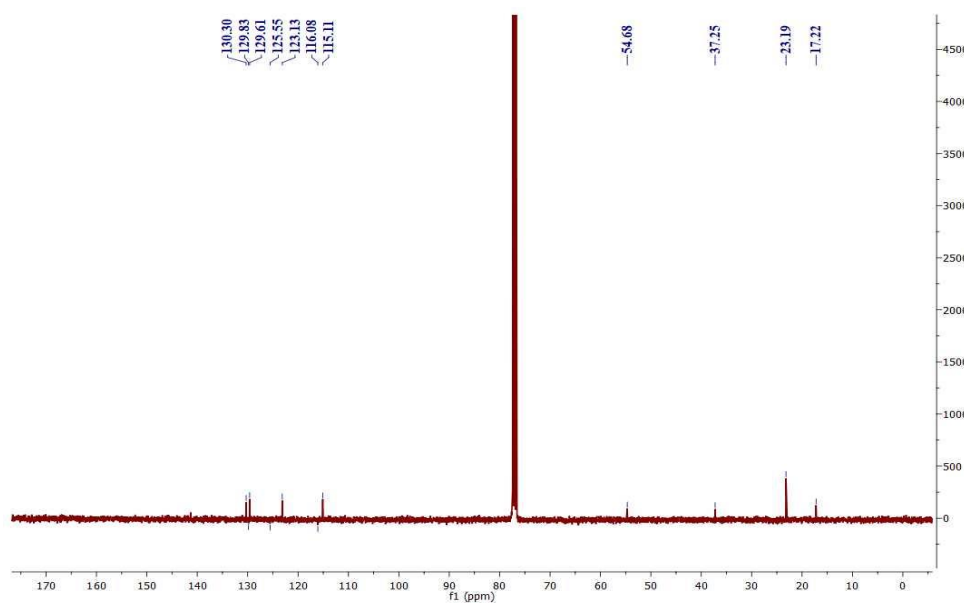
a) Synthesis of 1,2,3,3-Tetramethyl-3H-indol-1-ium (Iodide) (TI)

The methylation was carried out in a microwave oven by the known procedure.[30] In the microwave tube, the solution of 2,3,3-trimethyl-3H-indole in ethanol was taken. To the reaction mixture, 1 eq of methyl iodide was added and kept in the oven for five minutes at 90 °C. After completion, the reaction mixture was made to cool down to room temperature. A deep brown-red crystal was obtained. The crystals were washed with hexane and dried. It is

characterized by ^1H and ^{13}C NMR and well-matched with the reported data [31] ^1H NMR (400 MHz, CDCl_3) δ 7.70 – 7.64 m, 1H), 7.61 (ddd, $J = 7.3, 4.6, 2.7$ Hz, 2H), 7.57 (dd, $J = 6.0, 2.8$ Hz, 1H), 4.30 (s, 3H), 3.14 (s, 3H), 1.70 (s, 6H). ^{13}C NMR (101 MHz, CDCl_3) δ 141.30, 138.76, 130.30, 129.61, 123.13, 115.11, 54.68, 37.25, 23.19, 17.22 (Fig 4.1.1);



(a)

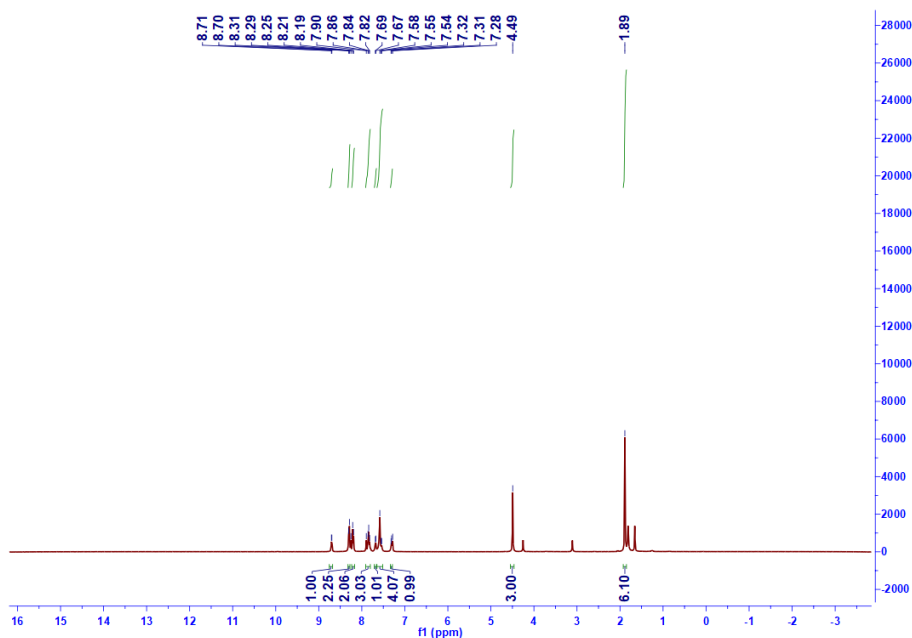


(b)

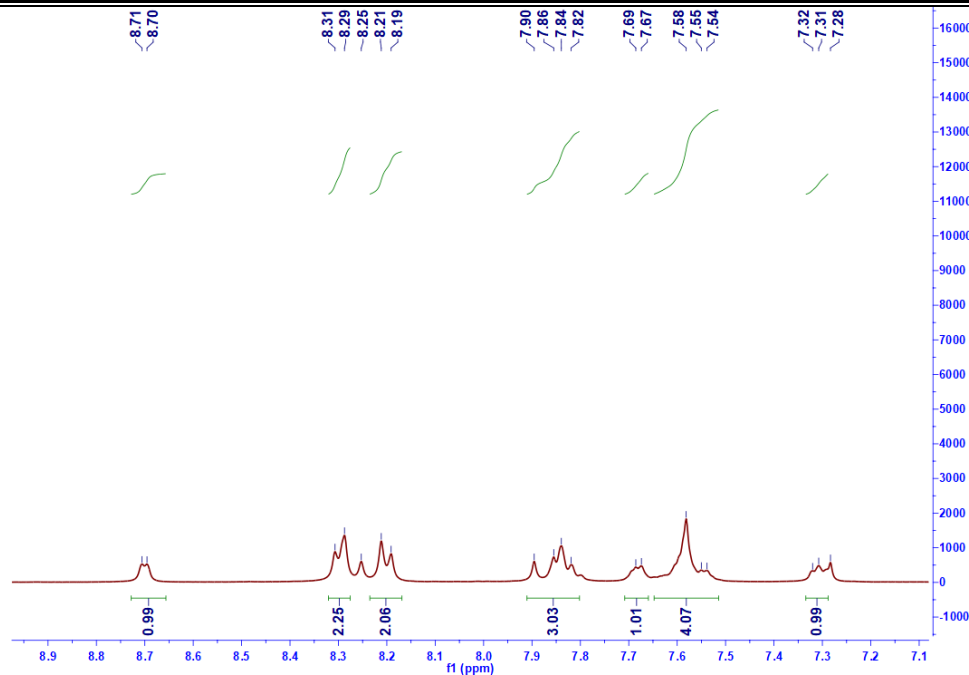
Figure 4.1.1 (a) ^1H NMR spectrum of TI (b) ^{13}C NMR spectrum of TI

b) Synthesis of 1,3,3-Trimethyl-2-(4-(pyridine-2-yl) styryl)-3H-indol-1-ium (I⁺) (TPSI I).

In a two neck round bottom flask, 1 eq of TI solution in dry methanol was taken and 1eq of 4-(pyridine-2-yl) benzaldehyde was added to it in continuous stirring. Reflux it for 12 to 14 hours. Monitor the reaction mixture by TLC. A deep red colour solution was visible. The solution was made to dry on rotavapor. The remaining residue was washed with hexane, then with different percentages of hexane and ethyl acetate like (1:2, 1:3, 1:4, and 1:5) to remove the unreacted part. The orange red colour powder was obtained. The single crystals were obtained by dissolving the powder in DCM and by layering in hexane (^1H NMR (400 MHz, CDCl_3) δ 8.70 (d, $J = 4.1$ Hz, 1H), 8.30 (d, $J = 7.8$ Hz, 2H), 8.20 (d, $J = 8.2$ Hz, 2H), 7.85 (dd, $J = 18.4, 12.1$ Hz, 3H), 7.68 (d, $J = 4.6$ Hz, 1H), 7.65 – 7.51 (m, 4H), 7.31 (d, $J = 5.0$ Hz, 1H), 4.49 (s, 3H), 1.89 (s, 6H). ^{13}C NMR (101 MHz, CDCl_3) δ 155.45, 153.82, 149.89, 144.26, 143.00, 141.50, 137.21, 134.09, 131.82, 130.17, 129.80, 129.53, 127.88, 123.32, 123.08, 122.60, 121.36, 115.11, 113.57, 52.68, 37.56, 26.90. HRMS of TPSI II given (Fig 4.1.2 a,b & Fig 4.1.3 a)) m/z -Found: (Exp-510.0819 $[\text{M}+\text{HCOO}]^+$, 524.1102 $[\text{M}+\text{CH}_3\text{COO}]^+$, 126.90 $[\text{I}-\text{M}]^+$ - Cal- $[m/z:- 465.0953]$. (Fig 4.1.3 b,c)

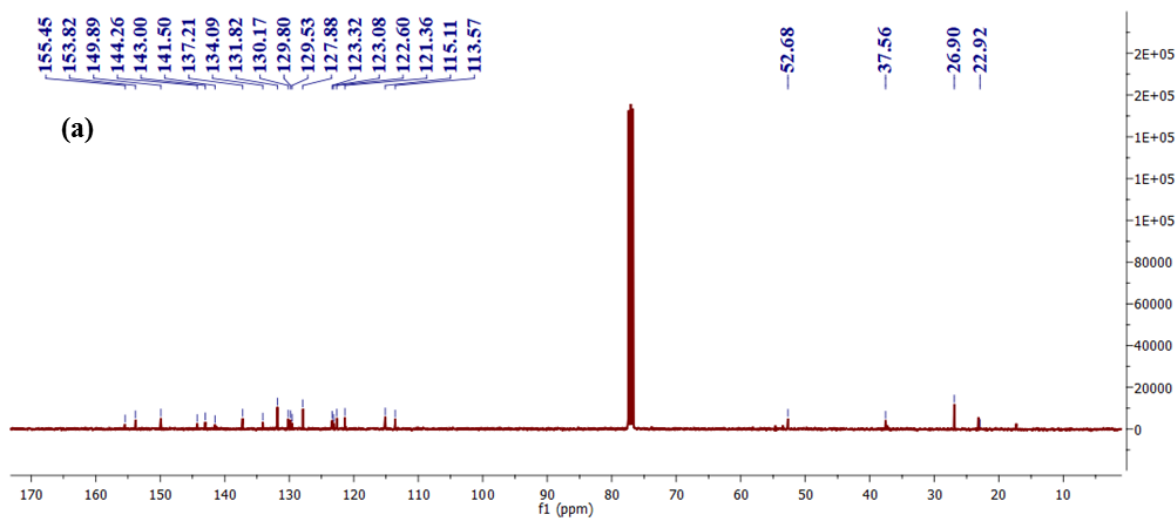


(a)



(b)

Figure 4.1.2 (a) ^1H NMR spectrum of TPSI I in CDCl_3 (b) It shows the zoomed aromatic region of ^1H NMR of TPSI I in CDCl_3



(a)

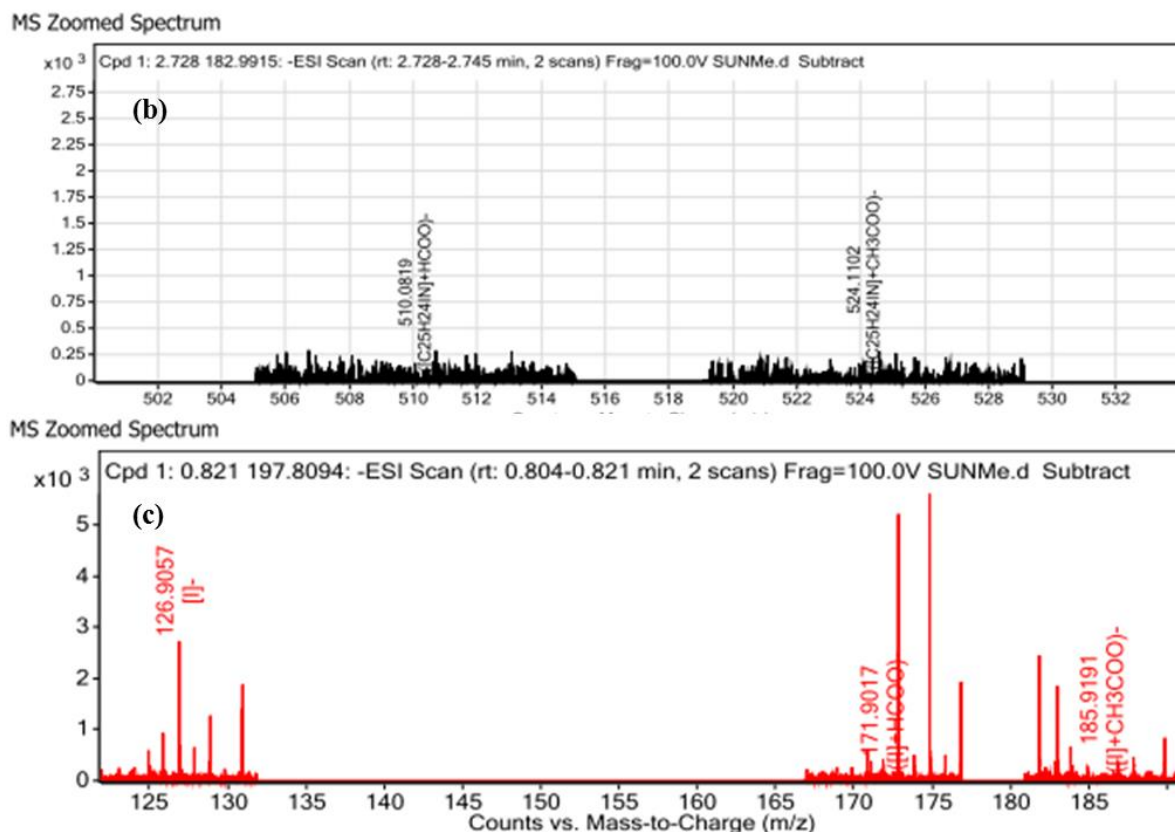


Figure 4.1.3(a) ^{13}C NMR spectrum of TPSI I (b) HRMS spectra of TPSI I (c) Counterion (I) of TPSI I

c) Synthesis of 1,3,3-trimethyl-2-(4-(pyridine-2-yl)styryl)-3H-indol-1-ium (PF_6^-) (TPSI PF_6^-) :-

In the microwave tube, TPSI I was dissolved in methanol/acetone. To this mixture, potassium hexafluorophosphate (5eq) was added, which was kept in a microwave oven for 15 min at 110°C under 600 rpm. After cooling it down at room temperature, a yellow colour crystal was separated. It was washed with hexane/ethyl acetate (1:3) mixture and dried it in the oven (80°C). The single crystals were obtained by dissolving the powder in DCM/hexane. The NMR shows the same peak as the TPSI I molecule. ^1H NMR (400 MHz, DMSO) δ 8.75 (s, 1H), 8.49 (d, $J = 16.3$ Hz, 1H), 8.35 (s, 4H), 8.18 (d, $J = 7.8$ Hz, 1H), 8.06 – 7.87 (m, 3H), 7.80 (d, $J = 16.4$ Hz, 1H), 7.66 (s, 2H), 7.46 (s, 1H), 4.20 (s, 3H), 1.83 (s, 5H). HRMS:- $m/z = 144.96$ [$\text{PF}_6^- \text{M}$] $^+$ (Fig 4.1.4 a,b)

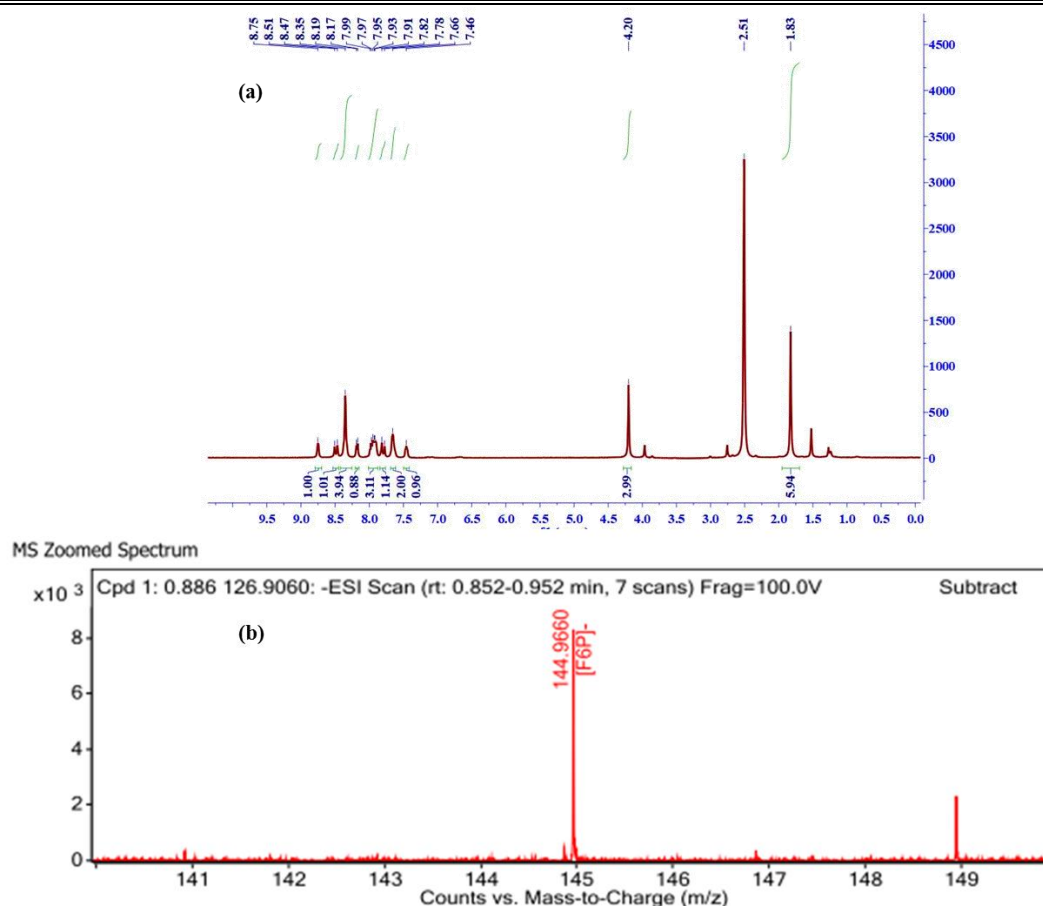


Figure 4.1.4 (a) ^1H NMR spectrum of TPSI PF_6 in DMSO (b) HRMS spectra of TPSI PF_6 counter ion.

4.2.2 Crystal Structure

Single crystals for both the compounds (TPSI I and TPSI PF_6) were produced by the diffusion method using the solvent mixture of DCM and hexane (1:9 ratio). Single-crystal X-ray diffraction data for the compounds were recorded on Bruker AXS KAPPA APEX-II CCD and solved using, and the crystal structures were solved by using SHELXS2013 (details are given in chapter -2 (experiments and methods). In both cases, the crystal structure and space group are triclinic and $P\bar{1}$, respectively. The ORTEP diagram of both compounds is given in in (Fig. 4.1.5 a, b). From the crystal structures (Figure 4.1.5 a, b), both the hydrogens present on double bonds ($-\text{HC}_{12}=\text{C}_{13}\text{H}-$) are *trans* to each other, leading a stable configuration for both TPSI I and TPSI PF_6 (an arrow in the ORTEP diagram indicating hydrogens). In TPSI I, one can see there are two molecules opposite to each other (head to tail), has two different dihedral angle (angle between the plane passing through the phenyl pyridine and cyanine group) 24.26 and 39.04 degrees (Fig 4.1.5 c, d) while TPSI PF_6 has one dihedral angle which is 36.08° (Fig 4.1.5 e)

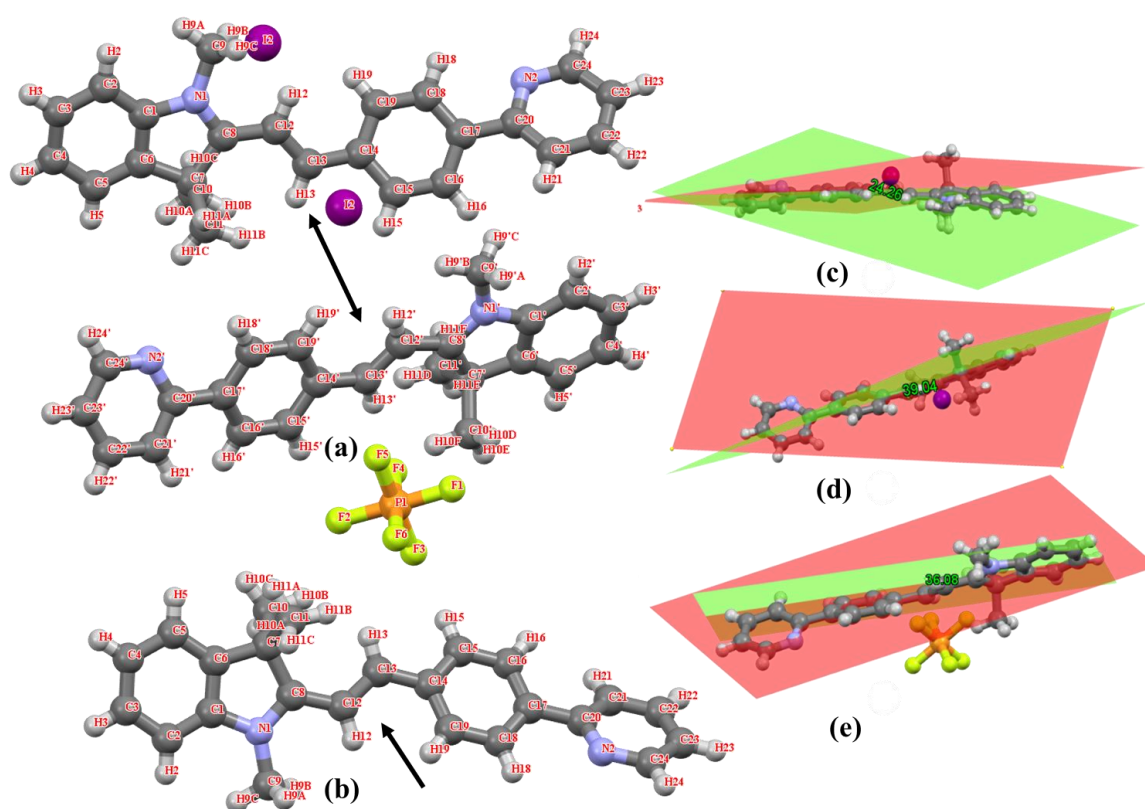


Figure 4.1.5 ORTEP diagram of a) TPSI I; b) TPSI PF₆. It shows the dihedral angle between the plane passing through the cyanine ring and phenyl pyridine ring (c, d) TPSI I and (e) TPSI PF₆ (Green colour plane = Plane passing through cyanine ring and red colour plane = Plane passing through the phenyl pyridine.).

4.2.3 Photophysical property studies

Similar to the reported cyanine analogues[1], TPSI I and TPSI PF₆ at room temperature in methanol exhibit absorption peaks at λ_{abs} , 399 nm and 403 nm, respectively for TPSI I and TPSI PF₆ (Fig 4.1.6 a) similar to those reported for other cyanine analogues[32], which may be assigned to the of π - π^* transition.[32, 33] In the solid phase, TPSI PF₆ shows strong emission ($\lambda_{\text{ex}} = 368\text{nm}$; $\lambda_{\text{em}} = 580\text{ nm}$), while TPSI I exhibits very weak emission ($\lambda_{\text{ex}} = 368\text{nm}$, $\lambda_{\text{em}} = 500\text{ nm}$) (Fig 4.1.6 b). It is well established that the cyanine type of probes is sensitive to certain external stimuli such as viscosity and polarity. [34] Both TPSI I and TPSI PF₆ tested for viscosity sensing experiments.

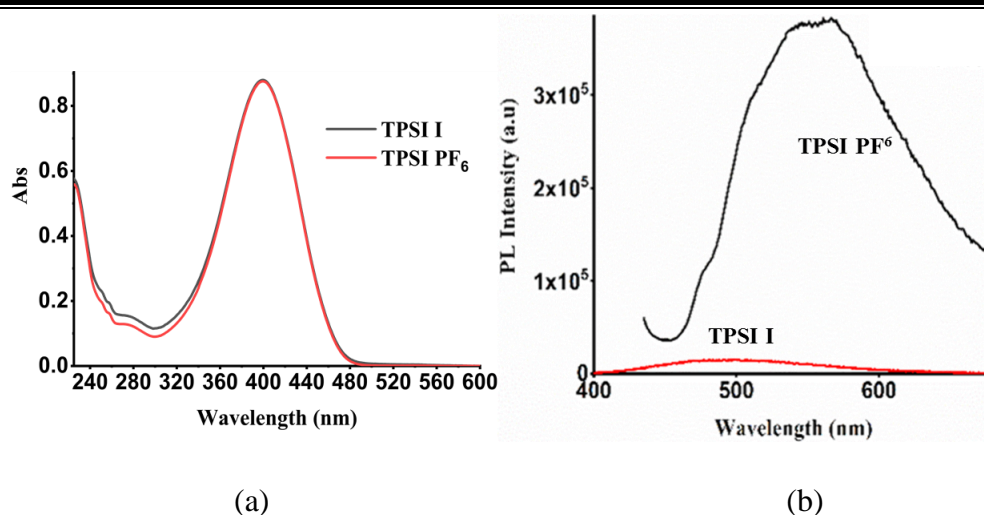


Figure 4.1.6 (a) Absorption spectra of TPSI I and TPSI PF₆ in methanol (1×10^{-5} M) (b) Emission spectra of TPSI I and TPSI PF₆ in solid-state.

4.2.3.1 Viscosity sensing.

The photoluminescence (PL) spectra of TPSI I was recorded in the presence of various solvents with increasing viscosity (0.521 cP in DCM to 190 cP in PEG600, cP = centipoise) and polarity (polarity index of solvents are according to literature value [35, 36]) (Fig 4.1.7).

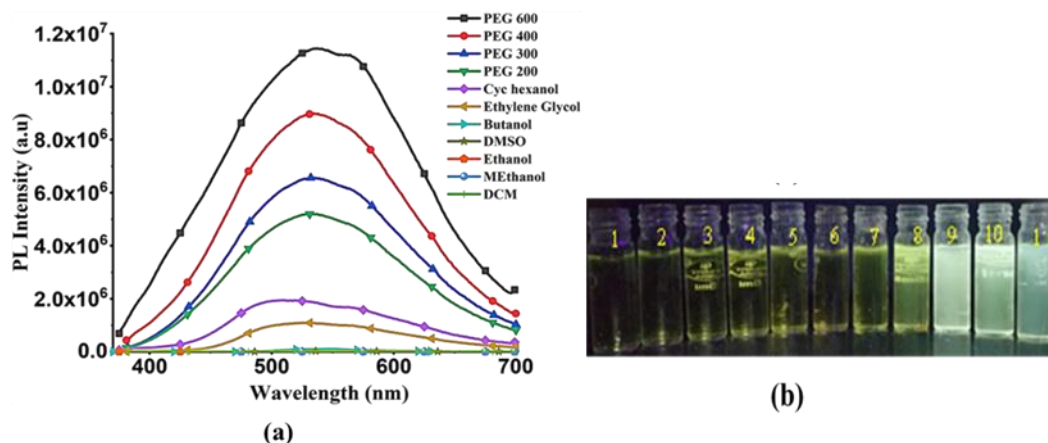


Figure 4.1.7 (a) Emission Spectra of TPSI I (0.4 mM) in the presence of the solvent with increasing viscosity, (b) Image of TPSI I was recorded under UV-Lamp ($\lambda_{\max}=365$ nm) (1 = DCM, 2 = Methanol, 3 = Ethanol, 4 = DMSO, 5 = Butanol, 6 = Ethylene glycol, 7= Cyclohexanol, 8 = PEG 200, 9 = PEG 300, 10 = PEG 400, 11= PEG 600) .

From the emission spectra, it is observed that emission intensity increasing drastically with the variation of viscosity (~ 255 times with increasing viscosity from 0.521 cP to 190 cP $\lambda_{\max} = 540$ nm). Thus, the experiment describes that the TPSI I is highly sensitive to the viscosity of the medium. The dependency of PL intensity of TPSI I and TPSI PF₆ on viscosity was

compared by recording the PL spectra with a gradual increment of the viscosity through the addition of PEG400 into the solution containing TPSI I in methanol (10^{-5} M) (Fig. 4.1.8)

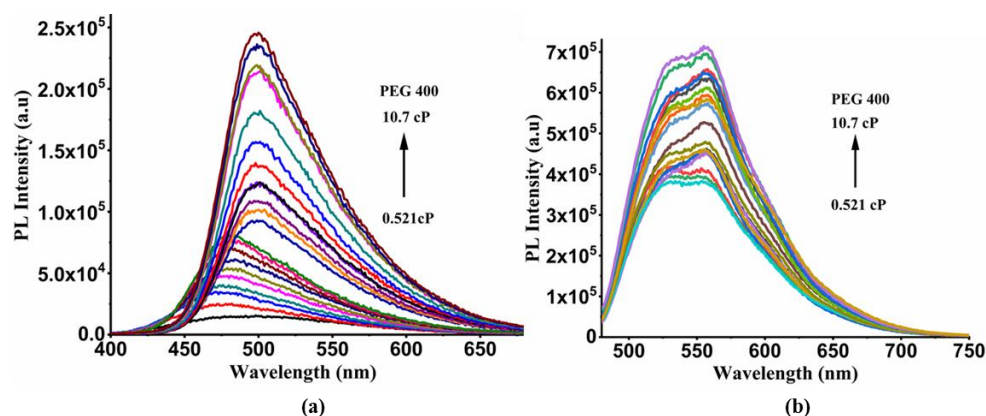


Figure 4.1.8 Emission spectra of (a) TPSI I and (b) TPSI PF₆ in methanol ($C = 1 \cdot 10^{-5}$ M) with gradually increasing the viscosity by adding PEG 400

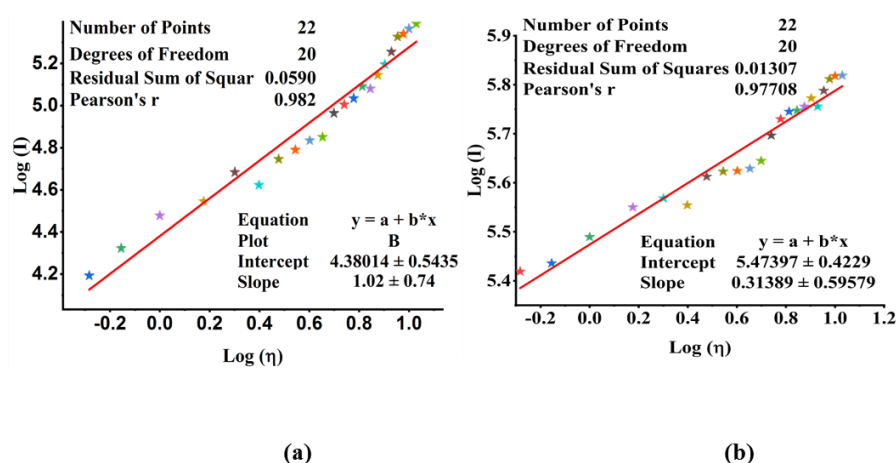


Figure 4.1.9 Linear fitting between $\log(I)$ ($I = \text{PL Intensity of TPSI I, TPSI PF}_6$; $c = 10^{-5}$ M, in methanol) and $\log(\eta)$ ($\eta = \text{viscosity of solvent}$), TPSI I = 1.02, $R^2 = 0.982$, TPSI PF₆ = 0.31, $R^2 = 0.977$

Moreover, the relation between the emissions of TPSI I and TPSI PF₆ with a viscosity of the solvent described using the Forester Hoffmann equation. The equation, $\log I = C + x \log \eta$ [37], in which η is the viscosity of the solvents, I is the emission intensity of the probes (here TPSI I and TPSI PF₆), C is temperature-dependent constant, and x is the viscosity sensitivity of the probes (here TPSI I and TPSI PF₆). By plotting the graph between $\log I$ vs $\log \eta$ for TPSI I and TPSI PF₆, we have determined the linear fitting values, $R^2 = 0.982$, $R^2 = 0.977$ for TPSI I and TPSI PF₆, respectively (Figure 4.1.9). The determined 'x' value for both the probes TPSI I and TPSI PF₆ are 1.02 and 0.31. respectively. To the best of our knowledge, the obtained

value of 'x' of TPSI I is 1.02, which is the highest out of the other reported probes for viscosity,[38-42] so far. The greater the value of x, the higher is the sensitivity of the probes towards the viscosity. The higher value of x obtained for TPSI I supports the high sensitivity to the viscous medium.

4.2.3.2 Photoinduced Isomerization in Solution State

In the probe molecule along with the rotation of the rotating units, the existing double bond that connects the cyanine ring and phenyl pyridine may be playing a major role in the increased sensitivity of TPSI I in a viscous medium. The photoinduced isomerization of the stilbene types of probes has been studied thoroughly for a decade.[43] These facts led us to predict the exceptionally high sensitivity of TPSI I compared to TPSI PF₆, and others on the viscosity might be associated with photoinduced *cis-trans* isomerization process.

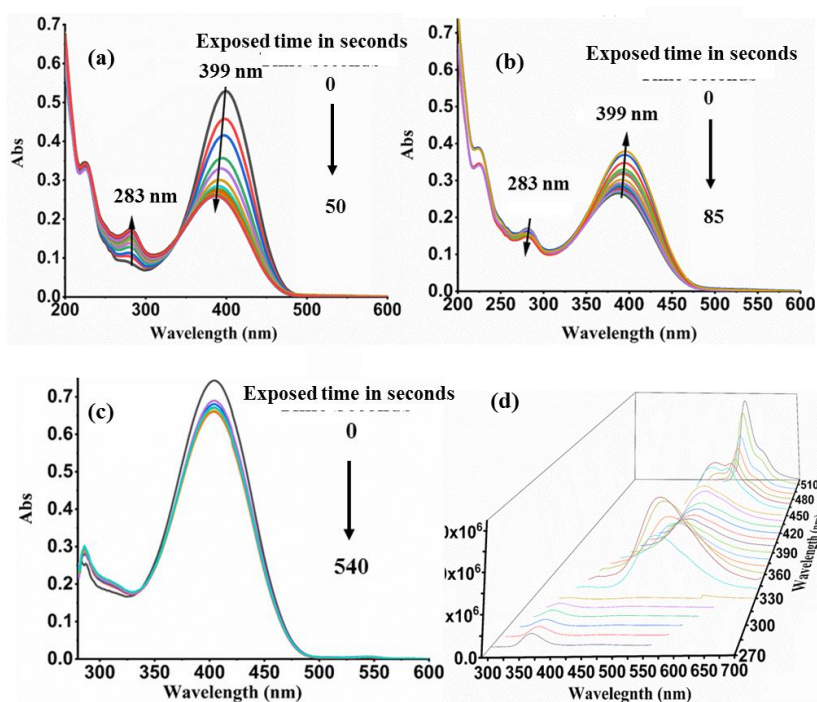


Figure 4.1.10 UV-Visible absorption spectra of TPSI I in methanol (1×10^{-5} M) a) recorded the spectra by irradiation with UV-Visible lamp ($\lambda_{exc} = 365$ nm); (b) absorption spectra were recorded by switching off UV-the lamp (c) UV-Visible absorption spectra of TPSI PF₆ in methanol (1×10^{-5} M) upon irradiation with a UV lamp ($\lambda_{ex} = 365$ nm) at different time intervals (d) Emission spectra of TPSI I (in methanol, $c = 1 \times 10^{-5}$ M) at different excitation wavelengths ($\lambda_{ext} = 330 - 520$ nm) (x-axis is the wavelength for the recorded emission, right-hand side y-axis is different excitation wavelength at which the emissions are recorded and left side z-axis is the photoluminescence intensity) (Approximately two minutes were taken to operate two consecutive reading)

To prove the fact, several controlled experiments were conducted on both the probes. The following experiment was carried out in two parts. Firstly, TPSI I and TPSI PF₆ were irradiated with a UV-Vis lamp ($\lambda_{\text{exc}} = 365 \text{ nm}$) at increasing time interval, and after each excitation, the UV-Vis absorption spectra were recorded. In the case of TPSI I, it was observed that the intensity of the long-wavelength absorption peak ($\lambda_{\text{abs}}, 399 \text{ nm}$) decreases gradually with a slight blue shift upon exposure to UV light ($\lambda_{\text{exc}}, 365\text{nm}$; 0-50 sec), and in parallel, the absorption of the new peak ($\lambda_{\text{abs}}, 283 \text{ nm}$) gradually increases (Fig. 4.1.10 a). In TPSI PF₆, there have no significant changes observed in the absorption peak upon exposure of the UV light even up to ten minutes (Fig. 4.1.10 c). Secondly, to check the weather the peaks are reverted, the absorption spectra of TPSI I (exposed compound by UV ray) were recorded at a different time interval (0-85 sec) (Fig. 4.1.10 b). It was observed that the peak at 281 nm was gradually decreased along with a broad absorption peak at 398nm increases with time. Such observation supports in favour of the *cis-trans* isomerization. To understand the change of emission property in TPSI I of the photo isomerized species, the emission spectra of TPSI I in methanol was recorded by gradual changing the excitation wavelength from 280 nm to 520 nm. From the spectra, it is observed that at the shorter wavelength, the intensity of the original emission wavelength (353 nm) is gradually decreasing with increasing excitation wavelength. A red-shifted emission peak around (500 nm) starts to appear with exciting at 330 nm for which the intensity increases with excitation up to 350 nm. The peak intensity gradually decreases with further increasing excitation wavelength, and a new emission peak at 566 nm starts to appear with exciting at 460 nm. The intensity of this new peak is gradually increasing until the excitation wavelength is increased to 520 nm (Fig. 4.1.10 d). These observed emissions at different excitation wavelengths may correspond to the transformation of *cis* to *trans* photoisomerization. The above two experiments support the presence of the photoinduced isomerization process that happens in TPSI I.

The reversibility test also carried out by gradually decreasing the viscosity of the medium containing TPSI I by increasing the volume of the methanol in the viscous solution. The emission intensity found to decrease gradually (Fig. 4.1.11). The experiment supports that the rotation of the rotating units (cyanine/ pyridyl) might be responsible for the observed enhanced PL intensity.

4.2.3.3 Solid State Photoinduced Isomerization

An UV-Vis absorption-based experiment was performed to support the fact that the molecules are in motion when photoexcited in the solid-state. A solid powder of TPSI I was

irradiated by UV lamp (λ_{ex} , 250 nm) at a certain interval then recorded the UV-Vis absorption spectrum. Similarly, the process was continued until 30 minutes. The characteristic absorption peaks of the compounds (λ_{abs} , 287nm; 409nm) were observed to change systematically with increasing time interval. In this case, the original absorption peak at 287 nm was increasing while the peak at 409 nm was gradually decreasing with the observation of isosbestic points at 360 nm and 450 nm (Fig. 4.1.12 a) The peak reaches to maximum absorption within 30 minutes of initiating excitation and then reverted slowly to the original absorption (Fig. 4.1.12 b). Also, it is observed the increase the absorption peak intensity at 409 nm with changing the excitation wavelength to 365 nm (Fig 4.1.12 c, d).

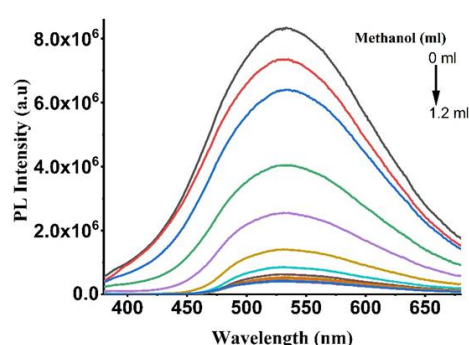


Figure 4.1.11 (a) Emission spectra of TPSI I (1×10^{-5} M) with gradually increasing the methanol in PEG400 solution; the PL intensity is gradually decreasing with increasing concentration of methanol into PEG

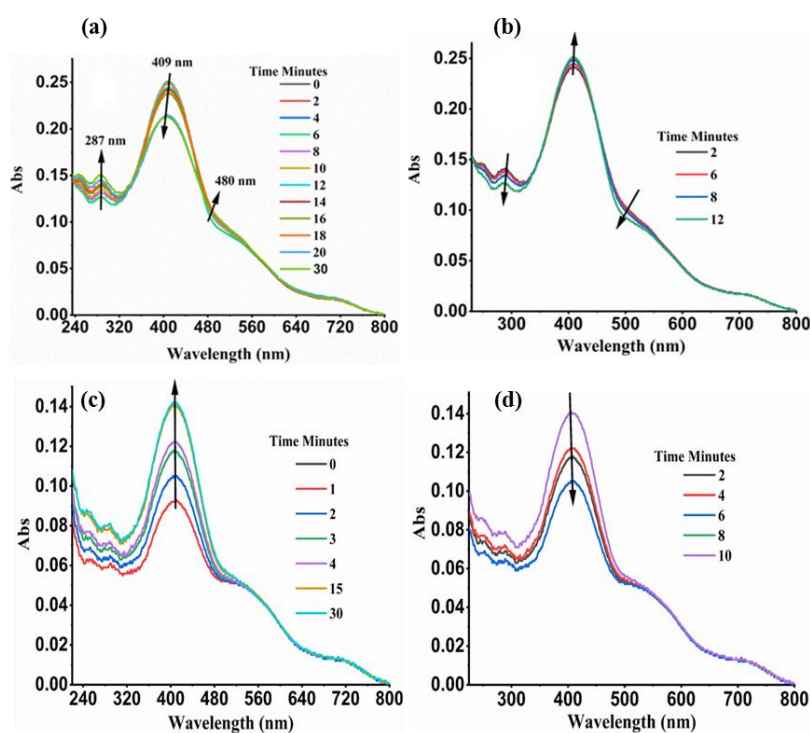


Figure 4.1.12 (a) UV–VIS spectral changes of TPSI I in solid-state (powder form) upon irradiation at 250 nm as a function of time (b) recoverable without irradiation in the dark for several minutes UV-Vis spectra of TPSI I after expt. (a); (c) on irradiation at 365 nm as a function of time of TPSI I (d) recorded spectra by switching off UV-the lamp after expt. (Approximately two minutes were taken to operate two consecutive reading)

On performing the similar absorption study of TPSI PF₆, there was no such change observed irrespective to the excitation wavelengths (Fig 4.1.13 a, b). The experiment supports that TPSI I gets unstable under photoexcitation and constantly be transformed into the photoinduced isomerized product or the flexible units in the molecular framework undergo movement. The absence of such phenomena in TPSI PF₆ rationalizing the non-emissive nature of TPSI I and the emissive nature of TPSI PF₆ in the solid-state.

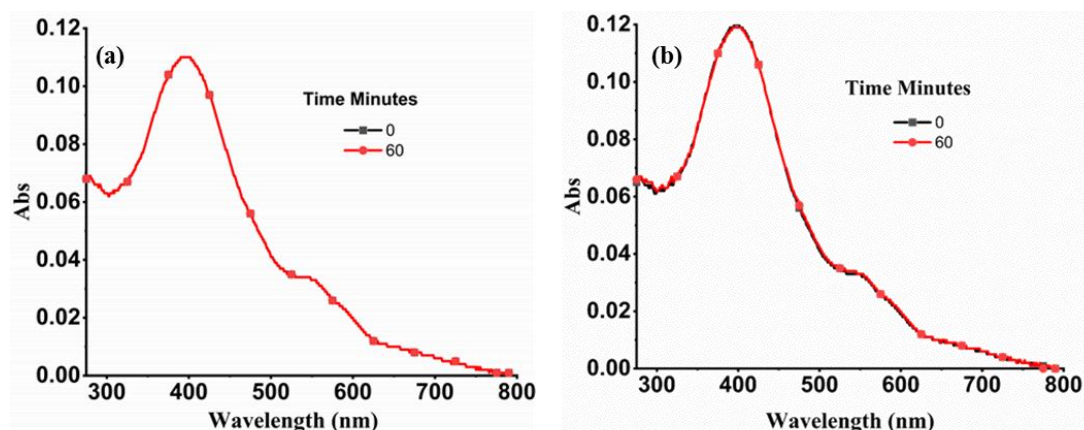
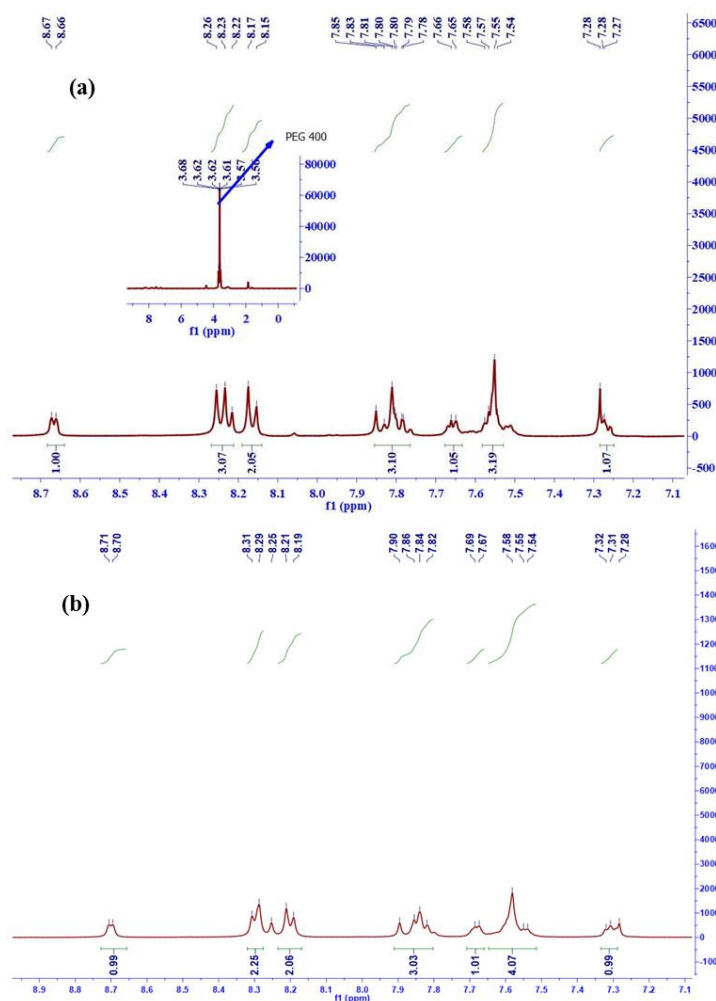


Figure 4.1.13 (a) UV–Vis spectral changes of TPSI PF₆ in the solid-state (powder form) upon irradiation at 250 nm as a function of time (b) UV-Vis spectra of TPSI PF₆ on irradiation at 365 nm as a function of time.

4.2.3.4 Mechanism for Photoisomerization

According to the recent report, the cyanine type of chromophore act as a rotor in the compound to which it is attached.[44] Hence, it is assumed that the attached cyanine in TPSI I and TPSI PF₆ also acting as a rotating unit. The ¹H NMR spectra of TPSI I with PEG400 was recorded to understand whether any sort of interaction (hydrogen bonding) playing between PEG400 and probe molecule, apart from viscosity effect. It is observed that there is only a slight change of chemical shifts of all the ¹H NMR peaks from deshielded to shielded region, which indicates that there is no specific interaction between OH of PEG and TPSI I, (Fig 4.1.14 a, b). Secondly, it is investigated the X-ray crystal structures of both compounds

to get further enlighten on the significant difference in viscosity sensing from these compounds. The unit cell of TPSI I consisting of four molecules that form a square type shape, with four iodides each one takes each corner (a single plane could be drawn that passes through all the four iodides (Fig 4.1.14 c). The four molecules present in the unit cell are oriented in such a way that these form a cage type of structure with a volume of $\sim 46.6 \text{ \AA}^3$ (Fig 4.1.14 d). In the unit cell, the distance between the two centroids (C1-C2) is 3.99 \AA , (Fig 4.1.15 a) which is beyond the range of π - π interaction ($3.3 - 3.9 \text{ \AA}$). Each iodide is involved in two interactions in the unit cell, I1 with H15 (3.051 \AA) & H11B (3.083 \AA), I2, I2' with H19' (3.008) & H9'B (3.140), and I1' with H11B' (3.284 \AA) & H15' (3.110 \AA) (Fig 4.1.143 e) Other than the iodide interaction, it has four more short contacts between two side by side molecules in the unit cell the nitrogen of phenyl pyridine (N2) with hydrogen (H2') of phenyl in cyanine ring (N2---H2', 2.680 \AA), C23 of pyridine ring with (H21') of the pyridine ring of the second molecule (C23---H21'-, 2.734 \AA), C18 of phenyl ring with C9 of cyanine ring (C18---C9-, 3.361 \AA) and hydrogen- hydrogen interaction between dimethyl group on cyanine ring (H10E-----H10B- 2.282 \AA) (Fig. 4.1.15 b).



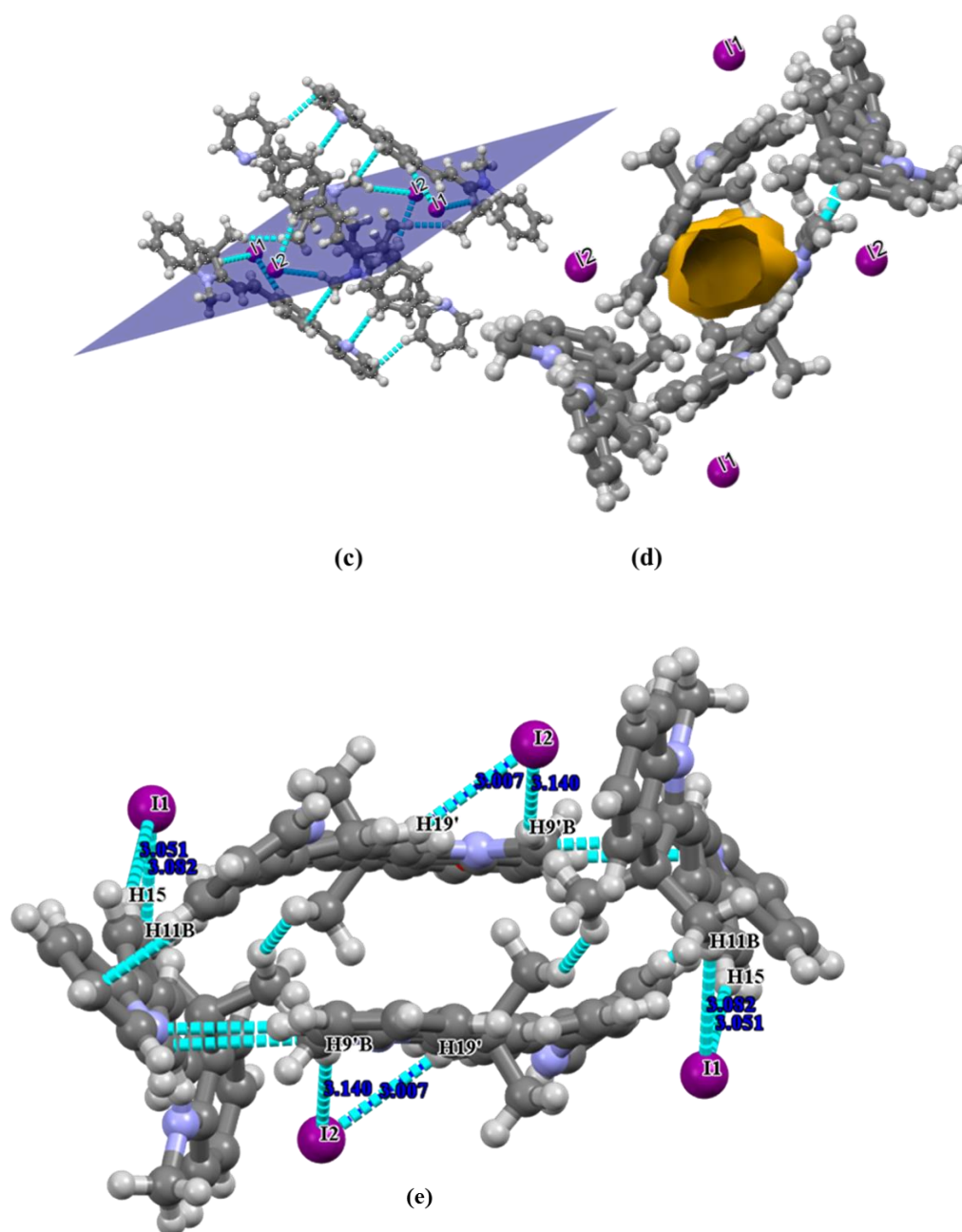


Figure 4.1.14 (a) ^1H NMR of TPSI I in presence of 1 equivalent of PEG 400; (b) ^1H NMR of TPSI I without PEG-400 (c) Unit cell of TPSI I consisting of four molecules and four iodides passing through one plane (d) It shows the cage type arrangement of four molecules with a space represented by yellow colour (e) It shows the measured distance between the Iodide and molecules in the packing unit cell of TPSI I

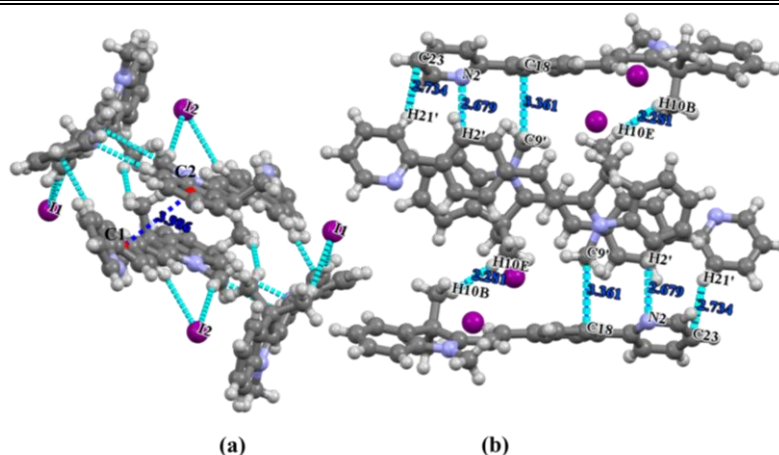


Figure 4.1.15 (a) Unit Cell of TPSI I shows the distance between the two centroids (C1-C2) is 3.99 Å (b) Rest of the short contacts between the molecules, apart from short-contacts containing iodide (N2---H2' - 2.680 Å, C23---H21'-2.734 Å, C18---C9-3.361 Å and H10E---H10B-2.282 Å)

On the other hand, the TPSI PF₆ has only two molecules present in the unit cell where no cage/ or void is observed. In this unit cell, each PF₆⁻ is involved in three interactions in the form of hydrogen bonding which are, F3---H15 (2.462 Å), F3---H13(2.596 Å) and F2---H10B (2.598Å) (Fig. 4.1.16 a). In TPSI I, each iodide forms two hydrogen bonds (one with phenyl hydrogen and the other with substituted N-methyl H of cyanine), whereas, in TPSI PF₆, potassium hexafluoride forms three hydrogen bonds (the two interactions are similar with the iodide in TPSI I and the third one with ethylene H) (Fig 4.1.16 b, c). The analysis of the observation of different packing's (*vide infra*) with the same cationic entity with variable counter ions, *i.e.*, PF₆⁻ and I⁻ is attempted.

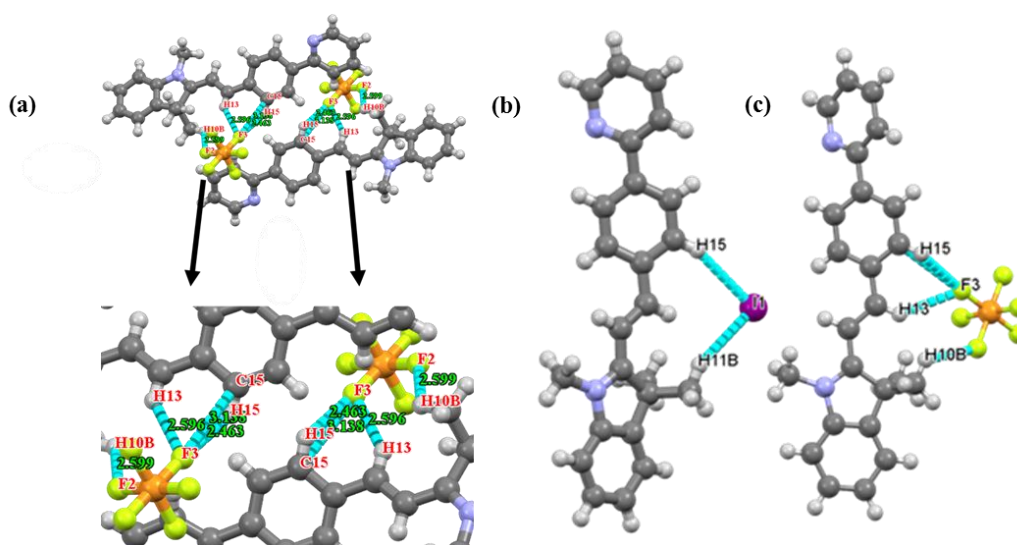
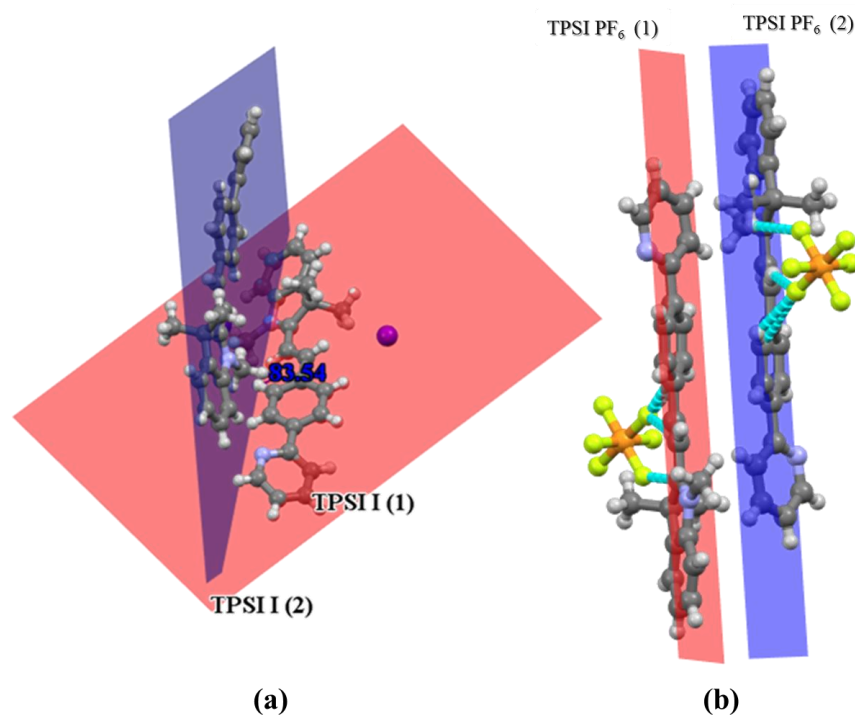


Figure 4.1.16 (a) It shows the measured distance between PF_6^- and the molecules in the unit cell of TPSI PF_6 (b) It shows the distance of I^- (I1) (iodide) with H15 and H11B in TPSI I (c) distance of PF_6^- with H15, H13 and H10B in TPSI PF_6 .

In TPSI I, the four molecules in the unit cell form square-shaped cage while the two molecules in TPSI PF_6 present in the unit cell are aligned in anti-parallel orientation (Figure 4.1.13 d & 4.1.17 b). The distance between the neighbouring molecules (centroid-centroid) in TPSI I (lying with an angle $\sim 84^\circ$, Fig 4.1.17 a) is $\sim 6\text{\AA}$ while in TPSI PF_6 the distance between the two molecules for the other compound is $\sim 8\text{\AA}$ [Fig. 4.1.17 (c,d)]. Hence, the role of the counterions would be important in explaining such observations. The bulkiness of PF_6^- , in comparison of iodide, would be responsible for keeping the molecules in TPSI PF_6 apart from each other. In the case of TPSI PF_6 , the smaller size of iodide makes it possible to have a relatively closer approach of the two neighbouring molecules. In this case, the interaction of the pyridyl aromatic of one molecule with the substituted cyanine in the second molecule drives the two neighbouring molecules to stay in close ($\text{N2} \cdots \text{H2}' - 2.680\text{\AA}$). The other end of the second molecule (pyridyl) interacts with the cyanine end of the third molecule and so on ($\text{C23} \cdots \text{H21}' - 2.734\text{\AA}$). The interaction on the two ends of the second molecule leaves it to align nearly perpendicular ($\sim 84^\circ$; Fig 4.1.17 a) lying within the first and third molecules.



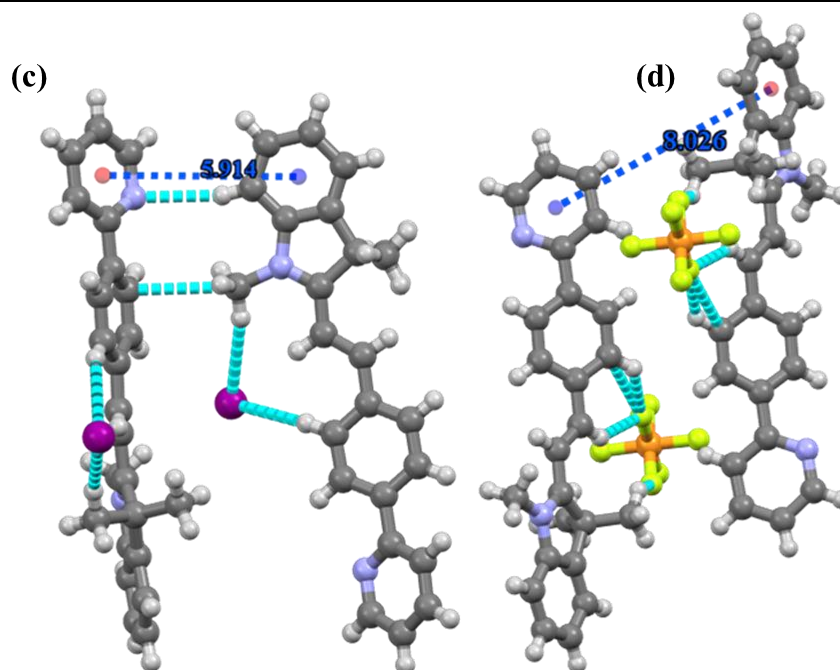


Figure 4.1.17 It shows the mean angle between the plane passing through the molecules (a) TPSI I (1) and TPSI (2) (83.54 degrees) (b) TPSI PF₆ (1) and TPSI PF₆ (1) (0 degrees), Crystal structure shows the distance between the neighbouring molecules (centroid-centroid) in (c) TPSI I is ~6Å (d) TPSI PF₆ ~8Å;

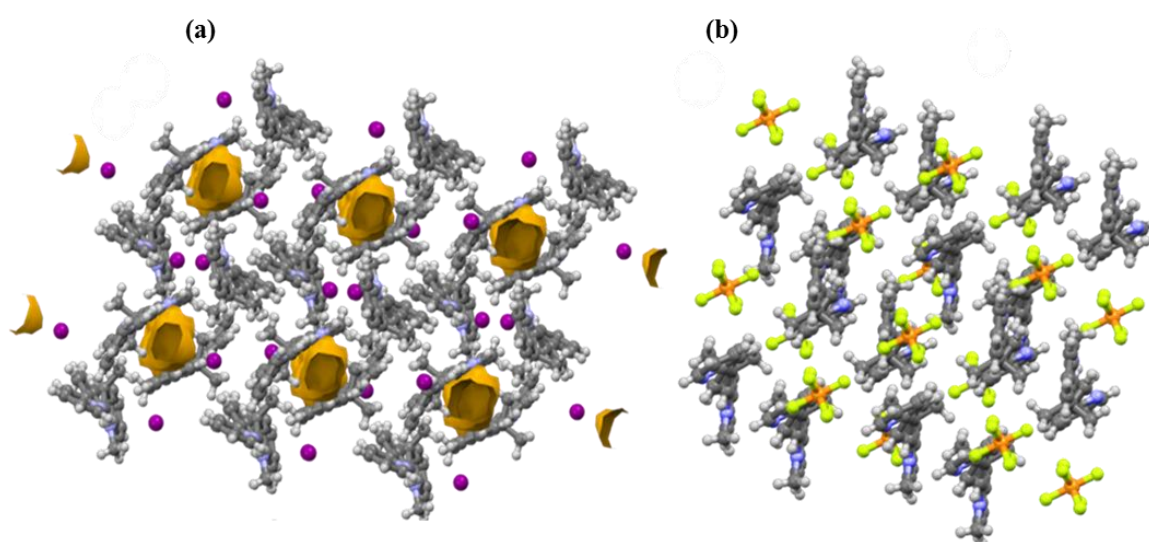


Figure 4.1.18 (a) Packing diagram of TPSI I showing a shape of the square box containing space (b) Packing diagram of TPSI PF₆ showing a stepwise wave structure.

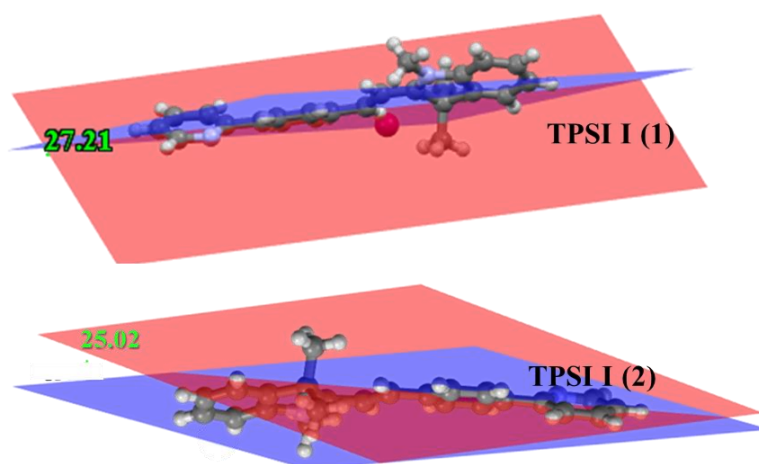


Figure 4.1.19 It shows two different dihedral angle between the plane passing through pyridine ring (orange colour) and a plane passing through the phenyl ring of phenyl pyridine (blue colour) in a unit cell (TPSI I (1) first molecule (27.21 degrees) and TPSI I (2) second molecule (25.02 degrees))

The third and the fourth molecules present in the unit cell orient in a similar fashion that is finally leading to a square-shaped enclosed surface with a void space (Fig. 4.1.18 a). It is observed the variable the angles between the plane passing through phenyl ring phenyl pyridine with the molecules present in the same unit cell for TPSI I (pyridyl and phenyl unit, 27.21° & 25.02° (Fig. 4.1.19 a, b) and cyanine and phenyl unit 24.26° & 39.04°) while this is not the case with TPSI PF₆.

The large size effect of PF₆ anion restricts the free rotation of the pyridyl and cyanine moieties that might be excluding the observation of such variable torsional angles, while smaller size effect of iodide anion permits multiple torsional angles. The presence of voids in the packing and the weak interactions of the molecules in TPSI I introduces molecular flexibility which leads to continuous motion in the solid-state. Thus, it is proposed that the excited energy dissipates in a non-radiative manner in case of TPSI I under excitation in contrast to the inflexible packing in TPSI PF₆ (Fig. 4.1.18 b).

Moreover, the significant extent of overlapping of emission and absorption spectra of TPSI I [Overlap integral $J(\lambda)$, 3.46×10^{16} ; Fig 4.1.20 (a, b)] lead to the self-absorption of the emitted energy justifies the non-emissive nature of it. The high sensitivity in TPSI I utilized in cell imaging.

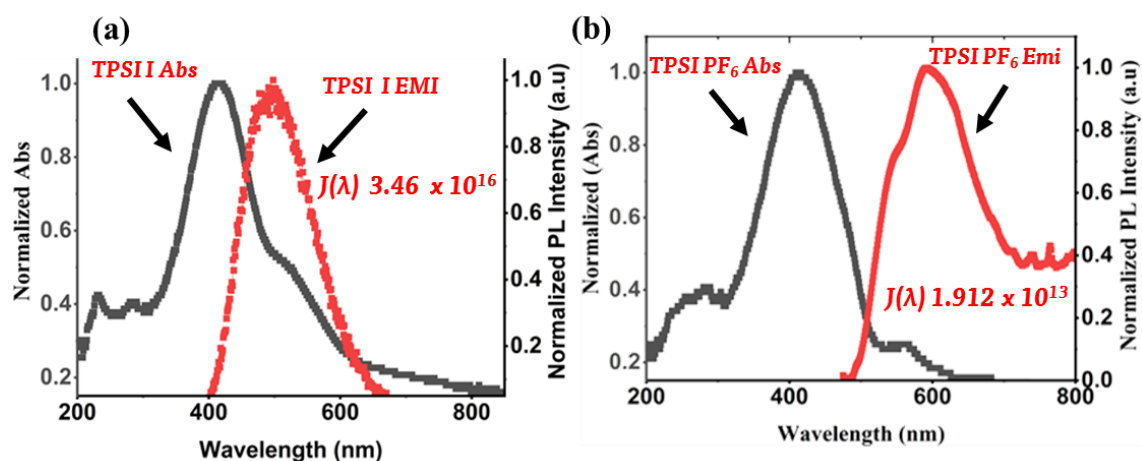


Figure 4.1.20 The Overlapping area of the absorption spectra with emission spectra of (c) TPSI I and (d) TPSI PF₆ absorption and emission in the solid-state. (Overlapped integral $J(\lambda)$ for TPSI I = 3.46×10^{16} and TPSI PF₆ = 1.912×10^{13})

4.3 Measurement of intracellular viscosity in cancerous and normal cells under different conditions

To understand the efficacy of the designed TPSI I compound in detecting alterations in viscosity; we initially analyzed the same in primary cells from human origin, the HUVEC cells. The compound was found to be non-cytotoxic to the HUVECs, as analyzed by XTT assay (DATA not shown). The cells were then treated with different concentration of glucose ranging from 5.5 to 40 mM, and the effect of glucose on alteration of the intracellular viscosity was measured. At the onset, we used a well-accepted position sensing device (PSD) based analysis for the measurement of intracellular viscosity. Using standard protocol as elaborated in the methodology section, we made the sequential measurements on the cell and the base. (Fig 4.1.21 a) shows the frequency response of the cell and the base captured using PSD system. We took the transfer function of the cell with respect to the base to take away all base related modes. The (Fig. 4.1.21) shows the transfer function of the cell. We evaluated the viscosity using the dynamic measurements as per the details provided in the methods section. The PSD system depicted an increase in intra-cellular viscosity with increase in the concentration of glucose. This experiment acted as an affirmation for an increase in intra-cellular viscosity with glucose exposure to cells.

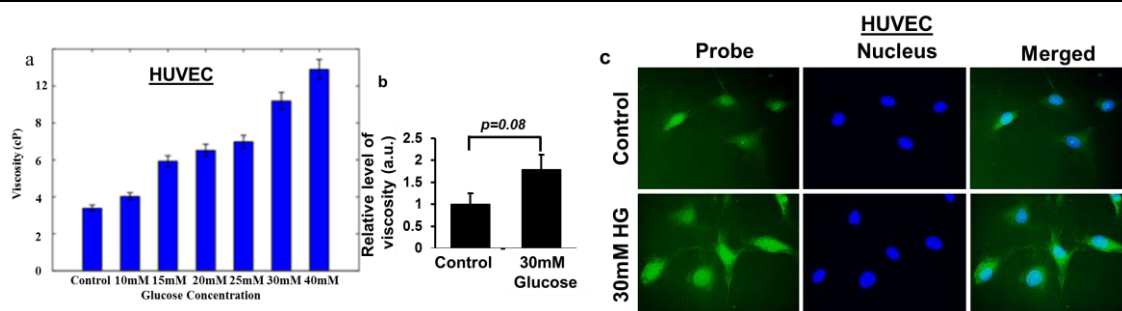


Figure 4.1.21 (a) Intracellular viscosity measurement by PSD analysis in HUVECs. A position sensing device-based analysis was performed to estimate alteration in intracellular viscosity of HUVECs after exposure to 30 mM glucose for 24 h. (b, c) Untreated cells served as control. Intracellular viscosity analysis of HUVECs treated with glucose. HUVECs were exposed to 30 mM of glucose and probe molecules (TPSI I, 10 μ M). Control cells were treated with probe only

After that, since a statistically significant increase in viscosity was observed with 30mM glucose in HUVECs, we selected the same dose for fluorescence microscopy-based analysis with the TPSI I compound. We found that HUVECs treated with 30mM of glucose was sufficient to cause an increase in intracellular viscosity detected through TPSI I fluorescence (Fig. 4.1.21 c). Although, a 1.8-fold increase in intracellular viscosity was observed, yet this change was not found to be statistically significant ($p=0.08$), at least by the current TPSI I staining protocol (Fig. 4.1.21 b).

Subsequently, we planned to analyse the potential of the probe for monitoring intracellular viscosity in tumour cell models. We cultured the human tumor cell line, Huh7 and exposed the cells to different concentrations of the compound-TPSI I. Dose kinetics for viability was performed to understand any cytotoxic effect imparted by the compound on the tumor cells. As evident from the (Fig 4.1.22 a), TPSI I was non-cytotoxic to the tumor cells as well, at the dose range studied.

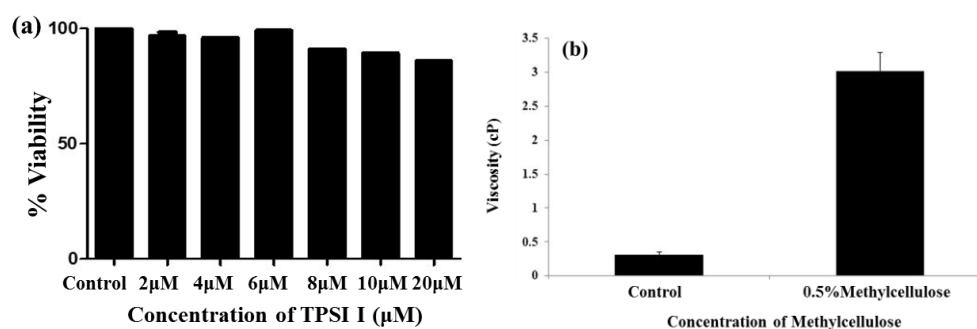
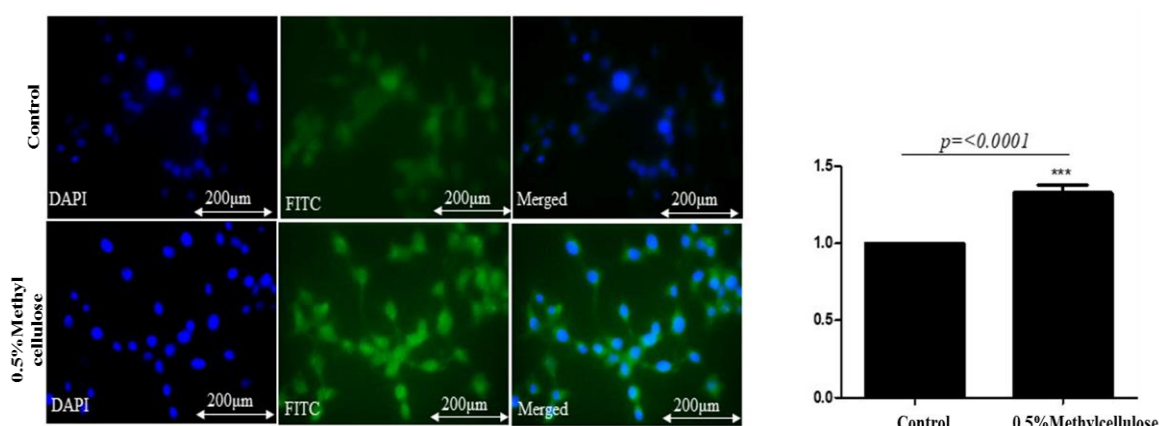
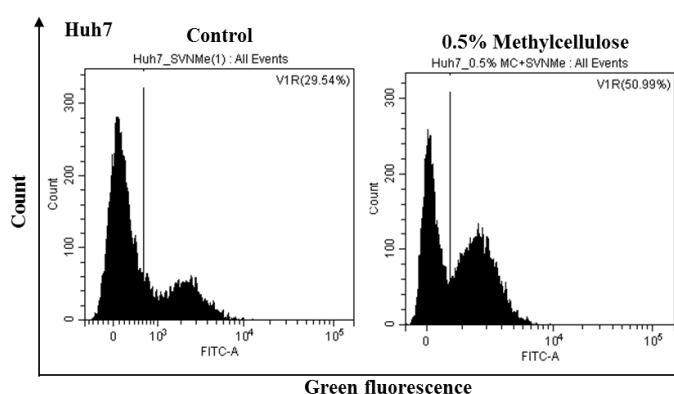


Figure 4.1.22 (a) Cytotoxicity analysis after exposure to different concentrations of TPSI I in Huh7 cells. (b) Intracellular viscosity measurement by PSD analysis in tumour cells. A position sensing device-based analysis was performed to estimate alteration in intracellular viscosity of Huh7 cells after exposure to 0.5% MC for 24 h. Untreated cells served as control

After that, we selected the compound methylcellulose (MC) to modulate and enhance the intracellular viscosity of the Huh7 cells; MC is already reported for its use in viscosity modulation.[45] A PSD analysis showed an approximately 3-fold increase in intracellular viscosity upon MC treatment (Fig. 4.1.22 b) supporting the fact that cellular viscosity indeed increases upon MC exposure. Following confirmation of the alteration of intra-cellular viscosity, we approached towards analysing the viscosity detecting function of the compound. Fluorescent microscopy images showed a substantial increase in green fluorescence intensity in TPSI I plus viscosity modulator (MC) treated cells when compared to only TPSI I exposed cells (Fig. 4.1.23 a). This is indicative of the fact that the fluorescence intensity of the compound TPSI I increase with an increase in intracellular viscosity. To have a quantitative evaluation of the same, we compared a shift in fluorescence through flow cytometry in Huh7 cells treated with TPSI I alone or TPSI I plus MC. Importantly, flow cytometric analysis also provided further evidence for viscosity probing function of TPSI I, as an increase in fluorescence events was observed (Fig 4.1.23 b)



(a)



(b)

Figure 4.1.23 (a) Intracellular viscosity analysis by fluorescence microscopy using TPSI I. Huh7 cells were treated with 0.5% MC and TPSI I (10 μ M). Only TPSI I treated cells served as control. DAPI was used to stain the nucleus. Scale bar: 200 μ m (b) Intracellular viscosity measurement by flow cytometry using TPSI I. Huh7 cells were treated with 0.5% MC and TPSI I (10 μ M). Only TPSI I treated cells served as control. Subsequently, a shift in green fluorescence was monitored through flow cytometry. The overlay images depict the shift.

4.4 Conclusion The present chapter describes the water-soluble novel ultrasensitive viscosity sensitive probe TPSI I, with the sensitivity of $x= 1.02$. The probe TPSI I freely rotated, photo isomerized and showed weak photoluminescence in a low-viscous environment, while in the high viscous medium, the emission intensity enhanced. The restriction of the motion in the high viscous medium reduced the dissipation of energy in the excited state and enhanced the photoluminescence intensity. The enhanced photoluminescence property was further applied to measure the intracellular viscosity using imaging technique in cancer and normal cells of human origin. The probe was able to distinguish the altered viscosity of cancerous and normal cells under viscosity modulating conditions. Therefore, we assume that the present probe, TPSI I hold the potential for it to be utilized in future for pre diagnosing various diseases linked to alteration in viscosity of cells. For example, it can be used to identify the altered viscous state of cells during different stages of cancer progression, thus enabling an imaging-based approach towards the disease stage diagnosis. Not restricted to cancer, the currently designed probe also opens a new vista for detection of different diseases, associated with viscosity changes, in a more precise and efficient way. Till date, the application of such probes in clinical settings is yet to be established.

4.5 Reference

[1] M. A. Haidekker and E. A. Theodorakis, *Org. Biomol. Chem.*, 2007, **5**, 1669-1678.

- [2] W. G. Hixon and D. G. Searcy, *Biosystems*, 1993, **29**, 151-160.
- [3] J. A. Dix and A. Verkman, *Biophys. J.*, 1990, **57**, 231-240.
- [4] P. D. Morse II, in *Methods in enzymology*, Elsevier, 1986, vol. 127, pp. 239-249.
- [5] M. K. Kuimova, S. W. Botchway, A. W. Parker, M. Balaz, H. A. Collins, H. L. Anderson, K. Suhling and P. R. Ogilby, *Nat. Chem.*, 2009, **1**, 69.
- [6] J. Guck, F. Lautenschläger, S. Paschke and M. Beil, *Integr. Biol.*, 2010, **2**, 575-583.
- [7] E. U. Azeloglu and K. D. Costa, in *Atomic Force Microscopy in Biomedical Research*, Springer, 2011, pp. 303-329.
- [8] B. A. Smith, B. Tolloczko, J. G. Martin and P. Grütter, *Biophys. J.*, 2005, **88**, 2994-3007.
- [9] G. Lee, S.-B. Han, J.-H. Lee, H.-W. Kim and D.-H. Kim, *ACS Biomater Sci Eng.*, 2019, **5**, 3735-3752.
- [10] Y. Xie, M. Wang, M. Cheng, Z. Gao and G. Wang, *J MECH BEHAV BIOMED*, 2019, **91**, 54-58.
- [11] A. Athanasiadis, C. Fitzgerald, N. M. Davidson, C. Giorio, S. W. Botchway, A. D. Ward, M. Kalberer, F. D. Pope and M. K. Kuimova, *Physical Chemistry Chemical Physics*, 2016, **18**, 30385-30393.
- [12] B. R. Arnold, V. Balaji, J. W. Downing, J. G. Radziszewski, J. J. Fisher and J. Michl, *J. Am. Chem. Soc.*, 1991, **113**, 2910-2919.
- [13] P. D. Boyer, *Nature*, 1999, **402**, 247-249.
- [14] J. Michl and E. C. H. Sykes, *Journal*, 2009.
- [15] K. Ichimura, Y. Hayashi, H. Akiyama, T. Ikeda and N. Ishizuki, *Appl. Phys. Lett.*, 1993, **63**, 449-451.
- [16] M. Xue and K. L. Wang, *Sensors*, 2012, **12**, 11612-11637.
- [17] G. S. Kottas, L. I. Clarke, D. Horinek and J. Michl, 2005, **105**, 1281-1376.
- [18] W.-E. Lee, C.-L. Lee, T. Sakaguchi, M. Fujiki and G. J. M. Kwak, 2011, **44**, 432-436.
- [19] R. Kotani, H. Sotome, H. Okajima, S. Yokoyama, Y. Nakaike, A. Kashiwagi, C. Mori, Y. Nakada, S. Yamaguchi and A. Osuka, *J. Mater. Chem.C.*, 2017, **5**, 5248-5256.
- [20] T. Xia, L. Wang, Y. Qu, Y. Rui, J. Cao, Y. Hu, J. Yang, J. Wu and J. Xu, *J. Mater. Chem.C.*, 2016, **4**, 5696-5701.
- [21] S.-C. Lee, J. Heo, H. C. Woo, J.-A. Lee, Y. H. Seo, C.-L. Lee, S. Kim and O.-P. Kwon, *Chem. Eur. J.*, 2018, **24**, 13706-13718.
- [22] J. Sutharsan, D. Lichlyter, N. E. Wright, M. Dakanali, M. A. Haidekker and E. A. Theodorakis, *Tetrahedron*, 2010, **66**, 2582-2588.
- [23] M. K. Kuimova, *Phys Chem Chem Phys.*, 2012, **14**, 12671-12686.

- [24] N. Boens, V. Leen and W. Dehaen, *Chem. Soc. Rev.*, 2012, **41**, 1130-1172.
- [25] D. Su, C. L. Teoh, L. Wang, X. Liu and Y.-T. Chang, *Chem. Soc. Rev.*, 2017, **46**, 4833-4844.
- [26] W. Sun, S. Guo, C. Hu, J. Fan and X. Peng, *Chem. Rev.*, 2016, **116**, 7768-7817.
- [27] X. Peng, Z. Yang, J. Wang, J. Fan, Y. He, F. Song, B. Wang, S. Sun, J. Qu, J. Qi and M. Yan, *J. Am. Chem. Soc.*, 2011, **133**, 6626-6635.
- [28] F. Liu, Y. Luo and M. Xu, *Tetrahedron Lett.*, 2018, **59**, 4540-4544.
- [29] S. J. Park, B. K. Shin, H. W. Lee, J. M. Song, J. T. Je and H. M. Kim, *Dyes Pigm.*, 2020, **174**, 108080.
- [30] H.-y. Tan, Y.-t. Qiu, H. Sun, J.-w. Yan and L. Zhang, *Chem. Comm.*, 2019, **55**, 2688-2691.
- [31] M. K. Burdette, R. Jenkins, Y. P. Bandera, H. Jones, I. K. Foulger, A. Dickey, A.-L. Nieminen and S. H. Foulger, *ACS Applied Bio Materials*, 2019, **2**, 3183-3193.
- [32] R. F. Khairutdinov and N. Serpone, *J. Phys. Chem. B.*, 1997, **101**, 2602-2610.
- [33] L. Qun, L. Guo-Liang, P. Bi-Xian and L. Zheng-Xin, *Dyes Pigm.*, 1998, **38**, 211-218.
- [34] Y. Xu, Y. Liu and X. Qian, *J. Photochem. Photobiol. A: Chem.*, 2007, **190**, 1-8.
- [35] C. Reichardt, *Chem. Rev.*, 1994, **94**, 2319-2358.
- [36] W. Zeng and J. Wu, *Mater. Chem. Front.*, 2019, **3**, 2668-2672.
- [37] W. Akers and M. Haidekker, *J. Biomech. Eng.*, 2004, **126**, 340-345.
- [38] I. López-Duarte, T. T. Vu, M. A. Izquierdo, J. A. Bull and M. K. Kuimova, *Chem. commun.*, 2014, **50**, 5282-5284.
- [39] S. Khopkar, M. Jachak and G. Shankarling, *Dyes Pigm.*, 2019, **161**, 1-15.
- [40] R. D. Telore and N. Sekar, *Dyes Pigm.*, 2016, **129**, 1-8.
- [41] M. Rajeshirke, A. B. Tathe and N. Sekar, *J MOL LIQ*, 2018, **264**, 358-366.
- [42] G. Zhang, Y. Ni, D. Zhang, H. Li, N. Wang, C. Yu, L. Li and W. Huang, *Spectrochim. Acta A*, 2019, **214**, 339-347.
- [43] Y. Dou and R. E. Allen, *J. Chem. Phys.*, 2003, **119**, 10658-10666.
- [44] Y. Shiraishi, T. Inoue and T. Hirai, *Langmuir*, 2010, **26**, 17505-17512.
- [45] G. Stephen, B. Anne and W. Margaret van, *In Vitro Cell. Dev. Biol. Anim.*, 1993, **29A**, 755-757.

Chapter-5

Aggregation-induced enhanced emission(AIEE) Active Probes for Ultrasensitive Low-cost Detection of Nitro Aromatic Based Explosive Materials

- * *A simple reaction condition has been utilized for the synthesis of AIEE active pyrene-pyridine derivatives for ultrasensitive detection of the nitro explosives*
- * *Conjugated Mesoporous Oligomers (CMOs) with improved quantum yield is utilized for low-cost sensitive detection of nitro explosives*

Small Organic Molecule and Oligomer based Emissive Probes: Ultra-Sensitive Detection of nitroaromatics

Part A. 5.1 Aggregation-induced enhanced emission (AIEE) active Pyrene derivatives for efficient detection of nitroaromatics

5.1.1 Section I A Multifunctional Pyrene-Pyridine based Ratiometric Explosive Sensing Probe

5.1.1.1 Introduction

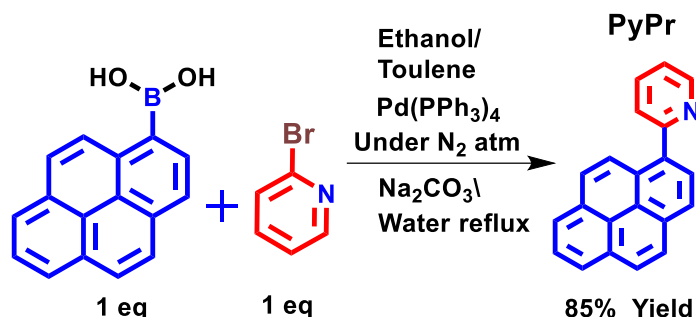
Nitroaromatic compounds are familiar for their explosive properties [1, 2]. The social evil groups widely use the nitroaromatic for the mass destruction in common places.[3] The nitro explosive can be classified as electron-deficient aromatics such as, trinitrotoluene (TNT), picric acid (PA), 2,4-dinitrotoluene (DNT), 1,3-dinitrobenzene (m-DNB), 2,4,6-trinitrotoluene (TNT) etc., and electron-deficient aliphatics like 2,3-dimethyl-dinitrobutane (DMNB), trinitroglycerin (TNG), 1,3,5-trinitroperhydro-1,3,5-triazine (RDX), octahydro-1,3,5,7-tetranitro-1,3,5,7-tetrazocine (HMX) etc. Among all the explosives RDX, HMX, TNT, TNP, TNG, PA are more hazardous and dangerous[4, 5]. Within the realm of sensor-based techniques, use of fluorescence gained much more interest because of the less response time, low cost, increased sensitivity and portability. [6-8] Sohn et al. explored the photoluminescence property of polysilole derivative through quenching its luminescence by explosive analytes like picric acid, TNT, DNT in air or seawater or underwater land mines.[9] The detection limit of this probe is 4 ppb in the air and 1.5 ppt in seawater for TNT, while 6 ppb for picric acid.[9] Though the polysilole derivative has a low detection limit[10, 11], these methods are less responsive at the time of intense background colour or background fluorescence.[10, 12] In this case, the fluorescent sensitive material [such as 4-N, N-dimethylamino-4 methylacryloylaminochalcone (DMC), pentiptycene polymer, Nile Red dye, liquid-crystalline (LC) polyfluorenes, etc.] is spread over the suspected area to get the image of an object. Sometimes, fluorescent light is directly flashed onto the object so that the suspected area gets illuminated and gives an indication for the presence of explosive compound or material[13, 14]. The fluorescence quenching approach has been explored for the analysis of nitrated explosives and also applied for the detection of RDX, HMX, TNT, nitromethane and ammonium nitrate.[15] For developing the solid luminescent small molecule sensor for detecting nitroaromatic explosives, three vital characteristics need to be taken into account. Firstly, the fluorescent probe should consist of an electron ring and π -

conjugated planar systems (such as pyrene, triphenylene and coronene), which are supposed to be highly beneficial in binding to the nitroaromatic explosives through π - π interactions.[16-18] Secondly, along with the rich electron system in the probe, there should be an electron-deficient heteroaromatic ring (such as pyridine, thiophene, oxazole), which can be effectively involve in charge-transfer.[19-21] The third one is that the bulky substituent groups attached to the peripheral of the fluorescent probe which are beneficial in hindering the formation of intermolecular excimers.[22, 23]. Recently, many small fluorescence-based chemosensors are reported in the literature. Still, the probe with high quantum yield, the high limit of detection, selective and sensitive towards the nitroaromatic explosives are rare.[24, 25] In the last few years, several fluorescent polymers, MOFs, quantum dots (QDs) and small molecule-based sensors have been developed for the detection of nitroaromatics.[26, 27] The Walt and Bakker groups have developed high-density microarray optical sensors for explosive-like vapours [28]. In 2015 M. K. C. et al. synthesized 1,8-naphthyridine based fluorescent sensors for the detection of the picric acid in the aqueous medium through both PET and RET.[29] J. Sun and his group reported sensitive detection of HMX and RDX with using substituted coumarin based fluorescent probes.[30] Among the synthesized molecule by J. Sun, one of the probes results in turn-on fluorescence because of C=N isomerization while the other results a unique turn-off response with fluorescence quenching because of TICT effect. Due to active monomer and excimer emission, pyrene based probes are extensively used for sensing.[31-33] Polyaromatic hydrocarbons (PAHs), (such as naphthalene, anthracene, phenanthrene, pyrene, etc.), are used to make luminescent probes.[34-36] In all the PAHs the pyrene is widely used as fluorescent probes in several type of applications. The monomer and excimer emission intensities are found to have high sensitivity towards guest molecules, various ions etc.[37] Many scientist desire the pyrene molecules that have strong fluorescent in the solid state and to prevent the self-quenching and/or aggregation at the desired concentrations for an ideal probe.[38] But the reported AIEE active pyrene derivatives are either Schiff base type or with a complex structure type molecules. Many of Schiff-base compounds are not stable under acidic conditions and have low quantum yield.[39-43]

All the consequences urge to develop solid luminescent pyrene derivatives, which should be stable under variable conditions (acids and bases). However, we want to build an AIE active small molecule-based electron-rich (Donor (D))-electron Acceptor (Acceptor (A)) system.

5.1.1.2 Results and Discussion

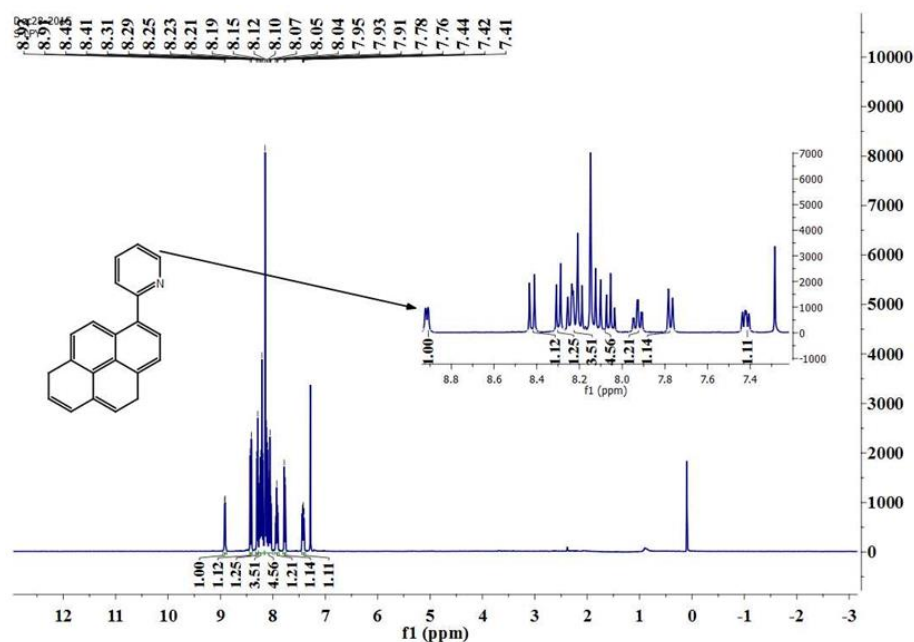
i) Synthesis and Characterization



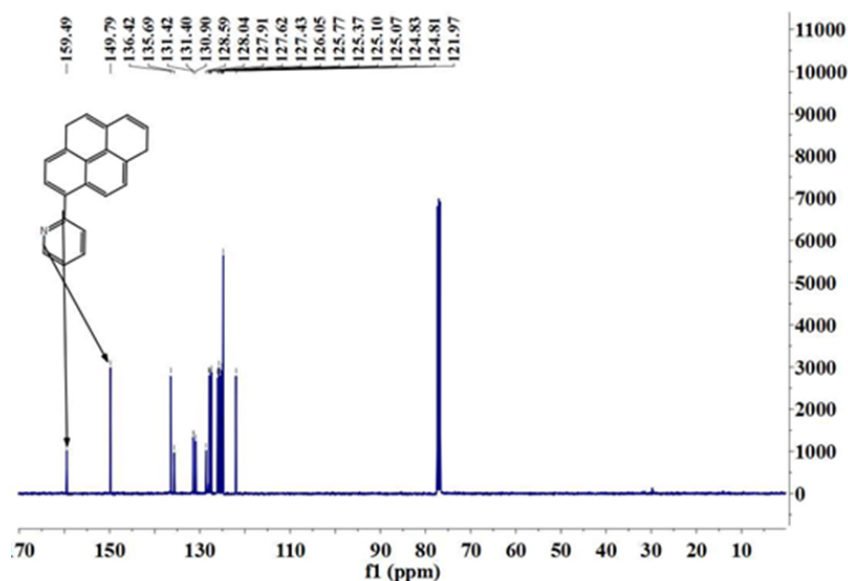
Scheme 5.1.1 Synthesis of PyPr [2-(pyrene-1-yl)pyridine]

Synthesis of the PyPr [2-(pyrene-1-yl)pyridine] was carried out by the reaction of pyrene-1-boronic acid, and 2-bromo pyridine by the Suzuki coupling reaction[44] and the product obtained was PyPr [2-(pyrene-1-yl)pyridine] (Scheme 5.1). ^1H , ^{13}C and mass spectroscopy characterized the synthesized compound. [Fig 5.1.1 (a, b, c)]

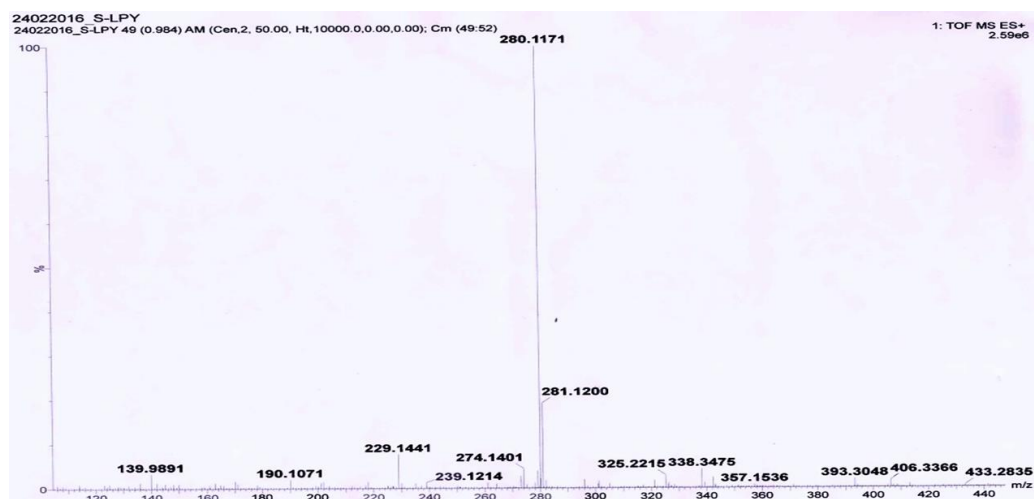
Characterization



(a)



(b)



(c)

Figure 5.1.1 (a) ^1H spectrum of PyPr (b) ^{13}C spectrum of PyPr (c) Mass spectrum of PyPr

PyPr: - ^1H NMR (400 MHz, CDCl_3) δ 8.92 (d, $J = 4.2$ Hz, 1H), 8.42 (d, $J = 9.3$ Hz, 1H), 8.30 (d, $J = 7.9$ Hz, 1H), 8.22 (dd, $J = 18.7, 7.8$ Hz, 3H), 8.15 – 8.01 (m, 4H), 7.93 (t, $J = 8.6$ Hz, 1H), 7.77 (d, $J = 7.8$ Hz, 1H), 7.45 – 7.38 (m, 1H). ^{13}C NMR (101 MHz, CDCl_3) δ 159.49, 149.79, 136.42, 135.69, 131.42, 131.40, 130.90, 128.59, 128.04, 127.91, 127.62, 127.43, 126.05, 125.77, 125.37, 125.10, 125.07, 124.83, 124.81, 121.97. HRMS data 280.1171/at m/z $[\text{M}+\text{H}]^+$ corresponds to the major fraction (Fig 5.1.1 c)

ii) Photophysical properties

a) Absorption and emission property study

From the emission spectrum of PyPr, a structured peak was observed with λ_{\max} at 388 nm and 405 nm in solution state these are attributed to the monomeric emission in dilute DCM and at 498 nm in the solid-state (an excimeric emission, vide supra) (Fig. 5.1.2 a). When compared to the pyrene ring, a minor bathochromic shift was observed at 245 and 277 nm when compared with the absorption spectrum of pyrene (Fig. 5.1.2 b). However, a noticeable change can be observed at $\lambda_{\max} = 345$ nm (Fig. 5.1.2 b), a broad peak with a redshifted band which signifies the charge transfer peak from pyrene to pyridine in PyPr ($c = 10^{-5}$ M, DCM) (Fig. 5.1.2 b).

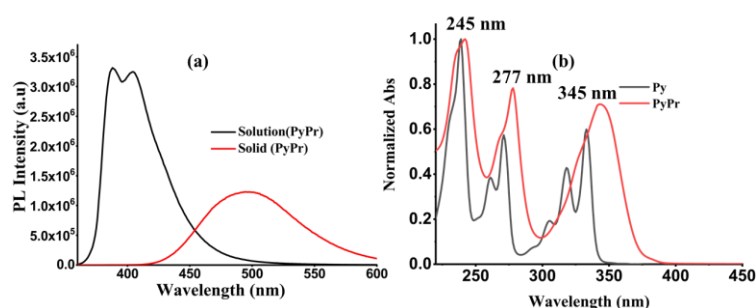


Figure 5.1.2 (a) Emission spectra of the PyPr (b) Absorption spectra of pyrene, PyPr and Py (Pyrene)

In PyPr, all the absorption peaks are observed in the range of 240–345 nm, which can be assigned using DFT based computational calculations.[45] In this case, the following sets of transitions were obtained: (i) HOMO to LUMO, (ii) HOMO-1 to LUMO and (iii) HOMO to LUMO+1, which are characteristic of $\pi-\pi^*$ transition of the pyrene chromophore in the monomeric form [46] (Table 5.1.1).

Table 5.1.1 Calculated major orbital excitation contributions (%), energy difference (in eV), obtained from electronic transitions analysis with TDDFT (B3LYP) method for PyPr.

Major orbital excitation contribution(%)	Energy gap(eV)	Calculated λ_{\max} (nm) oscillator strength in brackets (B3LYP)	Absorbance at λ_{\max} (nm), molar absorptivity in brackets, $\text{Lmole}^{-1}\text{cm}^{-1}$
HOMO \rightarrow LUMO (96)	3.37	367 (0.560)	374 (1750)
HOMO-1 \rightarrow LUMO (43.50)	3.64	339 (0.0060)	345 (2250)
HOMO \rightarrow LUMO +1 (60.36)	3.96	313 (0.0307)	277 (3170)
HOMO \rightarrow LUMO +2 (60.36)	4.20	291 (0.0032)	245 (21736)

b) Effect of Protonation (H^+) on PyPr

The absorption spectrum of PyPr in a methanol solution was recorded in the presence of TFA (trifluoroacetic acid) (Fig. 5.1.3 a). From the absorption spectrum apart from the three analogous peaks observed similar to PyPr, with $\lambda_{max} = 243, 280$ and 350 nm; a new broad peak appears at ~ 390 nm on protonation (Fig. 5.1.3 a). The appearance of a broad peak around 390 nm may imply that a new charge transfer state is formed after protonation on pyridine of PyPr.[47] The emission spectrum shows broadband with large red-shifted emission with $\lambda_{max} = 493$ nm (Fig. 5.1.3 b).

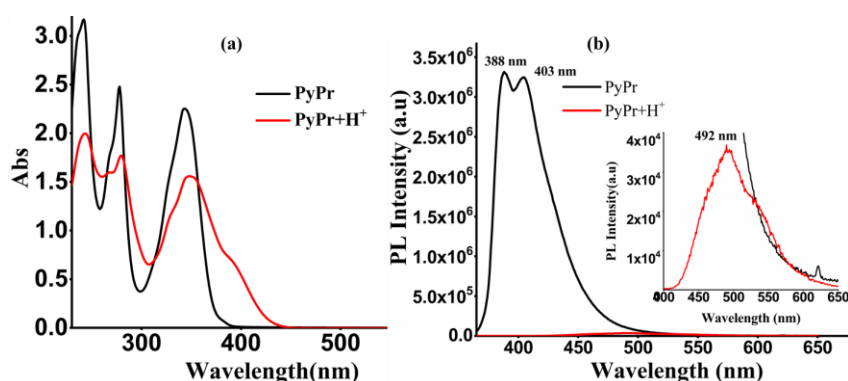


Figure. 5.1.3 a) UV-Visible spectra of PyPr and PyPr + H^+ [Methanol ($c = 10^{-5}$ M)]; b) Emission spectra of PyPr and PyPr + H^+ in DCM ($c = 10^{-3}$ M)

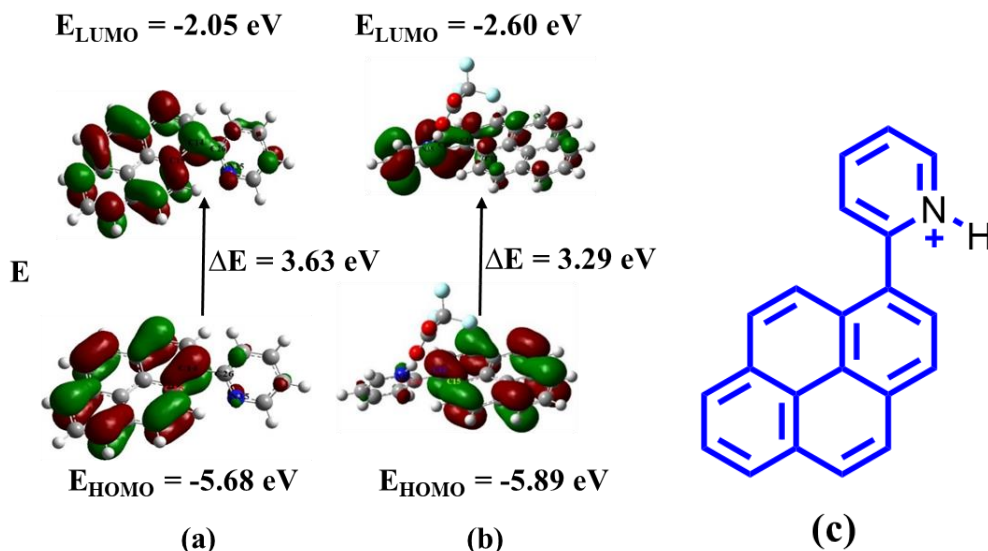


Figure 5.1.4 Frontier Molecular Orbital diagram of (a) PyPr and (b) PyPr + H^+ , calculated by using B3LYP/6-31 g ++(d, p) as implemented on Gaussian 09.[48] (c) Proposed structure for the PyPr+ H^+

The optimized geometry of PyPr using DFT with the 6-31g++(d,p) hybrid functional shows the electron distribution of HOMO significantly localized on the pyrene unit and LUMO is not only on pyrene but also some part on the pyridine unit (Fig. 5.1.4 a). On the other hand, the protonated pyrene (PyPr + H⁺) shows that the electron distribution of the HOMO is mainly localized on the pyrene unit while the LUMO is primarily localized on the pyridinium unit (Fig. 5.1.4 b). The shifting of electron density from the pyrene unit (a donor group) into the pyridine unit (an acceptor group) is due to the formation of the strong electron-withdrawing pyridinium ion which leads to an intramolecular charge transfer (ICT) from the pyrene unit to the pyridinium unit. The calculated energy gap of PyPr is changed from 3.63 eV to 3.29 eV after protonation. For understanding the solid-state emission property of PyPr after protonation, the emission spectra of the thin film recorded in the presence of acid (TFA) and base (trimethylamine Et₃N) (Fig 5.1.5 a). The thin film of PyPr exposed to the vapours of TFA results in a greenish-yellow emission ($\lambda_{\text{max}} = 474$ nm) which is reverted to its original emission maximum at 430 nm after passing vapours of Et₃N (Fig. 5.1.5 b). It is to be noted that the same emission colour change has been observed with exposure to other acids (HCl/CH₃COOH) instead of TFA.

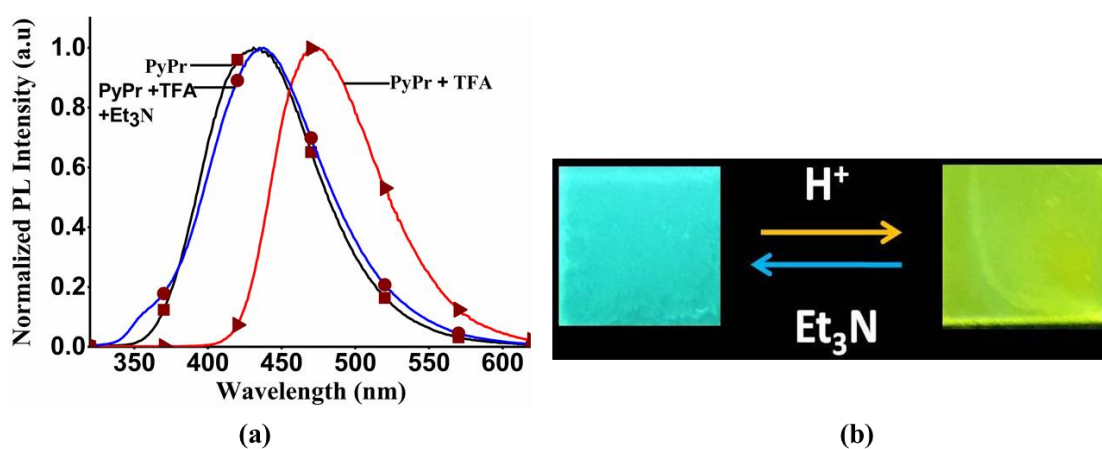


Figure 5.1.5 (a) The normalized emission spectra of PyPr on thin films ($c = 10^{-3}$ M) showing reversibility in the presence of acid-base ($\lambda_{\text{max}} = 433$ nm for PyPr and 473 nm for PyPr + H⁺); (b) Thin-film emission colour image of PyPr under exposure to acid and base.

The sensitivity of PyPr towards (H⁺) ions was tested by titration with TFA in methanol. The UV-Vis spectrum showed a new band at 390 nm, which gets intensified with increasing concentration of trifluoroacetic acid (TFA) concentration (Fig. 5.1.6 a). However, a continuous decrease in the original band positions at 347 nm and 280 nm has been observed in the absorption spectrum which may be due to the formation of a new species on increasing

the concentration of TFA. In the emission spectra, the peak intensity at $\lambda_{\max} = 390$ and 405 nm of PyPr decreases and a new broad peak appeared at 493 nm with gradually increasing concentration (0 – 0.1 eq.) (Fig. 5.1.6 b). Hence, two isosbestic points appear in the absorption spectra, and one isosbestic point is observed in the emission spectrum. The decrease in the band and appearance of a new band at 493 nm is indicative of the formation of a new species and based on the supports as given; we propose the new species is the conjugate acid of PyPr protonated species (Fig 5.1.6 c). A linear relationship has been established between I_{490}/I_{404} against the concentration variation of TFA (Fig. 5.1.6 d). The detection limit of the H^+ ion is calculated to be 2.4 nM (0.27 ppb), based on $3\sigma/m$, where σ corresponds to the standard deviation of the blank measurements and m is the slope in the plot of the intensity versus the sample concentration. The studied probe molecule (PyPr) has shown a high sensitivity toward H^+ detection in comparison with the other reported probe molecules.[49-52]

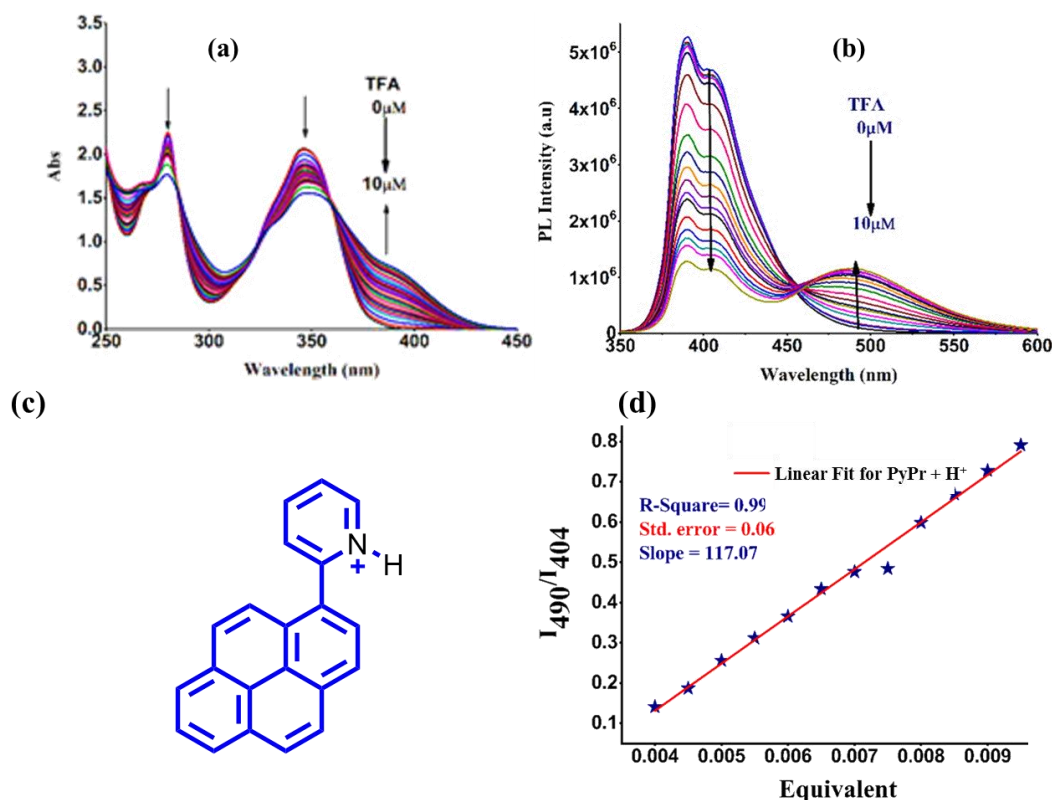


Figure 5.1.6. (a) Absorption spectra of PyPr (1×10^{-3} M) with different TFA concentration [1×10^{-3} M in methanol (0.01 eq)] (the isosbestic point at 284 & 360 nm); (b) Emission intensity of PyPr (1×10^{-3} M) with a gradual increase of acid concentration (isosbestic point wavelength = 456 nm; increasing concentration of TFA is marked in the spectrum) (d) Proposed structure of PyPr after protonation with TFA (A protonated form of PyPr = PyPr + H^+) and (c) linear fitting of PyPr with acid

c) Excimer Formation

Pyrene type of probe molecule is known to have monomeric and excimer form due to their planer structure. The concentration-dependent photoluminescence (PL) spectra of both the compounds PyPr in dichloromethane (from 10^{-1} M to 10^{-6} M in DCM) and PyPr + H^+ (from 10^{-3} M to 10^{-7} M in DCM) were recorded (Fig 5.1.7 a,c). A fine-tuning of emission colour from green to blue and yellowish-green to blue, respectively [Fig 5.1.7 (b,d)] was observed. At higher concentration (5×10^{-1} M), PyPr shows a weak and broad peak at 505 nm which is changed into a structured emission at 388 nm and 405 nm with gradual dilution by DCM solvent [which is similar to the emission obtained in dilute DCM as shown in (Fig. 5.1.3 b)].

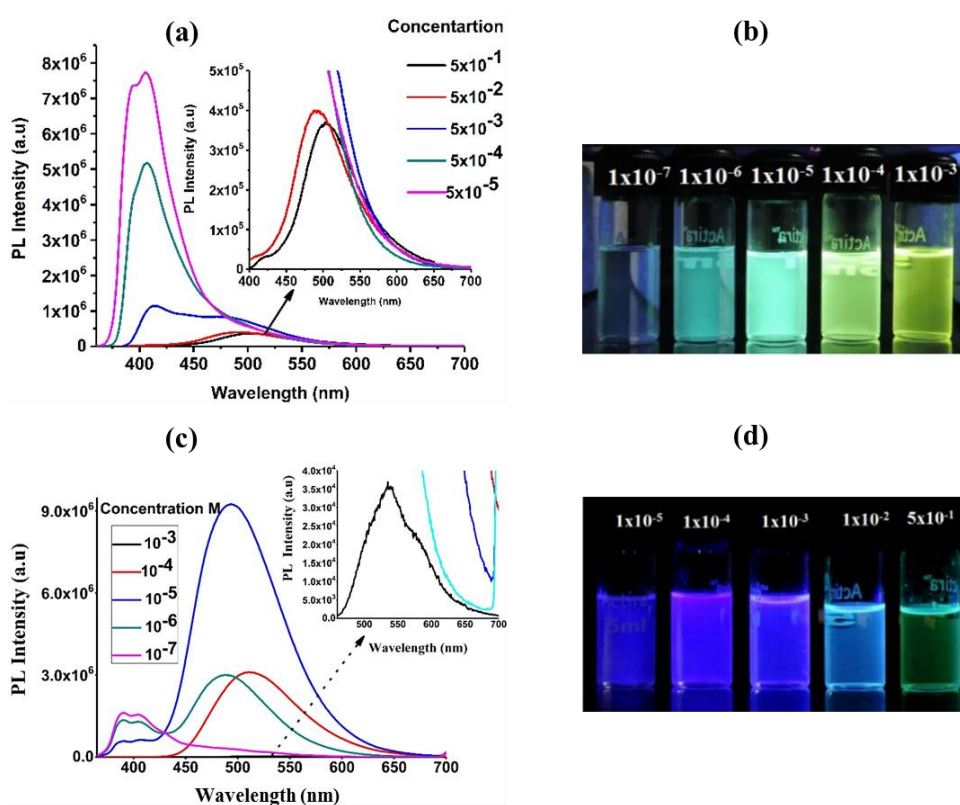


Figure 5.1.7 (a, c) Emission spectra of PyPr and PyPr + H^+ with a gradual increase in concentration, respectively; (b, d) image of PyPr and PyPr + H^+ , respectively with gradually increasing concentration under excitation at 365 nm.

The observation of such emission with λ_{max} at 505 nm may be due to the self-assembled excimer emission, but on dilution, the aggregated forms have been separated and result in a monomeric emission at 388 nm and 405 nm. A similar trend of emission was observed in the case of PyPr + H^+ where the emission changes from bright yellowish-green (537 nm) to weak blue (388 nm, 405 nm) by varying the concentration (Fig. 5.1.7 d). The quantum yield of L

and $\text{Pyr} + \text{H}^+$ was determined with varying concentration and found to be in the range of 1.0 - ~40% and 1.4- ~37.3% for PyPr and PyPr + H^+ , respectively.

(d) Study of Aggregation-induced emission enhancement (AIEE) property

For investigating the AIEE property of the both PyPr and PyPr + H^+ recorded the emission spectra using different water fraction (f_w) ($f_w = 0-90\%$) in methanol and acetonitrile respectively maintaining the overall concentration of the solution at 10^{-4} M. The emission intensity of PyPr enhanced to a water fraction up to $\sim f_w \leq 30\%$ and then started to decrease

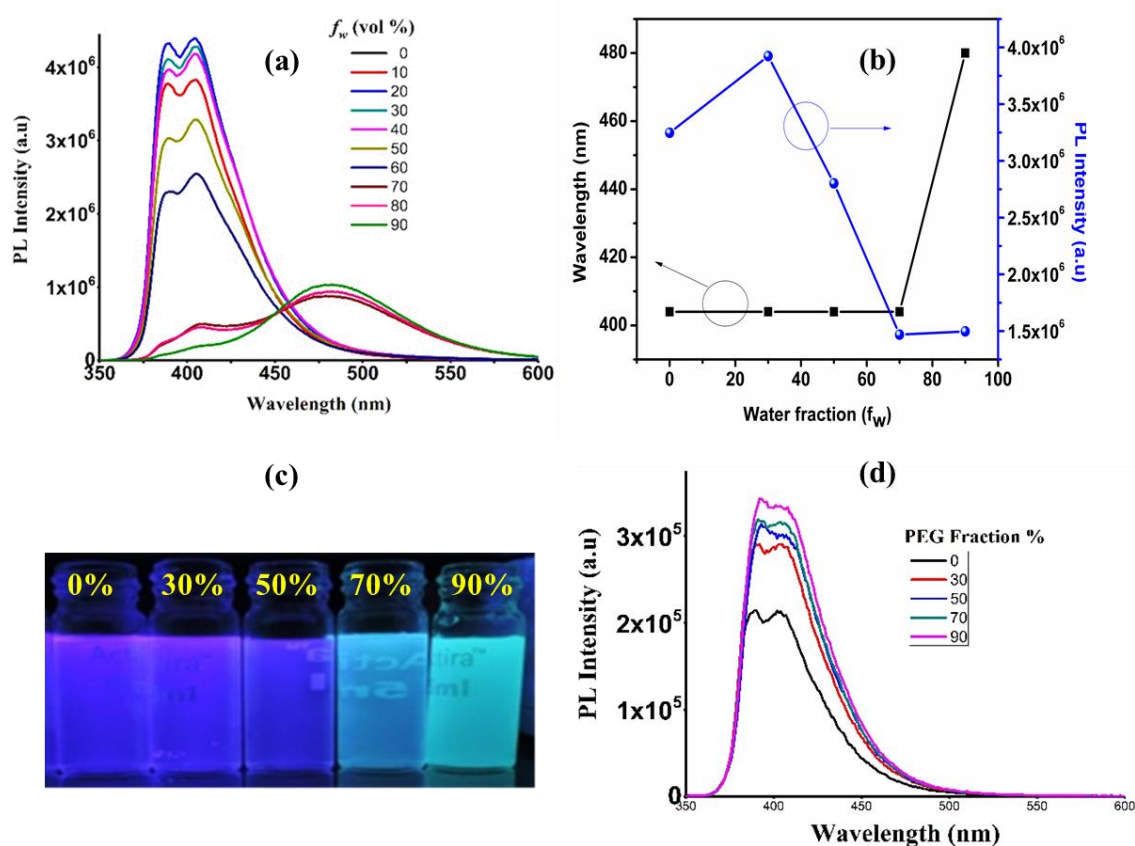


Figure 5.1.8 (a) Emission spectra of PyPr (0.1mM) with gradual increase in the water fraction in methanol (b) Plot of intensity (I) values of PyPr (c) Images of the emission of PyPr in methanol-water mixtures with different water volume fractions (f_w) taken under UV illumination (365 nm) (d) Emission spectra of PyPr (0.1mM) with a gradual increase in PEG concentration

with increasing the water fraction up to $\sim f_w \leq 70\%$ with the appearance of a new peak around $\lambda_{\text{max}} = 482$ nm. At $f_w = 90\%$, the original peak ($\lambda_{\text{max}} = 308, 405$ nm) disappeared and a single, broad and red-shifted emission with $\lambda_{\text{max}} = 482$ nm was observed (Fig. 5.1.8 a,b,c). Moreover, due to the restriction of the pyridine ring, the intensity gets enhanced. Further to support the

RIR mechanism for AIEE, the photoluminescence (PL) spectrum of PyPr was recorded by gradually increasing the PEG concentration. The emission intensity of PyPr gradually enhanced with increasing viscosity that supports the restriction intramolecular rotation (Fig. 5.1.8 d). A close inspection of the crystal structure of PyPr shows CH--- π interaction of 2.758 Å between two of the pyridine rings which blocks the rotation of the pyridine ring in the solid-state (Fig. 5.1.9 a). However, a very strong close-packed π - π interaction was observed in the range of 3.57–3.78 Å, (Fig. 5.1.9 b), which may result in the excimer emission in the solid-state. Hence, the observed short contacts and an increase in the intensity with increasing the viscous medium support the restriction of movement of the pyridine group in the solid-state. This may be the reason for blocking non-radiative pathways and subsequently opening up several new radiative pathways on progressive.

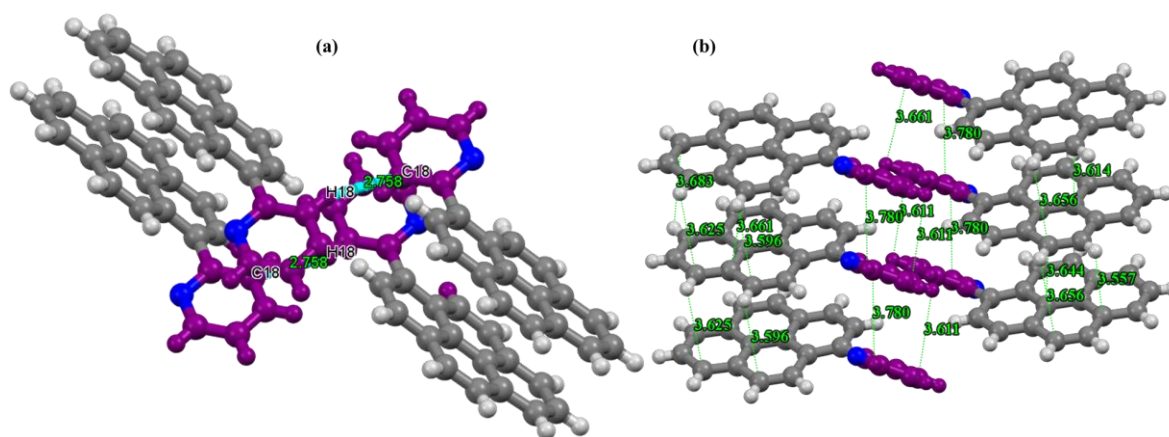


Figure 5.1.9 (a) shows CH--- π interaction of 2.758 Å (b) a strong π - π interaction between the centroids of the two pyrene rings with short contact, 3.57–3.78 Å.

The aggregates of 90% water fraction are amorphous, which is confirmed from the powder-based X-ray diffractometer study. This result is opposite to the original solid powder of PyPr (Fig. 5.1.9 a). The increment in the emission intensity of PyPr arises due to the restricted rotation of the pyridine ring in PyPr (Fig. 5.1.9 a) with increasing the content of water in the mixture, while the opposing force is playing increasing amorphous nature of the aggregates [supported by X-ray powder pattern (Fig. 5.1.11 d)] of the 90% aggregates decreases the PL intensity. Furthermore, the pyrene derivatives involved in π - π stacking with increasing (Fig. 5.1.9 b) aggregation may lead to quenching of the emission intensity. Hence, at 30%, the optimum PL intensity is observed. Then the PL intensity gets lowered with increasing water concentration. In a higher percentage of water, it emits through the excimer state. In the case of PyPr + H⁺ where the PL intensity almost remained unchanged up to 70% water content;

then a sharp increment is observed in the range of 70–90% of water concentration (Fig. 5.1.10 a, b, c).

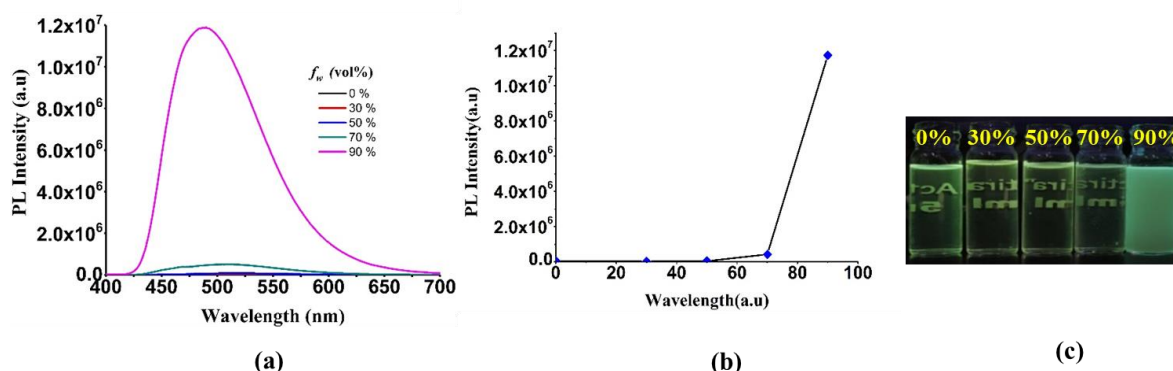


Figure.5.1.10 (a) Emission spectra of PyPr + H⁺ (0.1mM) with gradual increase in the water fraction in methanol (b) Plot of intensity (I) values of PyPr + H⁺ (c) Images of the emission of PyPr+ H⁺ in methanol-water mixtures with different water volume fractions (f_w) taken under UV illumination (365 nm)

The PL intensity of PyPr + H⁺ is found to be 192 times higher at $f_w = 90\%$ as compared to that in pure ACN solution. The enhancement in the emission intensity of PyPr + H⁺ may be attributed to the fact that relatively more twisting of the pyridyl substituent in PyPr + H⁺ in comparison with PyPr is supported by a relatively larger dihedral angle (N35C26C14C15 = 54.5 Å of PyPr + H⁺ vs N35C26C14C15 = 43.7 Å of PyPr) [Fig. 5.1.11 (a,b)] (supported by DFT calculations). Based on these facts and evidence, it is clear that due to the compact packing of PyPr + H⁺ in comparison with PyPr, there is a large increment of PL intensity. Furthermore, the lifetime of PyPr and PyPr + H⁺ were recorded in different water fractions with the resulting decay time in the range of 8.43 ns (for 0%) to 4.02 ns (for 90%) and 4.02 ns (for 0%) to 9.42 ns (for 90%) for PyPr and PyPr + H⁺, respectively (Fig 5.1.10 c). We calculated the quantum yield of PyPr and PyPr + H⁺ [10.2% (at $f_w = 0$, in MeOH), 30.8% (at $f_w = 30$), 15.7% (at $f_w = 90$), 14.3% (thin film) and 1.4% (at $f_w = 0$), 25.6% (at $f_w = 30$), 33.4% (at $f_w = 90$), 36.0% (thin film)], respectively which supports the AIEE nature of the compounds.

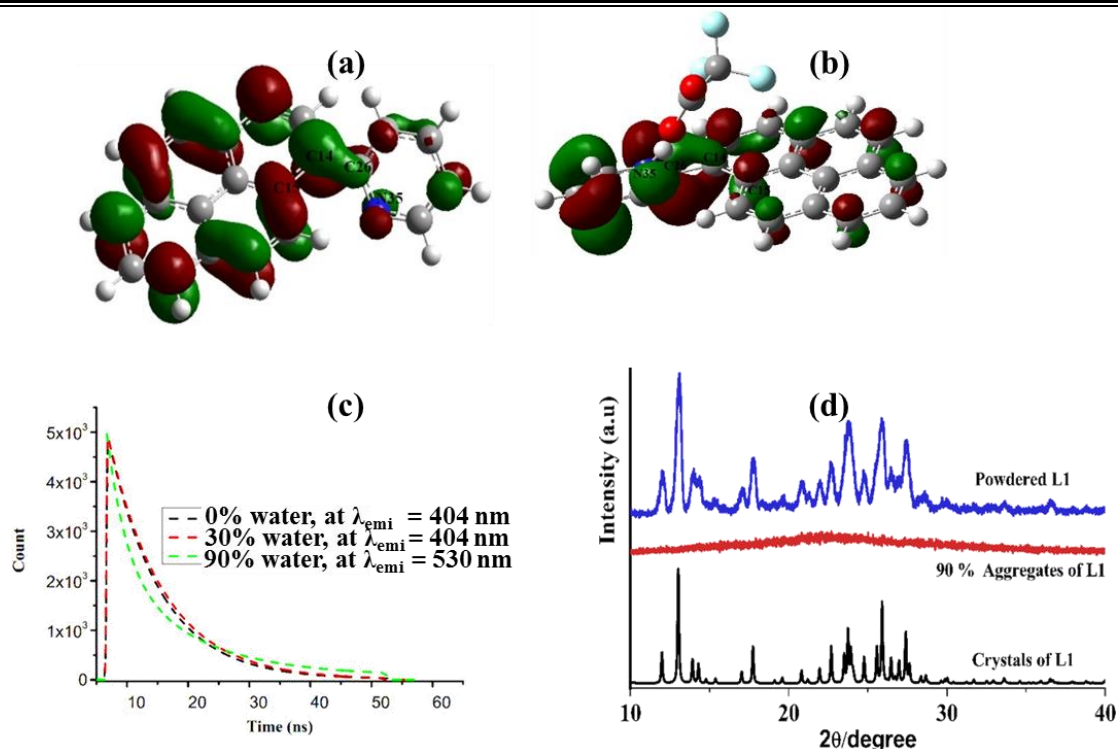


Figure.5.1.11 (a,b) LUMO level of PyPr and PyPr + H⁺ (c) Time-resolved fluorescence spectra of PyPr (0% water; black, 30% water; red, 90% water; green). (d) (i) Powder X-ray diffraction patterns of PyPr recorded for various states collected from (i) original form of PyPr, (ii) solid powder collected from 10:90 % MeOH: water mixture (iii) obtained from single-crystal data of PyPr.

e) Detection of nitroaromatic based explosives

The photoluminescence and UV-Visible absorption spectra of PyPr were recorded in the presence of different nitro aromatics along with a few non-nitro aromatic compounds such as (PA) picric acid, 3,5-dinitrotoluene (3,5 DNT), 2,4-dinitrophenol (2,5-NP), 1,3-dinitrobenzene (1,3 DNB), nitro toluene (NT), benzoic acid (BA) and phenol (P) [Fig. 5.1.12 (a,b)]. A new emission peak at $\lambda_{\max} = 522$ nm is observed with an overall quenching of fluorescence [Fig. 5.1.12 b(inset)] can be seen clearly in the image of PyPr in different explosives under UV lamp (365nm) (Fig 5.1.12 c). The absorption spectra also show a similar new peak absorbance at 390 nm with the gradual addition of PA (Fig.5.1.13 a). The results indicate the selectivity of PyPr toward PA. The emission spectrum of PyPr decreased gradually at 390 and 405 nm along with an additional new peak (522 nm) increase with increasing PA concentration (Fig 5.1.13 b). The newly appeared emission peak at 522 nm

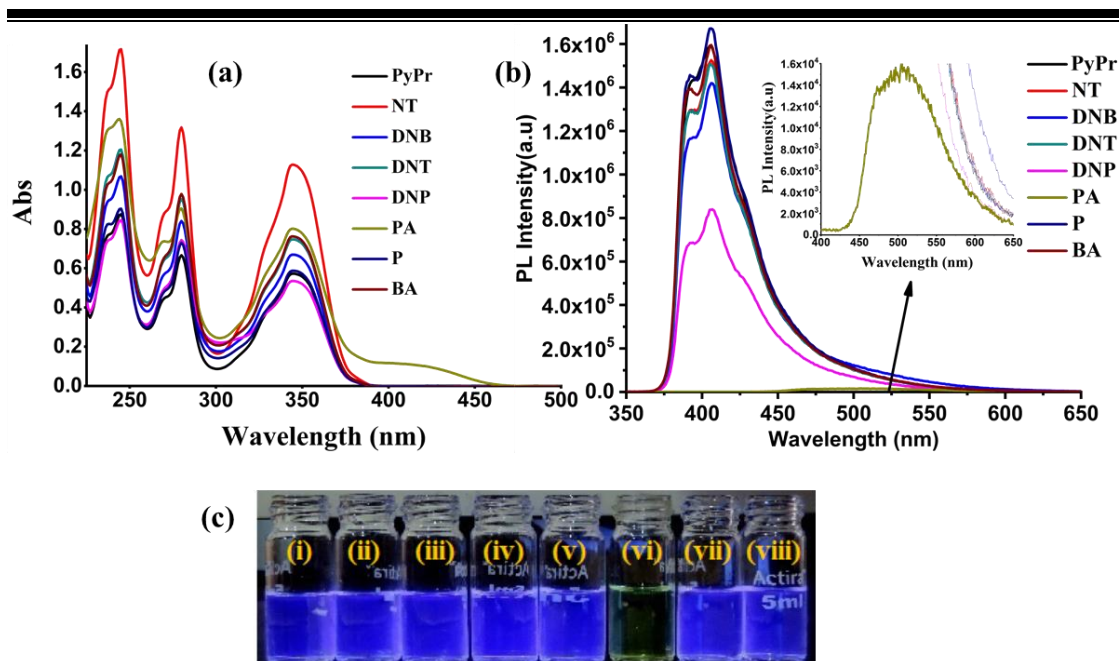


Figure 5.1.12 (a) Absorbance spectra of PyPr with $c = 1 \times 10^{-5}$ M upon the addition of 1 equivalent of different nitro-based explosive/non-explosive compounds (toluene, benzoic acid); (b) Emission spectra of different explosive/non-explosive compounds with PyPr; (c) It shows the image of PyPr with 1 equivalent of explosive/ non-explosive compounds, respectively (from left to right): (i) PyPr (blank); (ii) NT (4-nitrotoluene); (iii) DNB (1,3-dinitrobenzene); (iv) DNT (3,5-dinitrotoluene); (v) 2,4-DNP (2,4-dinitrophenol); (vi) PA (picric acid); (vii) P (phenol); (viii) BA (benzoic acid) (under $\lambda = 365$ nm excitation).

maybe attributed to the protonation at the nitrogen of the pyridyl. The ^1H NMR spectrum of PyPr-PA was recorded in CDCl_3 where the first proton peak (O-H) at $\delta = 9.23$ ppm of picric acid shifted to $\delta = 8.56$ ppm and a new deshielded peak at $\delta = 9.12$ ppm appeared, supporting the protonation on the pyridine ring (Fig. 5.1.13 d). The newly appeared peak at 410 nm in the UV-Visible spectra was indicative of charge-transfer in the system.[53] A linear relationship was obtained between the ratio of the emission intensities (I_{522}/I_{405}) and concentration of PA in the range of 5–100 mM (Fig. 5.1.13 c). For practical purposes, we can use this probe in basic and neutral medium. The detection limit of PA was calculated. The results are found to be 56 nM (12.82 ppb). By obtaining results from ^1H NMR (Fig. 5.1.13 d) and the UV-Vis spectra of PyPr in the presence of PA, the formation of a ground state charge transfer complex between PyPr and PA is proposed.[54] The formed complex isolated by mixing of PyPr and picric acid in DMF.

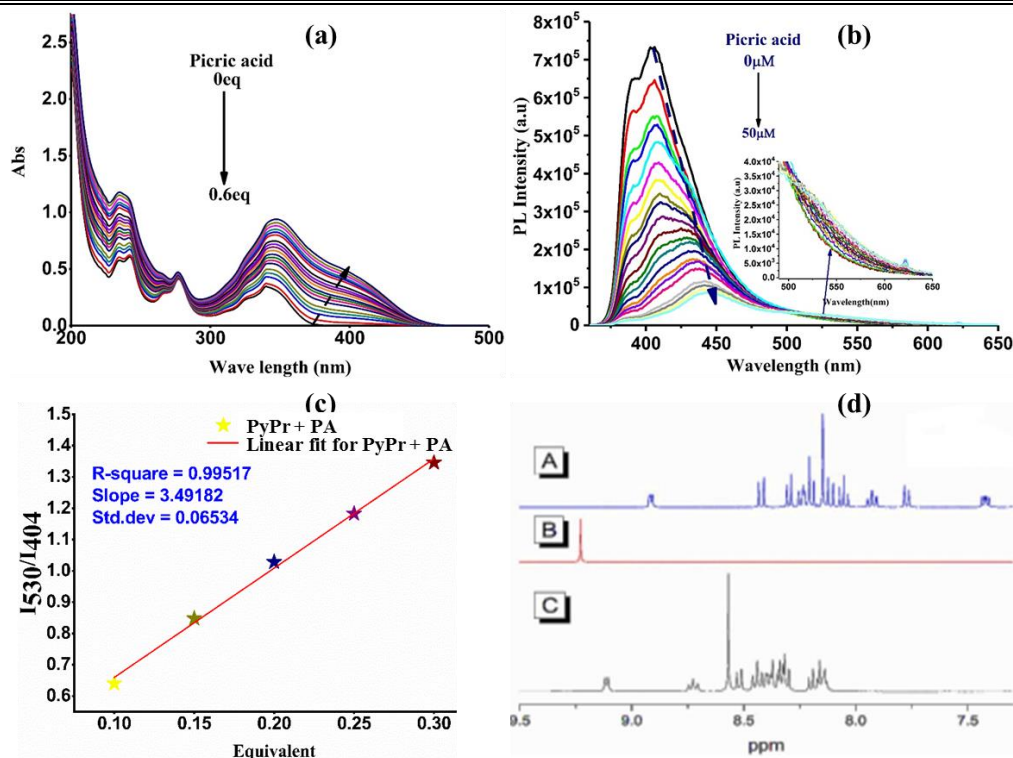


Figure 5.1.13 (a) The absorption spectra of PyPr in methanol (1×10^{-3} M) with a gradual increase in the PA (Picric acid) (1×10^{-3} M) concentration (solution of PA was prepared in methanol); (b) Emission spectra of PyPr (1×10^{-3} M) titrated with different concentration of PA; (inset a new peak at (522 nm) gradually increases with overall quenching of fluorescence) (c) linear fitting of PyPr with PA. (d) NMR spectra of (A) PyPr, (B) PA, and (C) PyPr + PA. The downfield ^1H signals in (C) indicate the presence of the strong interaction of PyPr with PA (PA = picric acid).

The intermolecular charge transfer followed by proton transfer was supported by the DFT (Gaussian 09) calculations. The energy difference between the LUMOs of PyPr and PA is 1.85 eV, whereas the energy difference between the HOMO–LUMO separations of PyPr is found to be 3.63 eV. The lower energy difference between the LUMOs of PyPr and PA facilitates the energy transfer between PyPr and PA (Fig 5.1.14 a). Along with the PET effect, we observed the overlapping of absorption spectra of PA in MeOH with the emission spectra of PyPr revealed the Resonance Energy Transfer (RET) occurring between PyPr and PA (Fig. 5.1.14 b) which lead to quenching the system. Based on this evidence, plausible mechanisms for PA detection may be occurring by both charge transfer and energy transfer between PyPr and PA.

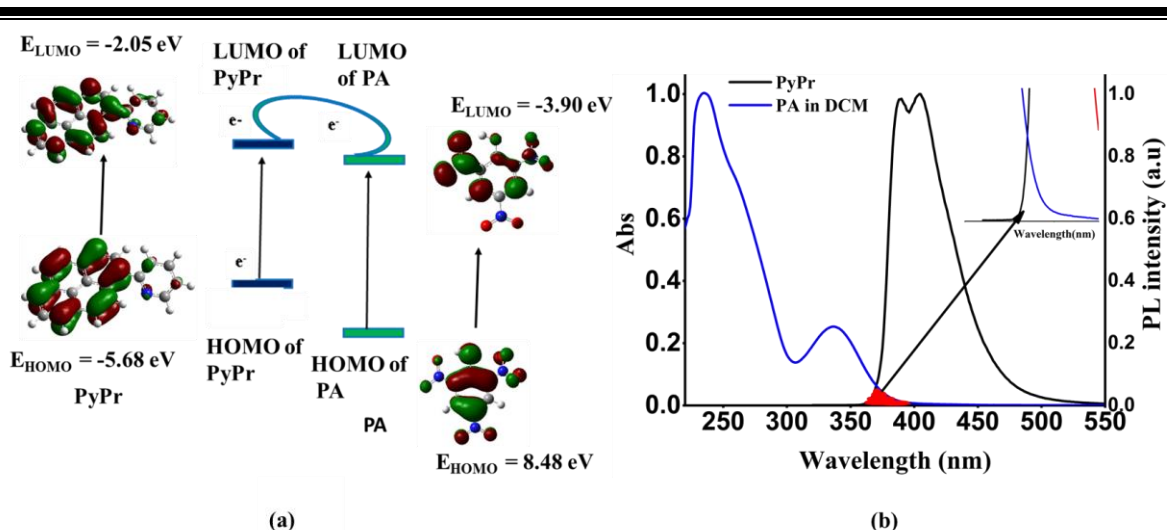


Figure 5.1.14 (a) Frontier molecular orbital images of HOMO and LUMO energy levels of PyPr (ligand) and Picric acid showing intermolecular charge transfer; LUMO of picric acid is less than LUMO of PyPr (b) Absorption spectra of PA and emission spectra of L1 in DCM; the spectral overlap between the emission of PyPr and the absorption of PA is shown in the inset.

Along with the detection of nitroaromatic explosive PyPr also sense Al^{3+} ion

f) Metal Ion Al (III) Sensing

The AIEE active organic molecule PyPr was screened with different metal ions with molecular formula M^{n+} such as $\text{Zn}(\text{II})$, Mg^{2+} , Ca^{2+} etc. We could observe ratiometric green emission ($\lambda_{\text{max}} = 388, 408$ and 524 nm) response only in the presence of Al^{3+} (Fig. 5.1.15 a). The interference of other metal ions maintaining the same conditions studied. It is represented with the bar diagram where the emission intensity of PyPr in the presence of the other metal ions (binary) is decreased after the addition of Al (III) (Fig. 5.1.15 b). The other cations used apart from Al (III) do not make any noticeable change in the emission colour under excitation at 365 nm (Fig. 5.1.15 c). To check the interference of other trivalent cations, PyPr was screened with the nitrates of La (III), Yb (III), Cr (III), Al (III), Eu (III), and Fe (III) (Fig 5.1.16 a). Among these ions, it is observed that Fe (III) and Cr (III) interfere and produce similar results with Al (III) (all these ions represent a common group of Group Separation of basic cations) (Fig 5.1.16 b). However, unlike the emission of Al (III), the emission intensity is low in Fe and Cr (III) (Fig. 5.1.16 c). UV-Vis and PL spectroscopic studies have been performed with increasing Al (III) concentration.

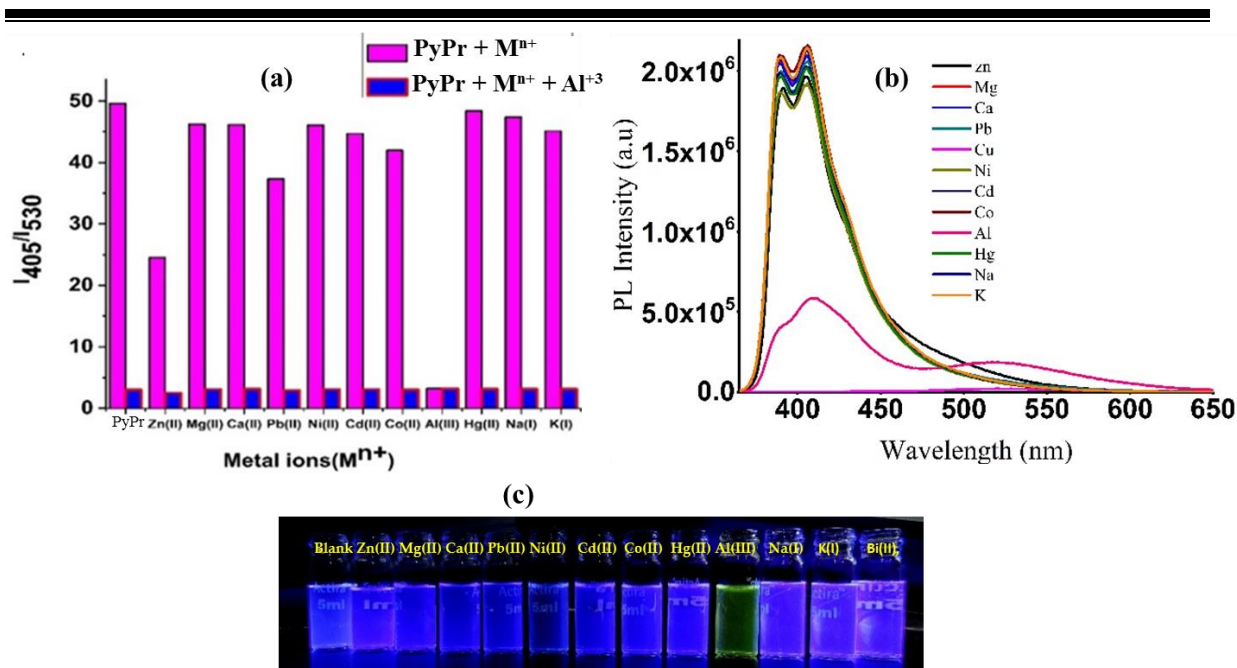


Figure 5.1.15 (a) Bar diagrams of the relative emission intensity of PyPr with different metal ions at I_{405}/I_{530} . Pink bars represent the addition of various metal ions to PyPr and blue bars represent the subsequent addition of Al^{3+} (1 equivalent) to the above-mentioned solutions (PyPr + different metal ions + Al^{3+}); (b) photoluminescence spectra of PyPr with $c = 10^{-3}$ M in methanol upon the addition of 1 equivalent of different metal ions; (c) Image of PyPr ($c = 10^{-3}$ M) in presence of 1 equivalent of different metal ions under excitation with a UV lamp ($\lambda_{max} = 365$ nm).

The UV-Vis spectrum of PyPr is shown to have some changes after the addition of Al (III); a continuous increment was observed at 390 nm, 342 nm and 278 nm, with the appearance of several isosbestic points (250 nm, 266 nm, 360 nm, 315 nm and 383 nm) (Fig. 5.1.16 d). The isosbestic points support a strong interaction occurring between PyPr and Al (III). The fluorescence titration experiment has resulted in a decrease in intensity at λ_{max} 390 and 405 nm with a new red-shifted emission observed at 525 nm (Fig. 5.1.16 e). A linear relationship was obtained in the range of 10–30 mM, which indicated the sensitivity of the ligand toward Al (III) (Fig. 5.1.16 f). The detection limit was estimated and found to be 2.3 nM (Fig 5.1.16 f). The change in the emission spectra indicated a strong complexation as observed between Al (III) with PyPr, which is supported by HRMS.

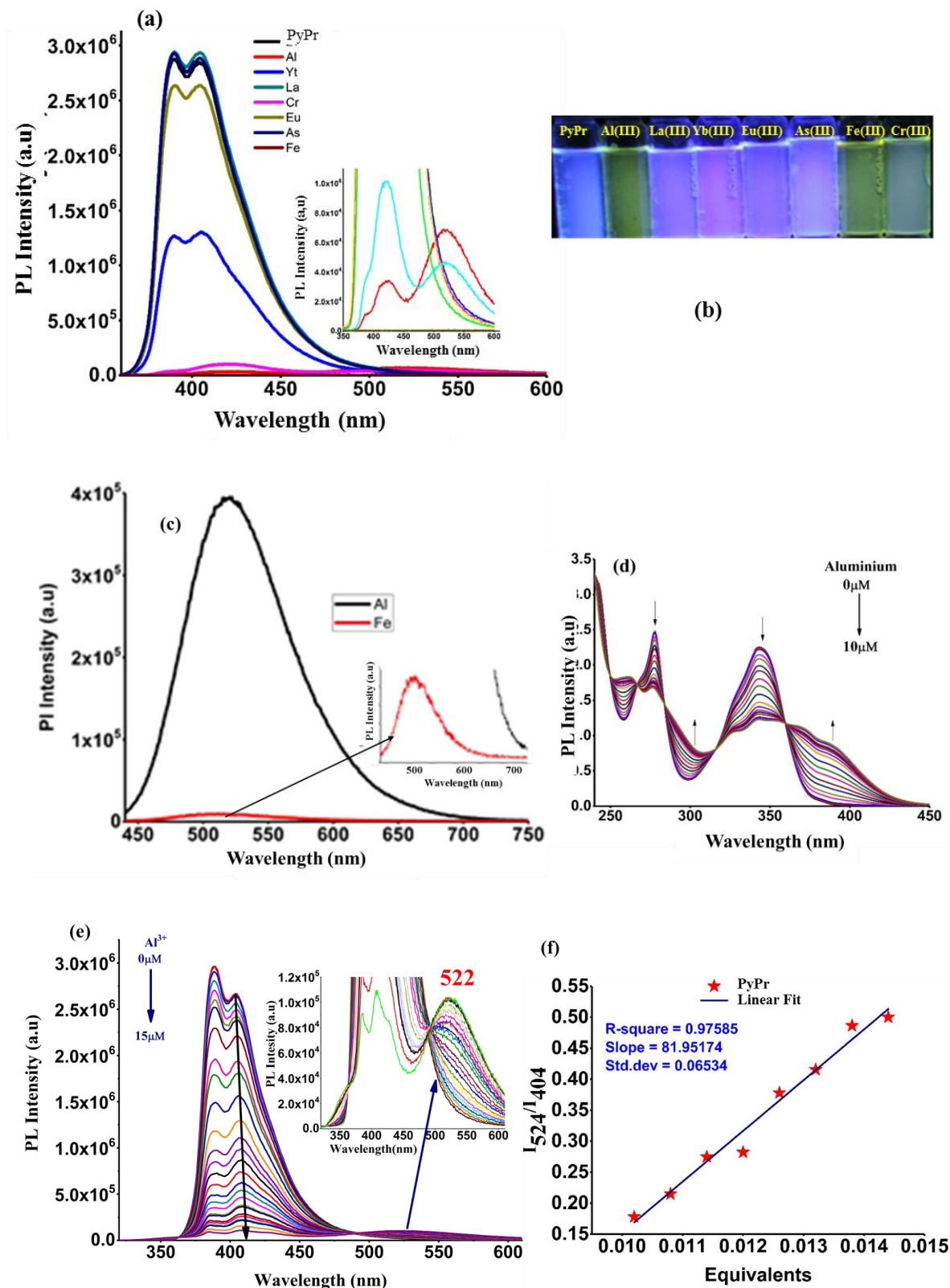
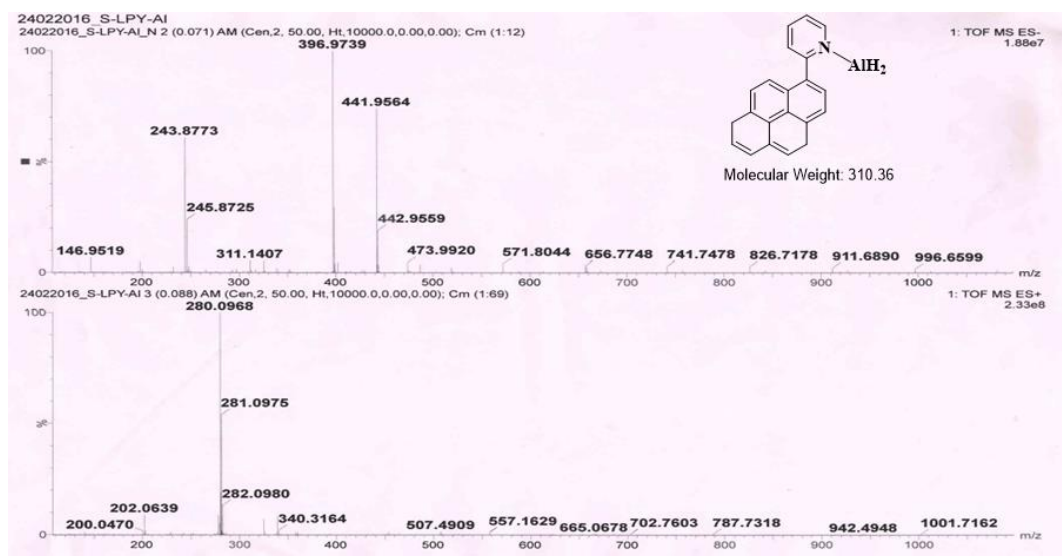


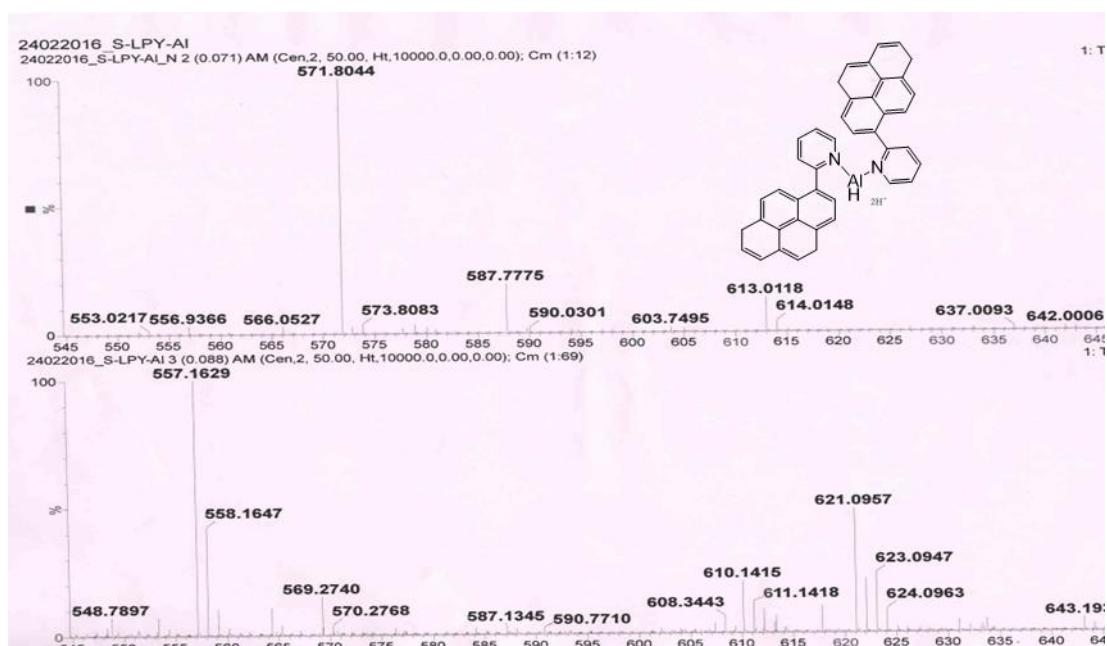
Figure 5.16 (a) The emission spectra of PyPr upon addition different trivalent metal ion. (b) image of PyPr ($c = 10^{-3} M$) with 1 equivalent of different trivalent metal ions, respectively; from left to right (under 365 nm UV lamp) (c) PL Intensity comparison between PyPr in the presence of Al(III) and Fe(III) (d) The absorption spectra of PyPr ($1 \times 10^{-3} M$) with gradual

Chapter 5

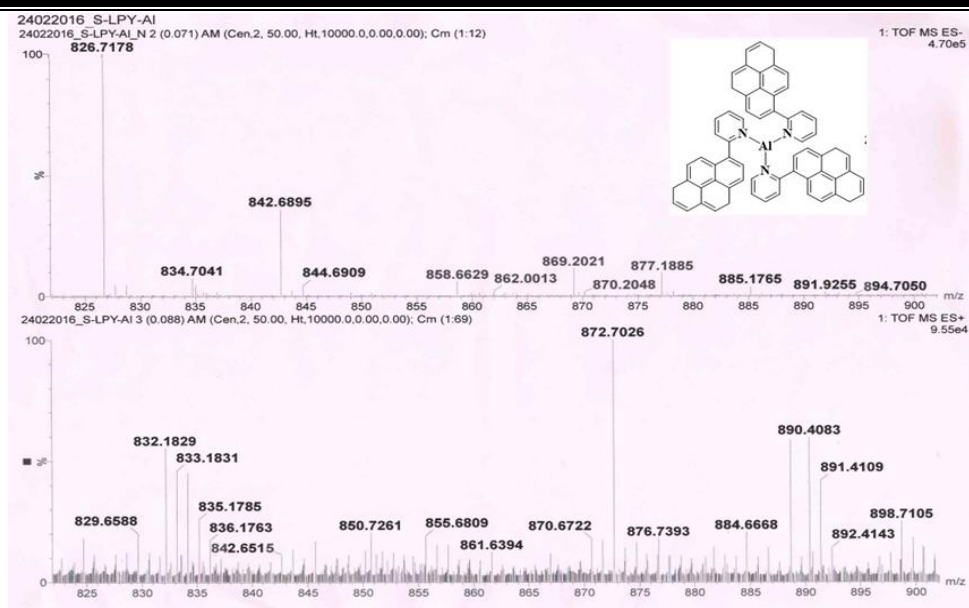
increase in the Al^{3+} ($1 \times 10^{-3} \text{M}$) concentration; (e) Emission spectra of PyPr ($1 \times 10^{-3} \text{M}$) titrated with different concentration of Aluminium nitrate; (f) Linear fitting of PyPr with the Al^{3+}



(a)



(b)



(c)

Figure 5.1.17 HRMS of PyPr with Al^{3+} (a) $[\text{Al}(\text{PyPr})+\text{H}]^+$ (b) $[\text{Al}(\text{PyPr})_2+2\text{H}]^+$, (c) $[\text{Al}(\text{PyPr})_3+3\text{H}]^+$

The ESI-HRMS measurements on a mixture of PyPr and 4.0 equivalent of Al (III) show a peak at m/z 872.36 which is assigned for $[\text{Al}(\text{PyPr})_3 + 2\text{H}]$, along with other fragments such as m/z 590.23 and 309.113 attributed to $[\text{Al}(\text{PyPr})_2 + \text{H}]$ and $[\text{Al}(\text{PyPr}) + \text{H}]^+$, respectively (Fig. 5.1.17 a,b,c). The reproducibility of the PyPr–Al complex was confirmed by PL measurement, where the addition of ethylene diamine tetraacetic acid (EDTA) to the Al^{3+} coordinated complex restored the emission of PyPr (Fig 5.1.18 a,b).

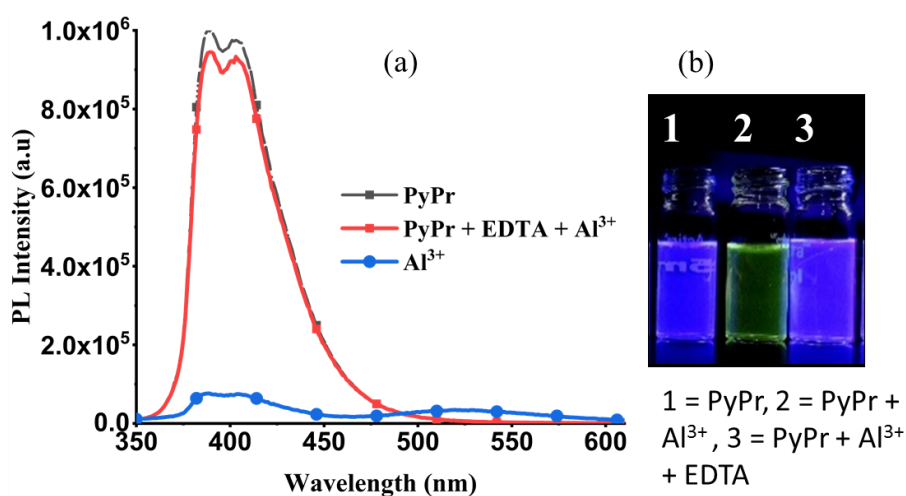


Figure 5.1.18 (a) PL emission spectra of PyPr in the presence of EDTA and Al^{3+} (b) Photograph of PyPr in the presence of EDTA and Al^{3+} . (365nm)

Section II Strategic Modification of Pyrene-derivatives to Improve Sensitivity in Explosive Sensing

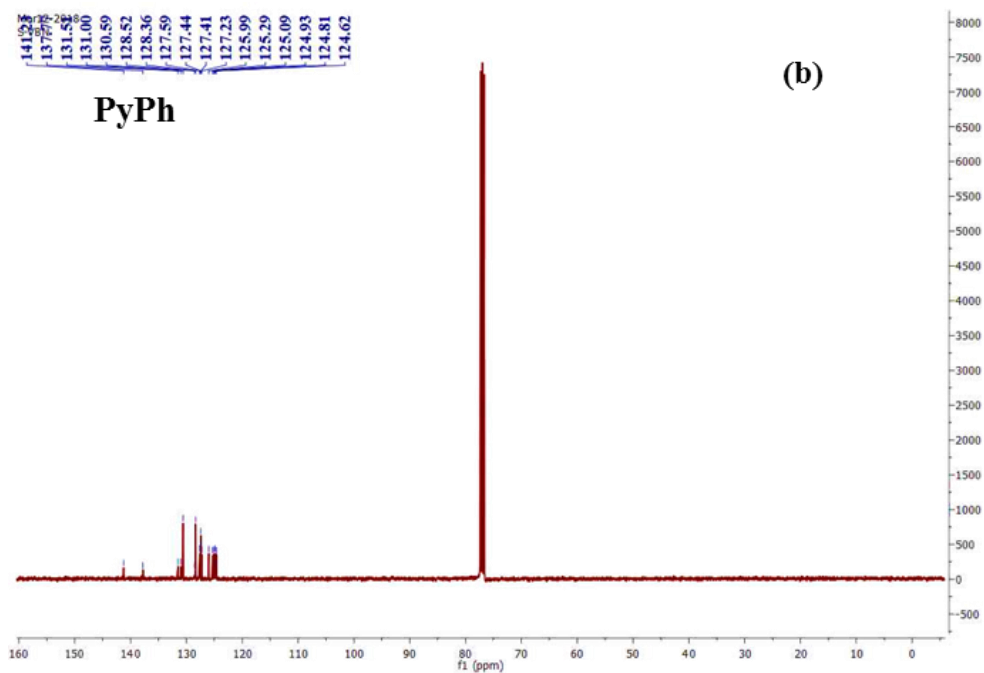
5.1.2 Introduction

Based on the result obtained by PyPr for detection of a nitroaromatic explosive and after the extensive literature survey, we found that most of the designed probes are based on Donor-Acceptor (D-A) type in nature.[10, 55, 56] Among the various mechanism for sensing nitro explosives Photo-induced electron transfer (PET) and energy transfer (ET) are mainly focused on designing the D-A type of probes.[55,56] These type of molecules has the advantage to have an easy variation of the structures to improve the sensitive and selective detection of the explosives. From the DFT calculations of PyPr, it was observed that in the pyrene-pyridine system the HOMO mainly localized on the pyrene and LUMO on pyrene (major) and pyridine (minor). Therefore, we got an idea that to improve the sensitivity of the probes, one way to increase sensitivity is to improve the quantum efficiency of AIE materials, on the other way is to facilitate the electron transfer process from the LUMO of the probes to the LUMO of explosive, the energy separation of LUMO (donor)-LUMO (acceptor) should be optimized. Therefore, considering these facts, design and syntheses of other four organic molecules with a D-A character carried out with a systematic variation of the substituents on the substituted pyrene, in the same framework of PyPr.

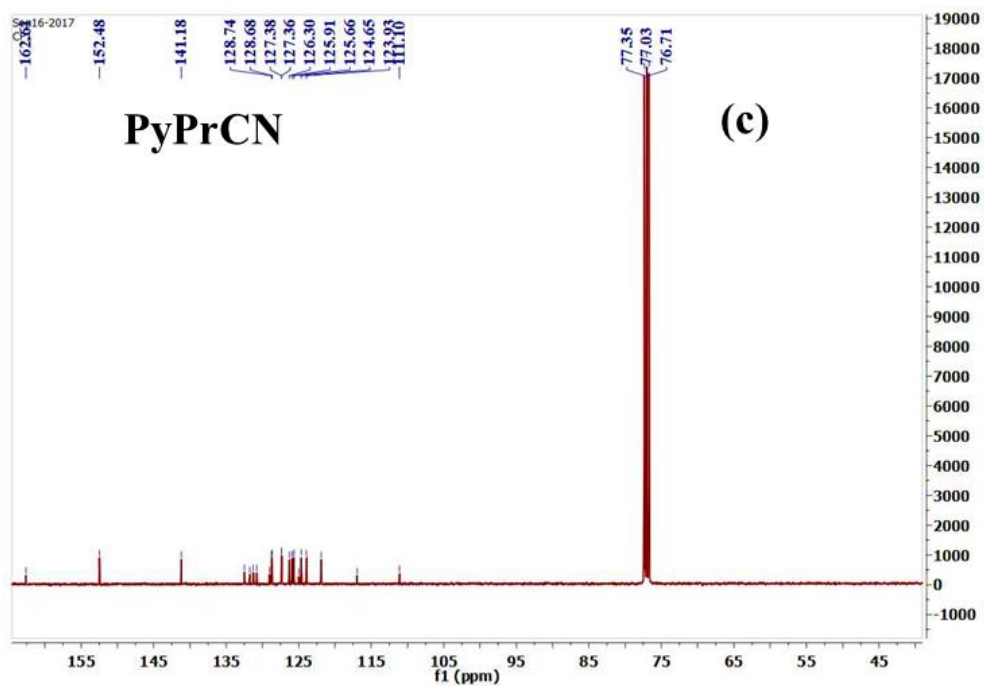
5.1.2.1 Result and Discussion

i) Synthesis and Characterization

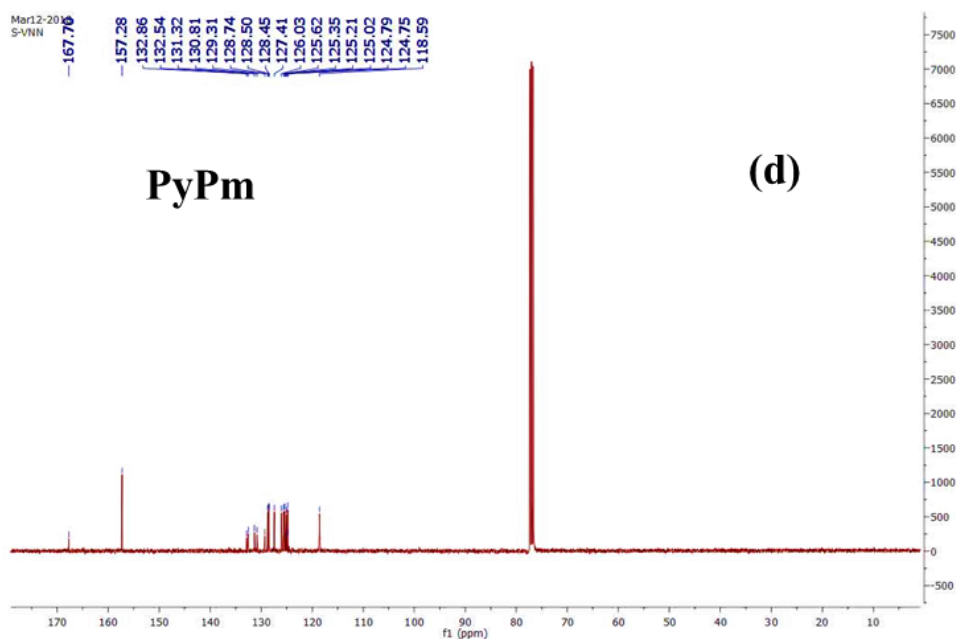
Synthesis of the compound (phenyl pyrene (PyPh), 2-(pyrene-1-yl)nicotinonitrile (PyPrCN), 2-(pyrene-1-yl)pyrimidine (PyPm), 2,4-dichloro-6-(pyrene-1-yl)-1,3,5-triazine (PyTr)) was carried out by the reaction of pyrene-1-boronic acid, and 2-Bromo substituted pyridine by the Suzuki coupling reaction and the product obtained was pyrene substituted pyridine derivative (PyPh-PyTr) (Scheme 5.1.2). ¹H, ¹³C and mass spectroscopy characterized these.



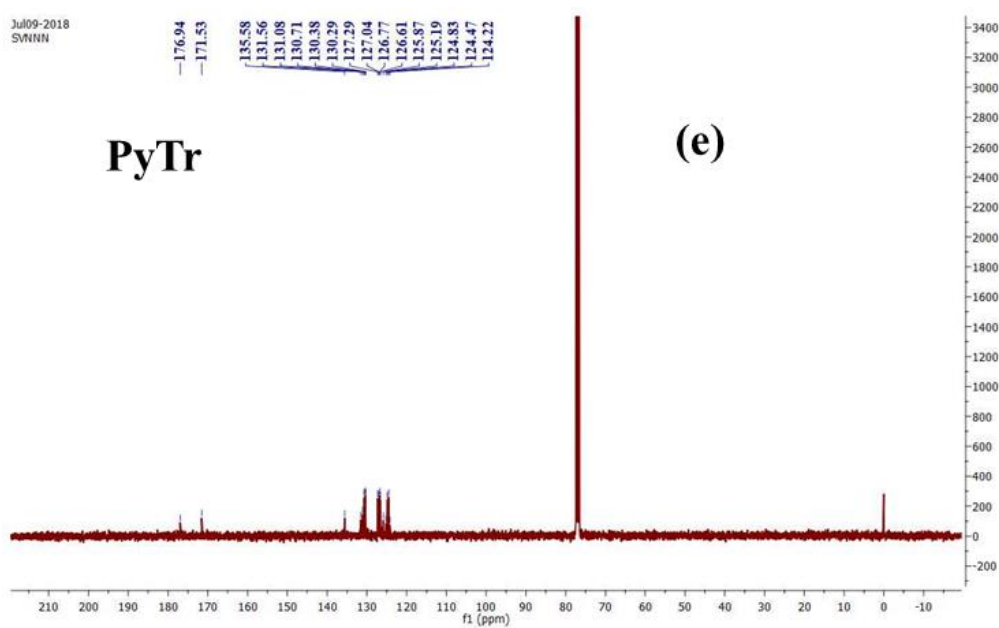
¹³C NMR spectrum of PyPh



¹³C NMR spectrum of PyPrCN



^{13}C NMR spectrum of PyPm



^{13}C NMR spectrum of PyTr

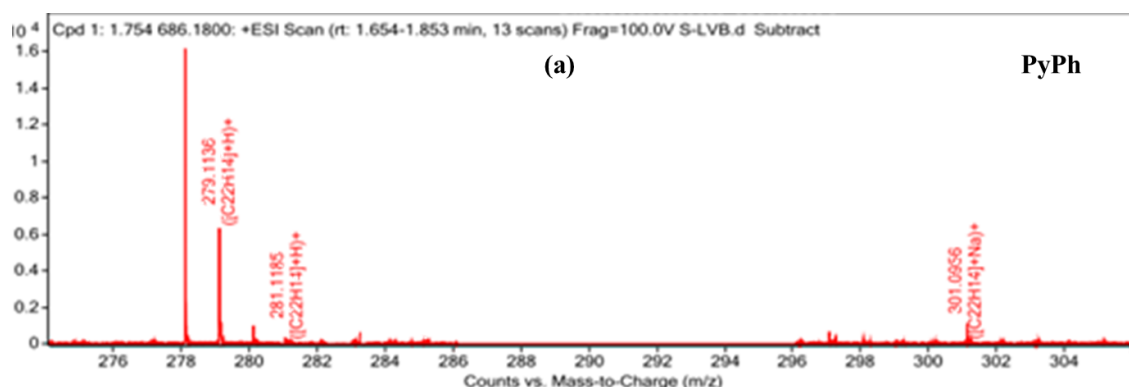
Figure 5.1.19 (a) ^1H NMR spectra of PyPh, PyPrCN, PyPm & (b-e) ^{13}C NMR spectra of PyPh, PyPrCN, PyPm & PyTr

Chapter 5

PyPh:- δ ^1H NMR (400 MHz, CDCl_3) 8.29 – 8.17 (1H, m), 8.13 (1H, s), 8.03 (1H, dd, J 14.9, 8.0), 7.70 – 7.64 (1H, m), 7.60 (1H, t, J 7.4), 7.52 (1H, t, J 7.3). δ ^{13}C NMR (100 MHz, CDCl_3) 141.23, 137.77, 131.51, 131.00, 130.59, 128.52, 128.36, 127.59, 127.44, 127.41, 127.23, 125.99, 125.29, 125.09, 124.93, 124.81, 124.62. HRMS data 279.1136 at m/z $[\text{M}+\text{H}]^+$ corresponds to the major fraction. PyPrCN:- δ ^1H NMR (400 MHz, CDCl_3) 9.07 (1H, dd, J 4.9, 1.8), 8.34 (1H, d, J 7.9), 8.29 – 8.23 (2H, m), 8.24 – 8.11 (4H, m), 8.08 (1H, t, J 7.6), 8.01 (1H, d, J 9.2). δ ^{13}C NMR (100 MHz, CDCl_3) 162.61, 152.48, 141.18, 132.48, 131.74, 131.29, 130.79, 129.02, 128.74, 128.68, 127.38, 127.36, 126.30, 125.91, 125.66, 124.99, 124.65, 123.93, 121.90, 116.95, 111.10, 77.35, 77.03, 76.71. HRMS data 305.1069 at m/z $[\text{M}+\text{H}]^+$ corresponds to the major fraction.

PyPm:- δ ^1H NMR (400 MHz, CDCl_3) 9.06, 9.05, 9.02, 8.65, 8.63, 8.33, 8.31, 8.26, 8.25, 8.24, 8.21, 8.19, 8.18, 8.17, 8.16, 8.08, 8.06, 7.39, 7.37, 7.36, 7.28. δ ^{13}C NMR (100 MHz, CDCl_3) 167.70, 157.28, 132.86, 132.54, 131.32, 130.81, 129.31, 128.74, 128.50, 128.45, 127.41, 126.03, 125.62, 125.35, 125.21, 125.02, 124.79, 124.75, 118.59. HRMS data 280.1069 at m/z $[\text{M}+\text{H}]^+$ corresponds to the major fraction.

PyTr δ ^1H NMR (400 MHz, CDCl_3) 9.51 (1H, d, J 9.5), 9.01 (1H, d, J 8.3), 8.35 (3H, dd, J 11.7, 5.3), 8.29 (2H, dd, J 8.6, 5.9), 8.18 – 8.12 (2H, m). δ ^{13}C NMR (100 MHz, CDCl_3) 176.94, 171.53, 135.58, 131.56, 131.08, 130.71, 130.38, 130.29, 127.29, 127.04, 126.77, 126.61, 125.87, 125.19, 124.83, 124.47, 124.22. HRMS data 350.0240 at m/z $[\text{M}+\text{H}]^+$ corresponds to the major fraction.



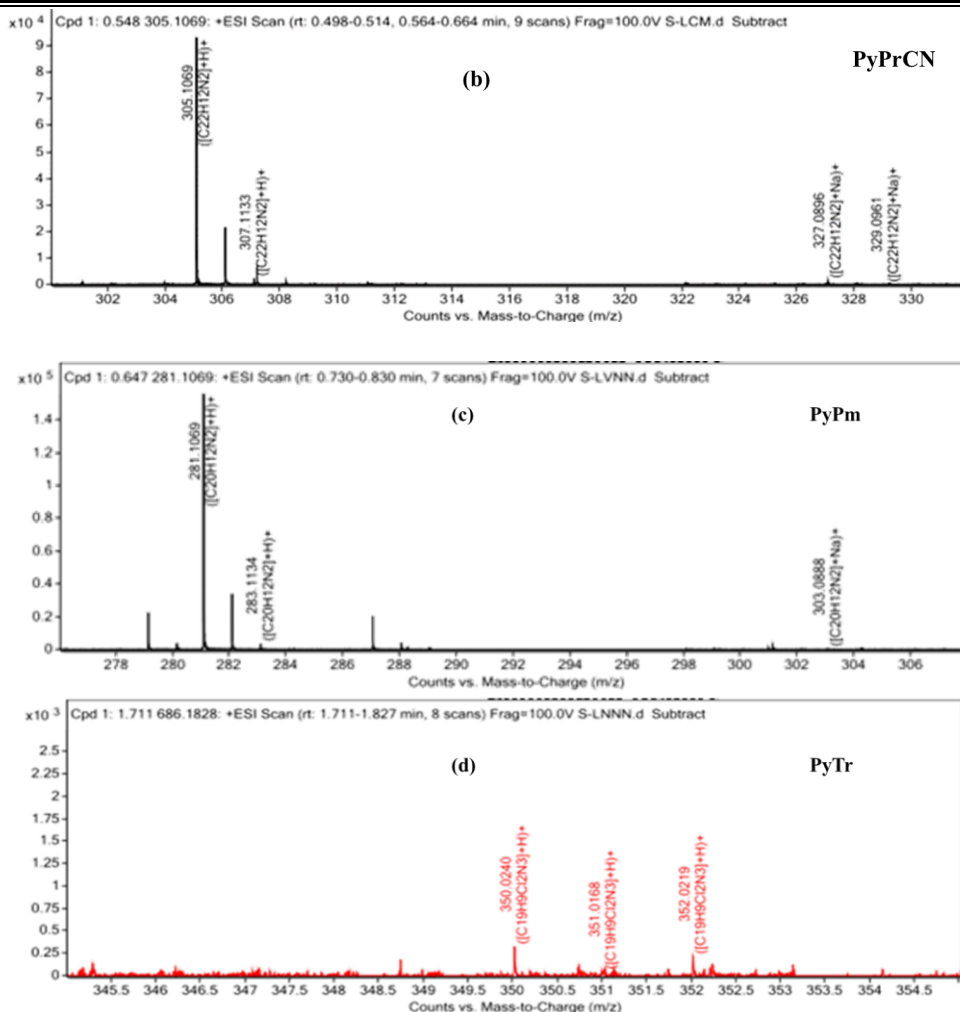


Figure 5.1.20 HRMS mass spectra of (a) PyPh (b) PyPrCN (c) PyPm (d) PyTr

ii) Photophysical properties

a) Absorption and Emission Spectra

Here all the synthesized probes (PyPh, PyPrCN, PyPm & PyTr) exhibited similar absorption pattern with a gradual red shifting observed for the higher wavelength transition. By the DFT calculation, all the absorption peak have been correlated with the experimental absorptions (Table 5.1.2). In all the probes, the set of transition in the range, 245- 421 nm corresponds to the characteristic peak of π - π^* transition of the pyrene chromophore in monomeric form.[45] In the case of PyPrCN, the solution itself has broad absorption peak due to the strong electron-withdrawing group in ortho position which increases the charge separation in between the donor and acceptor group resulting in a red-shifted broad peak. The PyPm pyrimidine based molecule results in a slightly red-shifted terminal absorption band, but the chlorosubstituted pyrazine based molecule (PyTr) results to a larger extent of the red-shifted

terminal absorption band in comparison to PyPrCN (Fig 5.1.21 a). In the emission spectra of the solution and solid-state, the bathochromic shift is visible from PyPh to PyTr (Fig 5.1.21 b, c). In PyPm (the molecule containing the pyrimidine) has the vibronic structure, in the solution emission spectra. However, it has the bathochromic shift ($\lambda_{\max} = 402$ and 421 nm) in comparison with PyPr.

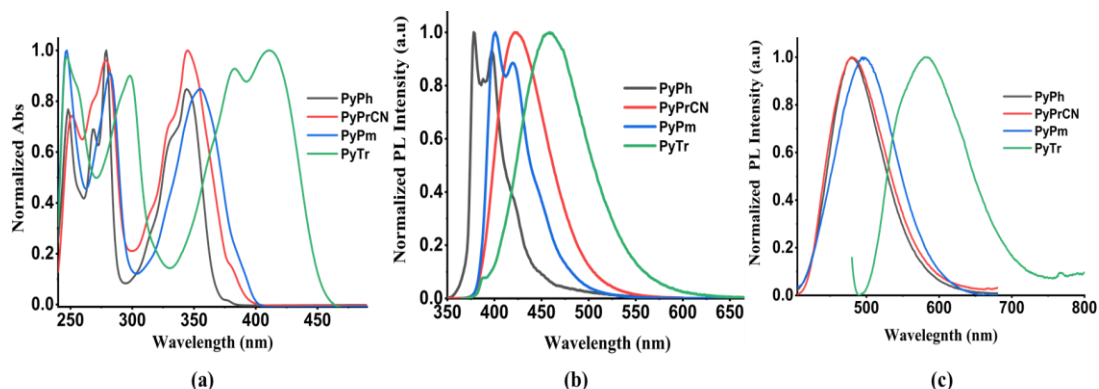


Figure 5.1.21 (a) Absorption spectra of PyPh, PyPrCN, PyPm & PyTr respectively in solution state (1×10^{-4} M) (b) Emission spectra of PyPh, PyPrCN, PyPm & PyTr respectively in solution (c) Emission spectra of PyPh, PyPrCN, PyPm & PyTr respectively in solution solid state.

Table 5.1.2 Calculated significant orbital excitation contributions (%), energy difference (in eV), obtained from electronic transitions analysis with TDDFT (B3LYP) method for PyPh, PyPrCN, PyPm & PyTr

Probe Molecule	States	Major orbital excitation contribution (%)	Energy gap (eV)	Calculated λ_{\max} (nm) oscillator strength in brackets (B3LYP)	Experimental λ_{\max} (nm), molar absorptivity in brackets ($L \text{ mole}^{-1} \text{ cm}^{-1}$)
PyPh	$S_0 \rightarrow S_1$	HOMO \rightarrow LUMO (92)	3.41	362(0.5721)	376 (8188) 343(6401)
	$S_0 \rightarrow S_2$	HOMO \rightarrow LUMO+1 (56)	3.65	339(0.0022)	329(2726)
	$S_0 \rightarrow S_3$	HOMO \rightarrow LUMO+2 (83)	4.14	299(0.0074)	279 (9561)
	$S_0 \rightarrow S_4$	HOMO-1 \rightarrow LUMO (52)	4.36	284(0.4163)	268(6838)
	$S_0 \rightarrow S_4$	HOMO \rightarrow LUMO+3(57)	4.43	279(0.0377)	
PyPrCN	$S_0 \rightarrow S_1$	HOMO \rightarrow LUMO (83)	3.12	396 (0.2003)	385 (1068)
	$S_0 \rightarrow S_2$	HOMO \rightarrow LUMO+1 (77)	3.43	360 (0.2441)	345 (9989)
	$S_0 \rightarrow S_3$	HOMO-1 \rightarrow LUMO+1 (42)	3.65	339 (0.0439)	332 (7237)
	$S_0 \rightarrow S_4$	HOMO \rightarrow LUMO+2 (66)	3.85	321(0.0703)	314 (3634)
	$S_0 \rightarrow S_5$	HOMO-1 \rightarrow LUMO+1(43)	4.10	302(0.0643)	279 (9536)
PyPm	$S_0 \rightarrow S_1$	HOMO \rightarrow LUMO (95)	3.08	401 (0.6818)	392 (1043)
	$S_0 \rightarrow S_2$	HOMO-1 \rightarrow LUMO (48)	3.48	355 (0.0269)	355 (8493)
	$S_0 \rightarrow S_3$	HOMO-2 \rightarrow LUMO (94)	3.71	333(0.0076)	328 (7023)
PyTr	$S_0 \rightarrow S_1$	HOMO \rightarrow LUMO (97)	2.76	449 (0.6191)	415 (9963)
	$S_0 \rightarrow S_2$	HOMO \rightarrow LUMO+1 (51)	3.38	373 (0.0432)	382 (9269)
	$S_0 \rightarrow S_3$	HOMO \rightarrow LUMO+1 (47)	3.83	366 (0.0436)	363 (6009)
	$S_0 \rightarrow S_4$	HOMO-2 \rightarrow LUMO (86)	4.00	323(0.0415)	298 (9002)
	$S_0 \rightarrow S_5$	HOMO \rightarrow LUMO+2 (78)	4.12	309(0.1561)	288 (7746)

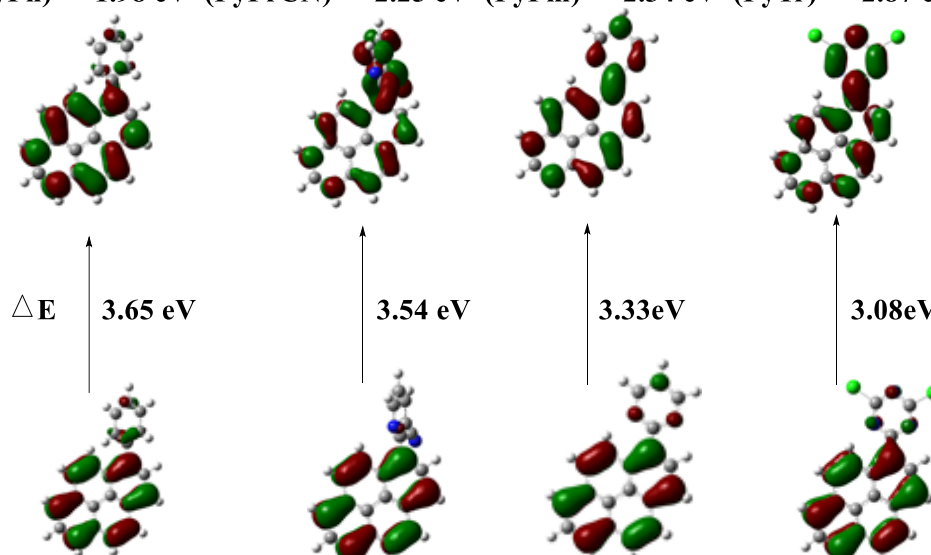
PyTr has more bathochromic shift with a broad peak at $\lambda=475\text{nm}$. Usually, most of the polyaromatic hydrocarbons show the excimeric emission in the solid-state due to the π - π stacking effect of the electron cloud in flat aromatic rings. In solid-state, the maximum emission wavelength (λ_{max}) for the compounds, PyPh-PyTr increased sequentially, and the compound PyTr showed a large solid-state emission spectral shift (119nm) [λ_{max} : 477nm for PyPh to 596 nm for PyTr (Fig. 5.1.21 c). It is observed that the energy gap and LUMO level is decreasing from PyPh to PyTr. HOMO sites distributed throughout the pyrene ring in all the probes. LUMO varies, PyPh has LUMO majorly in pyrene, PyPrCN majorly in pyridine ring and on cyano group, PyPm LUMO lies in both pyrene and pyridine ring (major) and PyTr major in triazine ring and minor percentage in pyrene (Fig. 1.5.22). From the above emission spectra and DFT-based calculations, it is observed that as the ring nitrogen increases the electron-withdrawing capacity increases, hence the energy of the LUMO state gets lowered.

b) AIEE property study

AIEE property for all the probes investigated separately with gradually increasing water fraction (f_w) in tetrahydrofuran (THF). The emission spectra for all the compounds (PyPh, PyPrCN, PyPm & PyTr) (concentration 10^{-4} M) were recorded for all the different water-fraction, f_w (0–90) %. In PyPh the emission intensity gradually enhanced up to 70% ($\lambda_{\text{max}} = 398$ nm), then above 80% with the appearance of a new peak at $\lambda_{\text{max}} = 480$ nm the emission intensity starts to decrease. At 90% water fraction, the emission intensity of red-shifted peak at $\lambda_{\text{max}} = 480$ nm increases [Fig. 5.1.23 (a, b & c)] To investigate the AIEE mechanism in PyPh, we have recorded the PL spectra by increasing the concentration of PEG 400 (PEG = polyethylene glycol) 0 to 90% [Fig.5.1.23 (d, e)]. The emission intensity increases as viscosity increases (in PyPh), and it shows a maximum at 90%, indicating the phenyl ring substituted on pyrene act as rotor group. Due to the intermolecular restriction in the aggregated state, the emission intensity is enhanced (Fig.5.1.23 e). The calculation of quantum yield of different water fraction has been made to 4.58% (at $f_w = 0$ in THF), 14.01% (at $f_w = 30$), 39.4% (at $f_w = 90$), respectively which supports AIEE nature of the compounds for PyPh. Similar experiments carried out on all the probe molecules (PyPrCN, PyPm & PyTr). In PyPrCN, one can observe the red-shifted emission spectra with a decrease in the intensity up to 80% from, $\lambda_{\text{max}} = 424$ nm to 456 nm. At 90%, there is an increment in the intensity with the

appearance of a new peak at 483nm [Fig. 5.1.24 (a, b, c)]. The emission peak of PyPm is similar to PyPh with little bathochromic structured peak ($\lambda_{\max} = 402$ nm, 421nm). The emission intensity increases with increasing water concentration by up to 60%. The peak structure also changes from structure to a broader peak.

$$E_{\text{LUMO}} (\text{PyPh}) = -1.98 \text{ eV} \quad (\text{PyPrCN}) = -2.25 \text{ eV} \quad (\text{PyPm}) = -2.34 \text{ eV} \quad (\text{PyTr}) = -2.87 \text{ eV}$$



$$E_{\text{HOMO}} (\text{PyPh}) = -5.63 \text{ eV} \quad (\text{PyPrCN}) = -5.79 \text{ eV} \quad (\text{PyPm}) = -5.67 \text{ eV} \quad (\text{PyTr}) = -5.95 \text{ eV}$$

Figure 5.1.22 Frontier molecular orbital image of HOMO and LUMO energy levels of ligands calculated by using B3LYP/6-31++g(d,p) as implemented on Gaussian09.

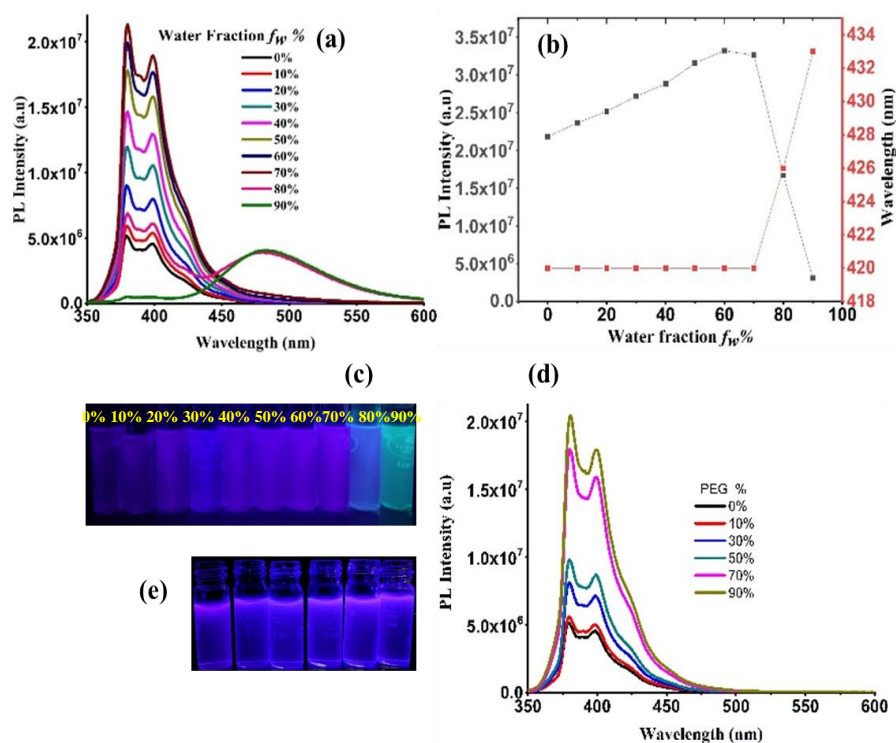


Figure.5.1.23 (a) Emission spectra of PyPh (1×10^{-4} M) in different fractions of water in THF (b) Plot of intensity (I) values of PyPh versus the compositions of the aqueous mixtures (c) Images of the emission of PyPh in THF–water mixtures with different water volume fractions (f_w) taken under UV illumination ($\lambda_{exc} = 365\text{nm}$); (d) Emission spectra of PyPh with increasing concentration of PEG. (e) Image of L with increasing viscosity taken under UV illumination ($\lambda_{exc} = 365\text{nm}$)

While increasing the water concentration beyond 60%, the PL intensity gets decreased [Fig. 5.1.25 (a, b, & c)]. In the case of PyTr, it is observed a red-shifted emission with decreasing peak intensity of 533 times from $\lambda_{max} = 475$ nm to $\lambda_{max} = 597$ nm with increasing water fraction (Fig. 5.1.25 e, f & g). Both in PyPrCN and PyPm, the emission intensity increases with increasing the concentration of PEG. (Fig 5.1.24 (d) & Fig 5.1.25 d).

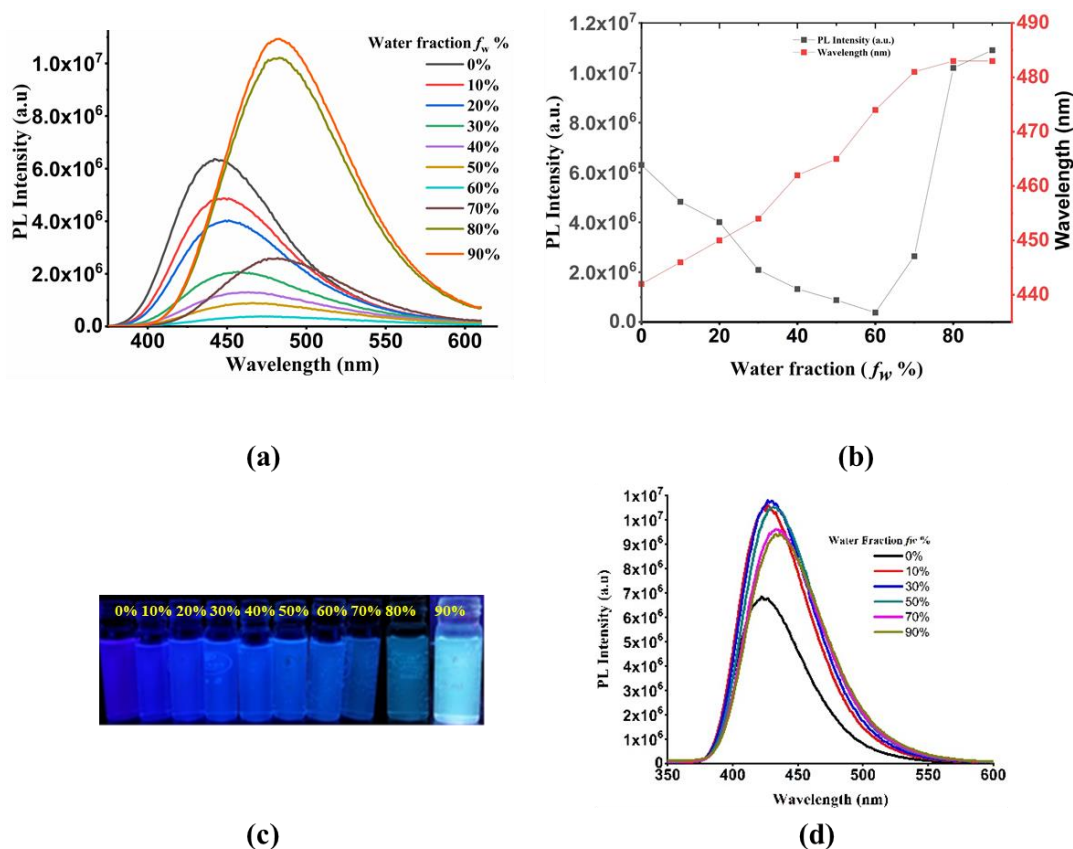
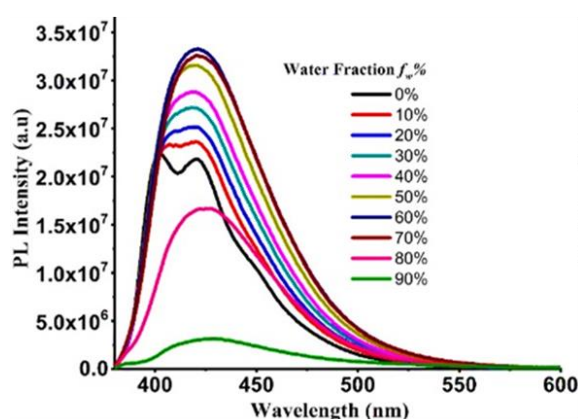
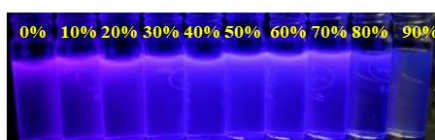


Figure.5.1.24 (a) Emission spectra of PyPrCN (1×10^{-4} M) in different Water/THF (0-90%) (b) Plot of intensity (I) values of PyPh versus the compositions of the aqueous mixtures (c) Images of the emission of PyPrCN in THF–water mixtures with different increase water fractions (f_w) taken under UV illumination ($\lambda_{exc} = 365\text{nm}$); (d) Emission spectra of PyPrCN with increasing concentration of PEG

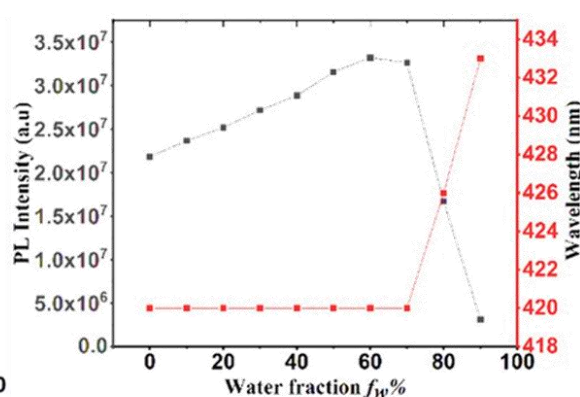
In PyTr, the bathochromic shift in emission spectra and the decreased quantum yield as observed in Table 5.1.3 with increasing water fraction is by the energy gap-law. To investigate the mechanism, we need to have a deeper understanding of the crystal structure. From the crystal packing of PyPrCN, one could observe five short contacts CN1—H22 (2.728 Å), CN1—H17 (2.671 Å) and C19—H13 (2.735 Å), CN1-H5 (2.722 Å) and N2—H3 (2.708 Å) (Fig. 5.1.26 a, b). It is observed that the cyano group acts as a bridge between the two adjacent layers of molecules (Fig. 5.1.26 c). The overall packing in crystals reveals that arrangement of molecules in the crystal is in a zig-zag manner from head to tail which indicates the formation J aggregates with π - π interaction and Interaction and the slippage angle $R^1 = 20.4^\circ < 32^\circ$, which support the formation of j aggregates (Fig. 5.1.26 d).



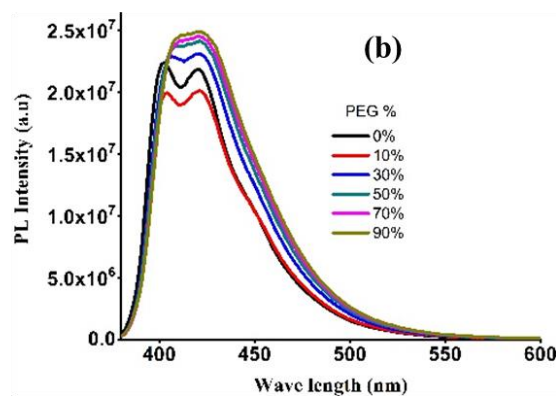
(a)



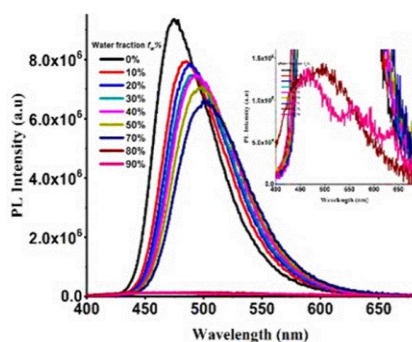
(c)



(b)



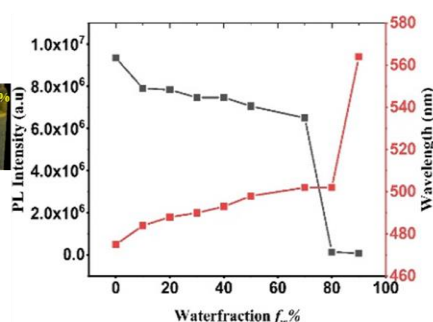
(d)



(e)



(f)



(g)

Figure 5.1.25 (a, e) Emission spectra of PyPm & PyTr (1×10^{-4} M) in different Water/THF (0-90%), respectively (b, g) Plot of intensity (I) values of PyPm & PyTr versus the compositions of the aqueous mixtures, respectively (c, f) Images of the emission of PyPm & PyTr in THF–water mixtures with different increase water fractions (f_w) taken under UV illumination ($\lambda_{exc} = 365\text{nm}$); (d) Emission spectra of PyPm with increasing concertation of PEG. (e) Emission spectra of PyTr (1×10^{-4} M) in different Water/THF (0-90%).

Table 5.1.3 Details of the absolute quantum yield of probes with increasing water fraction in THF

Probes	f_w (%)	0	10	20	30	40	50	60	70	80	90	Thinflim
PyPh		4.5	9.5	9.5	14.0	15.7	20.8	30.5	36.6	34.8	35.4	40.4
PyPrCN		38	42	44.5	47.8	49.7	52.3	53.1	53	21	40.6	42.4
PyPm		40.4	45.5	46.2	55.5	56.4	57.5	58.3	54.3	30.4	41.6	45.5
PyTr		76.8	68.0	66.3	65.0	63	62	58	42	6	4.	49.2

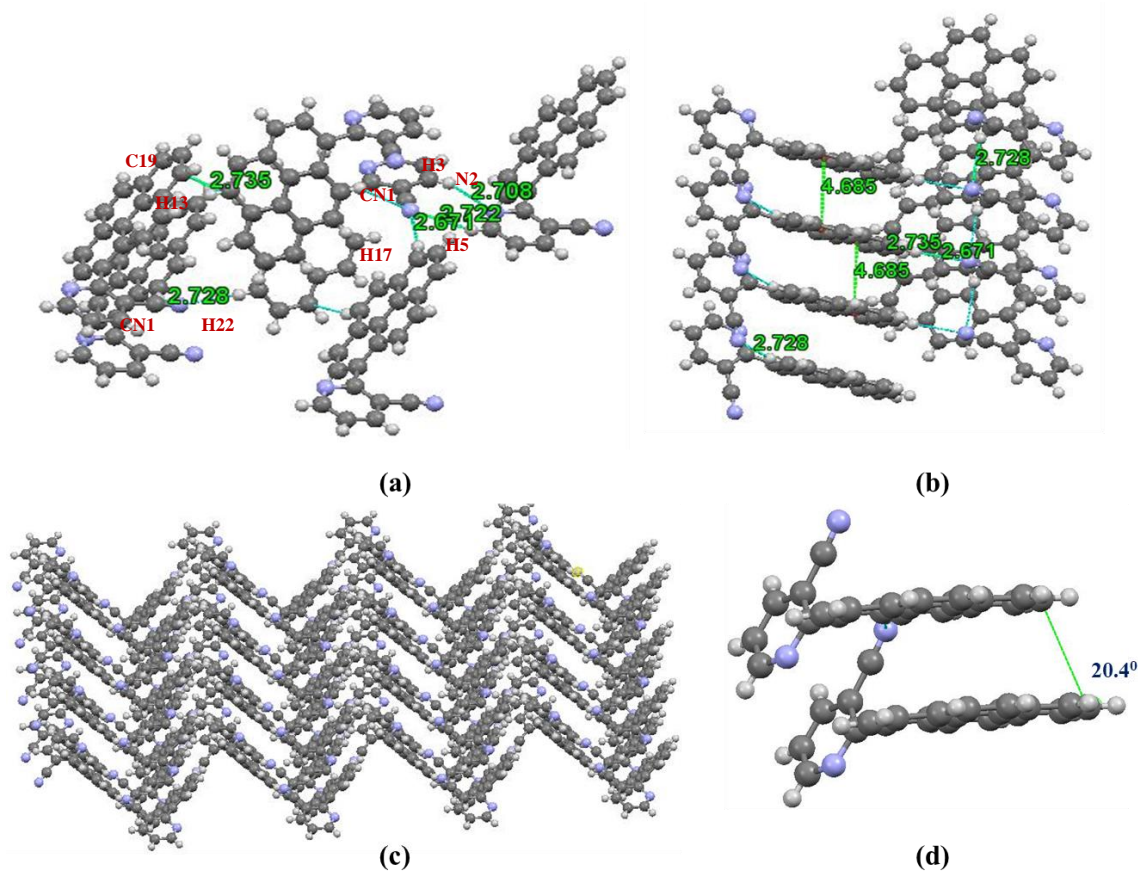


Figure 5.1.26 (a) The packing diagram of PyPrCN showing short intermolecular contacts, (b) CN1---H22 (2.728 Å), CN1---H17 (2.671 Å), CN1-H5 (2.722 Å), C19---H13 (2.735 Å), N2---H3 (2.708 Å) and π - π interaction (4.65 Å) (c) Showing Zig- Zag packing structure of L2 and (d) Slippage angle is $R^1 = 20.4^\circ$ (J-aggregate $R^1 < 32^\circ$).

In PyPrCN the distance between the flat pyrene rings is more, i.e., 4.685 Å (Fig 5.1.26 b) which is beyond the limit of π - π stacking interaction, therefore we may neglect the presence of π - π stacking interaction. In the single-crystal structure of PyPm, two short contacts have been observed of distance 2.886 Å & 2.624 Å (Fig 5.1.27 a, b) and in between the flat pyrene rings, it is observed that the distance is more 3.873-3.872 in comparison with PyPr(3.53–3.59 Å) (Fig 5.1.27 a). In PyPm there are two nitrogens in a ring both have short contacts with a neighbouring unit (Fig 5.1.27 b) which might be the cause for the increased distance in between two pyrene rings. The increased distance and short contacts may make the excimer formation in the higher concentration of water fraction (above 70%). The formation of the excimer may be the reason for the decrease in the emission intensity (λ_{\max} 423) above 70% water fraction of PyPm (Fig 5.1.25 b).

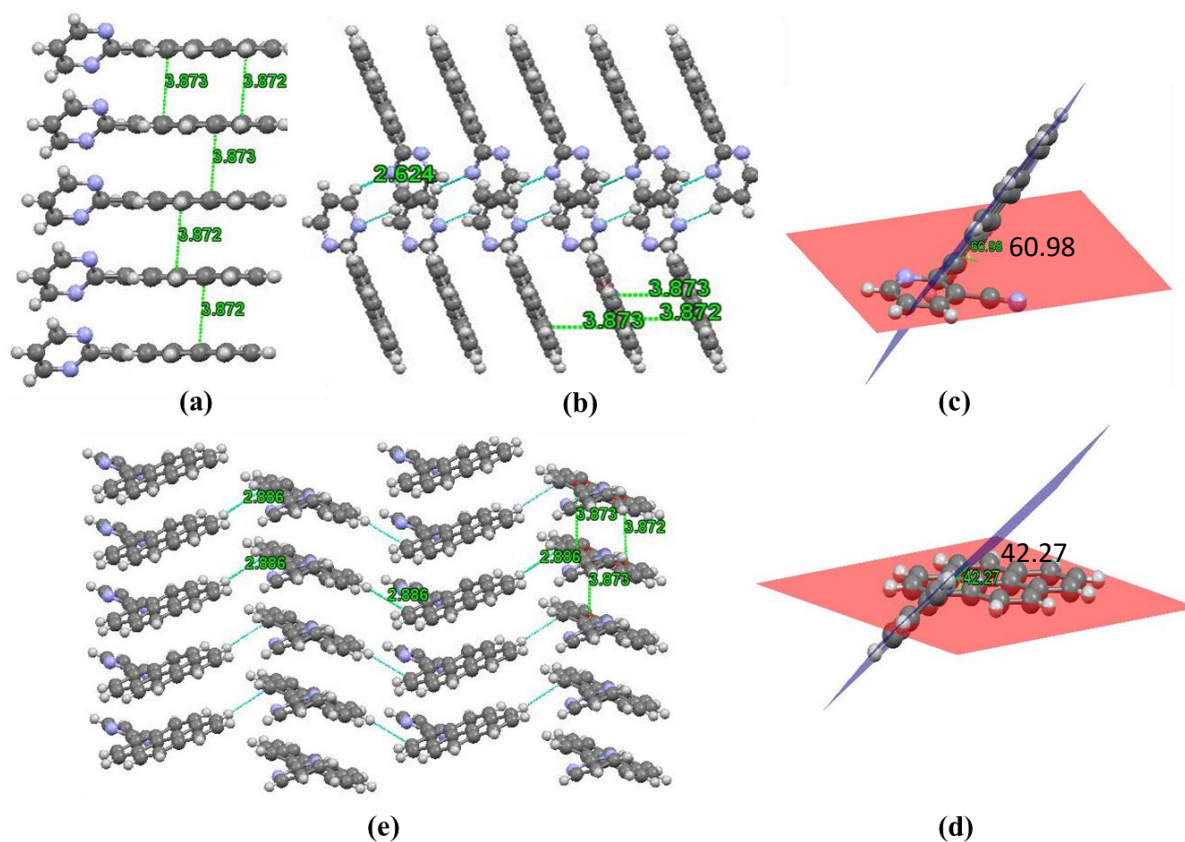


Figure 5.1.27 PyPm Crystal packing (a) shows a strong π - π interaction between the centroids of the two pyrene rings with short contact in the range of 3.872-3.873 Å, (b), (e)

Packing diagram shows the interaction of N1---H13 2.624 Å, C16---H6.886 Å, Indicating the dihedral angle (between the two planes passing through pyrene and pyridine substituted ring) of (c) PyPrCN and (d)PrPm

In PyPrCN, the dihedral angle between the plane passing through the pyridine and pyrene ring is more than PyPm (60.98° vs 42.27°) [Fig 5.1.27 (c, d)] (because of the presence of the cyano group the ring is little more twisted and also act as a bridging that makes the separation in between the pyrene rings (Fig 5.1.26 a,b,c)).

c) Excimer formation

The concentration-dependent emission spectra have been recorded for all the probes. Except PyPrCN remaining probes shows the prominent excimeric and monomeric emission [Fig. 5.1.28 (a, b, c, d)].

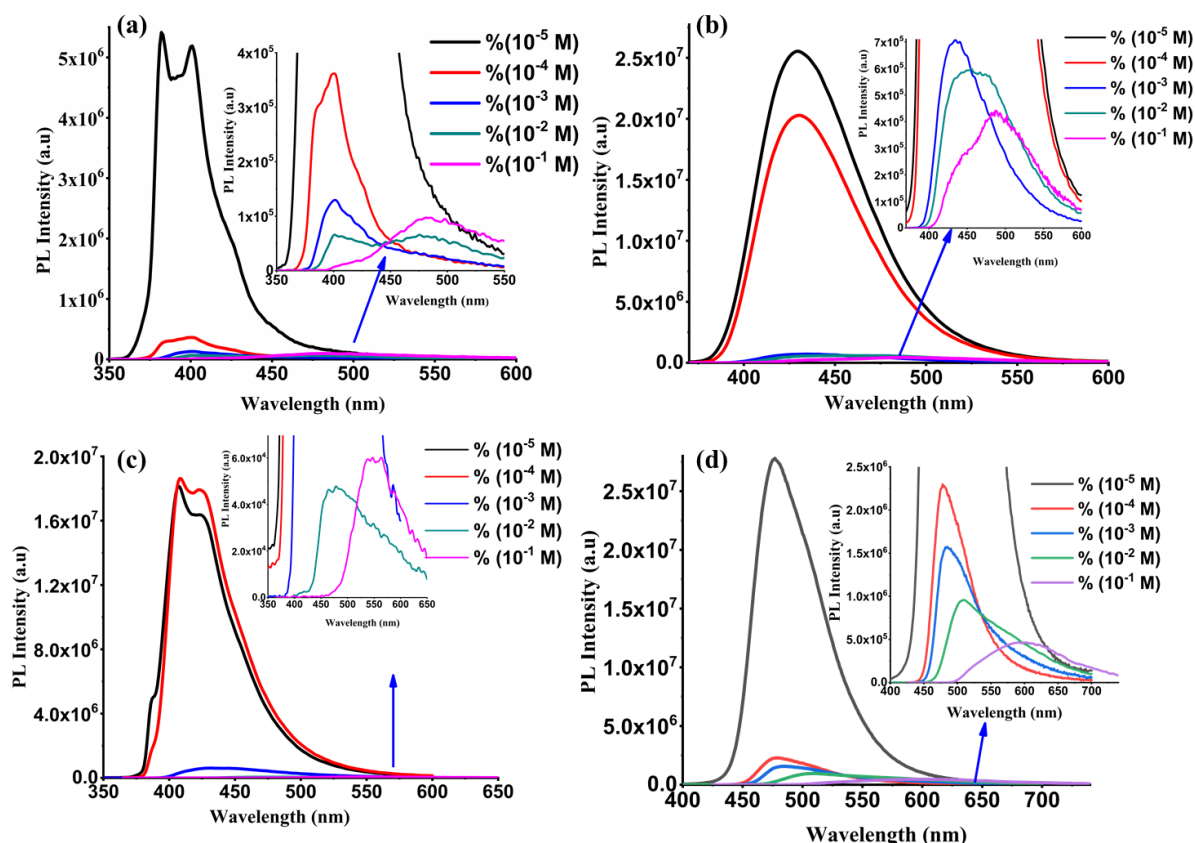


Figure. 5.1.28 Emission spectra of all the probe with varying the concentration from 10^{-1} M to 10^{-5} M solution in DCM (a) PyPh (b) PyPrCN (c) PyPm (d) PyTr.

The presence of cyano group present in the ortho position of nitrogen in PyPrCN the pyridine ring is little more twisted and also cyano act as bridging in crystal packing of PyPrCN.

Because of these consequences of cyano in PyPrCN tries to make a separation in between the pyrene causing interference in excimeric emission.

The quantum yield of (PyPh, PyPrCN & PyPm) (Table 5.1.3) increases with increasing the water fraction in water/THF mixed solvent, which supports the AIEE nature.

d) Explosive sensing

The probes (PyPh, PyPrCN, PyPm and PyTr) screened by various nitroaromatic explosive and non-explosive materials. The emission and absorption spectra of all the probes recorded in the presence of nitroaromatic and non-nitro aromatic compounds such as PA=picric acid, NT=nitro toluene, DNT = dinitrotoluene, DNP = dinitrophenol, NB = nitrobenzene, DNB = dinitrobenzene, DNBz = dinitrobenzoic acid, AmNP = aminonitrophenol, Nbz = nitro benzaldehyde, Bz = Benzene. Image of emission of all the probes (PyPh, PyPrCN, PyPm and PyTr) were taken in the presence of explosives under UV lamp (365nm) indicating the high selectivity towards the PA and less towards the DNP, ANP. [Fig. 5.1. 29 (a-d)]

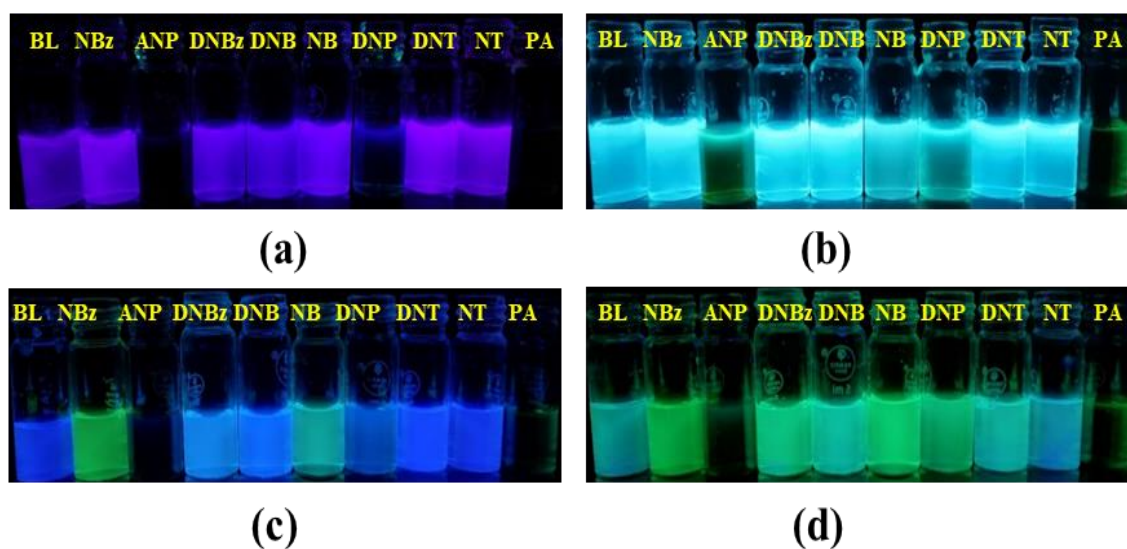


Figure 5.1.29 Image of the probe in THF (1×10^{-4} M) with 1 equivalent of explosive under UV lamp (365nm) respectively (a) PyPh (b) PyPrCN (c) PyPm (d) PyTr. PA=picric acid, NT=nitrotoluene, DNT = dinitrotoluene, DNP = dinitrophenol, NB = nitrobenzene, DNB = dinitrobenzene, DNBz = dinitrobenzoic acid, ANP = aminonitrophenol, Nbz = nitro benzaldehyde.

It was observed that in the absorption spectra of PyPh, PyPrCN, PyPm and PyTr a new peak appears in the presence of PA at longer wavelength $\lambda_{\max} = 422, 424, 430$ & 430 nm, respectively (Fig. 5.1.30 a-h). The same result observed in absorption spectra with gradually

increasing the concentration of PA concerning probes, the peak at $\lambda_{\max} = 422, 424, 430$ and 430 nm, respectively appears (Fig. 5.1.30 a-d). The result indicates the selectivity of the probes towards the picric acid. In the emission spectra, the peak of PyPh at $\lambda_{\max} = 378, 396$ nm decreases, in PyPrCN the peak at $\lambda_{\max} = 422$ nm, in PyPm peak at $\lambda_{\max} = 401, 420$ nm and in the PyTr the peak at $\lambda_{\max} = 459$ nm decreases gradually with increasing the concentration of the PA (Fig. 5.1.31 a-h). A linear relationship was obtained with plotting the graph in-between PL intensity of PyPh vs the concentration of PA for all the probes PL intensity of PyPh vs the concentration of PA for all the probes (Fig. 5.1.31 i-k). We have calculated the detection limit using the method $3\sigma/m$ (sigma (σ) is standard deviation of probe, $m =$ slope) [57] of PA, and it has been found to 73 nM (16 ppb) for PyPh, 29 nM (6.6 ppb) for PyPrCN, 8 nM (1.8 ppb) for PyPm and 0.5 nM (0.114 ppb/114 ppt) for PyTr

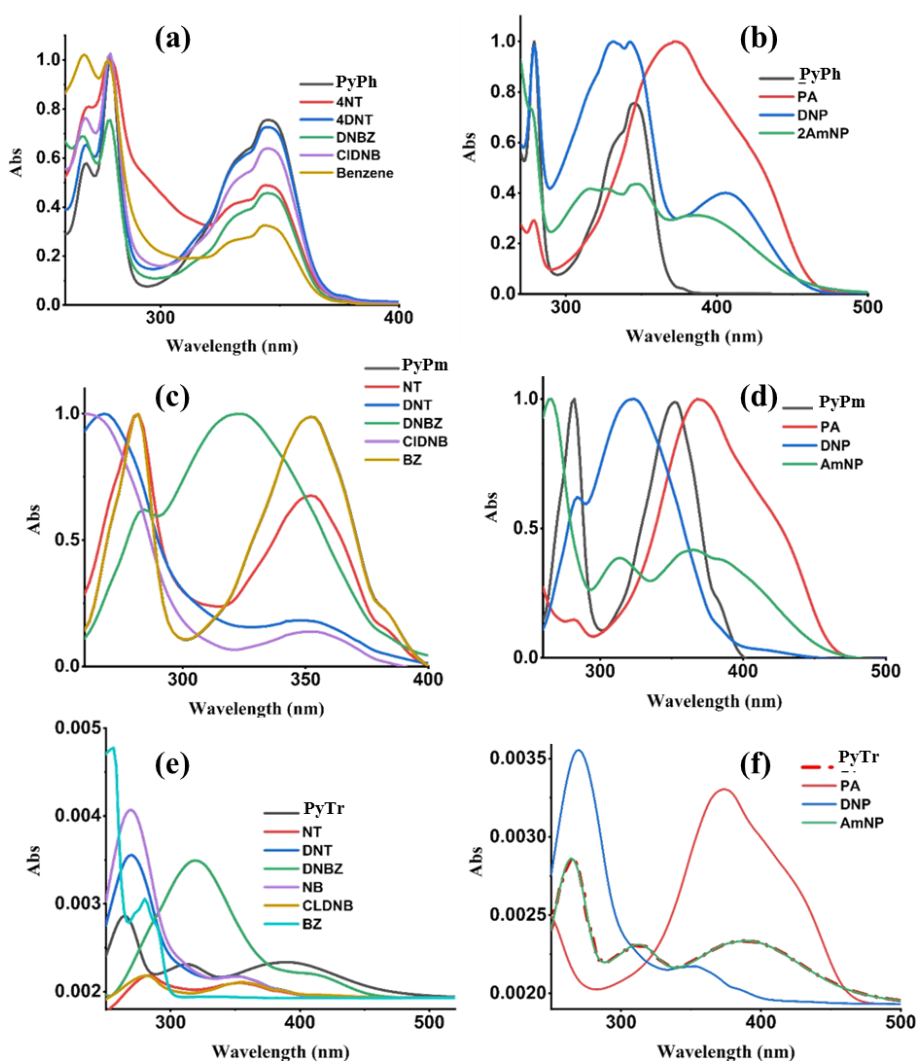


Figure 5.1.30 Absorption spectra of probes in presence of explosive materials (1 eq) (a, b) PyPr (1×10^{-5} M) (c, d) PyPm (1×10^{-5} M) (e, f) PyTr (1×10^{-6} M)

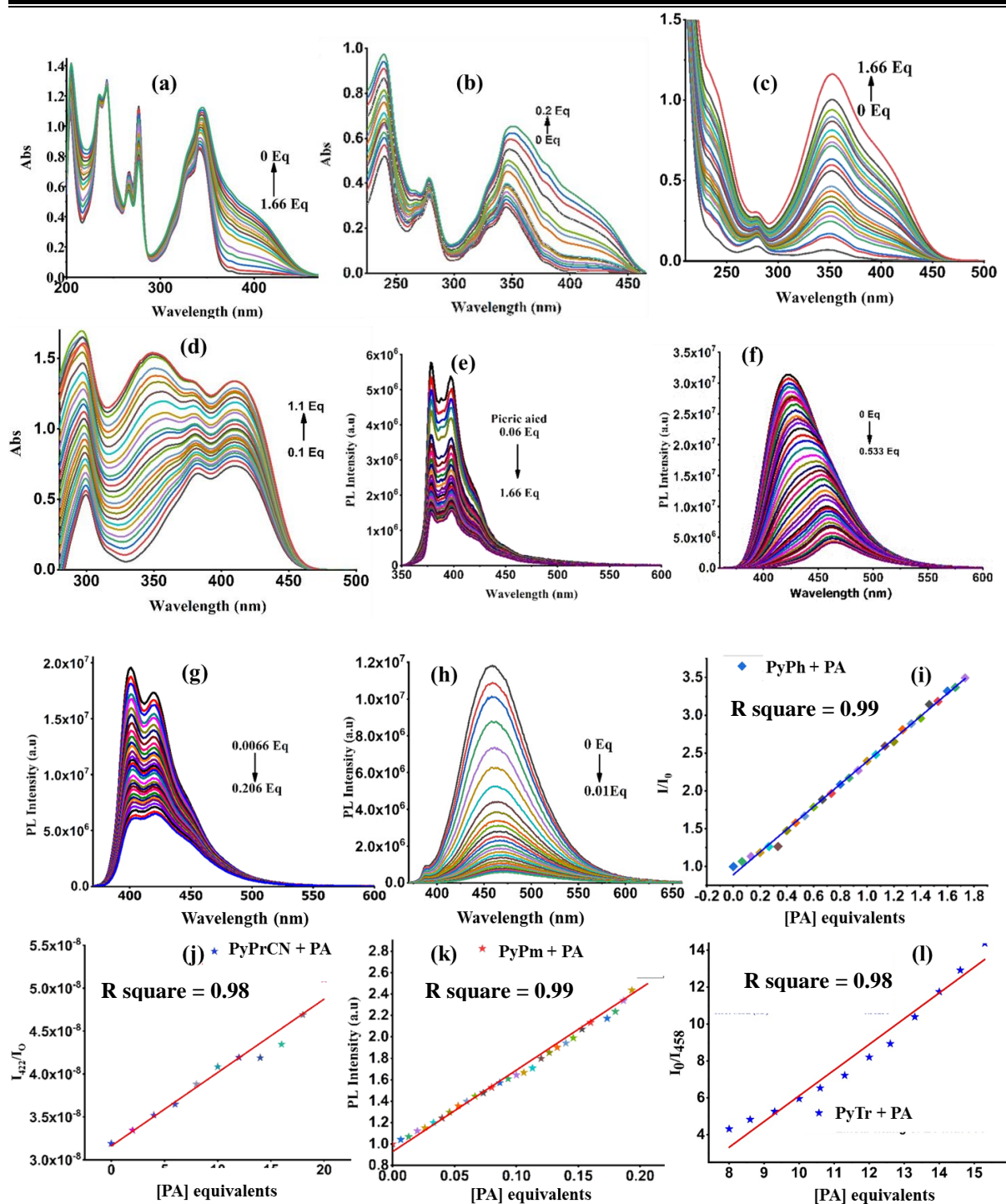


Figure 5.1.31 The absorption spectra of the probe ((a) PyPh, (b) PyPrCN, (c) PyPm (d) PyTr in thf (1×10^{-4} M) with a gradual increase in the PA (Picric acid) (1×10^{-4} M) concentration (solution of PA was prepared in water). Emission spectra of (e) PyPh (1×10^{-4} M), (f) PyPrCN (1×10^{-4} M), (g) PyPm (1×10^{-4} M), (h) PyTr (1×10^{-5}) titrated with different equivalents of PA. Linear fitting of (i) PyPh (j) PyPrCN (k) PyPm (l) PyTr with PA

The best detection limit was obtained in PyTr (0.5 nM/114 ppt). The detection limit has been determined for the case of the aggregates in mixed solvents where the maximum quantum yield is observed for all the probes. Similarly, the experiments were conducted with the water fraction mixture which has the highest quantum yield by gradually increasing the picric acid concentration in PyPh-70 % f_w , PyPrCN-90% f_w , PyPm-60% f_w (Fig. 5.1.32 a, b, c). A linear fitting obtained for PyPh, PyPrCN & PyPm (Fig. 5.1.32 d, e, f). The determined detection limit is 55 nM (f_w , 70%), 12 nM (f_w , 90%) and 1.9 nM for PyPh, PyPrCN & PyPm, respectively which shows the superior results in comparison with the respective quantum yield determined in original solution (f_w , 0%) (vide infra). The detection limit of the higher quantum yield water fraction towards PA certainly concluded that the AIEE nature of the probes results increasing of sensitivity.

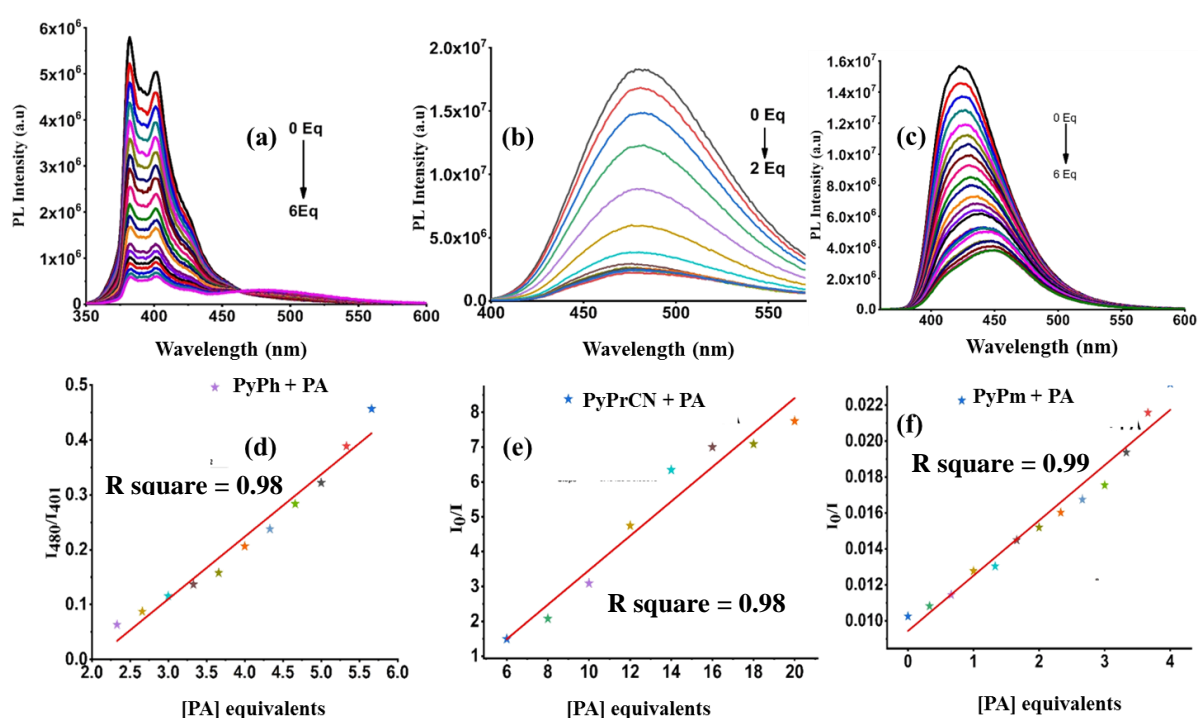
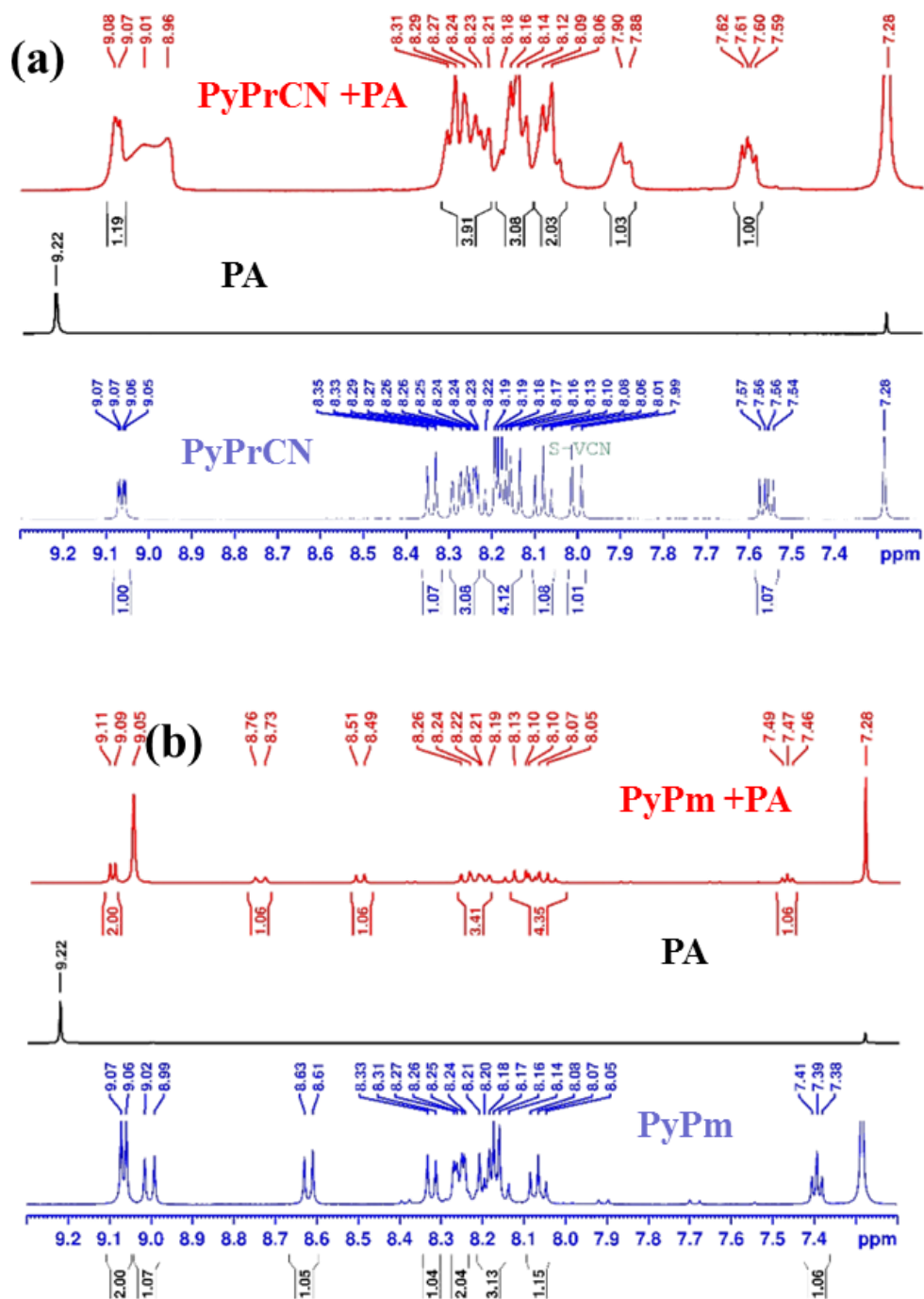


Figure 5.1.32 Emission spectra of (a) PyPh 70% f_w (1×10^{-5} M), (b) PyPrCN (1×10^{-5} M) 90% f_w (c) PyPm (1×10^{-5} M) 60% f_w , titrated with different equivalents of PA. Linear fitting of higher quantum yield water fraction (a) PyPh ($f_w = 70\%$) (1×10^{-5} M) with PA (b) PyPrCN (1×10^{-5} M) ($f_w = 90\%$) with PA (c) PyPm (1×10^{-5} M) ($f_w = 60\%$) with PA

The results encourage us to find out the mechanism for such highly selective and sensitive detectability of explosive materials by probes. Several experiments carried out to explore the mechanism. At first, we have recorded the ^1H NMR in the presence of Picric acid to observe any change any complex formed between picrate ion (picric acid in water) and probes. The

^1H NMR of PyPh, PyPrCN, PyPm and PyTr in the presence of PA does not show any major chemical shift which indicates that there is no complex formation in the ground state and also indicates no proton transfer between PA and probes. (Fig. 5.1.33 a,b,c)



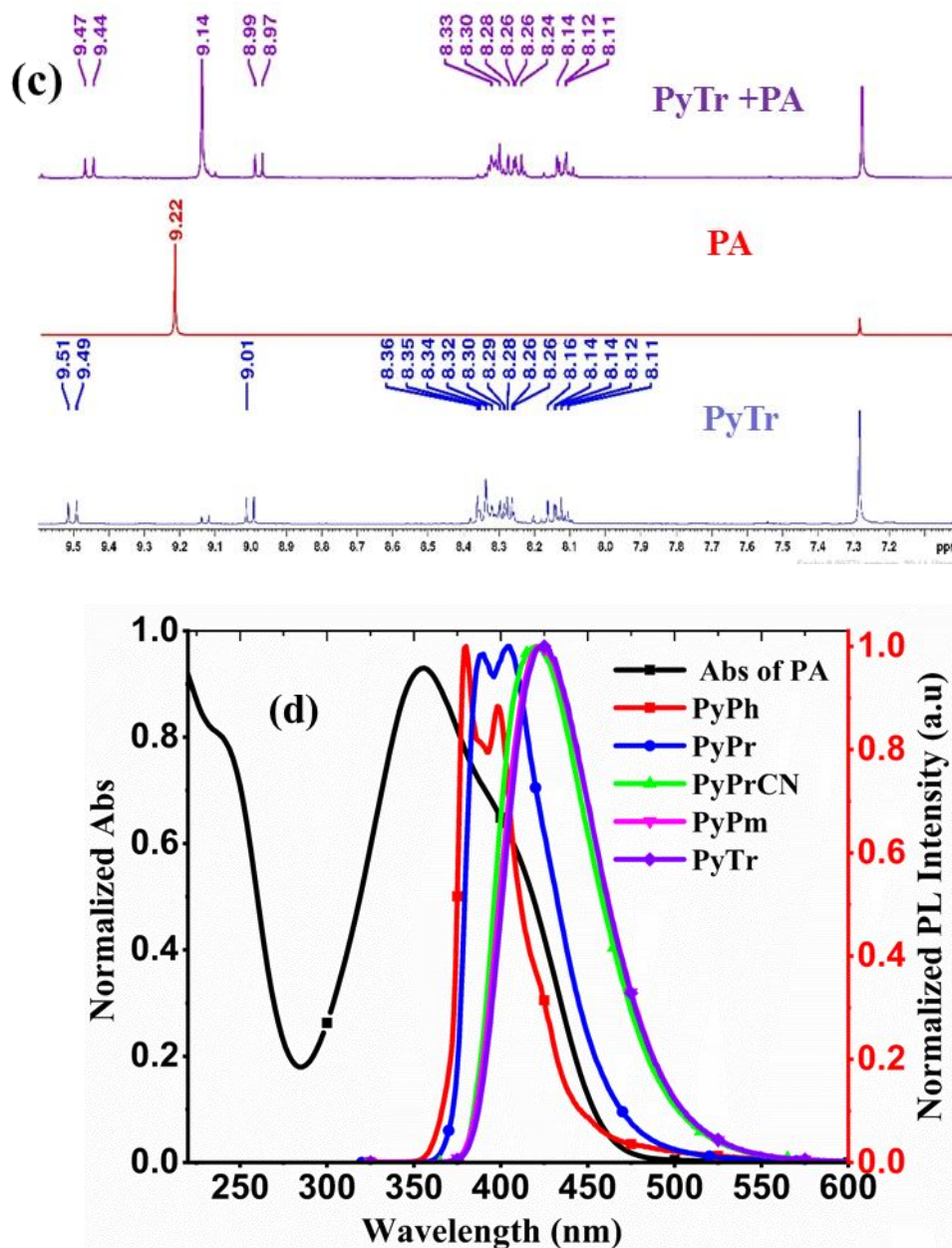


Figure 5.1.33 Stacked NMR spectra of a) PyPrCN with PA, b) PyPm with PA, c) PyTr with PA d) Spectral overlap is shown in the plot between absorption of PA and emission of PyPh, PyPrCN, PyPm and PyTr.

The extent of overlapping of absorption spectra of PA in water with the emission spectra of probes in solution revealed the ‘Resonance Energy Transfer (RET)’ occurring between PyPh, PyPrCN, PyPm and PyTr and PA, (Fig. 5.1.33 d) which may provide one of the pathways for quenching the system. The energy difference between the LUMO of PyTr and LUMO of PA is 1.22 eV which is the least when we compare the difference of LUMO level of other derivatives with PA. The lower energy difference between the Lumos of PyPh and PA facilitates the PET. It hence supports the charge-transfer from PyPh, PyPrCN, PyPm and

PyTrto PA. By all the results, the plausible mechanisms for PA detection may be occurring by both PET and energy transfer between probes and PA. For our deeper understanding, we have calculated the $J(\lambda) M^{-1} cm^{-1} nm^4$ overlap integral to know the degree of spectral overlap between the donor (PyPh, PyPrCN, PyPm and PyTr) and acceptor (PA) by using Matlab (R2018a).

The PyPh has the highest overlap integral, and PyTr has the least (Fig. 5.1.33 d). It indicates us that PyPh has maximum energy transfer. In support of our hypothesis, we have calculated the Forster distance R^0 and the distance between the donor and acceptor (r) by the formula given in the literature. PyPh has the least r and R^0 when we compare to other derivatives (Table 5.1.4).

Table 5.1.4 It shows quenching efficiency, detection limit, overlaps integral and distance between donor and acceptor

Probe	Quenching Efficiency, %	Detection Limit		PET [LUMO (D)-LUMO(A)]	J(λ) Spectral Overlap Integral	R^0 Forster Distance, nm	r (distance between Donor and acceptor), nm
		Solution, ppb	Highest .QY Water fraction, ppb				
PyPh	71	16	12	1.92	$1.6346 e^{14}$	4.42	3.80
PyPrCN	80	6.6	2.7	1.67	$1.5973 e^{14}$	6.29	4.63
PyPm	86	1.8	0.42	1.53	$1.5842 e^{14}$	6.32	4.46
PyTr	92	0.144	-	1.22	$1.5057 e^{14}$	6.98	4.64

Therefore, energy transfer is expected to be maximum for PyPh. When we compare both the PET and ET in all probes, it is observable that PyPh is highly selective for picric acid. Still, the detection limit is low and in PyTr selectivity for picric acid is less, but the detection limit is found to be very low. So by all the experimental evidence, it is clear that energy transfer increases the selectivity, and if PET increases then sensitivity increases. For practical application, we have extended the test of explosive sensing in filter paper. The filter paper was impregnated by PyTr at nine different spots by micropipette each with (10 μ l) of probes (1×10^{-6} M) and dried it for two hours in vacuum. Then 10 μ l of explosive materials (1×10^{-3} M) in water has been spilt over the spot. (Fig. 5.1.34). The place in the presence of picric acid quenches entirely as compared to other explosives.

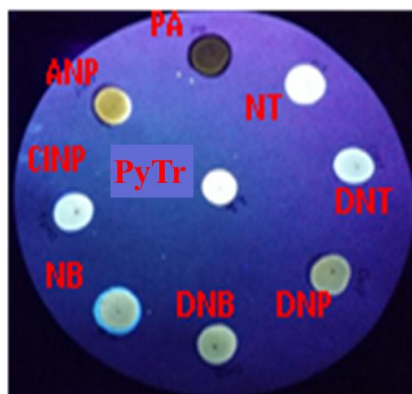
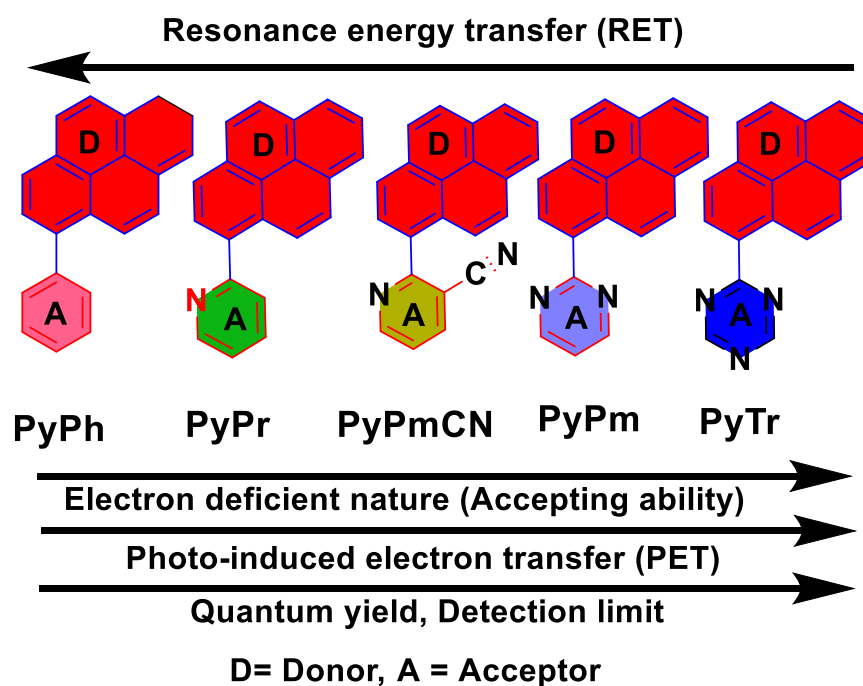


Figure 5.1.34 Image of filter paper making circular spot by PyTr and exposing through different explosive under a UV lamp.

5.1.3 Conclusion



Scheme 5.1.3 Schematic representation of the conclusion drawn from the experiments.

This chapter describes the importance of the small (D-A) type system which consist of polyaromatic hydrocarbon (pyrene) as an electron-rich group and demonstrate a quite straightforward reaction route for the synthesis of a new and simple multifunctional ratiometric probe (PyPr). Based on fluorescence signals, we have successfully demonstrated the ability of this probe molecule to behave as a selective and sensitive detector of picric acid, Al(III) and H⁺ ions. The tuned emission of the probes by simply substituting on the pyridine linked to pyrene shows the lowering of the detection limit. The probes (PyPh, PyPr, PyPrCN,

Chapter 5

PyPm) have detection limit in ppb level (16 ppb, 12ppb, 8.2 ppb, 1.8 ppb), respectively & PyTr has (114 ppt). A detailed study of the mechanism for sensing explained for selectivity and sensitivity test, which would help to design efficient explosive sensor (Scheme 5.1.3). For practical purposes, the explosive materials can be sensed in the aqueous medium, and it is extended for use in a cost-effective filter paper test. Furthermore, these results would encourage to design more sensitive probes to detect explosives in the vapour phase.

Part-B 5.2 Aggregation-induced enhanced emission (AIEE) Active Conjugated Mesoporous Oligomers (CMOs) for Low-Cost Detection of Nitro-Aromatic Based Explosives

5.2.1 Introduction

Porous materials have attracted intense interest from the researchers in the last two decades, and that play a vital role in many fields such as gas storage, the separation, and sensing of ions or molecules, catalysis, semiconductors, energy conversion, and energy storage.[58-62] Most naturally occurring porous materials are inorganic[63], which generally have high density and limited structural diversity. To prolong the scope of the porous materials, over the past decades, a class of synthetic porous materials has been developed extensively, including metal-organic frameworks (MOFs),[64-67] porous organic cages (POCs)[68],[69] hydrogen-bonded organic frameworks (HOFs)[70, 71] and porous organic polymers (POPs).[72, 73] Among them, POPs can be classified into crystalline and amorphous types. The class of amorphous POPs consists of various members, such as hyper cross-linked polymers (HCPs),[74-76] conjugated macroporous polymers (CMaPs)[77], conjugated mesoporous polymers (CMPs)[78, 79], conjugated microporous polymers (CMiPs)[80],[81] and polymers of intrinsic microporosity (PIMs).[62, 82, 83] While the class of crystalline POPs, covalent organic polymers (COPs)[84-87] emerged in 2005 and developed over the last decade. CMPs are constructed by linking building block monomers via a covalent bond, which makes the high chemical and thermal stability. CMPs gained particular attention because of their high degree of π -conjugation, high porosity, structural diversity and flexibility in molecular design and high specific surface area.[88, 89] Because of their aforementioned unique properties, Conjugated porous polymers materials have shown high potentials in various applications such as gas storage, separation, catalysis and optoelectronic devices.[80]

Out of the reported explosive sensing probes using small molecules and non-porous (non-conjugated & conjugated) polymers, the sensitivity was improved to some extent through controlling PET (Photo Induced Electron Transfer) or ET (Energy Transfer) based quenching mechanisms.[90] CMPs have the advantage of the formation of the porosity and electronic interconnectivity because of which the quantum yield and energy transfer efficiency could be increased more for ultrasensitive sensing of explosives.

Wu et al. synthesized TPE (tetraphenylethylene) containing conjugated polymers as explosive chemosensor and PLED. The group used TPE as a building block for AIE

activity.[91] Hu and co-workers synthesized a series of TPE containing conjugated polymers by using Suzuki, Wittig, and Sonogashira coupling reactions. The Lewis acid-base reaction between the TPE units of the conjugated polymers with electron-deficient (Picric acid) PA may play the key role in the quenching process.[92] Recently Namgung et al. synthesized conjugated microporous polymers via Suzuki coupling polymerization. Here the tetrafunctional TPE unit was linked to the diphenylene group to produce the porous structure. The quenching mechanism was found to be PET from TPE to electron-deficient, PA. Comparing with the other linear conjugated polymer, the porous polymers show better results because of the interaction of PA with TPE in the pores of TPE bases CMips (Conjugated Microporous Polymers).[93] Zhou et al. synthesized two unique AIE-active polymers poly(triphenylethene) and poly(tetraphenyl ethene) consisting of TPE and triphenylethene as a repeating unit, respectively, via the Suzuki coupling reaction.[89] The two polymers exhibit molecular weights M_n of $1.01\text{--}1.74 \times 10^4 \text{ g mol}^{-1}$. Using PA as an example, one of the polymers shows a higher K_{SV} ($1.80 \times 10^5 \text{ M}^{-1}$) than others, which is approximately 15 times higher ($1.22 \times 10^4 \text{ M}^{-1}$). The quenching is due to the PET effect.[94] Yin and Lu et al., describe a simple reaction for synthesizing conjugated polymers with TPE units in the backbone via oxidative dehydrogenation of poly(1,3 cyclohexadiene-alt-trans stilbene) prepared by the copolymerization of 1, 3 cyclohexadiene and trans-stilbene. Quenching constant was $4.2 \times 10^2 \text{ M}^{-1}$. Here the mechanism was excited state electron transfer from polymer to TNT.[95] Still out of the reported explosive sensing probes using small molecules and non-macroporous (non-conjugated & conjugated) polymers, the sensitivity was improved to some extent through controlling PET (Photo Induced Electron Transfer) or ET (Energy Transfer) based quenching mechanisms.[90] CMPs have the advantage of the formation of the high porosity and electronic interconnectivity because of which the quantum yield and energy transfer efficiency could be increased more for ultrasensitive sensing of explosives. The oligomers may combine the advantages of both small molecules and also macromolecules, such as ease of synthesis in the modification of small molecules[1] and the molecular wire effect[56] or super-quenching effect [96] of conjugated polymers to increase the sensitivity.[97] The tedious procedure for synthesis of polymers may lead to the poor reproducibility of the sensors.[1, 98]

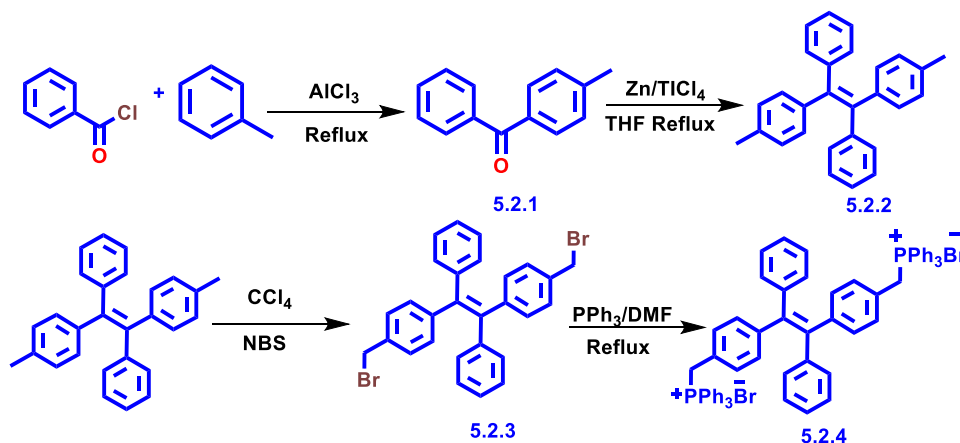
This part of the chapter explains a straightforward strategy for the design and synthesis of highly luminescent conjugated mesoporous oligomers (CMOs) with 'Aggregation-induced enhanced emission' (AIEE) feature through Wittig polymerization of

the molecular rotor. Typical molecular rotors such as triphenylamine (TPA) and tetraphenylethene (TPE) as B2, A4 & A3 type nodes have been used to construct AIEE active CMOs, namely CMO1 & CMO2. The quick dissipation of the excited photons was successfully controlled by the restriction of rotation of the phenyl units through the formation of the porous network scaffold in solid/thin film, which provides the high quantum yields for the interlocked CMOs system. Both the oligomers are found to be sensitive to nitroaromatic. The larger pore size and pore density in the mesoporous network of CMO1 are found to be responsible for the greater extent of energy transfer from CMO1 to picric acid. Furthermore, CMO1 has been employed for low-cost filter paper-based detection of trace nitroaromatic containing explosive materials.

5.2.2 Experimental section

i) Synthesis (CMO1 and CMO2)

(a). **Synthesis of monomers:** Compounds phenyl(p-tolyl)methanone (5.2.1), 2-Bis(4 methyl phenyl)-1,2-diphenylethene (5.2.2), 1,2-bis(4-(bromomethyl)phenyl)-1,2-diphenylethene (5.2.3) and 1,2-Bis1,2-diphenylethene (5.2.4) were synthesized according to the synthetic procedures given in our previous report.[99]



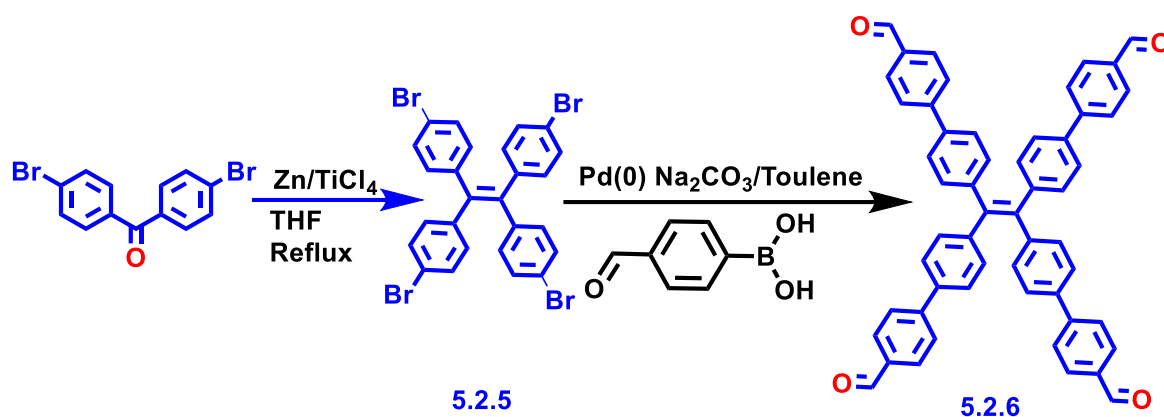
Scheme 5.2.1. Synthesis of TPE ylide monomer 5.2.4 (NBS = N-Bromosuccinimide)

(b) Tetrakis(4-bromophenyl)ethylene (5.2.5):

In a 250ml three-neck round bottom flask fitted with a condenser were placed 1.67 ml (0.015 moles) of TiCl_4 and 1.96g (0.03 mole) of Zn powder in freshly dried 70 ml of THF. The reaction suspension was refluxed for 2 hours under nitrogen atmosphere. A solution of

Chapter 5

4,4'-Dibromobenzophenone (5.1g, 0.015 moles) in 20 ml of dry THF was added dropwise into the suspension of TiCl_4 , and the reaction mixture was refluxed at 80°C for 24 hours. The reaction mixture was cooled to room temperature then quenched with 10 % aqueous K_2CO_3 . The crude product was extracted by dichloromethane three times and washed with brine solution then finally dried with MgSO_4 . Compound **5.2.5** was purified by column chromatography using hexane as eluent. White-coloured solid was isolated in 68% yield



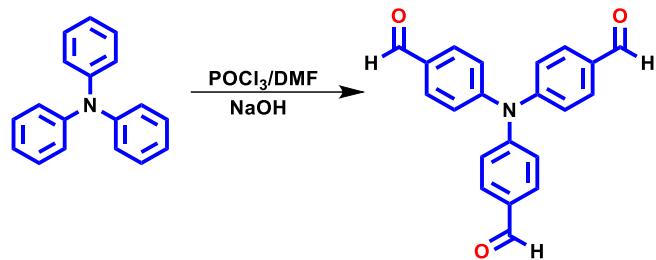
Scheme 5.2.2 Synthesis of Tetrakis(4-bromophenyl)ethylene (5.2.5) and 1,1,2,2-tetrakis(4-formyl-(1,1'-biphenyl)) ethane monomer (5.2.6)

(c) **Synthesis of 2.3. 1,1,2,2-tetrakis(4-formyl-(1,1'-biphenyl)) ethane (TBPE) (5.2.6)..**

Compound 5.2.6 was prepared by Suzuki coupling reaction using palladium (0) as a catalyst. Compound 5.2.5 (684 mg, 1mmol) and 4-formylphenylboronic acid (900 mg, 6 mmol) were added to a three-necked round bottom flask connected to a condenser and a nitrogen inlet and outlet followed by the addition of toluene (80 mL). The reaction mixture was degassed by purging nitrogen gas several times. An aqueous solution of Na_2CO_3 (1.66 g, 12 mmol) in water (15 mL) was then added, followed by $\text{Pd}(\text{PPh}_3)_4$ catalyst (10mg). The reaction mixture was stirred at 85°C for 24 hours. After cooling to room temperature, the reaction mixture was poured into water, and the crude product was extracted by ethyl acetate. The crude product was washed three times with water and brine solution and finally dried with MgSO_4 . The crude product was purified by column chromatography using an ethyl acetate/hexane mixture (20:80). The green-coloured solid was yielded by 69%. (Scheme 5.2.2)

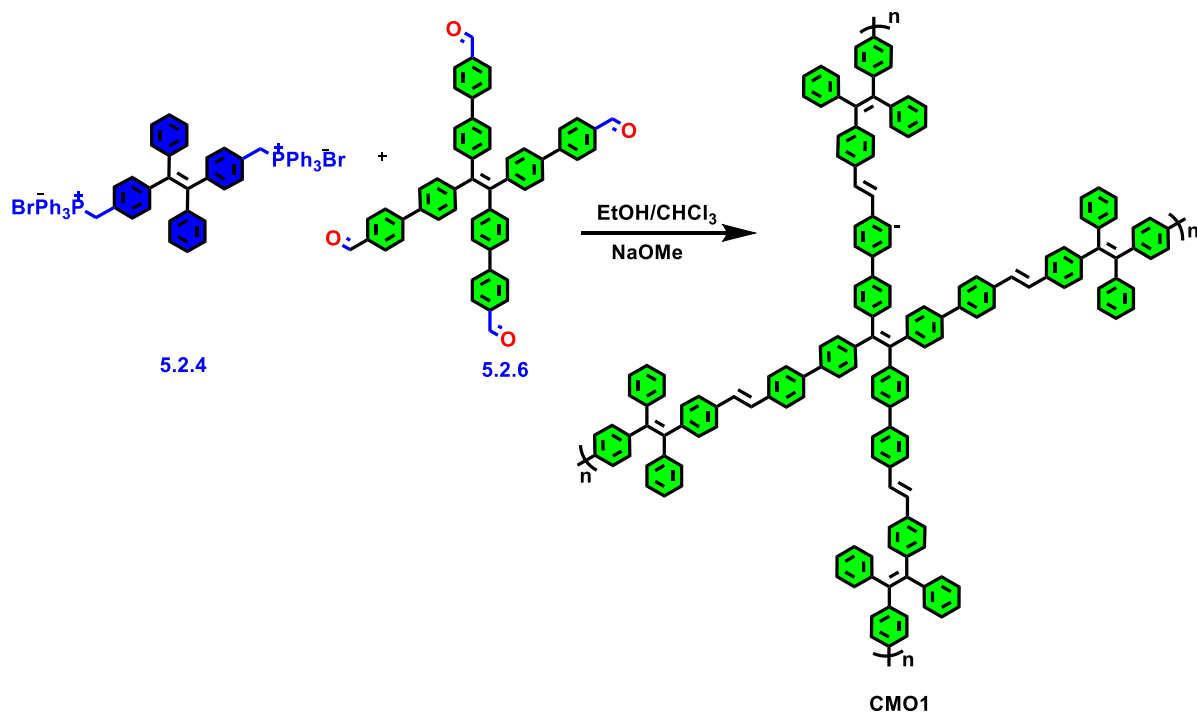
(d) **Synthesis of Tris(4-formyl phenyl)amine (5.2.7)**

Compound 5.2.7 was prepared according to the previously reported Vilsmeier–Haack formylation procedure.[100] (Scheme 5.2.4)

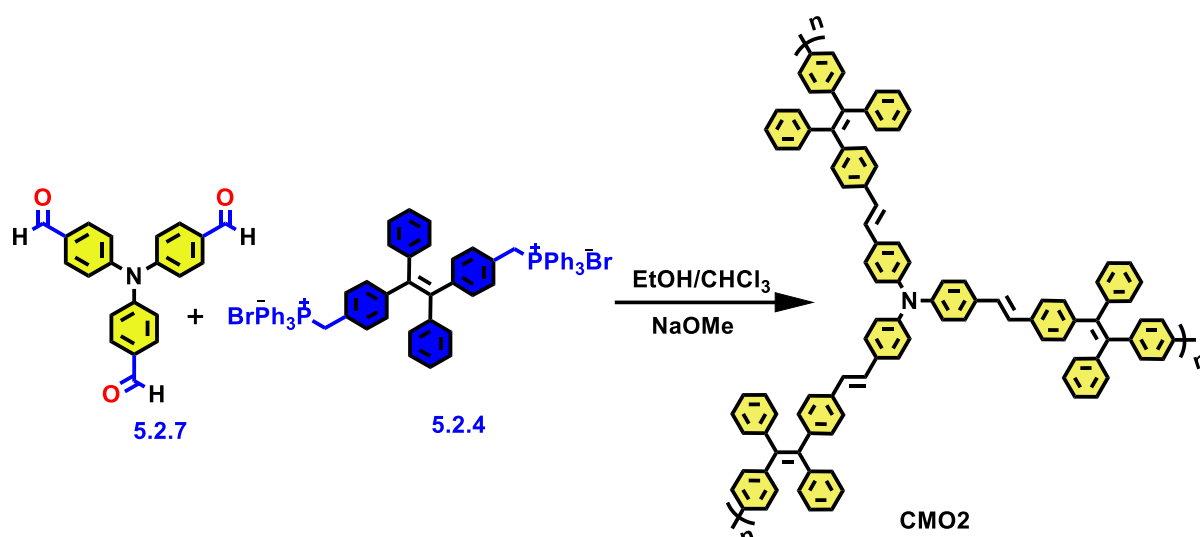


Scheme 5.2.3 Synthesis of Tris(4-formyl phenyl)amine (5.2.7)

(e) **Synthesis of Conjugated Mesoporous Oligomers (CMO1 and CMO2).** 1 eq of compound (5.2.4) and 1eq of compound (5.2.6) was added to the three-necked round bottom flask, and in separated three-necked round bottom flask 1eq of compound (5.2.4) and 1eq of compound (5.2.7) was added, which was connected to a condenser and a nitrogen inlet. Absolute ethanol and dry chloroform 12 ml (3:1 v/v) were then added, maintaining the N₂ atmosphere. A pre-determined amount of NaOMe (25 wt%) in CH₃OH was added to the mixture. (Scheme 5.2.4 and Scheme 5.2.5). This was followed by continuous at 50°C for 24 hours. The product obtained was poured into the large volume of methanol, and the yellow-coloured precipitates were collected by condensation and Whatman paper filtration, the precipitates were collected via centrifugation in methanol in an 80-85% yield.



Scheme 5.2.4 Synthesis of CMO1



Scheme 5.2.5 Synthesis of CMO2

ii) Characterization

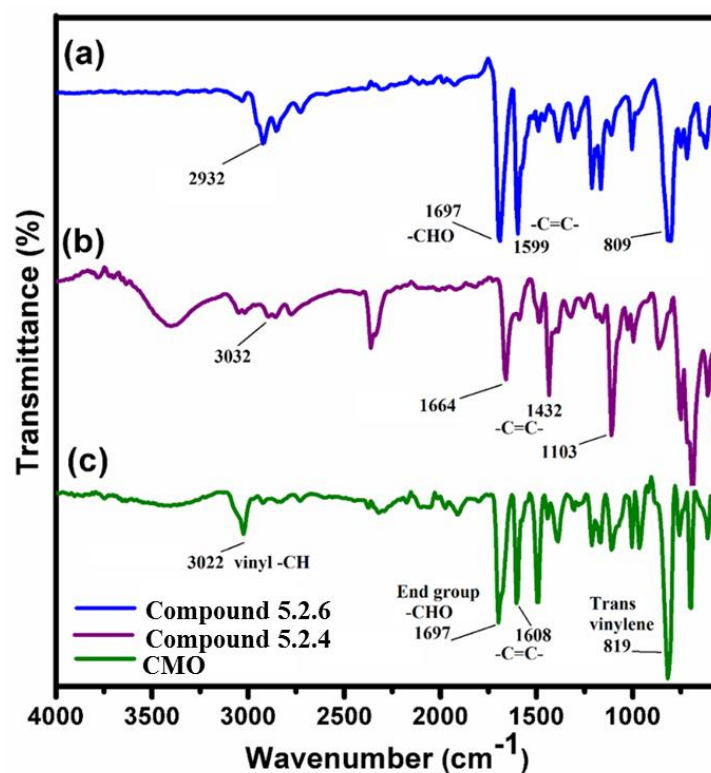


Figure 5.2.1 FT-IR spectrum of (a) compound 1, 1, 2, 2-tetrakis(4-formyl-(1,1'-biphenyl))ethane (5.2.6), (b) compound 1,2-Bis1,2-diphenylethene (5.2.4) and (c) CMO1 oligomer

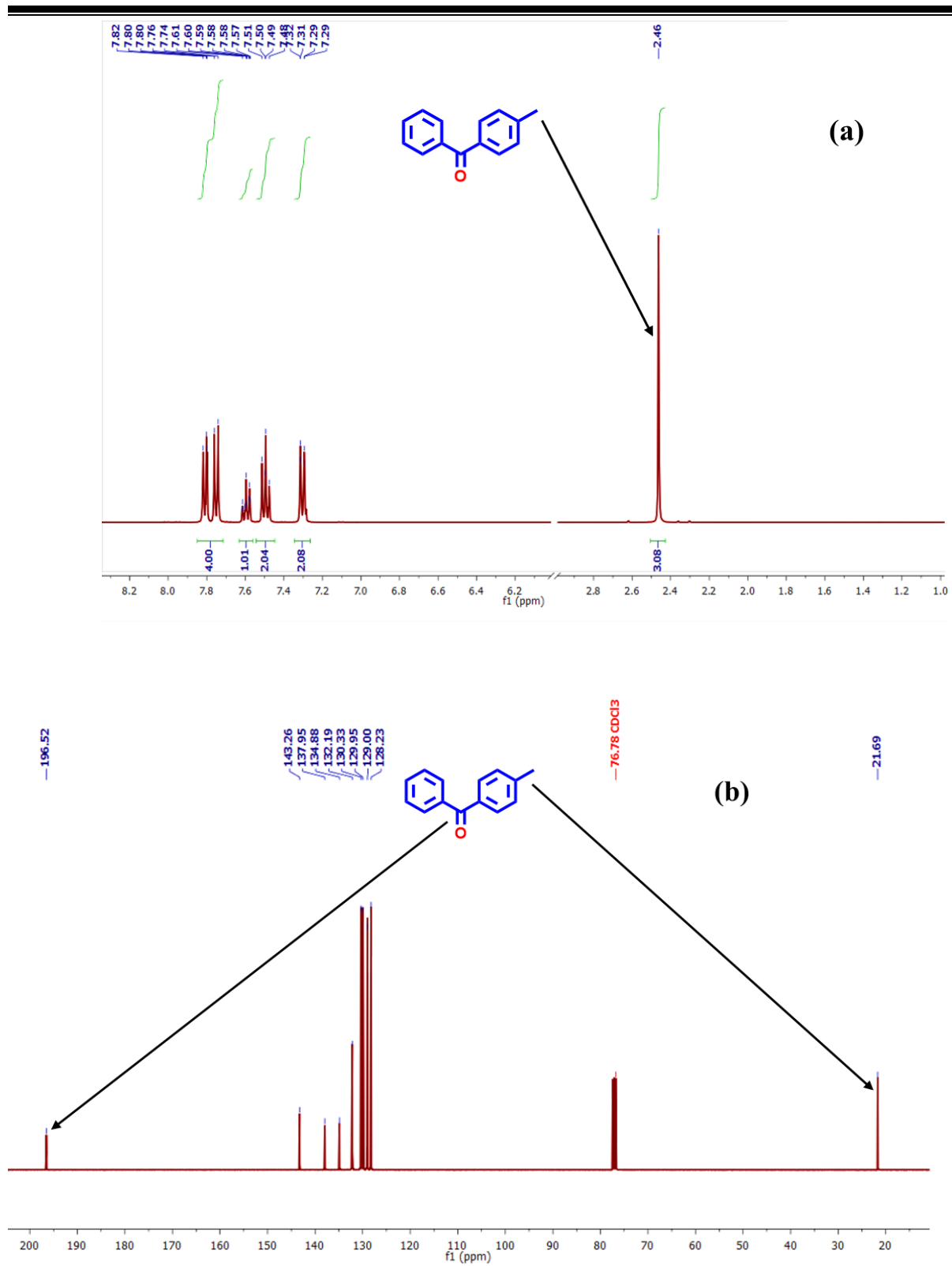


Figure 5.2.2 (a) ^1H and (b) ^{13}C NMR spectrum of phenyl(p-tolyl)methanone (5.2.1)

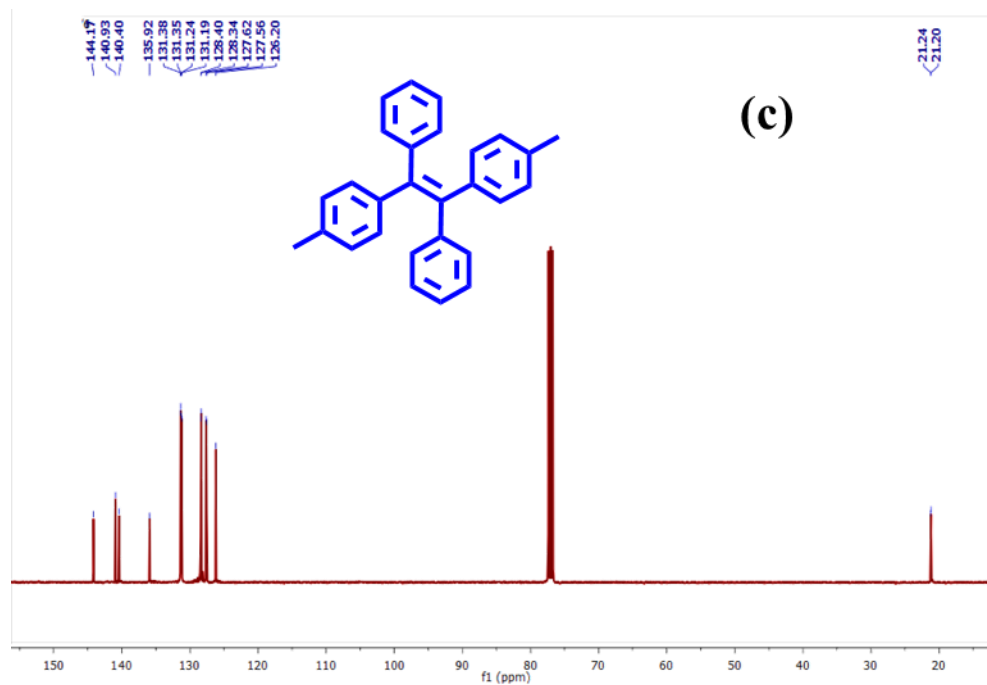
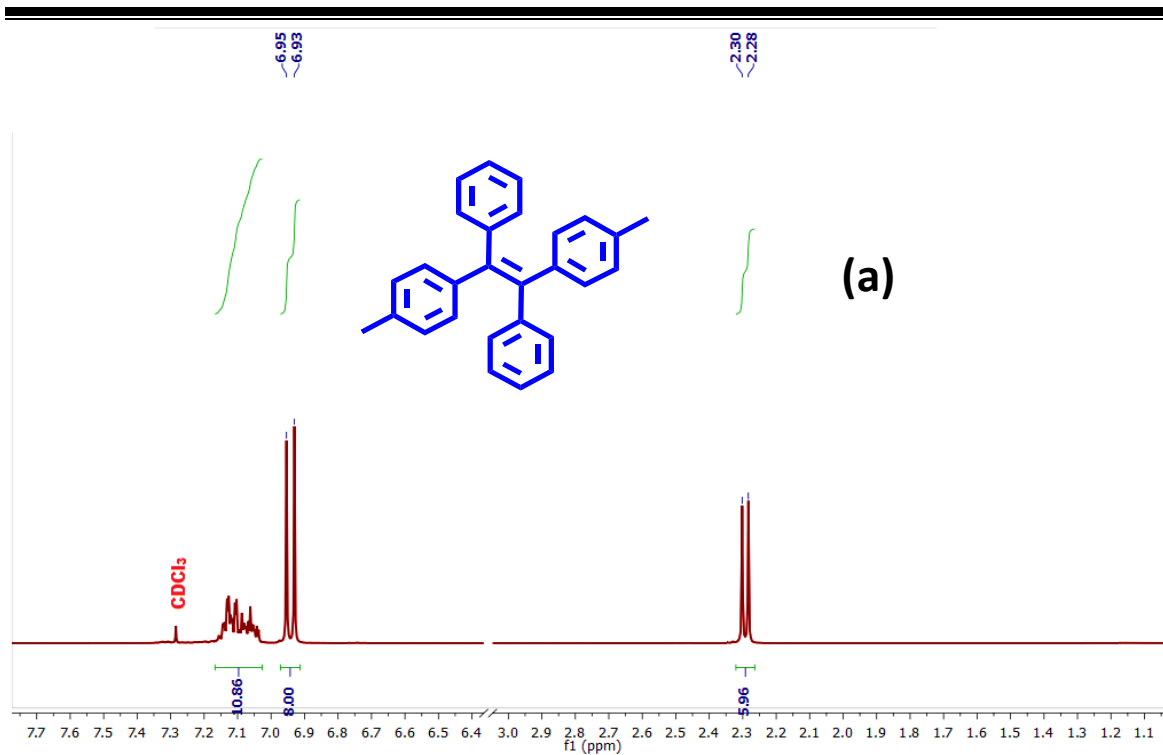


Figure 5.2.3 (a) ¹H and (b) ¹³C NMR spectrum of 2-Bis(4 methyl phenyl)-1,2-diphenylethene (5.2.2)

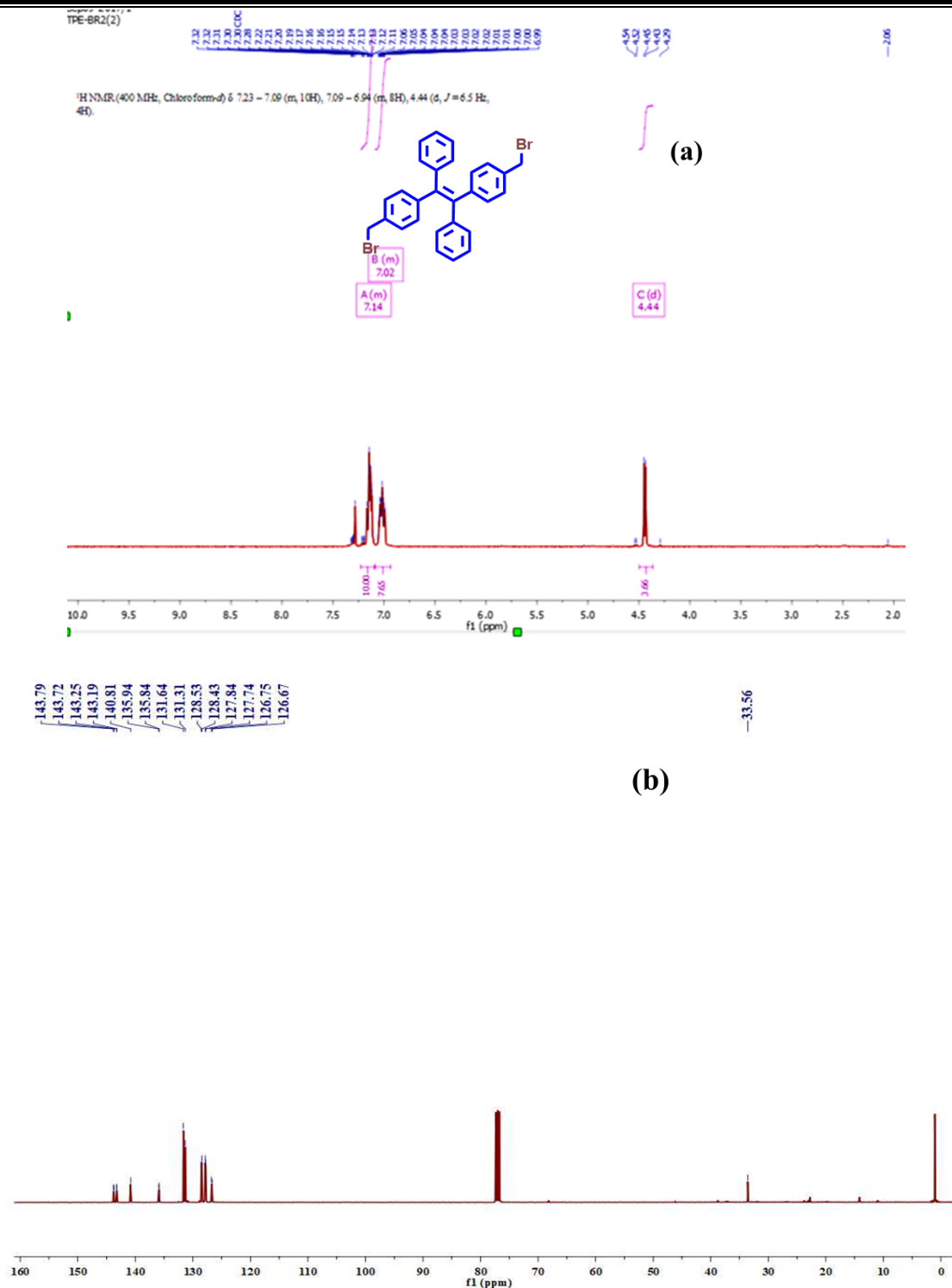


Figure 5.2.4 (a) ¹H and (b) ¹³C NMR spectrum of 1,2-bis(4-(bromomethyl)phenyl)-1,2-diphenylethene (5.2.3)

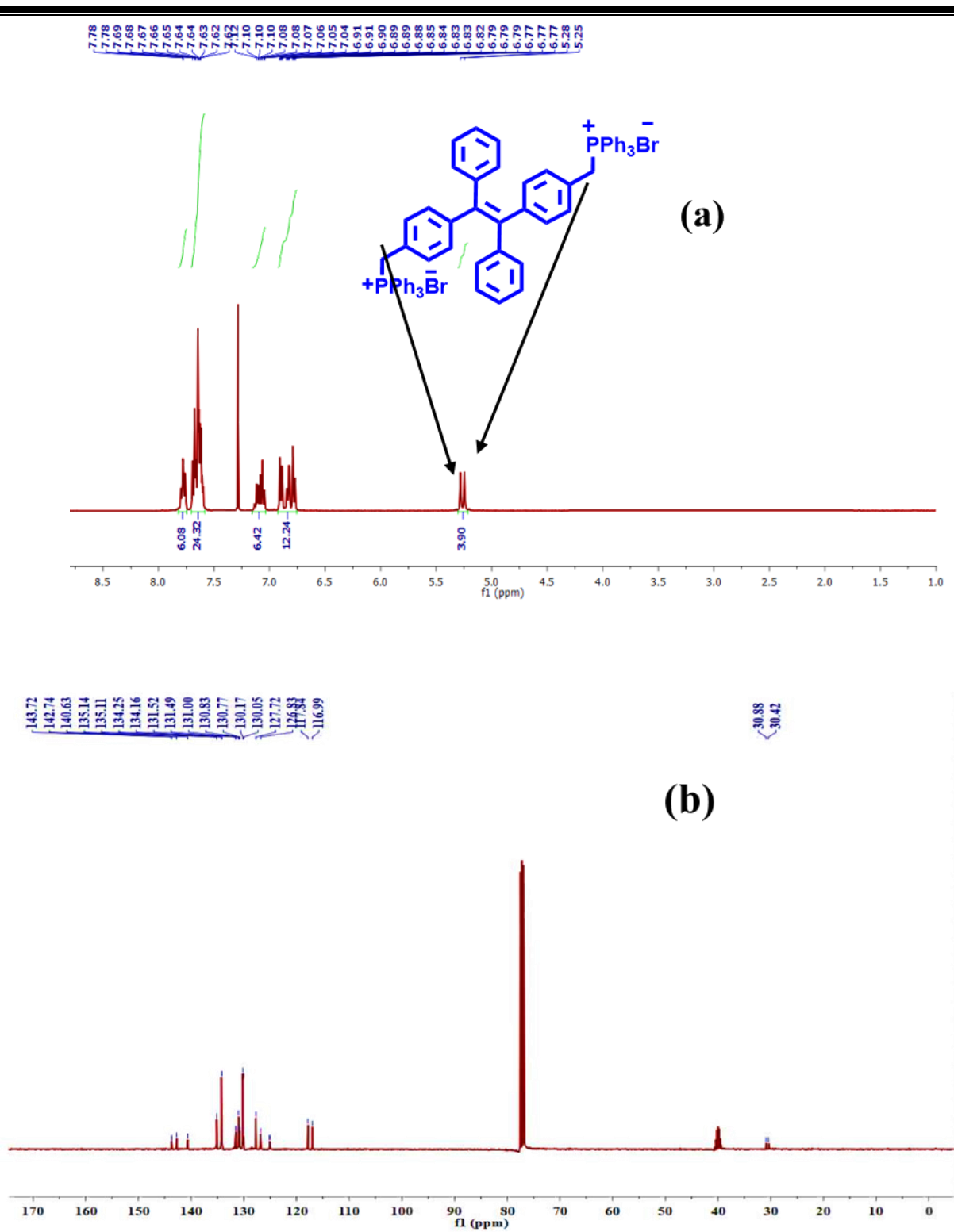


Figure 5.2.5 (a) ^1H and (b) ^{13}C NMR spectrum of 1,2-bis(1,2-diphenylethene) dibromide salt (5.2.4)

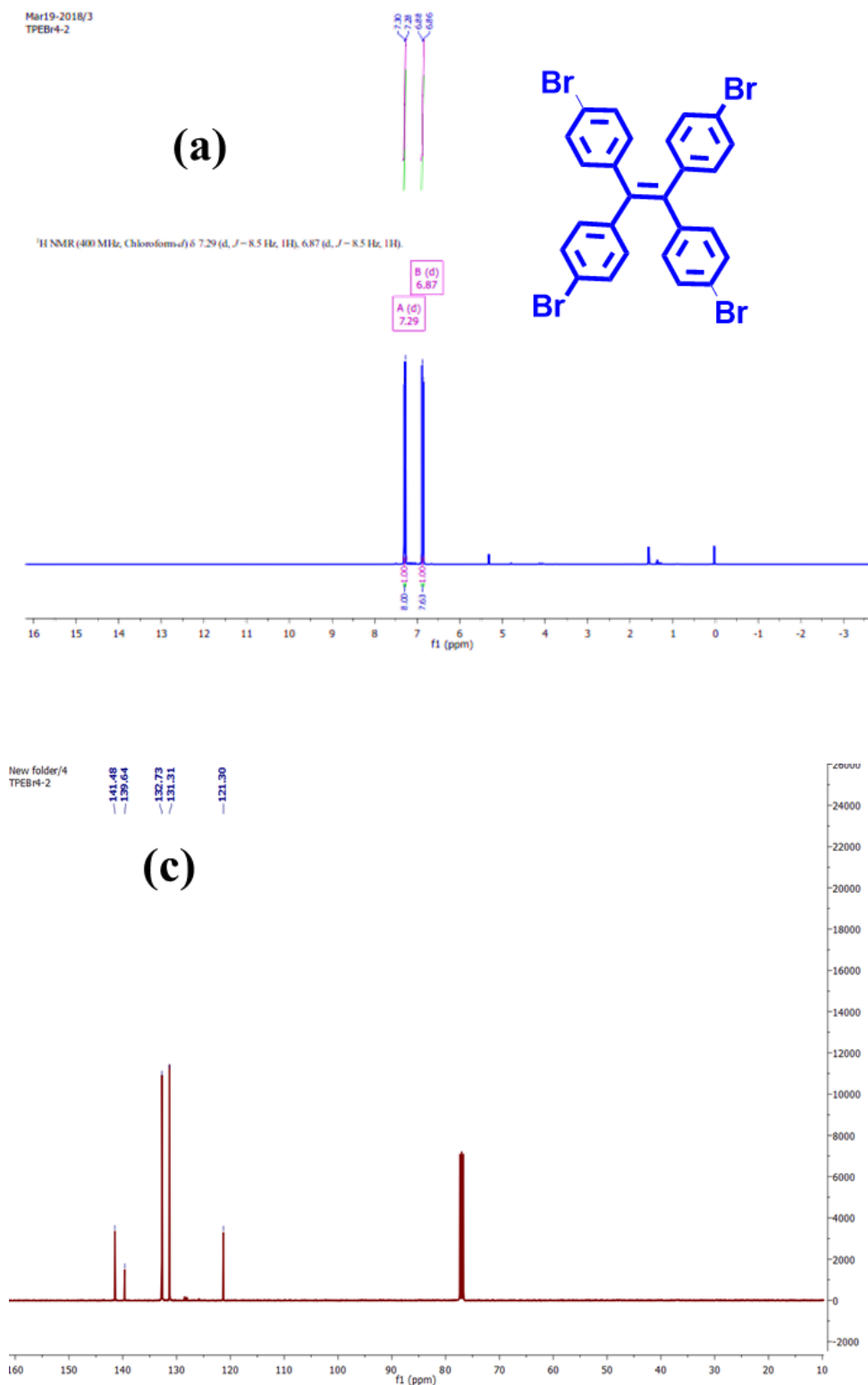


Figure 5.2.6 (a) ¹H and (b) ¹³C NMR spectrum of Tetrakis(4-bromophenyl)ethylene (5.2.5)

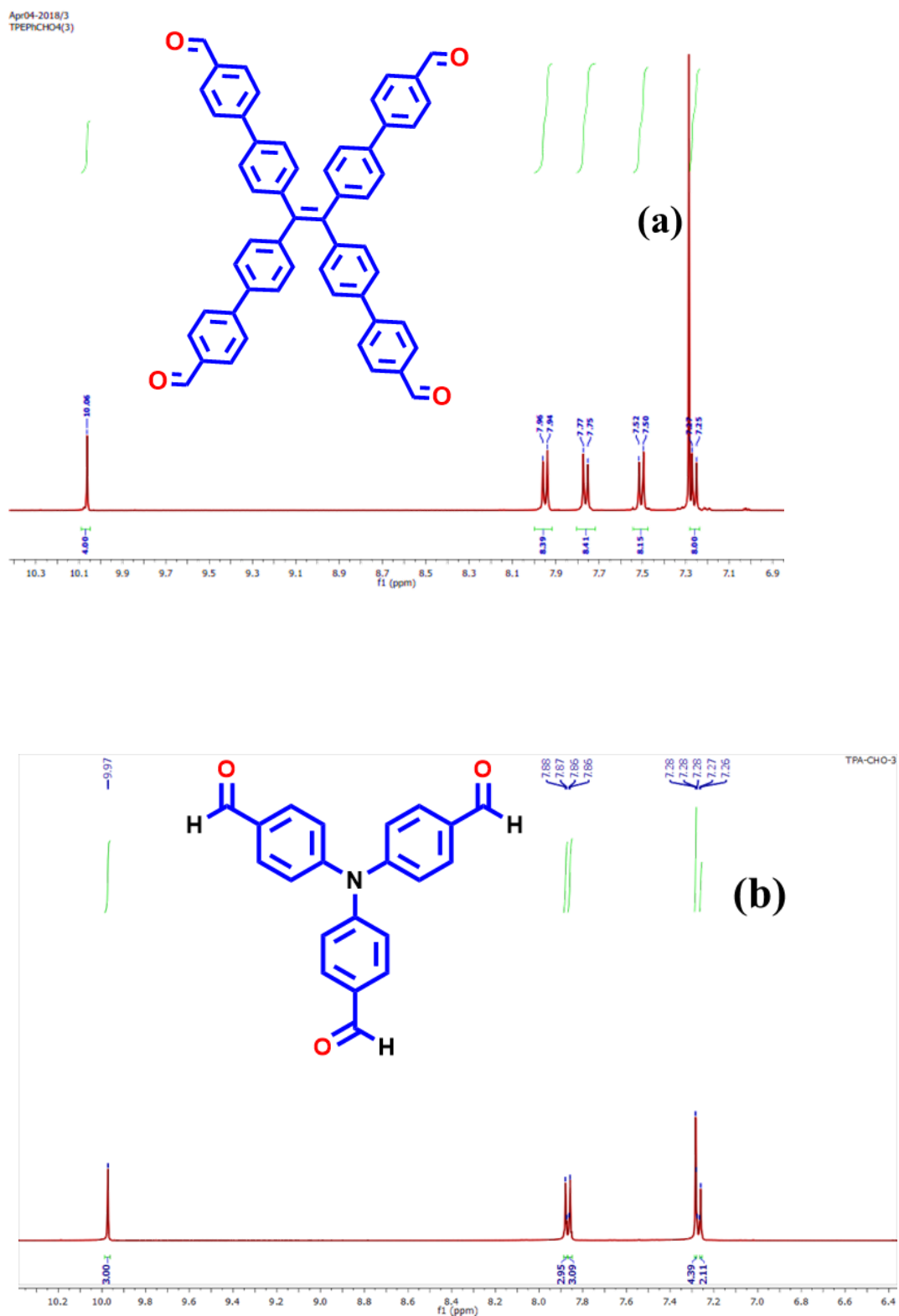


Figure 5.2.7 (a) ^1H NMR spectrum of 1,1,2,2-tetrakis(4-formylphenyl)ethane (5.2.6) (b) ^1H NMR spectrum of Tris(4-formylphenyl)amine (5.2.7)

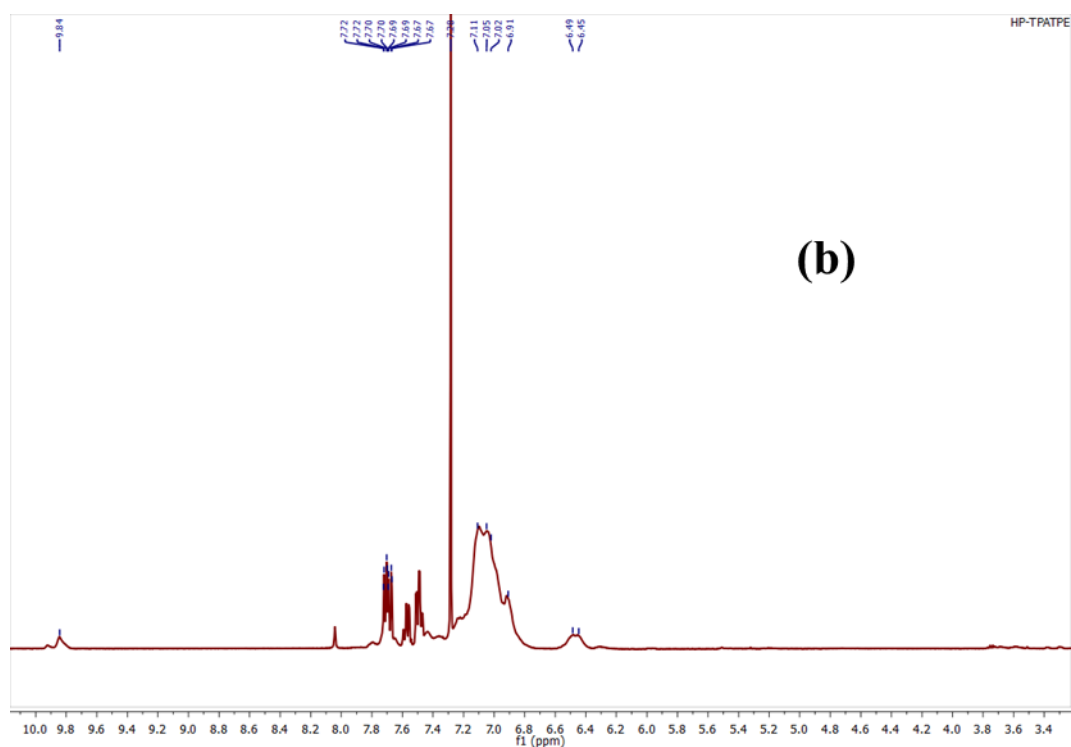
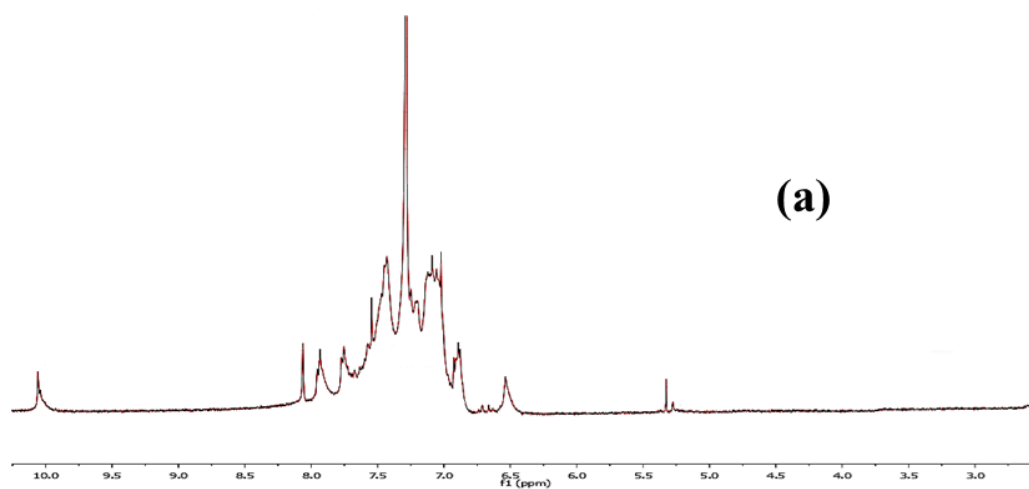
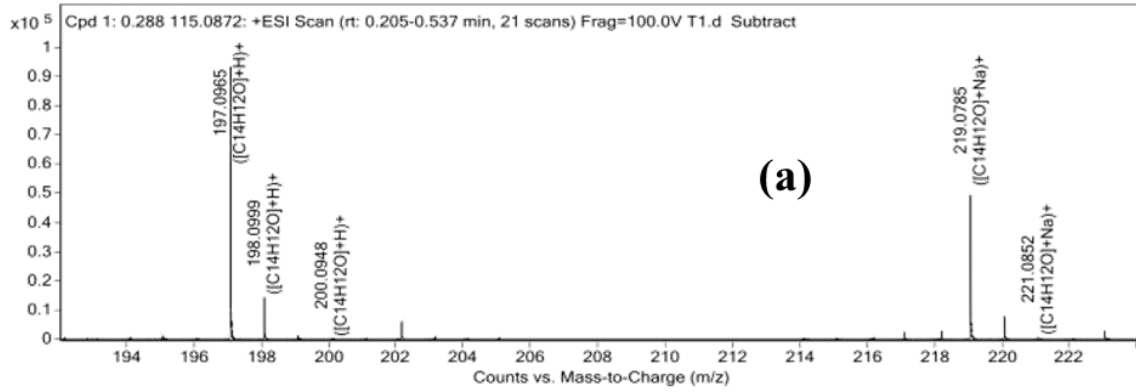
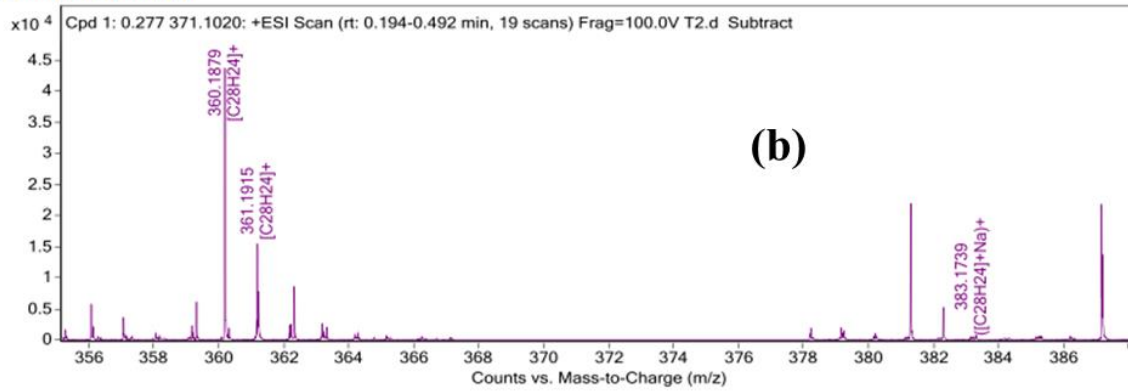


Figure 5.2.8 (a) ^1H NMR spectrum of CMO1 (b) ^1H NMR spectrum of CMO2

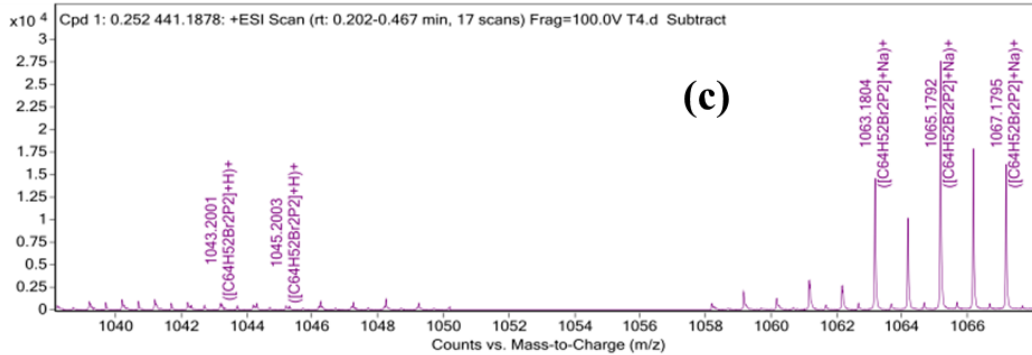
MS Zoomed Spectrum



MS Zoomed Spectrum



MS Zoomed Spectrum



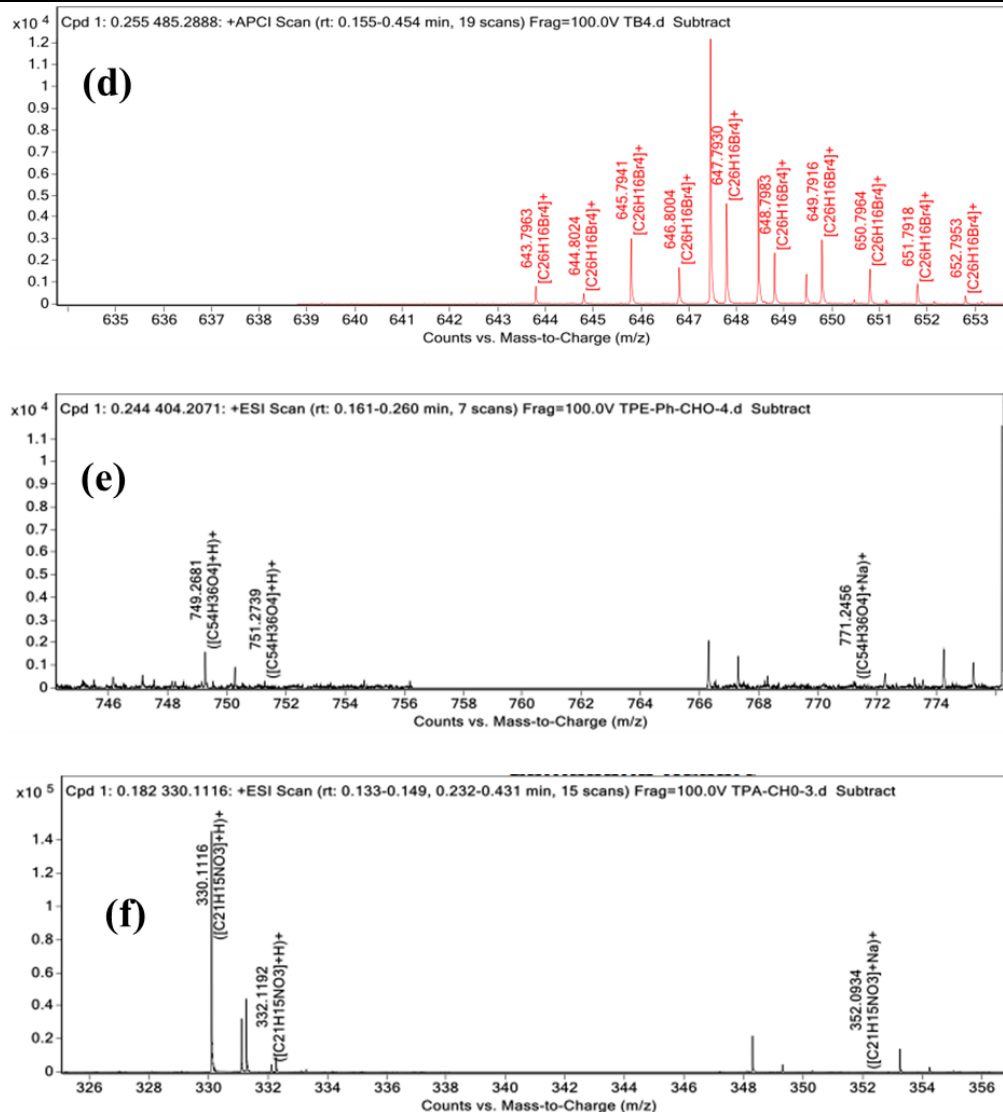


Figure 5.2.9 (a) Mass spectrum of compound phenyl(p-tolyl)methanone (5.2.1) (b). Mass spectrum of compound 1,2-bis(4-(bromomethyl)phenyl)-1,2-diphenylethene (5.2.2) (c). Mass spectrum of compound 1,2-Bis1,2-diphenylethene (5.2.4) (d). Mass spectrum of compound Tetrakis(4-bromophenyl)ethylene (5.2.5) (e) Mass spectrum of compound 1, 1, 2, 2-tetrakis(4-formyl-(1,1'-biphenyl))ethane (5.2.6) (f). Mass spectrum of compound Tris(4-formyl phenyl)amine (5.2.7)

5.2.3 Results and Discussion

i) Synthetic Strategy and Characterization of Pores

the synthesis of CMOs, we employed tetrakis (4-bromophenyl)ethylene, which is well-known AIE materials. To improve the interchain conjugation connectivity, we have attached one more benzene ring to each side called 1,1,2,2-tetrakis(4-formyl-(1,1'-biphenyl))ethane (TBPE) (6). Before studying the Wittig Polymerization of AIE active monomers, we

synthesized TPE and TPA containing compounds [5.2.4, 5.2.6 & 5.2.7]. Compounds 5.2.4 & 5.2.6 were prepared by multi-step synthetic routes shown in Scheme 5.2.1 & 5.2.2. Compound 5.2.1 was developed by Friedel-Craft acylation of toluene with benzyl chloride in the presence of AlCl_3 . The resulting product was used to prepare AIE active compound 5.2.2 by McMurry coupling reaction using low valent titanium tetrachloride with Zinc powder (Scheme 5.2.2). Compound 5.2.3 was obtained from the bromination of compound 5.2.2 with NBS as a brominating agent with a free radical initiator. The triphenylphosphine was reacted with compound 5.2.3 in DMF to result in TPE phosphonium ylide (compound 5.2.4). Two-step synthetic routes have been followed to synthesis compound 5.2.6. Initially, McMurry coupling of 4,4-dibromobenzophenone with low valent titanium tetrachloride and Zn powder resulting in the compound, 5.2.5. Then, the reaction of 5.2.5 with 4-formyl phenylboronic acid in the presence of palladium (0) catalyzed Suzuki cross-coupling resulting in 5.2.6. The sodium carbonate was used as a base in toluene as solvent resulted in AIE active tetraaldehyde compound 5.2.6 (A4-type node) with a moderate yield. The Vilsmeier–Haack formylation was carried out for the preparation of compound 5.2.7. (Scheme 5.2.4) Triphenylamine was used to prepare 5.2.7 by treating with POCl_3 and DMF at 0°C (Scheme 5.2.3)

Here, all the synthesized monomers are luminescent. In this work, TPE cored tetra aldehyde 5.2.6 (A4), and TPA cored trialdehyde 5.2.7 (A3) were prepared as functional bridging moieties to link with the TPE ylide 5.2.44 (B2) and introduce the AIEE characteristic in the oligomer. The synthetic routes of CMOs are shown in Scheme 5.2.4 & 5.2.5). AIEE active Mesoporous conjugated oligomers CMO1 & CMO2 were successfully prepared by Wittig polymerization using rigid, bulky molecular rotors TPE and TPA cored (5.2.6 & 5.2.7) A4 & A3 monomers respectively with B2 type TPE monomer 4 in 1:1 molar ratio in the presence of a catalytic amount of a base sodium methoxide in DMF solution at 60°C for 24 hours. The polymerization was terminated by adding methanol into the reaction mixture, and the mixture was poured into a large amount of methanol. The resulting oligomers were purified by reprecipitation method using methanol-THF solvents. All the synthesized compounds were characterized by standard spectroscopic analysis. They gave the results satisfactory to their corresponding molecular structure of the compounds (Fig 5.2.1-5.2.9) All the synthesized monomers and oligomers CMO1 & CMO2 are obtained with satisfying yields (70-75%), and they were readily soluble in common organic solvents such as DCM, CHCl_3 , THF, and DMSO etc.

The molecular structures of the synthesized monomers are characterized by nuclear magnetic resonance (NMR) and high-resolution mass spectrometry (HRMS). The obtained results are in good agreement with the expected molecular structures of monomers. ^1H , ^{13}C NMR and HRMS spectra of compounds 5.2.1-5.2.7 are given in characterization. (Fig 5.2.1 to 5.2.9) The molecular ion M^+ peaks at 643.7963 (calc 643.7986), 749.2681 (calc 748.2614), and 330.1116 (calc 330.1052) in their HRMS spectra as shown for compound 5.2.5, 5.2.6 and 5.2.7, respectively confirming the formation of expected products. FT-IR spectra of compounds 5.2.6, 5.2.5 and CMO are given in Figure 5.2.1 as an example. In the FT-IR spectrum of 5.2.6, the influential absorption bands observed at 687 and 745 cm^{-1} are ascribed to the C-Br and C-P stretching frequency in the AIE active TPE ylide monomer. Whereas, the intense absorption band found at 1697 cm^{-1} is attributed to $-\text{CHO}$ functional moiety present in the AIE active TPE monomer 5.2.6. After polymerization, the FT-IR spectra of CMO1 show the absence of C-Br, C-P, and the less intense peak is observed for $-\text{CHO}$ moiety. Additionally, the characteristic central peak at 1608 cm^{-1} could be assigned to the stretching vibration of $-\text{C}=\text{C}-$ in the FT-IR spectrum of CMO1, which confirms the TPE moiety was successfully introduced into the CMO skeleton. Additionally, the *trans* vinylene stretching frequency is observed at 819 cm^{-1} . In the ^1H NMR spectra of 5.2.6 & 5.2.7 [Fig 5.2.7 (a, b)], the sharp, intense peak is observed at 10.06 and 9.97 ppm ascribed to the tetraaldehyde and trialdehyde protons of TPE and TPA moieties. The methylene and aromatic protons signals of the phosphonium ylide monomer 5.2.4 are observed at 5.26 and 7.78-7.58 ppm, respectively. In the case of CMO1 & CMO2 [Fig 5.2.8 (a, b),] the TPE and TPA aromatic protons signals show broad multiplets and are found in the range of 6.8-8.12 ppm, and less intense peaks are observed at 10.09, and 9.81 ppm are owing to the end group aldehyde proton signal. Additionally, a new peak is observed at 6.51 ppm is attributed to the *trans* vinylene proton present in the oligomer chain.[99]. These results confirm the formation of *trans* vinylene and the absence of methylene protons in both CMOs indicate that the polymerization proceeded successfully. The molecular weight of both CMOs was characterized by Gel Permeation Chromatographic (GPC) technique. The moderate molecular weight (M_w) of CMO1 and CMO2 was observed to 8616 and 6800, respectively. Each oligomer has around 8-9 repeating units. By utilizing the molecular rotor 5.2.4, 5.2.6 & 5.2.7 as B2, A4 & A3 types nodes, respectively we were successful in creating the porous polymeric network structure in solid. The N_2 absorption-desorption isotherm of CMO1 and CMO2 are shown in [Fig 5.2.10 (a, b)].

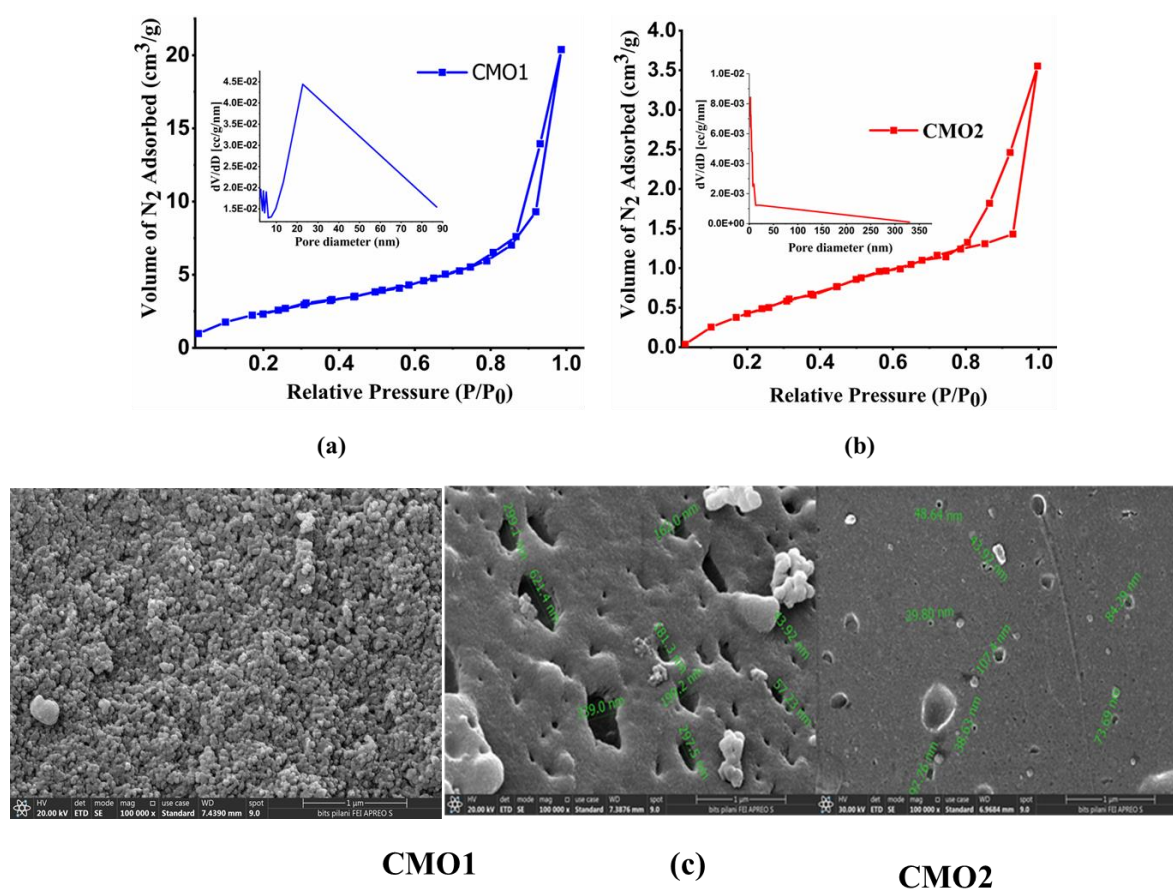


Figure 5.2.10 (a) Nitrogen adsorption-desorption isotherms and the inset show the pore size distribution curves of (a) CMO1 and (b) CMO2, (c) FESEM of CMO1 (left) and CMO2 (right) in a powdered form showing the different size of the porous network

The obtained isotherms of CMO1 and CMO2 belongs to type-IV with H2 hysteresis loop at higher relative pressure for CMO1. It confirms the characteristics of mesopore. The observed type of H2-type hysteresis loops indicates that the pores are not uniform and made up of an interconnected network of different sizes.[101-103] The pore size and the surface area of CMO1 and CMO2 were obtained by the Barrett-Joyner-Halenda (BJH) method.[104, 105] For CMO1, the surface area is found to $14.923 \text{ m}^2\text{g}^{-1}$ (unit), with a pore diameter of 2.207 nm and for CMO2 surface area is found to $4.22 \text{ m}^2\text{g}^{-1}$ (unit), with a pore diameter of 2.518 nm [Fig 5.2.10 (a,b)]. FESEM image of both the solid oligomers of CMO1 and CMO2 clearly showing the porous network structure interconnected with each other of different sizes (Figure 5.2.10 c). For CMO1 the asymmetrical spherical particle with aggregates was also observed in SEM image (Fig 5.2.10 cleft side). Therefore, from both the

experiments and pore size distribution plot, [Fig 5.2.10 (a,b)]. it may be concluded that both the oligomers have a non-uniform interconnected porous network

ii) Photophysical studies

a) Absorption and Emission Properties

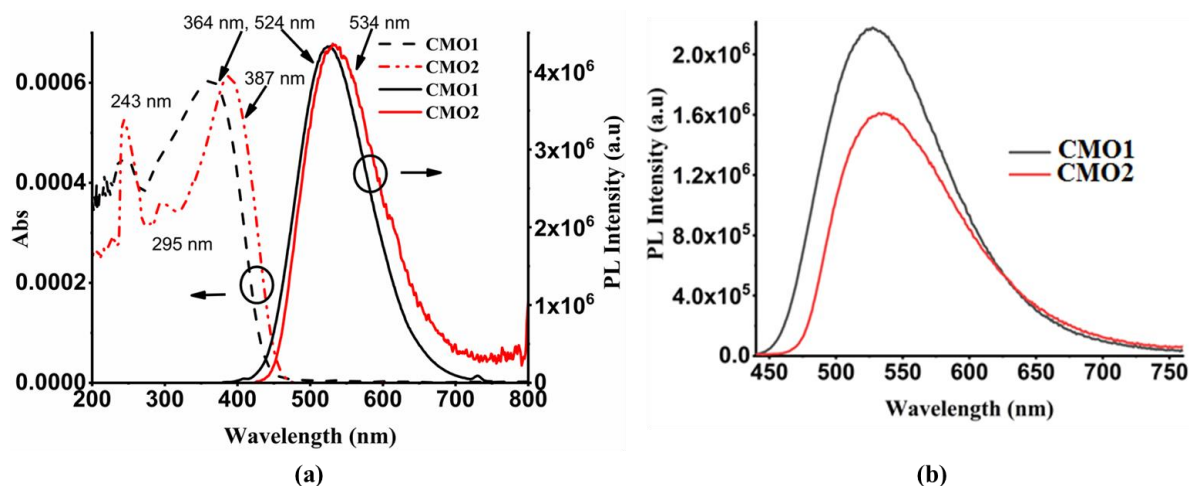


Figure 5.2.11 (a) The absorption and emission spectra of CMO1 and CMO2 in solution (THF (tetrahydrofuran)) 1mg in 10ml (black = CMO1 and red = CMO2), left side of the graph is absorbance, and the right side is PL intensity (b) Solid-state emission spectra of CMO1 and CMO2

The absorption and emission spectra of CMO1 and CMO2 were shown in (Figure 2) indicating that there is a redshift in both absorbance and emission spectra in CMO2 (364 nm vs 387 nm & 524 nm vs 534 nm), respectively. The small redshift is due to the involvement of an electron-donating group (triphenylamine) in CMO2. The solid-state emission spectrum of CMO2 also shows the redshifted broad peak with $\lambda_{\text{emi}} \sim 535$ nm in (Fig 5.2.11 b). According to the previous report for aromatic hydrocarbons, 6-311 G basis set was used to optimize monomers of both the oligomers by using density functional theory (DFT) in the Gaussian 09 package. The electron distribution in HOMO and LUMO is almost uniformly delocalized throughout the four arms of the species [Fig 5.2.12 (a, b)]; hence there was no charge separation observed in between the two TPE units, while in CMO2 the electron distribution is delocalized in HOMO but localized in LUMO in a certain part of the species (Fig 5.2.12 c), which reduces the energy gap and favours the bathochromic shift in the CMO2 in comparison with CMO1.

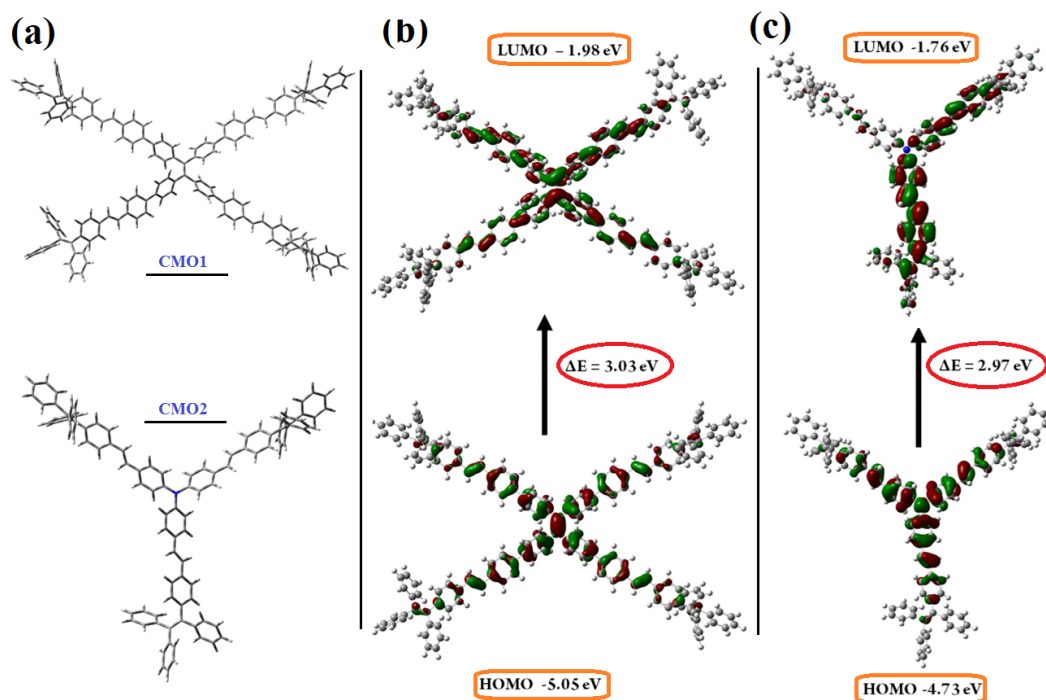


Figure 5.2.12 Geometry optimization through density functional theory in 9.0 Gaussian software using 6-311G (d,p) as a basis set. (a) Optimized structures of CMO1 & CMO2, (b) HOMO & LUMO energy level diagram of a single repeating unit of CMO1, (c) HOMO & LUMO energy level diagram of a single repeating unit of CMO2

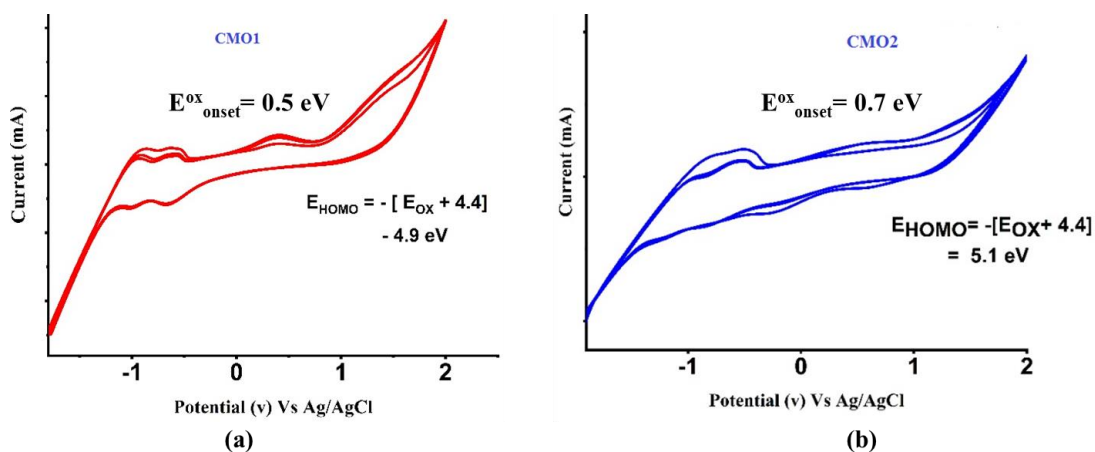


Figure 5.2.13 Cyclic voltammogram of (a) CMO1 (b) CMO2 (a Pt wire counter electrode and a Pt disc working electrode; an Ag/AgCl pseudo reference electrode; dry acetonitrile containing both polymer and 0.10 M LiClO₄ (100mg); ferrocene was used as internal reference). Scan rates: 50 mV/s; E_{ox} onset was (a) 0.5 eV so experimental HOMO is 4.9 eV. (b) 0.7 eV so experimental HOMO is 5.1 eV

The experimentally calculated value of HOMO & LUMO energy levels for CMO1 was - 4.90 eV and -2.14 eV and for CMO2 were - 5.10eV and -2.40 eV, respectively (Fig5.1.13). Moreover, the difference between HOMO and LUMO of CMO1, CMO2 are ($\Delta E = 2.76$ eV) and ($\Delta E = 2.70$ eV) respectively, which supports the bathochromic shift in emission spectra. The difference in the electron distribution of HOMO and LUMO in CMO2 in comparison with CMO1 induce the charge separation in CMO2, and hence CMO2 is more dipolar nature (hence will be affected by polar solvents) in comparison to CMO1. To prove the above statement, the change in the emission spectra of CMO2 and CMO1 in different solvents was recorded. The emission property of CMO1 and CMO2 were studied in different solvents with increasing polarity (excited at $\lambda = 367$ nm) (Fig 5.2.14 a, b). On increasing the solvent polarity, there was no observable change in the maximum emission wavelength in CMO1 (Fig 5.2.14 a), while a bathochromic shift (509 to 531 nm) was observed for CMO2 (Fig 5.2.15b) on increasing the solvent polarity. These results in solvents indicate that the CMO2 is more sensitive to the solvent dipole.

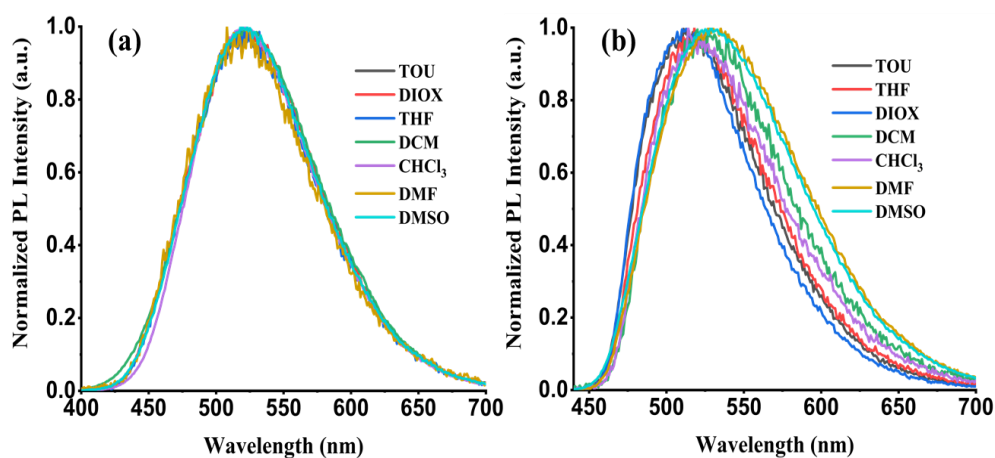


Figure 5.2.14 Emission spectra of (a) CMO1; (b) CMO2 in different solvent (TOU = toluene, DIOX = dioxane, THF= tetrahydrofuran, DCM= methylene dichloride, CHCl₃ = chloroform, excited at 367 nm, 0.4 mg of both the oligomers were dissolved in 5 ml of each solvents).

b) Aggregation-induced enhanced emission (AIEE)

In this article, the primary objective of incorporating the TPE unit is to provide the AIE characteristic in the CMOs. TPE is a typical AIE chromophore in which the rotation of the peripheral phenyl rings decays the excitation energy and reduces the luminescence intensity in solution. The TPE unit has four phenyl rings, which acts as a rotor group. Therefore, the

experiments were carried out in a solution and aggregated state. Here, the AIEE experiment was carried out by dissolving CMO1 and CMO2 in THF solvent (1mg/10ml). The CMOs were insoluble in water. Each CMO solution (0.5 ml) was taken and made into ten 5ml vials with an increasing concentration of water from 0% to 90%. The vials kept aside for the ultrasonication for five minutes to have a homogenous mixture. In CMO1, the emission intensity increases with increasing the concentration of the water [Fig 5.2.15 (a, b)]. The emission intensity increases when the formation of the aggregates increases. The enhanced emission intensity was seen in the plot between the intensity of CMO1 vs concentration of water (the image was taken under 365 nm excitation) (Figure 5.2.15 a, c). However, for CMO2, the emission intensity increases to 50% of water concentration, then it starts to decrease till 80% water concentration, followed by an enhanced intensity at 90%. (Fig 5.2.15 (d, e, f))

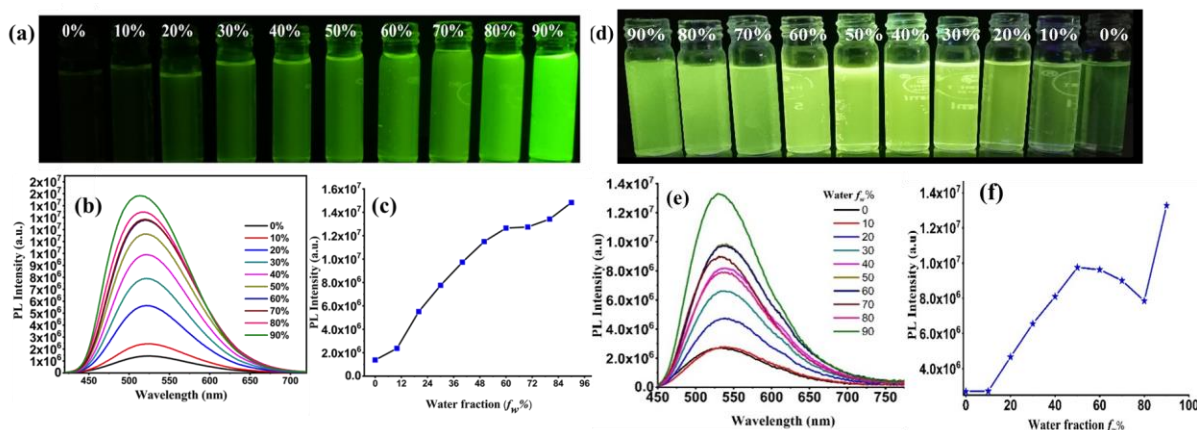


Figure 5.2.15 Photographs of (a) CMO1 (d) CMO2 in THF/water mixtures with different fractions of water taken under UV illumination (365 nm). PL spectra of (b) CMO1, (e) CMO2 in THF/water mixed solvents with varying portions of water (f_w) with excitation at 367 nm. The changes of the PL intensity of (c) CMO1, (f) CMO2 with a variation of water fraction in THF (f_w) with excitation at 367 nm.

The absolute quantum yield of the three different percentages, including solid-state, was recorded are as follows for CMP1 (0% = 3.1, 50% = 28.0, 70% = 35.0, 90% = 45.9) and for CMO2 are (0% = 3.2, 50% = 15.8, 70% = 12.3, 90% = 24.6). The enhancement of the PL intensity in the aggregated state is certainly proving these as AIEE nature.

For investigating the mechanism of AIEE, the PL spectra of CMO1 & CMO2 were recorded with a different mixture of THF and high viscous solvent (PEG) (Fig 5.2.16). The emission intensity was gradually enhanced by increasing the viscosity. The viscosity

experiment indicates that AIEE mainly operated through the ‘Restriction of Intramolecular Rotation’ (RIR) (two phenyls are still free in the oligomer). Here, the four branched TPE moieties are interlinked to the other two branched TPE molecules through the conjugated spacer resulting in a mesoporous interlocked network structure. Some of the unconjugated phenyl rotors remain free and become responsible for dissipating the excited energy through rotation and shows the non-emissive in solution. In the aggregated state, the interconnected TPE units form the polymeric assemblies where the rotation of the free rotors is restricted. The rigidifications of the interconnected network of phenyl ring units further increase the quantum yield of the CMO1. The Mesoporous extended conjugated network makes the CMO1 more luminescent and increases the quantum yield.

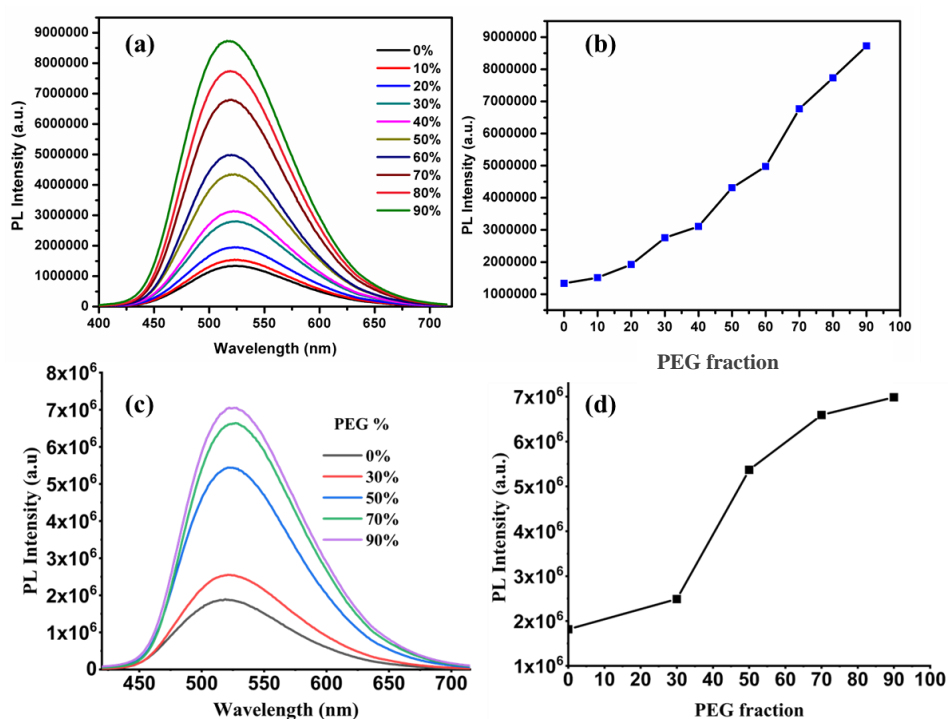


Figure 5.2.16 PL intensity spectra of (a) CMO1 (c) CMO2 in THF/PEG mixtures vs wavelength (b) CMO1-Plot of PL intensity values versus the fraction of PEG in the mixture. Solution concentration: 1 mg in 10ml; excitation wavelength: 365 nm. (d) CMO2- Plot of PL intensity values versus the fraction of PEG in the mixture of PEG-water. Solution concentration: 1 mg in 10ml ; excitation wavelength: 365 nm. (PEG = Polyethyleneglycol)

Further to support the enhanced emission is due to the formation of the aggregates and not because of the polarity change, we have carried out the AIEE experiment in DCM/hexane mixture (hexane is a less polar solvent than the DCM). In this case, the polarity of the medium is decreased with increasing hexane concentration into the mixture. It is observed that the emission intensity increases with increasing the concentration of the hexane (Fig

5.2.17 a) The enhanced emission intensity was observed in the plot between the intensity of CMO1 vs concentration of hexane (the image was taken under 365 nm excitation) (Fig 5.2.17 b, c). The results from the AIEE experiment in DCM and hexane proves that the enhanced emission is due to the formation of the aggregates and not because of the increased polarity.

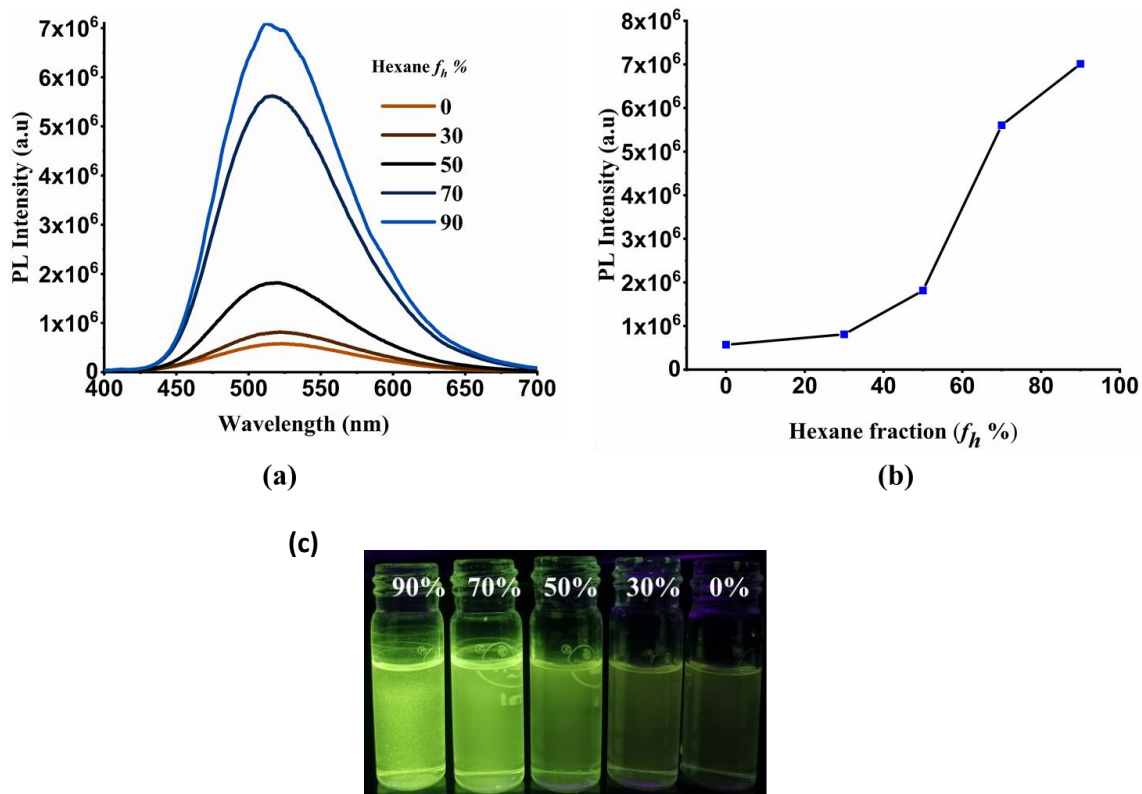


Figure 5.2.17 (a) PL spectra of CMO1 in DCM/hexane mixed solvents with varying fractions of hexane (f_h %) with excitation at 367 nm, and (b) the changes of the PL intensity of CMO1 in DCM with different hexane fraction (f_h %) (excited at 367 nm). (c) Photographs of CMO1 in DCM/Hexane mixtures with different fractions of hexane taken under UV illumination [From the stock solution (1mg of CMO1 in 10ml solvent), 0.5 ml of solution was made into five different vials varying the different concentration of Hexane]

The decreased quantum yield from 50% to 80% may be attributed to the CT (charge transfer) with CMO2. The PL emission wavelength of the CMO2 has a slight redshift on increasing the water concentration because of the increment of the polarity of the aggregates 0% (only THF) to 80% (THF-Water) (Fig 5.2.15 e). The water-THF mixture is more polar than the THF solution. In the 90% (THF-Water) mixture, the AIEE character dominates over the solvent polarity. Due to the difference in the electron localization in the molecules, CMO2 is sensitive to polarity; this might be the reason for the unusual behaviour of CMO2 in different water fraction [106, 107] Further, the stability of the polymer dispersions in 90% THF-H₂O solution was studied by recording the emission spectra and average zeta size of

CMO1 and CMO2 at different time intervals (0-45h). (Figure 5.2.18 a,b) The emission intensity decreases with time (Fig 5.2.18 b, c). The decrease in the emission intensity might be due to an increase in the average size. Due to the increase in the size of the aggregates, only surface molecules able to emit the fluorescence[108]

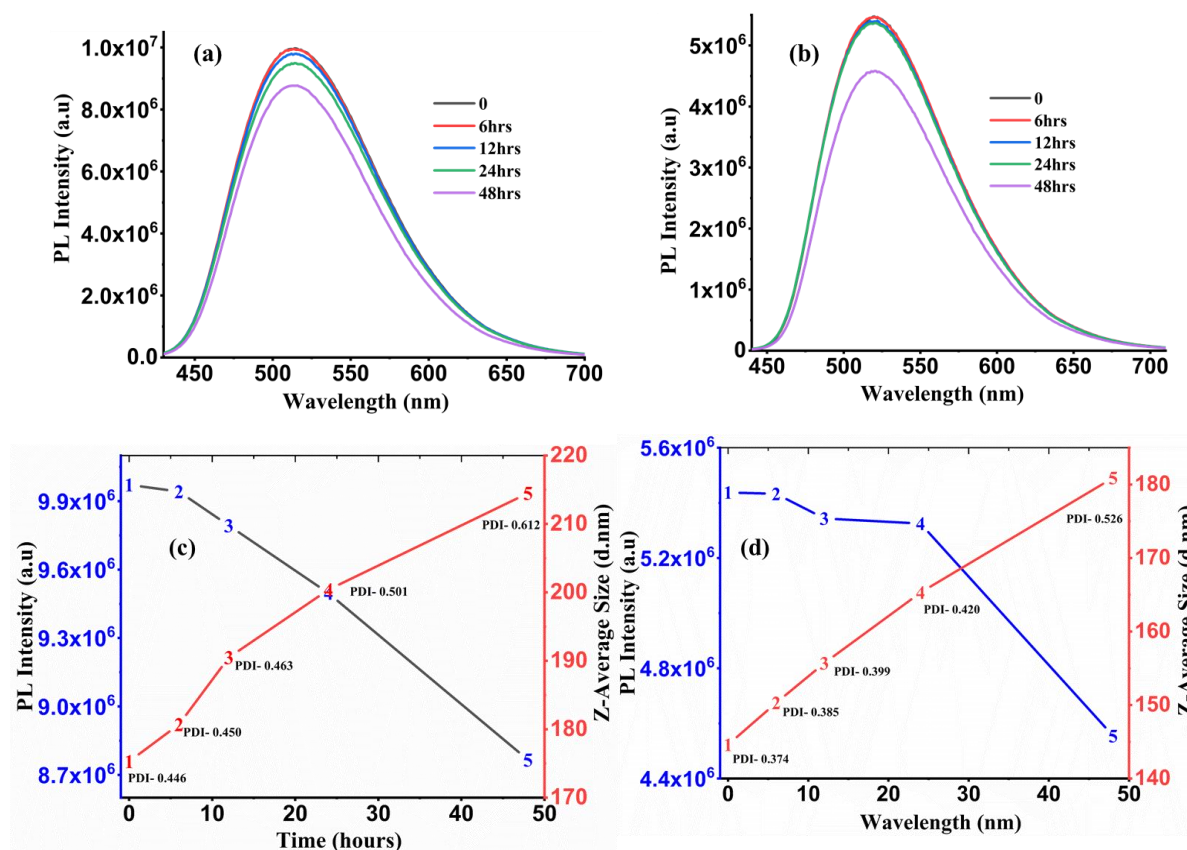


Figure 5.2.18 Emission plot of 90% aggregate solution (THF-H₂O) with respect to time (a) CMO1 and (b) CMO2. The stacked plot between the emission intensity and average zeta size concerning time (c) CMO1 and (d) CMO2

c) Explosive sensing

Here 90% THF-Water fraction of CMO1 has the highest quantum yield than the remaining fractions (Table 1). Therefore, 90% was selected for conducting all the experiments. On comparing the photoluminescence intensity of 0% solution with 90% aggregated form for the detection of picric acid (PA), the decrement in the emission intensity is much more is observed in 90% aggregated solution (Fig. 5.2.19).

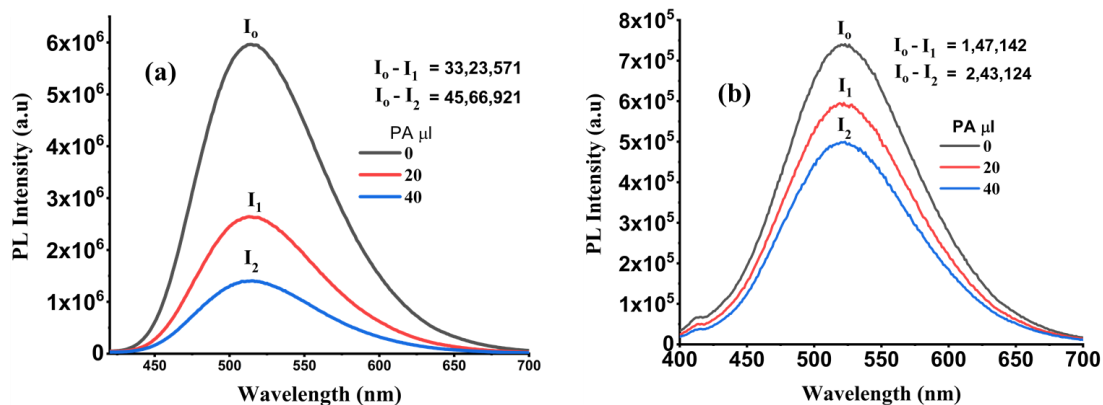


Figure 5.2.19 Comparative experiments between the photoluminescence spectra of CMO1 (a) 90% (THF-Water, aggregated solution) (b) 0% (non-aggregated state) with the addition of PA. (1mg/10ml stock solution of CMO1 and concentration of PA is 1mM).

Table 5.2.1 It shows the difference in the intensity of CMO1 in aggregated and non-aggregated form

	Emission intensity (I_0)	After addition of picric acid (I_1)	The difference in the intensity	No. of times decrease in the emission intensity (I_0/I_1)
CMO1 (90% aggregates Soluitor)	5962931	$I_1 = 2639360$	$I_0 - I_1 = 3323571$	2.5
		$I_2 = 1396010$	$I_0 - I_2 = 4566921$	4.2
CMO1 0% (non-aggregates soluiton)	738653	$I_1 = 591511$	$I_0 - I_1 = 147142$	1.2
		$I_2 = 465529$	$I_0 - I_2 = 243124$	1.5

The difference in the emission intensity of CMO1 before the addition of PA (I_0) with emission intensity after the addition of PA (I_1 , I_2) is observed to more in 90% than the 0% solution of CMO1 (Fig 5.2.19, Table 5.2.1). Therefore, 90% of aggregated solutions were screened with different nitroaromatics (in water 2eq) and recorded the photoluminescence (PL) spectra. The PL intensity of both compounds was completely quenched in the presence of picric acid (Fig 5.2.20). The selective efficiency of the probe was observed in 3d bar diagram in which the red colour pyramid is a probe, picric acid and other aromatic nitro based explosives / or non-explosive compounds, and front side pyramids are the compound, aromatic nitro based explosives / or non-explosive compounds (Fig 5.2.21(a,b)) and (Fig 5.2.22 (a,b)). The sensitivity of the probes was determined by recording the PL spectra of

oligomers with progressively increasing the concentration of picric acid. The emission spectra decrease steadily with an increase in the concentration of picric acid (Fig 5.2.21 c & Fig 5.2.21 c)). By plotting the Stern-Volmer (SV) plot between (I/I_0) ((I) Intensity of polymer with quencher)/ (I_0) Intensity of polymer without quencher) Vs. The concentration of picric acid, a linear fitting was observed for both the oligomers (CMO1 and CMO2) in the range $0\mu\text{l}$ - $35\mu\text{l}$ & $0\mu\text{l}$ - $28\mu\text{l}$, respectively (Fig 5.2.21 d and Fig 5.2.22 d).

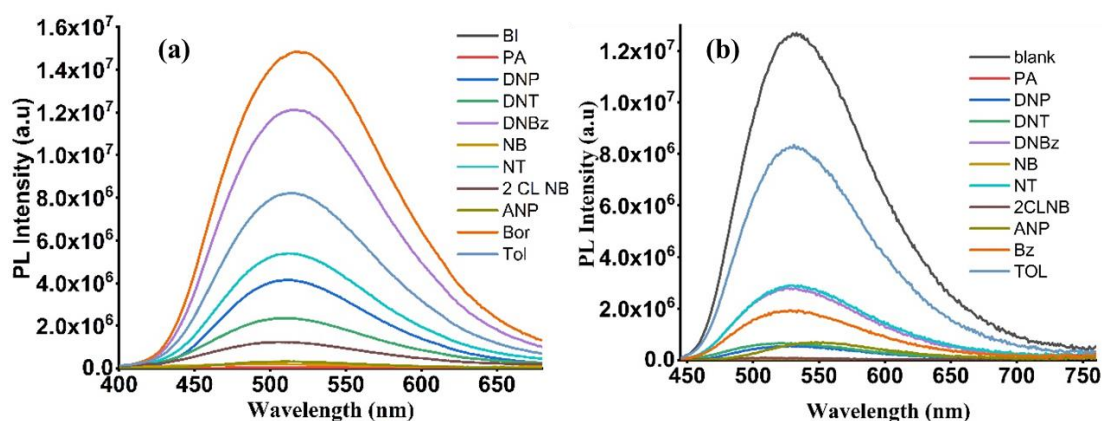


Figure 5.2.20 Emission spectra of (a) CMO1 (f_w , 90% in the mixed solvent) (b) CMO2 (f_w , 90% in the mixed solvent) in presence of different nitro aromatics and non nitro aromatics. Tol = Toluene, 2.Bor = boric acid, 3.ANP = 2-Amino-4-nitrophenol, 4. 2Cl NB = 2,4 dinitro chlorobenzene, 5. NT= 4-Nitrotoluene, 6.NB = 4-Nitrobenzene, 7. DNBz = 3,5 Dinitrobenzoic acid, 8= DNT= 2,6 dinitrotoluene, 9 = DNP = 2,4 dinitrophenol, 10. PA= Picric acid, 11.BI = Blank

The Stern-Volmer quenching constant was calculated by the formula, $K_{sv} = K_q\tau_0$ (where K_q bimolecular quenching constant and τ_0 is the lifetime of the fluorophore in the absence of the quencher).[109] For CMO1 and CMO2, was $2.6 \times 10^6 \text{ M}^{-1}$ and $3.40 \times 10^4 \text{ M}^{-1}$, respectively which is found to be the best result for all the reported conjugated polymers used for explosive detection[91, 110, 111]. There were several ways by which the quenching of the fluorescent molecules are resulted such as, Inner filter effect (IFE), photoinduced electron transfer(PET), energy transfer (ET), proton transfer (PT), collision and static quenching.[112] For developing efficient, sensitive probes in the vapour phase, there is a need to study the relationship between the molecular structure and the mechanism of the quenching process. Although many theories and explanations were given on the detection of explosives through quenching mechanics.[113]

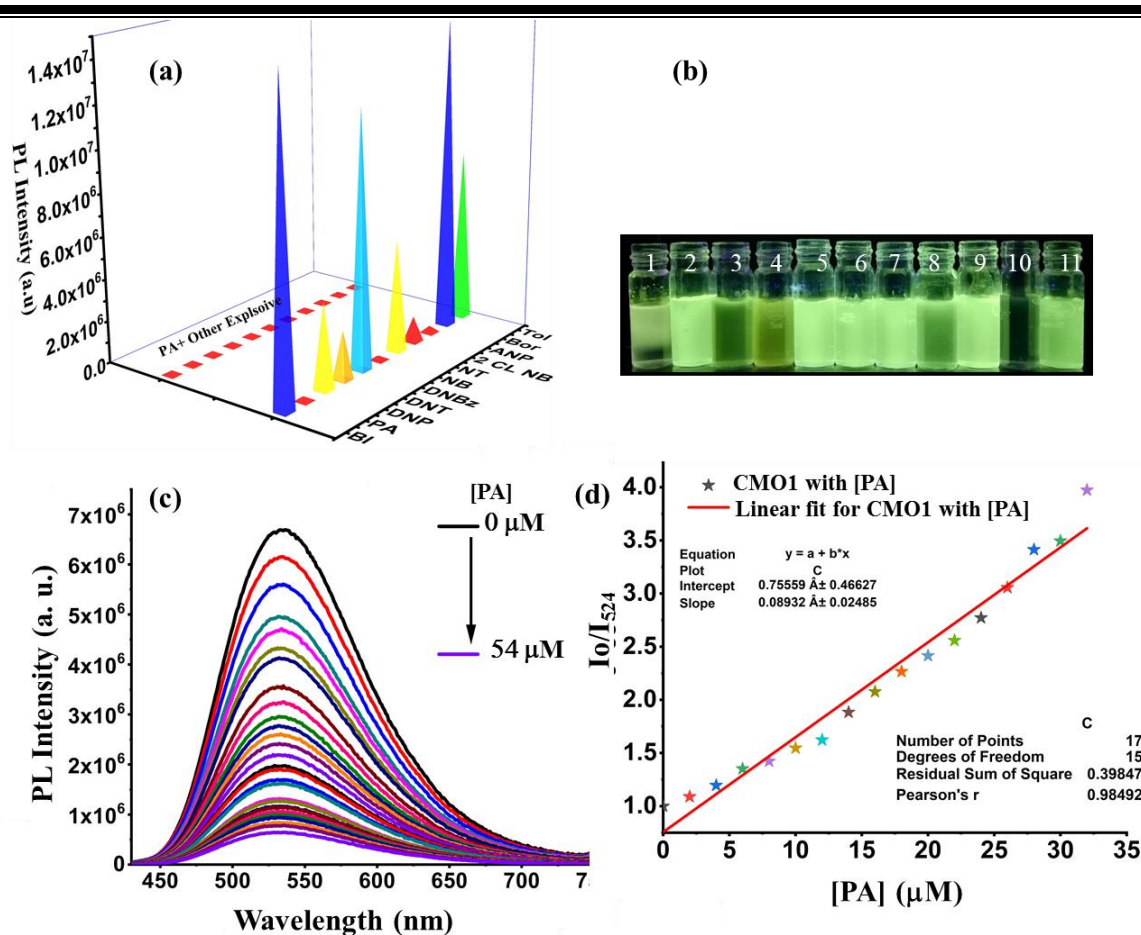


Figure 5.2.21 (a) 3d bar diagram is representing the emission intensity of CMO1 [1mg/ml at fw = 90% (in water/THF)] in the presence of different nitro-based explosives and non-explosive compounds. (Right side red color cones indicate the quenched intensity of CMO in the presence of PA + different nitroaromatic rings / or non-explosive compounds, left colorful side cones to indicate the intensity of CMO1 + different nitroaromatics / or non-explosive compounds. b) Photoluminescence image of CMO1 in the presence of different explosives (1eq) and non-explosive (1eq) taken under UV-visible lamp (1.Tol = Toluene, 2.Bor = boric acid, 3.ANP = 2-Amino-4-nitrophenol, 4. 2Cl NB = 2,4 dinitro chlorobenzene, 5. NT= 4-Nitrotoluene, 6.NB = 4-Nitrobenzene, 7. DNBz = 3,5 Dinitrobenzoic acid, 8= DNT= 2,6 dinitrotoluene, 9 = DNP = 2,4 dinitrophenol, 10. PA= Picric acid, 11.Bl = Blank. c) Emission spectra of CMO1 in THF-Water (v/v =1:9) titrated with different amount of PA. (d) Linear fitting for CMO1 with PA

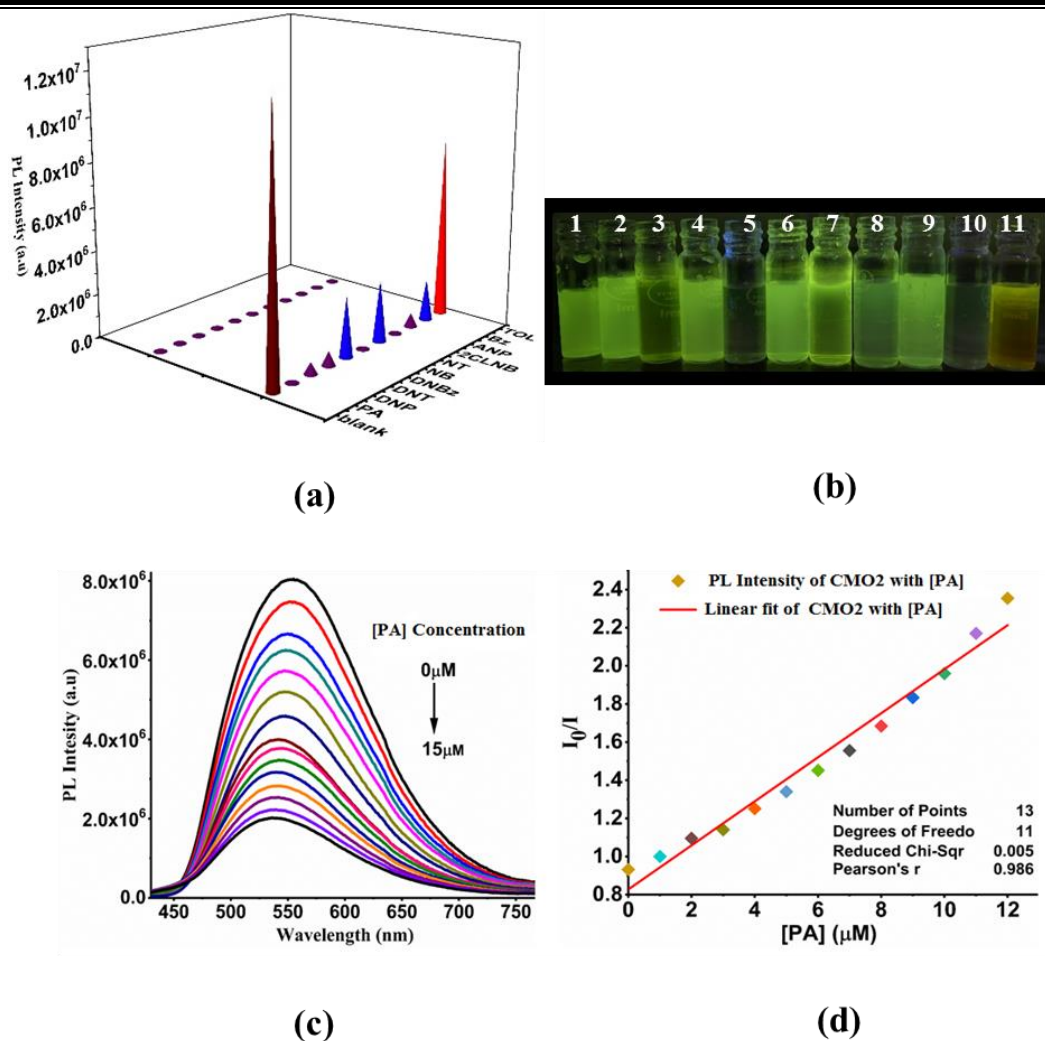
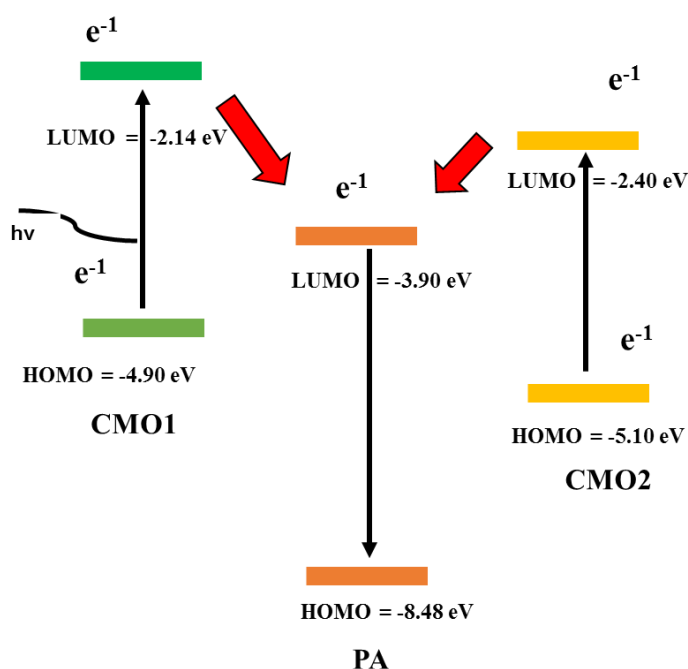


Figure 5.2.22 (a) 3d bar diagram is representing the emission intensity of CMO2 [1mg/ml at fw = 90% (in water/THF)] in the presence of different nitro-based explosives and non-explosive compounds. (Right side red color cones indicate the quenched intensity of CMO2 in the presence of PA + different nitroaromatic rings / or non-explosive compounds, left colorful side cones to indicate the intensity of CMO2 + different nitroaromatics / or non-explosive compounds. (b) Photoluminescence image of CMO2 in the presence of different explosives (1eq) and non-explosive (1eq) taken under UV-visible lamp (1.Tol = Toluene, 2.Bor = boric acid, 3.ANP = 2-Amino-4-nitrophenol, 4. 2Cl NB = 2,4 dinitro chlorobenzene, 5. NT= 4-Nitrotoluene, 6.NB = 4-Nitrobenzene, 7. DNBz = 3,5 Dinitrobenzoic acid, 8= DNT= 2,6 dinitrotoluene, 9 = DNP = 2,4 dinitrophenol, 10. PA= Picric acid, 11.Bl = Blank. (c) Emission spectra of CMO2 in THF-Water (v/v =1:9) titrated with different amount of PA. (d) Linear fitting for CMO2with PA

Chapter 5

However, the results were not focused on what combination of mechanisms/ or properties of the probes should be included in designing for new efficient probes for the detection in the vapor phase in recent years. The experimentally calculated value of HOMO and LUMO levels indicates the impact of photoinduced electron transfer (PET)(Scheme 5.2.6) from electron-rich oligomers to electron-deficient nitro explosives. The energy gap between HOMO and LUMO levels of the probe is more (for CMO1 = 2.76 eV & CMO2 = 2.70 eV) as compared to the difference between the LUMO levels of the probe (donor) and picric acid (acceptor) (for CMO1 = 1.76 eV & CMO2 = 1.50 eV), so the electron transfer is facilitated from donor to acceptor (Scheme 5.2.6). One can notice if only the PET effect were playing the leading role in the quenching process, then the efficient probe should be CMO2 because of the difference between the LUMO levels of CMO2 and PA is less as compared to CMO1. The experimental result was found the opposite to our expectation, and the sensitivity was found more in the case of CMO1 as compared to CMO2.



Scheme 5.2.6 Schematic illustration of photoinduced electron transfer (PET) mechanism

Therefore, there might be another process i.e., inner filter effect (IFE) that may be caused quenching. For IFE to be effective, there should be an overlap between the absorption spectrum of the targeting material with the excitation or emission spectrum of the probe. While for resonance energy transfer (RET) can be caused by the overlap between the absorption spectrum of the targeting material and emission spectrum of the probe.[114]

Therefore, two mechanisms can play a critical role in sensing. However, for RET is a dynamic quenching process in which the lifetime of the probe molecules changes when it meets analyte while IFE is a static quenching process in which it does not require any covalent linking between the fluorophore and a receptor. In the case of CMO1 and CMO2, we could observe the overlapping area between the absorption of the picric acid and excitation/emission spectra of both the probes (Fig 5.2.23).

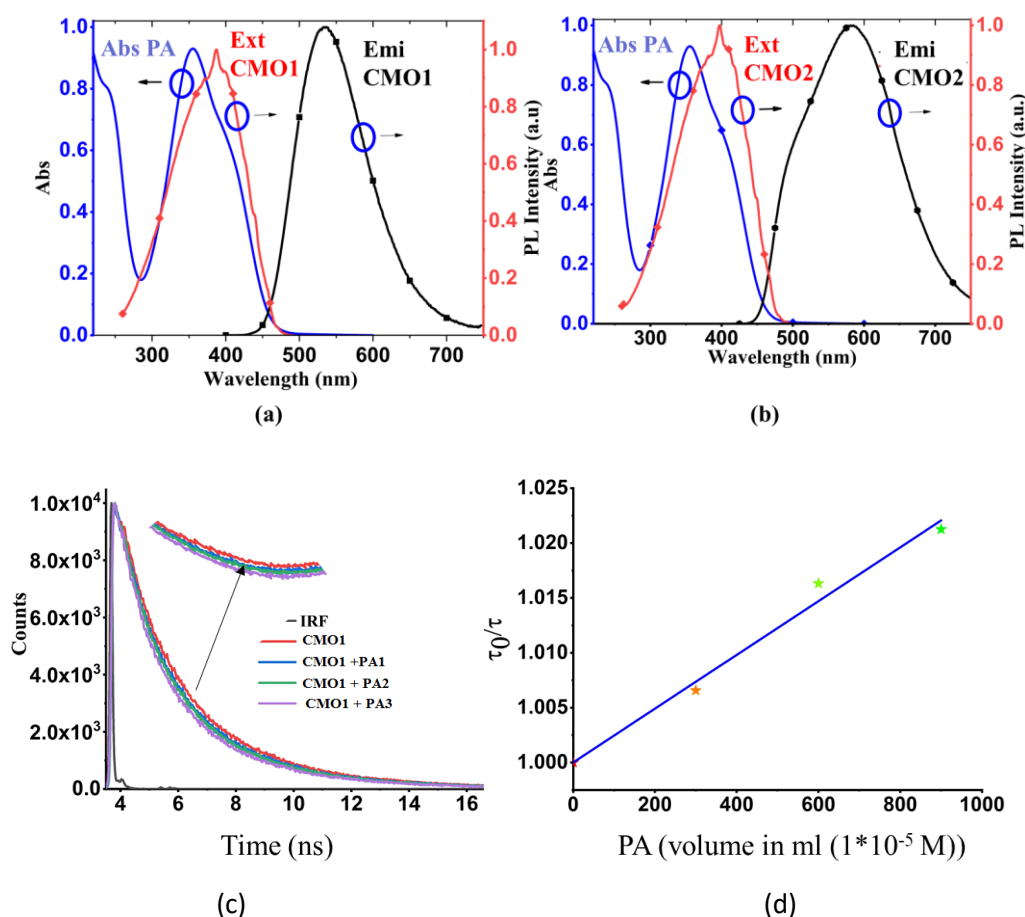


Figure 5.2.23 It shows the spectral overlap between the absorption of PA and emission & excitation of (a) CMO1 (b) CMO2 indicating the possibility of either inner filter effect or resonance energy transfer mechanism from CMO1, CMO2 to PA, respectively. (PA in water = 1×10^{-5} M, CMO1 CMO2 = 90 % aggregates solution in THF/water fraction (c) Excited State lifetime of CMO1 with gradually increasing the picric acid (PA) amount (PA1 = 200 μ l [1×10^{-5} M], PA2 = 500 μ l [1×10^{-5} M] and PA3 = 1 ml [1×10^{-5} M]) (d) Stern-Volmer plot between the excited state lifetime of CMO1 and with increasing volume of PA. (IRF = instrument response function)

Here both the probes CMO1 and CMO2 show linear Stern-Volmer plot. In CMO1, the excited state lifetime decreases on the addition of the picric acid and have linear Stern-

Chapter 5

Volmer plot with the lifetime [Fig 5.2.23 (c, d)]. These two facts support the dynamic quenching process. Therefore, the RET process plays a vital role in quenching the emission intensity of the probes.[115] (Fig 5.2.23). To study the efficiency of energy transfer from the probes to PA, the overlapping integral $J(\lambda)$ $M^{-1}cm^{-1}nm^4$ was calculated from the (R2018a)[116, 117]. This overlap integral denotes the degree of spectral overlap between CMO1 and PA (similarly, CMO2 and PA). For CMO1, the calculated $J(\lambda)$ value is $3.80 \times 10^{14} M^{-1}cm^{-1}nm^4$ and for CMO2 the value is $2.64 \times 10^{14} M^{-1}cm^{-1}nm^4$. The Forster distance between the donor (CMOs) and acceptor (PA) was calculated by using the formula $R_0^6 = 8.79 \times 10^{-5}(\kappa^2 n^{-4} Q.D J(\lambda))$ (in \AA^6) (R_0 is Forster distance, κ^2 is orientational factor generally it is assumed to be 2/3, n is the refractive index of the medium used, and QD is the quantum yield of the donor in the absence of the acceptor) [Table 5.2.2]. The Forster distance for CMO1 is more in comparison to CMO2 (7.45 nm vs 6.30 nm). By substituting the values of relative fluorescence intensity (F) of the donor (D), in the absence (FD) and presence (FDA) of the acceptor (A) in formula ($E = 1-FD/FDA$), one could calculate the energy transfer efficiency (E) of CMO1 (87 %) which is more in comparison to CMO2 (80 %).[118] From the values of R and E , the actual distance between the donor and acceptor (r) for CMOs was calculated (value of (r) are 5.40 nm and 4.97 nm, respectively).[118] The larger Forster distance of CMO1 is due to the larger quantum yield of CMO1. Hence the donor-acceptor distance (r) is 1.08 times more for CMO1 than CMO2. In CMO1, the distance between donor and acceptor (r) was 0.72 times less than the foster distance (R_0) (r/R_0) and the same in CMO2 (r) is 0.77 times less than R_0 . Therefore, energy transfer efficiency is observed more in CMO1. The calculated rate of energy transfer [$k_T(r)$] is $2.65 ns^{-1}$ for CMO1 in comparison to $2.32 ns^{-1}$ observed for CMO2 [$k_T(r) = (1/\tau_D)*(R_0/r)^6$] where τ_D = life-time of the probe.[118] From above all the experiments, it may be concluded that the energy transfer also depends upon the porosity of the probes.

Table 5.2.2 It shows the calculated value of $J(\lambda)$ overlap integral, (R_0) Forster distance, (r) distance between the donor and acceptor.

	$J(\lambda) M^{-1}cm^{-1}nm^4$	R_0 (nm)	r (nm)	Eq%	$K_T(r) s^{-1}$
CMO1	$3.68 * 10^{14}$	7.45	5.4	87	2.12
CMO2	$2.67 * 10^{14}$	6.35	5.04	80	2.8

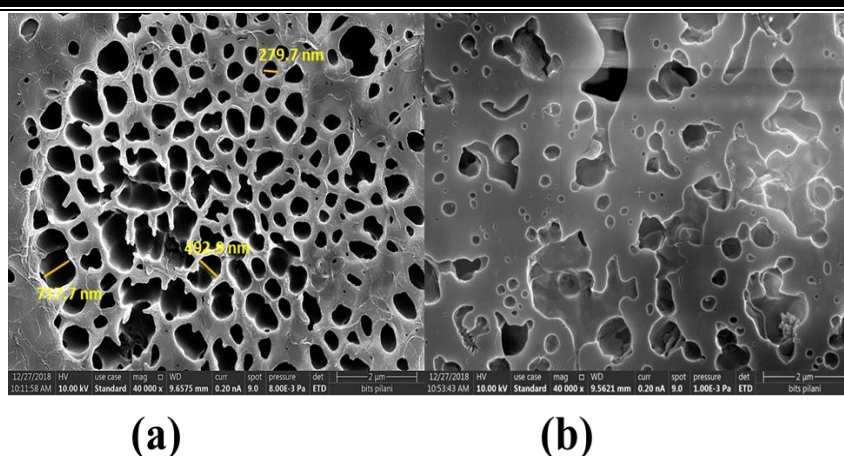


Figure 5.2.24. (a) FESEM images of CMO1 thin film before exposing to the PA vapours. (b) FESEM images of CMO1 after exposure to the PA vapours

To prove this, the thin films of both the oligomers have made to expose to the vapours of the picric acid for one day. After one day, the thin film was characterized by FESEM (field emission scanning electron microscope) and FTIR spectroscopy. From the FESEM image of the thin film before exposure, one could observe a large non-uniform porous structure in CMO1. The thick, dense network between the pores is due to the extended conjugation, which makes the phenyl rings interlock between themselves and self-assemble due to hydrophobic interaction [Fig 5.2.24 (a, b)]. This could be the reason for the increased quantum yield. After exposing the thin film to the PA, the FESEM image reveals that particles of the PA fill the macropores (Fig 5.2.24 b). One can notice the hollow space was now closed or packed by molecules of picric acid. The support was also given by infrared spectra (IR).

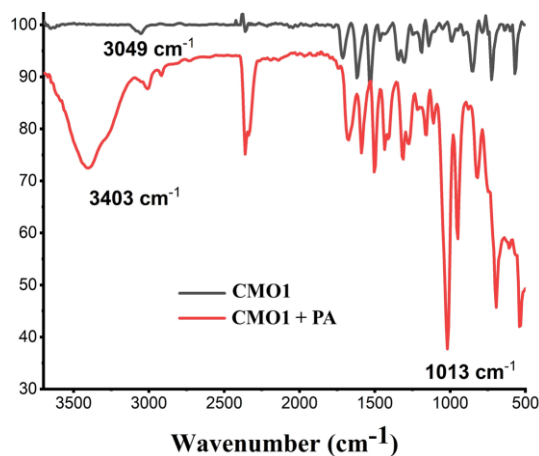


Figure 5.2.25. (a) FT-IR spectra of the CMO1 before and after exposure to PA.

The IR spectra of the CMO1 after exposing to the vapour of the PA show the new peaks around 3403 cm^{-1} , 1485 cm^{-1} , 1013 cm^{-1} which corresponds to peaks of OH, NO_2 and C-O and also the peak at 3403 cm^{-1} was broad indicates that pores were filled by more picric acid molecules (Figure 5.2.25). The FESEM image of CMO2 shows a relatively less porous network and a thick, dense web-like network (Fig 5.2.26). The results of the chemical composition analysis by EDS (Energy Dispersive X-Ray Spectroscopy) showed that the amount of carbon content is exclusively 100% before exposing to PA while the amount of the elements in thin-film after exposing to PA is as follows: carbon, 85.14%; oxygen, 11.81%; nitrogen, 3.05%. The above results of EDS on thin film before and after exposure further supporting the presence of PA in Mesoporous of CMO1.[119] The CMO1 has large non-uniform pores in a thin film with a densely interconnected network, which is observed in the SEM image. The thin film was exposed to the PA vapour for one night in a closed chamber to occupy the pores present in the CMO1 completely. Overnight exposure of PA causes the vapours of PA to move and occupy the pores and eventually settle on the surface of CMO1 due to the over-saturation of PA molecules. The presence of PA is also supported by the IR spectra which were collected before, and after exposure of PA to the thin film Due to the overexposure to PA, the morphology of the thin film might be changed.

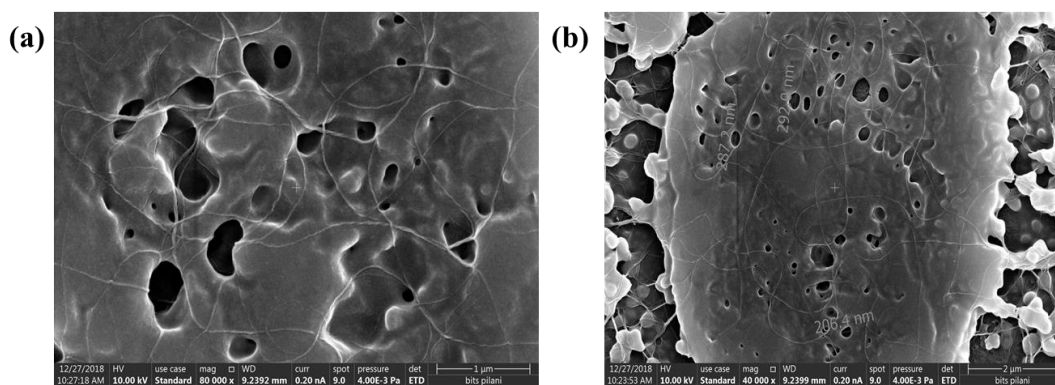


Figure 5.2.26 FESEM image of CMO2

The sensitivity of CMO1 with TNT (Trinitrotoluene) was determined by recording the PL spectra of CMO1 with progressively increasing the concentration of TNT. By plotting the Stern-Volmer plot, a linear fitting was observed between $0\mu\text{l}$ - $2500\mu\text{l}$. The emission spectra decrease steadily with an increase in the concentration of TNT. The quenching constant was found to be $2.3 \times 10^3\text{ M}^{-1}$ (Fig 5.2.27 a, b).

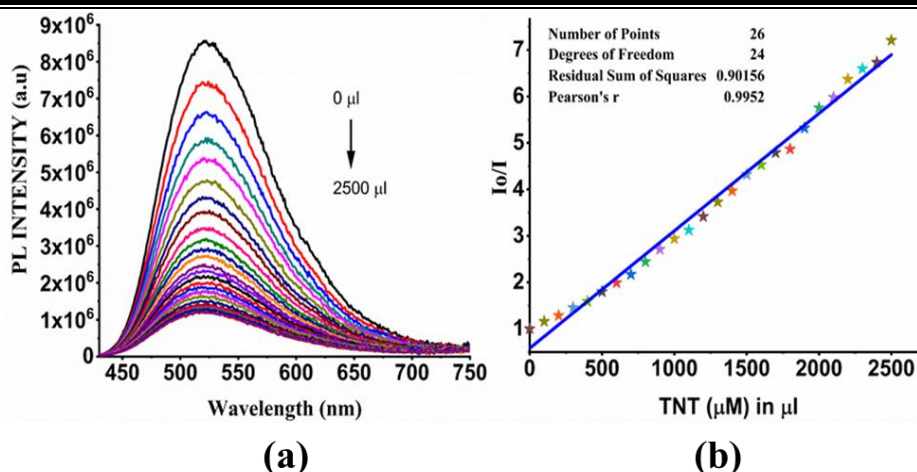


Figure 5.2.27 (a) Emission spectra of CMO1 [1mg/ml at $f_w = 90\%$ (in water/THF)] titrated with increasing concentration of TNT (10^{-6} M). (b) Linear fitting plot of I_o/I [I_o = Photoluminescence (PL) intensity without any probe; I = PL intensity at variable concentration of TNT] for CMO1 with TNT.

The quenching constant of the TNT is very low as compared to the quenching constant of PA. The energy transfer mechanism could support such difference in the quenching constant. The overlapping area between the absorption of PA and the emission of the CMO1 molecule indicates the occurrence of energy transfer between PA and CMO1. There is no overlapping observed for the case of TNT. This might be the reason for the observation of such high quenching constant in PA in comparison to TNT. (Fig 5.2.28)

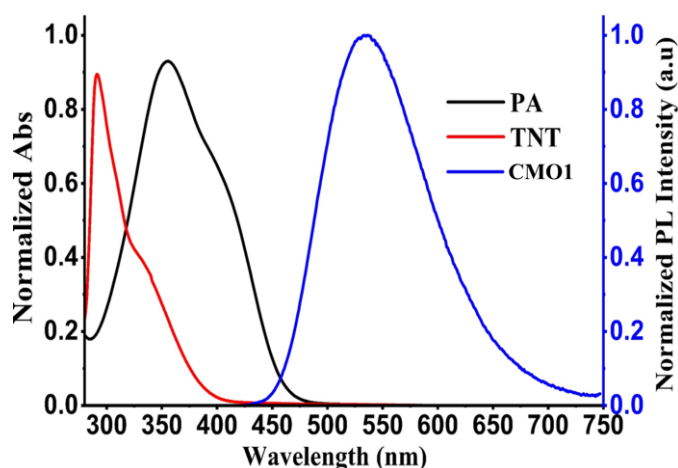


Figure 5.2.28. Overlapped area of the absorption spectra of PA and TNT with the emission spectrum of CMO1 indicating the energy transfer from CMO1 to PA, respectively. (PA and TNT in water (1×10^{-5} M) and CMO1 90% aggregates solution in thf/water fractions)

For real-time application, CMO1 was also used to detect PA in contact mode by applying small spots (10 μ L) of various concentrations of PA solution into CMO1 impregnated test strips. A dark colour spot was observed not only at higher concentrations (0.1 mM) of PA but also at nanomolar concentrations [Fig 5.2.29 a (top)]. These observations confirm that the test strips containing CMO1 are responsive to PA even at low concentrations. Solid PA is detected using CMO1 and then visualized under 365 nm UV-Vis lamb. The dark spot is observed under the area of the rubbed surface [Fig 5.2.29 a (bottom)].

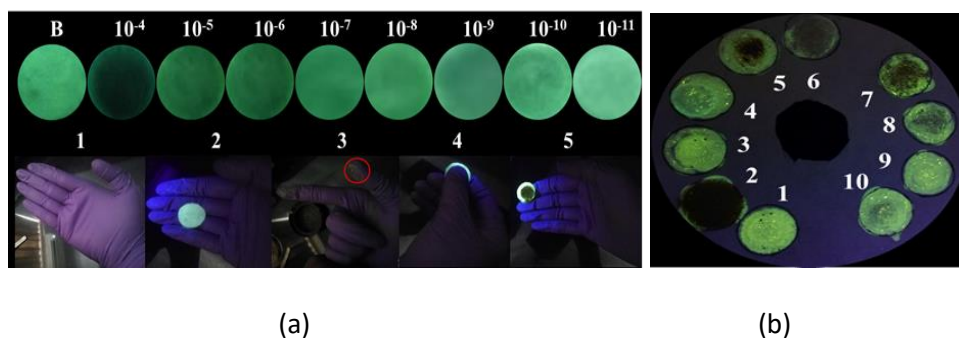


Figure 5.2.29 a) Top Shows the photographs of CMO1 impregnated test strips with varying concentrations of PA upon illumination at 365 nm; from left to right: blank (B), 1×10^{-4} M, 1×10^{-5} M, 1×10^{-6} M, 1×10^{-7} M, 1×10^{-8} M, 1×10^{-9} M, 1×10^{-10} M, 1×10^{-11} M. below:- Shows the image was taken upon illumination at 365 nm (1) gloves without a trace of picric acid, (2) impregnated test strips without any contact of PA. (3) Gloves showing the powder of picric acid on thumbs (marked with a red circle), (4) Image of the CMO1 impregnated test strips while applying the PA traces, (5) Image of CMO1 impregnated test strips rubbed with PA. (b) Photograph of CMO1 impregnated test strips at ten different places exposing to the powder of various explosives [(1) blank CMO1, (2) Picric acid, (3) 4-Nitrobenzene, (4) 3,5-Dinitrobenzoic acid, (5) 2-Amino-4-nitrophenol, (6) 2,6 trinitrotoluene, (7) 2,4 dinitrophenol, (8) 4-Nitrotoluene, (9) benzoic acid, (10) boric acid].

After the successful attempt to detect in the solid phase, the selectivity test was also performed by making 10 circular spots of CMO1 on filter paper. Different explosives and non-explosives were rubbed on the CMO1 impregnated filter paper (Fig 5.2.29 b). One can observe the difference in the extent of quenching level in the form of darker to lighter spots on the filter paper. This test supports the successful use of the probes in differentiating different explosives in the solid phase. Therefore, paper strips prepared by dip-coating a solution of the oligomer provide a simple, portable, sensitive, selective and low-cost method for the detection of nitro explosive and also for differentiating the explosive material without

any tedious instrumentation, which could lead to real-time applications such as onsite detection, forensic, research, etc. From above all the results and discussion, the sensitivity towards picric acid in conjugated Mesoporous oligomers depends on the combination of the two to three factors. To have a very sensitive probe, one should design the probes with a high quantum yield and that which could be bound by the efficient interlocking system.

5.2.4 Conclusion

This part of the chapter described the straightforward synthesis of AIEE active conjugated oligomers, namely CMOs with Mesoporous network architecture, by Wittig polymerization with moderate molecular weight. The integration of typical AIE building blocks such as TPE and TPA in the CMO skeleton endowed them with AIEE characteristics. The resulting CMOs are weakly emissive in solution, enhanced and robust emission observed in the solid-state, implying the phenomenon of AIEE. Because of increased conjugation, the phenyl ring in the TPE moiety is interlinked in such a way that they are interlocked in the polymeric backbone, forming a highly porous dense network. These interlocking of the phenyl ring are the reason for the increased quantum yield in the aggregated state. The 90 % aggregated solution formed in the mixed solvent showing the highest quantum yield, and it was utilized in the sensing of picric acid. Calculated quenching constant of picric acid ($2.6 \times 10^6 \text{ M}^{-1}$) was high as compared to the literature value of polymeric materials.[56, 90] The CMO1 was also utilized for TNT sensing with sensitivity ($2.3 \times 10^3 \text{ M}^{-1}$). A very facile paper strip of low-cost detection and differentiation of the nitro explosives was possible by using CMO1. The mechanism was explained in detail. The synthesized conjugated mesoporous oligomer is highly porous, which facilitate extended exciton migration pathway and increase the energy transfer efficiency. The article inspires to design new probes for non-contact mode-based vapour phase sensing and could be applied for real-time application for low-cost paper strip detection of unknown explosives.

5.3 Reference

- [1] T. Liu, K. Zhao, K. Liu, L. Ding, S. Yin and Y. Fang, *J. Hazard. Mater.*, 2013, **246-247**, 52-60.
- [2] C. Zhang, *J. Hazard. Mater.*, 2009, **161**, 21-28.
- [3] H. Schubert and A. Kuznetsov, *Detection and disposal of improvised explosives*, Springer Science & Business Media, 2006.

- [4] Z. Hu, K. Tan, W. P. Lustig, H. Wang, Y. Zhao, C. Zheng, D. Banerjee, T. J. Emge, Y. J. Chabal and J. Li, *Chemical Science*, 2014, **5**, 4873-4877.
- [5] M. E. Germain and M. J. Knapp, *Chem. Soc. Rev.*, 2009, **38**, 2543-2555.
- [6] N. Niamnont, N. Kimpitak, K. Wongravee, P. Rashatasakhon, K. K. Baldrige, J. S. Siegel and M. Sukwattanasinitt, *Chem. Comm.*, 2013, **49**, 780-782.
- [7] G. Sathiyam, B. Balasubramaniam, S. Ranjan, S. Chatterjee, P. Sen, A. Garg, R. K. Gupta and A. Singh, *Materials Today Chemistry*, 2019, **12**, 178-186.
- [8] G. B. Demirel, B. Daglar and M. Bayindir, *Chem. Comm.*, 2013, **49**, 6140-6142.
- [9] H. Sohn, M. J. Sailor, D. Magde and W. C. Troglor, *J. Am. Chem. Soc.*, 2003, **125**, 3821-3830.
- [10] X. Sun, Y. Wang and Y. Lei, *Chem. Soc. Rev.*, 2015, **44**, 8019-8061.
- [11] A. Saxena, M. Fujiki, R. Rai and G. Kwak, *Chem. Mater.*, 2005, **17**, 2181-2185.
- [12] M. A. Reppy, in *Advanced Fluorescence Reporters in Chemistry and Biology II*, Springer, 2010, pp. 357-388.
- [13] N. Venkatramaiah, S. Kumar and S. Patil, *Chemical Communications*, 2012, **48**, 5007-5009.
- [14] S. Singh, *J. Hazard. Mater.*, 2007, **144**, 15-28.
- [15] J. Goodpaster and V. McGuffin, *Analytical chemistry*, 2001, **73**, 2004-2011.
- [16] S. Shanmugaraju, S. A. Joshi and P. S. Mukherjee, *Journal of Materials Chemistry*, 2011, **21**, 9130-9138.
- [17] H.-X. Zhang, Q. Chen, R. Wen, J.-S. Hu and L.-J. Wan, *Analytical chemistry*, 2007, **79**, 2179-2183.
- [18] S. Shanmugaraju, S. Joshi and P. Mukherjee, *J. Mater. Chem.*, 2011, DOI: 10.1039/C1JM10406C, 9130.
- [19] A. Kumar, A. Pandith and H.-S. Kim, *Sens. Actuators B Chem.*, 2016, **231**, 293-301.
- [20] G. V. e. Zyryanov, D. S. Kopchuk, I. S. Kovalev, E. V. Nosova, V. L. Rusinov and O. N. Chupakhin, *Russian Chemical Reviews*, 2014, **83**, 783.
- [21] E. V. Verbitskiy, G. L. Rusinov, O. N. Chupakhin and V. N. Charushin, *Dyes Pigm.*, 2020, 108414.
- [22] J. Suk, Z. Wu, L. Wang and A. J. Bard, *J. Am. Chem. Soc.*, 2011, **133**, 14675-14685.
- [23] T. T. Vu, S. Badré, C. Dumas-Verdes, J.-J. Vachon, C. Julien, P. Audebert, E. Y. Senotrusova, E. Y. Schmidt, B. A. Trofimov and R. B. Pansu, *J. Phys. Chem. C*, 2009, **113**, 11844-11855.
- [24] R. J. S. R. Bogue, *Sensor Review*, 2015.

- [25] M. J. Lefferts and M. R. Castell, *Analytical Methods*, 2015, **7**, 9005-9017.
- [26] P. Kumar, A. Deep and K.-H. Kim, *Trends in Analytical Chemistry*, 2015, **73**, 39-53.
- [27] Y. Zhang, Y.-Y. Fu, D.-F. Zhu, J.-Q. Xu, Q.-G. He and J.-G. Cheng, *Chin. Chem. Lett.*, 2016, **27**, 1429-1436.
- [28] I. Buryakov, T. Buryakov and V. Matsaev, *Journal of Analytical Chemistry*, 2014, **69**, 616-631.
- [29] M. K. Chahal and M. Sankar, *Analytical Methods*, 2015, **7**, 10272-10279.
- [30] J.-B. Chen, B. Li, Y. Xiong and J. Sun, *Sensors and Actuators B: Chemical* 2018, **255**, 275-282.
- [31] S. Sarkar, S. Roy, A. Sikdar, R. Saha and S. S. Panja, *Analyst*, 2013, **138**, 7119-7126.
- [32] K. Huang and A. A. Martí, *Anal. Bioanal. Chem.*, 2012, **402**, 3091-3102.
- [33] G. Sivaraman, T. Anand and D. Chellappa, *Analytical Methods*, 2014, **6**, 2343-2348.
- [34] W. E. Acree Jr, *Encyclopedia of Analytical Chemistry: Applications, Theory Instrumentation*, 2006.
- [35] A. Konishi, T. J. P. Kubo and C. o. G. G. t. Nanographene, *Physics and Chemistry of Graphene: Graphene to Nanographene* 2019, 309.
- [36] M. A. Meador, D. S. Tyson and U. F. Ilan, *Journal*, 2012.
- [37] M. M. Islam, Z. Hu, Q. Wang and C. R. X. Feng.
- [38] M. Shellaiah, T. Simon, V. Srinivasadesikan, C.-M. Lin, K. W. Sun, F.-H. Ko, M.-C. Lin and H.-C. Lin, *J. Mater. Chem.C.*, 2016, **4**, 2056-2071.
- [39] X. Zhang, Z. Chi, B. Xu, C. Chen, X. Zhou, Y. Zhang, S. Liu and J. Xu, *J Mater. Chem.*, 2012, **22**, 18505-18513.
- [40] M. Shyamal, S. Maity, P. Mazumdar, G. P. Sahoo, R. Maity and A. Misra, *J. Photochem. Photobiol. A: Chem.*, 2017, **342**, 1-14.
- [41] M. Shyamal, P. Mazumdar, S. Maity, G. P. Sahoo, G. Salgado-Morán and A. Misra, *J. Phys. Chem. A*, 2016, **120**, 210-220.
- [42] A. S. M. Islam, M. Sasmal, D. Maiti, A. Dutta, B. Show and M. Ali, *ACS omega*, 2018, **3**, 10306-10316.
- [43] V. Srinivasan, M. A. Jhonsi, N. Dhenadhayalan, K. C. Lin, M. Jaccob and A. Kathiravan, *Chemistry Select*, 2017, **2**, 1353-1359.
- [44] H. Zhang, Y. Wang, K. Shao, Y. Liu, S. Chen, W. Qiu, X. Sun, T. Qi, Y. Ma, G. Yu, Z. Su and D. Zhu, *Chem. Comm.*, 2006, DOI: 10.1039/B515433B, 755-757.
- [45] K.-S. Focsaneanu and J. C. Scaiano, *Photochem. Photobiol. Sci.*, 2005, **4**, 817-821.

-
- [46] K.-S. Focsaneanu and J. Scaiano, *Photochem. Photobiol. Sci.*, 2005, **4**, 817-821.
- [47] J. Chaudhary, V. Mittal, S. Mishra, A. Daiya, R. Chowdhury, I. R. Laskar and R. K. Roy, *J. Phys. Chem. C*, 2020, **124**, 15406-15417.
- [48] M. Frisch, G. Trucks, H. Schlegel, G. Scuseria, M. Robb, J. Cheeseman, J. Montgomery Jr, T. Vreven, K. Kudin and J. Burant, 2013.
- [49] J. Sun, P. Xue, J. Sun, P. Gong, P. Wang and R. Lu, *J. Mater. Chem.C.*, 2015, **3**, 8888-8894.
- [50] P. Xue, J. Sun, B. Yao, P. Gong, Z. Zhang, C. Qian, Y. Zhang and R. Lu, *Chem. Eur. J.*, 2015, **21**, 4712-4720.
- [51] Y. Zhan, J. Zhao, P. Yang and W. Ye, *Rsc. Adv.*, 2016, **6**, 92144-92151.
- [52] Y. Zhan, P. Yang, G. Li, Y. Zhang and Y. Bao, *New J. Chem.*, 2017, **41**, 263-270.
- [53] A. Chowdhury and P. S. Mukherjee, *J. Org. Chem.*, 2015, **80**, 4064-4075.
- [54] S. Ghosh and P. S. Mukherjee, *Organometallics*, 2008, **27**, 316-319.
- [55] C. Vijayakumar, G. Tobin, W. Schmitt, M.-J. Kim and M. Takeuchi, *Chem. Comm.*, 2010, **46**, 874-876.
- [56] H. Zhou, M. H. Chua, B. Z. Tang and J. Xu, *Polym. Chem.*, 2019, **10**, 3822-3840.
- [57] A. Shrivastava and V. B. Gupta, *Chron. Young Sci.*, 2011, **2**, 21.
- [58] H. Furukawa and O. M. Yaghi, *J. Am. Chem. Soc.*, 2009, **131**, 8875-8883.
- [59] Z. Kang, Y. Peng, Y. Qian, D. Yuan, M. A. Addicoat, T. Heine, Z. Hu, L. Tee, Z. Guo and D. Zhao, *Chem. Mater.*, 2016, **28**, 1277-1285.
- [60] S.-Y. Ding, J. Gao, Q. Wang, Y. Zhang, W.-G. Song, C.-Y. Su and W. Wang, *J. Am. Chem. Soc.*, 2011, **133**, 19816-19822.
- [61] G. Lin, H. Ding, D. Yuan, B. Wang and C. Wang, *J. Am. Chem. Soc.*, 2016, **138**, 3302-3305.
- [62] R.-R. Liang and X. Zhao, *Org. Chem. Front.*, 2018, **5**, 3341-3356.
- [63] M. E. Davis, *Nature*, 2002, **417**, 813.
- [64] A. J. Howarth, Y. Liu, P. Li, Z. Li, T. C. Wang, J. T. Hupp and O. K. Farha, *Nat. Rev. Mater.*, 2016, **1**, 15018.
- [65] S. Qiu, M. Xue and G. Zhu, *Chem. Soc. Rev.*, 2014, **43**, 6116-6140.
- [66] W. Lu, Z. Wei, Z.-Y. Gu, T.-F. Liu, J. Park, J. Park, J. Tian, M. Zhang, Q. Zhang and T. Gentle III, *Chem. Soc. Rev.*, 2014, **43**, 5561-5593.
- [67] C. Wang, X. Liu, N. K. Demir, J. P. Chen and K. Li, *Chem. Soc. Rev.*, 2016, **45**, 5107-5134.
- [68] G. Zhang and M. Mastalerz, *Chem. Soc. Rev.*, 2014, **43**, 1934-1947.
-

- [69] F. Beuerle and B. Gole, *Angew. Chem., Int. Ed.*, 2018, **57**, 4850-4878.
- [70] Y.-F. Han, Y.-X. Yuan and H.-B. Wang, *Molecules*, 2017, **22**, 266.
- [71] A. Karmakar, R. Illathvalappil, B. Anothumakkool, A. Sen, P. Samanta, A. V. Desai, S. Kurungot and S. K. Ghosh, *Angew. Chem., Int. Ed.*, 2016, **55**, 10667-10671.
- [72] A. Trewin and A. I. Cooper, *Angew. Chem., Int. Ed.*, 2010, **49**, 1533-1535.
- [73] W. Wang, M. Zhou and D. Yuan, *J. Mater. Chem. A*, 2017, **5**, 1334-1347.
- [74] L. Tan and B. Tan, *Chem. Soc. Rev.*, 2017, **46**, 3322-3356.
- [75] L. Monnereau, M. Nieger, T. Muller and S. Bräse, *Adv. Funct. Mater.*, 2014, **24**, 1054-1058.
- [76] L. J. Abbott and C. M. Colina, *Macromolecules*, 2014, **47**, 5409-5415.
- [77] K. Shen, L. Zhang, X. Chen, L. Liu, D. Zhang, Y. Han, J. Chen, J. Long, R. Luque, Y. Li and B. Chen, *Science*, 2018, **359**, 206-210.
- [78] Q. Chen, D.-P. Liu, J.-H. Zhu and B.-H. Han, *Macromolecules*, 2014, **47**, 5926-5931.
- [79] C. Su, H. He, L. Xu, K. Zhao, C. Zheng and C. Zhang, *J. Mater. Chem. A*, 2017, **5**, 2701-2709.
- [80] Y. Xu, S. Jin, H. Xu, A. Nagai and D. Jiang, *Chem. Soc. Rev.*, 2013, **42**, 8012-8031.
- [81] Q. Liu, Z. Tang, M. Wu and Z. Zhou, *Polym. Int.*, 2014, **63**, 381-392.
- [82] N. B. McKeown and P. M. Budd, *Chem. Soc. Rev.*, 2006, **35**, 675-683.
- [83] B. Shrimant, S. V. Shaligram, U. K. Kharul and P. P. Wadgaonkar, *J. Polym. Sci. Pol. Chem.*, 2018, **56**, 16-24.
- [84] C. S. Diercks and O. M. Yaghi, *Science*, 2017, **355**, eaal1585.
- [85] F. Yuan, J. Tan and J. Guo, *Sci. China. Chem*, 2018, **61**, 143-152.
- [86] M. S. Lohse, T. Stassin, G. Naudin, S. Wuttke, R. Ameloot, D. De Vos, D. D. Medina and T. Bein, *Chem. Mater.*, 2016, **28**, 626-631.
- [87] R. P. Bisbey and W. R. Dichtel, *ACS Cent. Sci.*, 2017, **3**, 533-543.
- [88] S. Karak, S. Kumar, P. Pachfule and R. Banerjee, *J. Am. Chem. Soc.*, 2018, **140**, 5138-5145.
- [89] Y. Zhang, P. Lu, Y. Yuan, L. Xu, H. Guo, X. Zhang and L. Xu, *CrystEngComm*, 2017, **19**, 4713-4719.
- [90] Y.-w. Wu, A.-j. Qin and B. Z. Tang, *Chin. J. Polym. Sci.*, 2017, **35**, 141-154.
- [91] W. Wu, S. Ye, R. Tang, L. Huang, Q. Li, G. Yu, Y. Liu, J. Qin and Z. Li, *Polymer*, 2012, **53**, 3163-3171.
- [92] R. Hu, J. L. Maldonado, M. Rodriguez, C. Deng, C. K. Jim, J. W. Lam, M. M. Yuen, G. Ramos-Ortiz and B. Z. Tang, *J. Mater. Chem.C.*, 2012, **22**, 232-240.

-
- [93] H. Namgung, J. J. Lee, Y. J. Gwon and T. S. Lee, *RSC Advances*, 2018, **8**, 34291-34296.
- [94] H. Zhou, X. Wang, T. T. Lin, J. Song, B. Z. Tang and J. Xu, *Polym. Chem.*, 2016, **7**, 6309-6317.
- [95] Q. Yin, J. Lu, Q. Lv and B. Han, *Materials Letters*, 2020, **269**, 127645.
- [96] H. Zhang, F. Tao, Y. Cui and H. Wu, *Mater. Chem. Phys.*, 2020, **243**, 122657.
- [97] F. Nabeel, T. Rasheed, M. F. Mahmood and S. U.-D. Khan, *J. Mol. Liq.*, 2020, **308**, 113034.
- [98] Y. Chen, H. Bai, Q. Chen, C. Li and G. Shi, *Sens. Actuators B Chem.*, 2009, **138**, 563-571.
- [99] S. Dineshkumar, A. Raj, A. Srivastava, S. Mukherjee, S. S. Pasha, V. Kachwal, L. Fageria, R. Chowdhury and I. R. Laskar, *ACS Appl. Mater. Interfaces*, 2019, **11**, 31270-31282.
- [100] T. Mallegol, S. Gmouh, M. A. A. Meziane, M. Blanchard-Desce and O. Mongin, *Synthesis*, 2005, **2005**, 1771-1774.
- [101] M. Myilsamy, M. Mahalakshmi, N. Subha and V. Murugesan, *J. Nanosci. Nanotechnol.*, 2018, **18**, 925-935.
- [102] G. Rasines, C. Macías, M. Haro, J. Jagiello and C. O. Ania, *Microporous Mesoporous Mater.*, 2015, **209**, 18-22.
- [103] I. A. Mastrangelo, M. Ahmed, T. Sato, W. Liu, C. Wang, P. Hough and S. O. Smith, *J. Mol. Biol.*, 2006, **358**, 106-119.
- [104] X. Zhou, X. Cheng, W. Feng, K. Qiu, L. Chen, W. Nie, Z. Yin, X. Mo, H. Wang and C. He, *Dalton Trans.*, 2014, **43**, 11834-11842.
- [105] Z. U. Rahman, N. Wei, Z. Li, W. Sun and D. Wang, *New J. Chem.*, 2017, **41**, 14122-14129.
- [106] S. Dineshkumar and I. R. Laskar, *Polym. Chem.*, 2018, **9**, 5123-5132.
- [107] A. M. Bonch-Bruevich, E. N. Kaliteevskaya, T. K. Razumova, A. D. Roshal' and A. N. Tarnovskii, *Opt. Spectrosc.*, 2000, **89**, 216.
- [108] R. Hu, J. L. Maldonado, M. Rodriguez, C. Deng, C. K. W. Jim, J. W. Y. Lam, M. M. F. Yuen, G. Ramos-Ortiz and B. Z. Tang, *J Mater. Chem.*, 2012, **22**, 232-240.
- [109] P. Alam, G. Kaur, V. Kachwal, A. Gupta, A. Roy Choudhury and I. R. Laskar, *J. Mater. Chem. C*, 2015, **3**, 5450-5456.
- [110] L. M. Martelo, L. F. Marques, H. D. Burrows and M. N. Berberan-Santos, 2019.
- [111] H. Namgung, J. J. Lee, Y. J. Gwon and T. S. Lee, *RSC Adv.*, 2018, **8**, 34291-34296.
- [112] S. J. Toal and W. C. Trogler, *J Mater. Chem.*, 2006, **16**, 2871-2883.
-

- [113] S. Fan, G. Zhang, G. H. Dennison, N. FitzGerald, P. L. Burn, I. R. Gentle and P. E. Shaw, *Adv. Mater.*, 2020, **32**, 1905785.
- [114] A. S. Tanwar, S. Hussain, A. H. Malik, M. A. Afroz and P. K. Iyer, *Acs Sensors*, 2016, **1**, 1070-1077.
- [115] A. S. Tanwar, L. R. Adil, M. A. Afroz and P. K. Iyer, *ACS Sensors*, 2018, **3**, 1451-1461.
- [116] I. L. Medintz, A. R. Clapp, H. Mattoussi, E. R. Goldman, B. Fisher and J. M. Mauro, *Nat. Mater.*, 2003, **2**, 630.
- [117] V. Kachwal, M. Joshi, V. Mittal, A. R. Choudhury and I. R. Laskar, *Sens. Biosensing. Res.*, 2019, **23**, 100267.
- [118] J. R. Lakowicz, *Principles of fluorescence spectroscopy*, Springer Science & Business Media, 2013.
- [119] K. Simunovic, L. Slokar and S. Havrlisan, *Philos. Mag.*, 2017, **97**, 248-268.

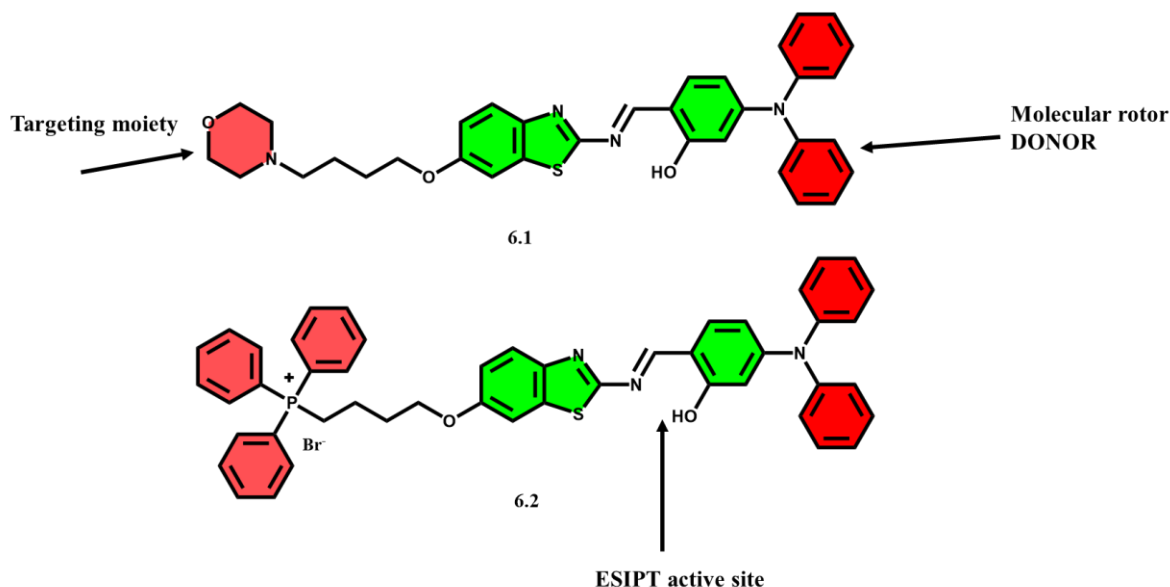
Future Scope of the Work

Design and synthesis of “Aggregation-induced emission (AIE)” active organic and metal complex based molecular machines.

1. Strategically designing the AIE active probes for sensitive sensing of important environmental parameters (temperature, viscosity, polarity, pressure & pH),
2. As, the parameters (temperature, viscosity, polarity, pressure & pH) could be utilized for sensing any change in the pathological conditions inside the cells. Therefore, tuning the designed AIE active probes appropriately for target-specific imaging.
3. For probing explosive materials selectively and sensitively.
4. Utilization of these probes in theranostic applications.

Design and synthesis of new “Aggregation-induced emission (AIE)” active organic and metal compounds for ratiometric probe intracellular pH.

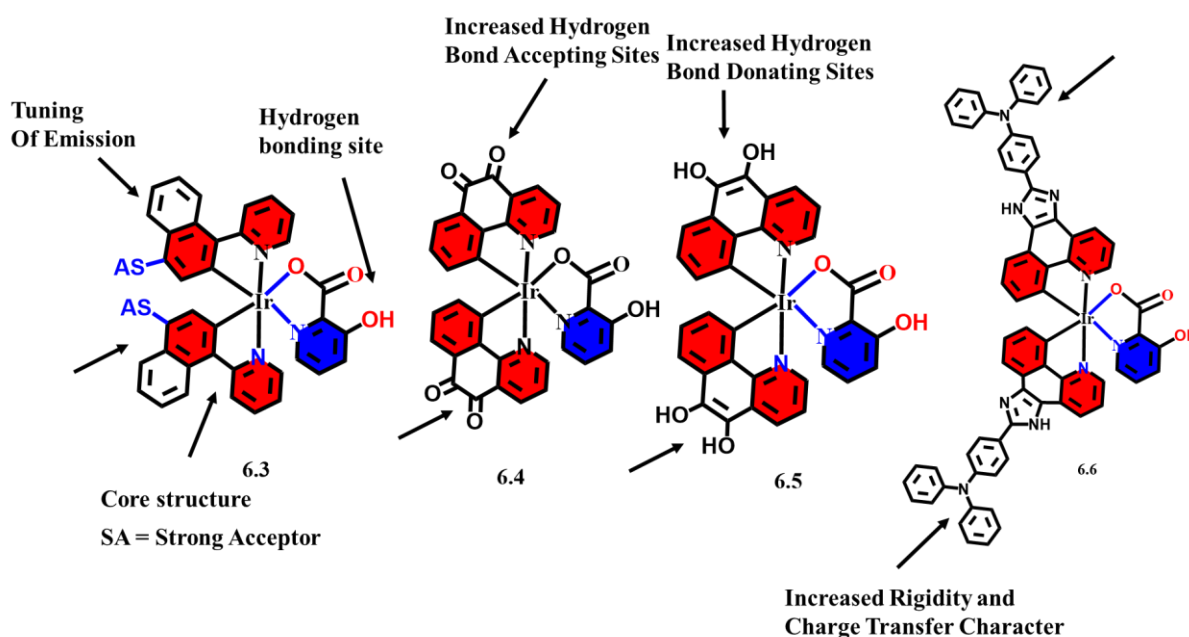
Recently, we developed a combination of both “Excited State Intramolecular Proton Transfer” (ESIPT) and “Aggregation-induced emission” (AIE) active Schiff Base based type of materials are efficient for the multi stimuli sensing. A further opportunity for improving the present probe is by introducing more rigid donor type rotor to have high quantum efficiency and introducing organelle-specific moiety for targeting organelle.



Scheme 6.1 Chemical structure of modified Schiff base.

Design and synthesis of new “Aggregation-induced emission (AIE)” active biscyclometalated complex for efficient multi-stimuli probes.

Bis Cyclometalated Ir(III) complex can be modified by using the present complex structure. The more hydrogen bonding sites would help the complex for ratiometric changes. The emission of the complex could be tuned to the NIR region by increasing the accepting ability of the ancillary ligand. Selective and sensitive detection of different proteins can be done by combining both hydrogen bonding and hydrophobic effect. Increased charge transfer character would help the complex to be more sensitive to the polarity of the medium. The complex could be a more efficient multi-stimuli probe.



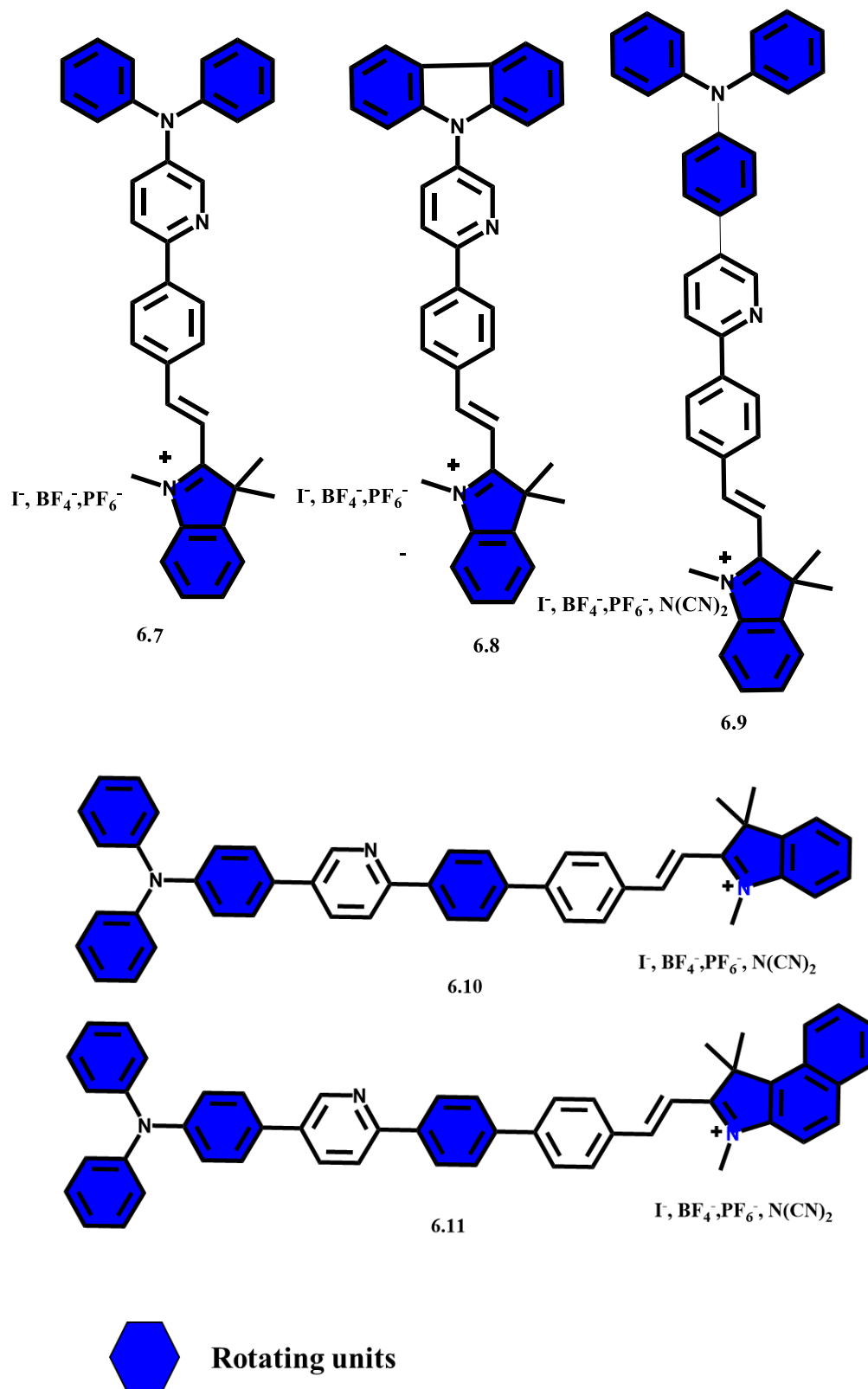
Scheme 6.2 Chemical structure of modified Ir (III) bis-cyclometallated Complex.

Design and synthesis of new FMRs (Fluorescence molecular rotors) for target-specific intracellular viscosity detection.

Viscosity is one of the important factors for the detection of any pathological changes (structural changes, changes in ROS generation etc.) caused inside the cells. We have successfully explained that viscosity could lead us to detect unhealthy cells. Moreover, we have seen that changing the counterion also changes the property of the probe. Therefore, by little modification of the probe, it could be utilized for theranostic applications. By increasing the greater number of molecular rigid rotor group, the fluorescence contrast could be increased.

Moreover, the different rotating speeds of the rotor would be helpful for efficient calibration of the viscosity. Furthermore, functionalization of, these probes by specific organelle targeting moiety would make these probes highly efficient for location-specific intracellular

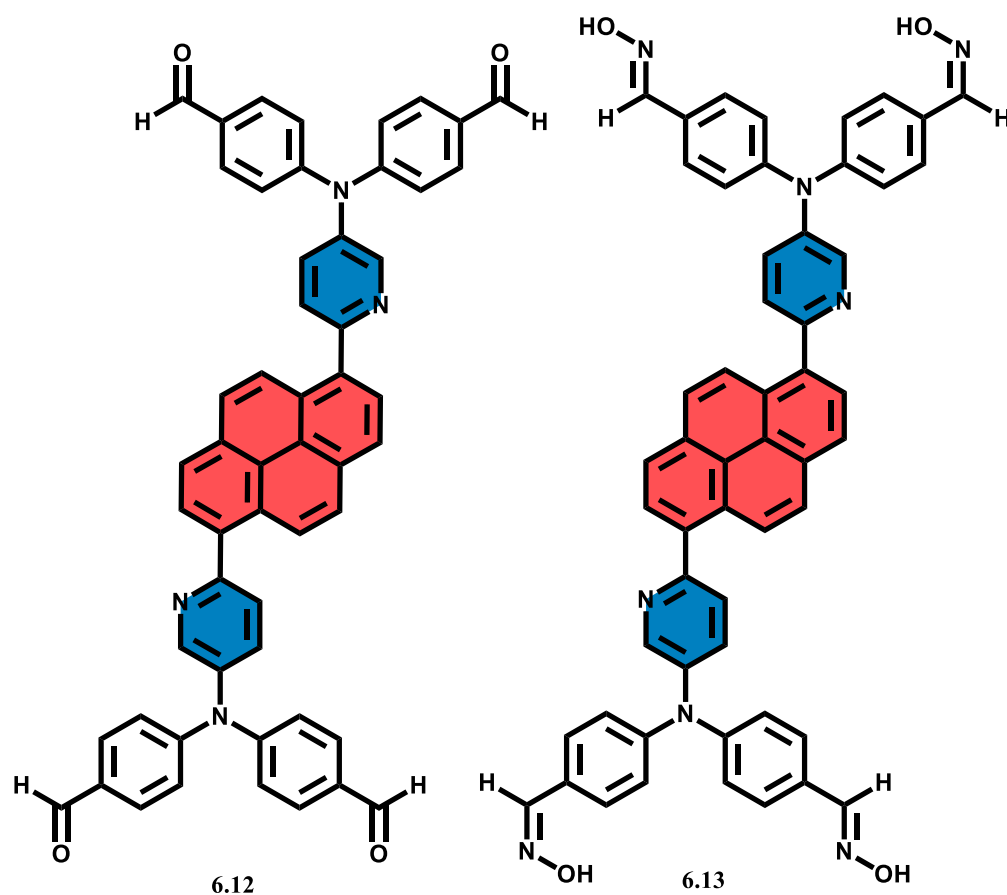
viscosity sensing. The twisted conformations help the probe to be more flexible and sensitive to the viscous medium.



Scheme 6.3 Chemical structure of modified Viscosity sensitive probes.

Design and synthesis of new “Aggregation-induced emission (AIE)” active compounds for nitro explosive vapor phase sensing

In present days nitro explosive sensing in the vapour phase is very important to stop the mass killing by the terrorists. We have successfully demonstrated tuning of emission in small poly aromatic pyrene-based molecules. By modifying the molecular rotors over the pyrene molecules would increase the quantum efficiency. The donor and acceptor nature in the molecule would help us to lower the LUMO level of the probe molecules for efficient PET (photoinduced electron transfer).



Scheme 6.4 Chemical structure of modified pyrene probes for sensitive nitro explosive detection.

List of Publications [A-1]

1. Sengottuvelu Dineshkumar^{#*}, **Vishal Kachwal**[#], Pramod Raichure, Tarun Raghav and Inamur Rahaman Laskar, "Aggregation-induced enhanced emission (AIEE) Active Conjugated Mesoporous Oligomers (CMOs) with Improved Quantum Yield and Low-cost Trace Nitro Aromatic Explosives Detection" ACS Appl. Mater. Interfaces, 2020, 12, 31875-31886.
 2. **Vishal Kachwal**, Parva Sarmah, Amrit Sarmah, Shibasish Chowdhury, Inamur Raskara. "Multistimuli Responsive Heteroleptic Iridium (III) Complex: Role of Hydrogen Bonding in Probing Solvent, pH and Bovine Serum Albumin (BSA)." Journal of Materials Chemistry C, 2020, 8, 6605 - 6614.
 3. **Vishal Kachwal**, Mayank Joshi, Vibhor Mittal, Angshuman Roy Choudhury, Inamur Rahaman Laskar. Strategic design and synthesis of AIEE (Aggregation Induced Enhanced Emission) active push-pull type pyrene derivatives for the ultrasensitive detection of explosives" Sensing and Bio-Sensing Research, 2019, 23, 100267.
 4. **Vishal Kachwal**, I. S. Vamsi Krishna, Leena Fageria, Jagrity Chaudhary, Ram Kinkar Roy, Rajdeep Chowdhury, Inamur Rahaman Laskar, Exploring the Hidden Potential of Benzothiazole Based Schiff base "AIE and ESIPT" active for pH Sensing, Intracellular Imaging and Ultrasensitive & Selective detection of Aluminium (Al³⁺). Analyst, 2018, 143, 3741-3748.
 5. **Vishal Kachwal**, Parvej Alam, Hare Ram Yadav, Sheik Saleem Pasha. , Angshuman R. Choudhury, Inamur Rahaman Laskar, "Simple ratiometric push-pull with an 'aggregation induced enhanced emission active pyrene derivative: a multifunctional and highly sensitive fluorescent sensor". New Journal of Chemistry, 2018, 42(2), 1133-1140.
 6. Sengottuvelu Dineshkumar, Abhishek Raj, Abhilasha Srivastava, Sudeshna Mukherjee, Sheik Saleem Pasha, **Vishal Kachwal**, Leena Fageriab, Rajdeep Chowdhury and Inamur Rahaman Laskar. Facile Incorporation of 'Aggregation Induced Emission' Active Conjugated Polymer into Mesoporous Silica Hollow Nanospheres: Synthesis, Characterization, Photophysical Studies and Application in Bioimaging". ACS Applied Materials & Interfaces, 2019, 11, 31270-31282.
-

List of Publications [A-1]

7. Parvej Alam, **Vishal Kachwal**, Inamur Rahaman Laskar "A Multi-stimuli Responsive "AIE" Active Salicylaldehyde-based Schiff Base for Sensitive Detection of Fluoride". *Sensors and Actuators B*, 2016, 228, 539. Parvej Alam, Gurpreet Kaur,
8. Parvej Alam, Gurpreet Kaur, **Vishal kachwal**, Asish Gupta, Angshuman Roy Chaudhury and Inamur Rahman Laskar. Highly Sensitive Explosive Sensing by "Aggregation Induced Phosphorescence" Active Cyclometalated Iridium(III) Complexes". *Journal of Materials Chemistry C*, 2015, 3, 5450-5456.

Research Article Under Preparation

1. **Vishal Kachwal**, Abhilasha Srivastava, Sudeshna Mukherjee, Rajdeep Chowdhury and Inamur Rahaman Laskar Viscosity Triggered Induced Emission (VIE) from a light Non-luminiscent Cyanine Based Molecular Motor: An Efficient Fluorescence Tool to Distinguish the Cancerous Cell (Under Review).
 2. **Vishal Kachwal**, Ram Prasad Bhatt, Mayank Jhoshi and Inamur Rahaman Laskar, "Substitution effect on ancillary ligand of Ir(III) monocyometalated complex with Temperature-induced enhanced emission (TIEE)"(Under review).
-

List of Oral/Poster Presented in Conferences / Workshops [A-2]

- GIDW 2020(Global Inorganic Discussion Weekdays) Virtual Poster Competition 11-13 July 2020. (**Best Dalton Transaction Poster award**)
 - National Symposium on Convergence of Chemistry & Materials (CCM-2019) BITS Pilani, Hyderabad Campus, during 17-18 December 2019. (**Poster**)
 - International Conference on Energy, Functional Materials and Nanotechnology & Sustainable Environment Management (ICEFN-SEM 2019) held at Kumaun University, during May 24-26 Nainatal, India (**Oral**).
 - The sixteenth Theoretical Chemistry Symposium (TCS-2019) held at BITS PILANI, Pilani campus, India, during February 13-16 2019 (**Participated**)
 - International Conference by Indian Society of Chemists and Biologists (ISCBC-2018) held at Manipal University, Jaipur, India, during January 11-15 (**Poster**)
 - National conference on New Frontiers in Chemistry - From Fundamentals to Applications (NFCFA 2017), held at BITS Pilani, Goa Campus, India, during 28-29 January
 - International conference on Nano and Functionalized Materials (NFM-2017) held at BITS Pilani, Pilani Campus, India, during 15-18 November, 2017 (**Best Poster**)
 - National conference on Organic Chemistry in Sustainable Development: Recent Advances and Future Challenges (OCSD-2016), held at BITS Pilani, Pilani Campus, India, during 29-30 August, 2016 (**Poster**)
 - International conference on Nascent Developments in Chemical Sciences: Opportunities for Academia-Industry Collaboration (NDCS-2015) held at BITS Pilani, Pilani campus, India, during 13-18 October, 2015 (**Poster**)
 - National workshop on Basic Aspects of Quantum and Theoretical Chemistry and Applications (BAQTCA 2015) held at Poornima University, Jaipur, during 12-16 August, 2015. (**Participated**)
 - National conference on Nano and Functionalized Materials (NFM-2014), BITS Pilani, Pilani Campus, India, during 7-8 November, 2014 (**Poster**)
-

Brief Biography of the Candidate [A-3]

Name : Vishal Kachwal

Born at Mancheria, Telengana, India

He did his M.Sc 5yrs Integrated Chemistry from Chaitanya Post Graduate College, Deemed to be university, Hanamkonda, Warangal, Telengana (India) in 2014. He has been working on the project "Design and synthesis of smart solid luminescent materials: Applications in Sensing and Bioimaging". He has published eight research articles in peer reviewed international journals and presented papers in ten conferences/symposiums.

Permanent address:-

Vishal Kachwal
S/o:- Venugopal Kachwal
19-495/4, Shree Shyam Kunj, ward no-16th
RAMNAGAR
MANCHERIAL, TELANGANA 504208
India

Email:- vishkachwal4@gmail.com

Brief Biography of the Supervisor [A-4]

Currently, Prof. Inamur Rahaman Laskar has been employed as an Associate Professor at Department of Chemistry, Birla Institute of Technology & Science, Pilani Campus, Pilani, Rajasthan, India. He was awarded Ph. D. degree in Inorganic Chemistry from 'Indian Association for the Cultivation of Science (IACS)', Kolkata, India in 2000. He was working as a Lecturer at Ananda Mohan College (affiliated to the University of Calcutta), Kolkata, India during Sept. 1999–July 2001. He worked as a postdoctoral associate at NCTU Taiwan, during April 2002–March 2006 and NTHU Taiwan, during July 2001–Feb. 2002. Further, he did his Postdoctoral (as JSPS Postdoctoral Fellow) research work at Kochi University, Japan in the period of April 2006–March 2008. He joined the Department of Chemistry, BITS Pilani on August 2008. His current research interest is mainly focused on the design and syntheses of novel luminescent and AIE active luminescent materials, exploring the AIE mechanism, detailed study of luminescent behaviour and targeted these materials in various applications such as applications in bio-imaging and cancer therapy, sensing (explosive/toxic analytes from solution and vapor phase), mechanofluoro chromic, piezochromic and organic light-emitting diodes etc. Modelling of the synthesized luminescent materials to explore the excited state properties and validation into the spectroscopic data of these complexes remains his further interest.

Email:- ir_laskar@pilani.bits-pilani.ac.in
